Solid-State NMR Studies of Polymeric and Biomembranes

Justin D. Spano

Dissertation submitted to the faculty of the Virginia Polytechnic Institute and State University in partial fulfillment of the requirements for the degree of

Doctor of Philosophy
In
Chemistry

Sungsool Wi, Chair
John R. Morris
Louis A. Madsen
Harry C. Dorn
Gordon T. Yee

4 May 2011
Blacksburg, Virginia

Keywords: solid-state NMR, dynamics, relaxation time, magic-angle-spinning, reverse osmosis, antimicrobial peptide

Solid-State NMR Studies of Polymeric and Biomembranes

Justin D. Spano

ABSTRACT

The objective of this dissertation is to demonstrate different applications of ssNMR, with particular emphasis on uses in polymeric and biosciences. First, dynamics investigations on two polymers will be discussed: (1) disulfonated poly(arylene ether sulfone)s /poly(ethylene glycol) blends (BPS-20_PEG), which are under development as chlorine-resistant reverse osmosis (RO) membrane alternatives to aromatic polyamide (PA) technology, and (2) poly(arylene ether sulfone)s modified with 1,4-cyclohexyl ring units to improve processability. Simple cross-polarization magic-angle-spinning (CPMAS) experiments compared the chlorine tolerance of BPS-20_PEG and PA. Techniques capable of detecting motional geometries and rates on timescales from nanoseconds to seconds, including relaxation time measurements, were applied. Correlations were established between relaxation time and water permeability for the RO membranes, and between relaxation time and polydispersity in the 1,4- cyclohexyl ring modified polymer.

Next, ^{31}P and ^{2}H static ssNMR experiments evidencing the formation of toroidal pores and thinned bilayers in oriented zwitterionic and anionic phospholipid bilayers, (biomembrane mimetic systems), by the antimicrobial peptides (AMPs) magainin-2 and aurein-3.3, will be mentioned. The toroidal pore geometries induced by magainin-2 were different than those produced by aurien-3.3. The most prominent features were observed in ^{2}H spectra, implying greater interaction of the peptides with hydrophobic lipid acyl chains.

Following this, a new two-dimensional homonuclear dipolar recoupling MAS experiment, capable of correlating long range ^{13}C-^{13}C spin pairs in a uniformly/ extensively ^{13}C-labeled biomolecule, will be introduced. This technique was demonstrated on ^{13}C-labeled versions of Glutamine and Glycine-Alanine-Leucine. Experiments involving the recoupling of all ^{13}C-^{13}C spin pairs, and experiments with

selective recoupling using Gaussian or cosine-modulated Gaussian pulses, were demonstrated.

Finally, work using static ^{1}H- ^{13}C CP ssNMR to selectively detect interfacial water around hydrophobic C_{60} will be recounted. This project exploited the distance limitation of CP, and ^{1}H spin-lattice relaxation times, to separate the influence of bulk and interfacial water on the spectra. Results indicated that the tumbling of interfacial water is slowed by a factor of 10^{5} compared to bulk water, providing it with a solid-like character, and allowing the hydration shell to be stable at temperatures above the freezing point of water.

Acknowledgements

Above all, I praise God. While that is really all that is needed, and there is no way to be complete in listing all he deserves praise for, I simply acknowledge his providing opportunities here to learn and see this facet of his world, and for his carrying me through the experiences.

I thank my research advisor, Prof. Sungsool Wi, for patiently and kindly leading me through my research, instilling in me an appreciation for magnetic resonance science, and helping me to develop into a better scientist. His enthusiasm and curiosity is inspiring. It is rare to not see him smiling and laughing, which always made for a light mood.

I thank my family and friends; especially my father, Frank, mother, Donna, and siblings, Evan and Dianna. They have always been a constant source of love and support.

I could not have accomplished what I did without the guidance from my committee: Prof. Sugsool Wi, Prof. Harry Dorn, Prof. Gordon Yee, Prof. John Morris, and Prof. Louis Madsen. Their constructive advice greatly helped in my development. Prof. Dorn and Prof. Madsen have been instrumental in helping to cement within me an appreciate for magnetic resonance science. Additionally, I am thankful that Prof. Morris allowed me to work with his research group the summer before my first semester, and Prof. Yee allowed me to work with his research group during the Summer of 2004 as part of a NSF REU program, which is what introduced me to Virginia Tech.

I thank Prof. Mark Anderson for being a mentor during my REU program and helping me to return to Virginia Tech.

I am very thankful for the friends and professors I had during my undergraduate education at Lock Haven University of Pennsylvania. My time there stands as one of the highest points in my life.

I am deeply indebted to Ali Cross, Sami Codario, Ricardo Boulware, Kelly Epps, Emily Mikkelson, and Allison Wood for all of their help. They deserve more than this acknowledgement provides.

I thank Prof. Cecil Dybowski, Prof. Tatyana Polenova, and Dr. Alex Vega for having introduced me to solid-state NMR and the power of NMR science.

Attribution

Below is described the contributions of the co-authors for the manuscripts comprising the chapters in this dissertation.

Prof. Sungsool Wi (Department of Chemistry, Virginia Tech) served as research advisor. He guided and collaborated with the author in all aspects of the research portion of graduate studies including conducting/analyzing experiments, and preparing written manuscripts. Prof. Wi also guided Dr. Chul Kim and Dr. Eun-Kyung Park in the work described in Chapter 5, and Ms. Ying Chen in the work described in Chapter 4.

Dr. Chang Hyun Lee (Department of Chemistry, Virginia Tech) provided the polymer samples studied in Chapters 2 and 3.

Mr. Desmond VanHouten (Macromolecules and Interfaces Institute, Virginia Tech) conducted dynamic mechanical analysis studies of the polymers described in Chapter 2.

Dr. Ozma Lane (Macromolecules and Interfaces Institute, Virginia Tech) conducted AFM measurements of the polymers described in Chapter 2.

Prof. James E. McGrath (Department of Chemistry and Macromolecules and Interfaces Institute, Virginia Tech) guided Dr. Lee, Mr VanHouten, and Dr. Lane in the research towards the development of the polymers described in Chapters 2 and 3.

Mr. Jianbo Hou (Department of Chemistry and Macromolecules and Interfaces Institute, Virginia Tech) conducted water diffusion measurements on the polymers described in Chapter 2.

Prof. Louis A. Madsen ((Department of Chemistry and Macromolecules and Interfaces Institute, Virginia Tech) guided the research on water diffusion measurements described in Chapter 2.

Mr. Joseph Cook (Department of Chemical Engineering, Center for Energy and Environmental Resources, University of Teaxas at Austin) tested the reverse osmosis properties of the polymers described in Chapters 2 and 3.

Ms. Hee Jeung Oh (Department of Chemical Engineering, Center for Energy and Environmental Resources, University of Teaxas at Austin) tested the reverse osmosis properties of the polymers described in Chapter 2.

Mr. Geoffrey M. Geise (Department of Chemical Engineering, Center for Energy and Environmental Resources, University of Teaxas at Austin) provided helpful discussions for the work described in Chapter 2.

Mr. Wei Xie (Department of Chemical Engineering, Center for Energy and Environmental Resources, University of Teaxas at Austin) conducted experiments on the polyamide samples described in chapter 2.

Prof. Benny D. Freeman (Department of Chemical Engineering, Center for Energy and Environmental Resources, University of Teaxas at Austin) guided Mr. Joseph Cook, Mr. Wei Xie, and Ms. Hee Jeung Oh in the work described in Chapters 2 and 3.

Mr. Bin Zhang (Department of Chemistry and Macromolecules and Interfaces Institute, Virginia Tech) provided in the polymer samples described in Chapter 4.

Ms. Ying Chen (Department of Chemistry, Virginia Tech) simulated the centerband-only detection of exchange (CODEX) data in Chapter 4.

Prof. Richard Turner (Department of Chemistry and Macromolecules and Interfaces Institute, Virginia Tech) guided Mr. Bin Zhang in the polymer synthesis/characterization for the polymers described in Chapter 4.

Dr. Chul Kim (Department of Chemistry, Hannam University), a former postdoctoral researcher under Prof. Wi, conducted the majority of the sample prepartation, experiments, and data analysis in Chapter 5.

Dr. Eun-Kyung Park (Department of Chemistry, Virginia Tech), a former visiting scientist under Prof. Wi, aided in preparing samples described in Chapter 5.

Prof. William A. Ducker (Department of Chemical Engineering, Virginia Tech) provided the C_{60} samples described in Chapter 8.

Additionally, Dr. Lee, Prof. McGrath, Prof. Madsen, Prof. Ducker, Prof. Turner, Mr. Hou, Ms. Chen, Dr. Kim, and Mr. Zhang aided in understanding NMR data through many helpful discussions for chapters to which they have been attributed.

Table of Contents

Page

List of Figures

List of Tables

Chapter 1
Introduction to Nuclear Magnetic Resonance Spectroscopy

1.1. History, Breadth, and the Zeeman Interaction

Since the discovery of the nuclear magnetic resonance phenomena in 1946,[1,2] nuclear magnetic resonance spectroscopy (NMR) has evolved into a cornerstone analytical technique for investigations of the structure and dynamics of molecules disregard of the sample's morphology. It is a non-destructive method, so samples are preserved for experiments with different technique that can complement or validate NMR results. NMR is made possible by the fact that some nuclei undergo radio-frequency transitions between nuclear spin energy levels defined by the Zeeman quantized spin angular momentum. This spin angular momentum is a quantum mechanical property intrinsic to the nucleus in the external magnetic field. The nuclear spin angular momentum quantum number, I, is an integer or half-integer for NMR active nuclei (I = 0 designates an NMR-inactive isotope, and I > ½ designates a quadrupolar nucleus). NMR-active nuclei are routinely referred to simply as "spins"; henceforth the terms "nuclei" or "nucleus" will be referring to one that is NMR-active, and "spin" ("spins") and "nucleus"("nuclei") may be used interchangeably. The potential of NMR to provide a wealth of valuable data is evidenced by the fact that there are over 100 NMR-active isotopes, spanning ~79 elements.[3] NMR's capability for elucidating structural and dynamic information has led to advancements in a wide range of fields, including biological and materials sciences.[4] Solid-state NMR(ssNMR), the focus of this dissertation, in particular can be recognized as a powerful tool because it provides anisotropic tensorial information of nuclear spin interactions and is not limited by sample properties such as size, solubility, long-range order, or crystallinity.

The spin property of nuclei imparts to them a magnetic dipole moment, $\vec{\mu}_i$. When a sample, an ensemble of *i* spins, is placed in a magnetic field, $\vec{B}$, (i.e., $\vec{B}_0$ the applied external magnetic field of the NMR spectrometer, which defines the z-axis of a lab frame Cartesian coordinate system) the magnetic moments can align with $\vec{B}$ and produce a net magnetization vector, $\vec{M}$ (Eq.1.1). This interaction, the Zeeman interaction, is the strongest interaction that the nuclei experience under the influence of $\vec{B}_0$, and is described by Eq.1.2 and1.3:

$$\vec{M} = \sum_i \vec{\mu}_i \tag{1.1}$$

$$\hat{H}_z = -\hat{\mu} \bullet \vec{B}_0 \tag{1.2}$$

where

$$\hat{\mu} = \gamma \hbar \hat{I} \tag{1.3}$$

In the equations above $\hat{H}_z$ is the Zeeman Hamiltonian, $\hat{\mu}$ is the nuclear magnetic momement operator, γ is the magnetogyric ratio, ħ is Planck's constant divided by 2π, and $\hat{I}$ is the nuclear spin angular momentum operator ($\hat{I}_z$ for $\hat{H}_z$). The Zeeman interaction splits the degenerate spin energy levels, with the energy level difference increasing with $\vec{B}_0$ strength. For simplicity, the spin magnetic moments can be depicted as being parallel (α state; low energy) or antiparallel (β state; high energy) to the $\vec{B}_0$ direction (Figure 1.1). When the ensemble of spins comes to equilibrium in $\vec{B}_0$, the distribution between β and α is given by the Boltzmann distribution:

$$\frac{n_\beta}{n_\alpha} = e^{-(\frac{\Delta E}{kT})} \tag{1.4}$$

where n represents the spin population in the designated energy level, ΔE is the energy level difference between the α and β states (= $\gamma \hbar \vec{B}_0 = \hbar\omega_0$), T is absolute temperature, and k is Boltzmann's constant (1.38066 x 10^{-23} J K^{-1}). Notably, the excess population in α at equilibrium is very small (i.e. 1 out of 10^5 spins), necessitating a large amount of sample for adequate signal intensity; hence NMR is labeled an insensitive technique. The ΔE dependence on γ clarifies why nuclei with high γ (i.e ^{1}H (267.522 x 10^6 rad s^{-1} T^{-1}), ^{19}F (251.815 x 10^6 rad s^{-1} T^{-1}), and ^{31}P (108.394 x 10^6 rad s^{-1} T^{-1})) produce strong signals. Viewing Eq. 1.4, it is clear that a larger ΔE, which is produced by a larger γ, will also produce the greatest population difference.[5]

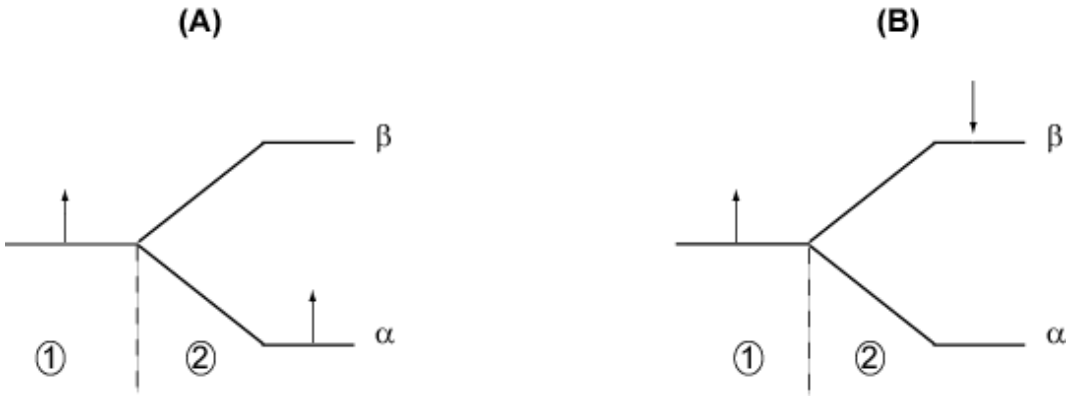

Figure 1.1. Illustration of Zeeman splitting. Asingle spin ½ is used for simplificity. The dotted line separates the time periods when the sample is outside (1) or inside (2) the magnetic field. Upon absorption of energy at ω_0 a spin can transition from the α (A) to the β state (B).

1.2. Local Interactions in NMR

Within the context of an NMR experiment, a given spin can be exposed to many different interactions; this is described by the total nuclear spin Hamiltonian, $\hat{H}_T$:

$$\hat{H}_T = \hat{H}_Z + \hat{H}_{rf} + \hat{H}_{CS} + \hat{H}_Q + \hat{H}_{SR} + \hat{H}_D + \hat{H}_J \qquad (1.5)^6$$

where the Hamiltonians on the right side account for the Zeeman interaction ($\hat{H}_z$), effect of applied radio frequency (RF) irradiation ($\hat{H}_{rf}$), chemical shift ($\hat{H}_{cs}$), quadrupolar interaction ($\hat{H}_Q$), spin rotation ($\hat{H}_{SR}$), dipolar coupling ($\hat{H}_D$), and scalar coupling ($\hat{H}_J$), respectively. $\hat{H}_T$ is simplified by considering that scalar coupling is ignored in solid samples since it is much smaller than dipolar coupling strength (the opposite would be true for solutions), quadrupolar coupling is only relevant when dealing with quadrupolar nuclei, and spin rotation does not contribute in NMR of solids because motion is frozen or insignificant. In Eq.1.5, $\hat{H}_z$ and $\hat{H}_{rf}$ are external Hamiltonians because they are due to sources outside of the nuclear environment, and the additional terms on the right of Eq.1.5 represent internal Hamiltonians because they are

determined by the structural and motional properties of a sample system under consideration.

Internal Hamiltonians can be generalized using bilinear tensor expressions. In addition to the Zeeman interaction, for a general local interaction, A_{loc} (where A is a second rank tensor designating the influence of the spin interaction at different polar angles of the molecular portion [i.e. electron distribution or internuclear vector] considered), the Hamiltonian can be given as:

$$\hat{H}_A = \gamma(\hat{I}_x \quad \hat{I}_y \quad \hat{I}_z)\begin{pmatrix} A_{xx} & A_{yx} & A_{zx} \\ A_{xy} & A_{yy} & A_{zy} \\ A_{xz} & A_{yz} & A_{zz} \end{pmatrix}\begin{pmatrix} \hat{J}_x \\ \hat{J}_y \\ \hat{J}_z \end{pmatrix} \qquad (1.6)^7$$

where J represents, for example, a second spin or a local magnetic field which associates with the I spin to produce bilinear coupling. Eq. 1.6 is applicable for calculating chemical shift, dipolar coupling, quadrupolar coupling, etc. Due to this orientation dependence, nuclear spin interactions are classified as anisotropic. For the chemical shift (or shielding) interaction, which arises from $\vec{B}_0$'s perturbation of the electron distribution around a nucleus, in Eq. 1.6, A would be the chemical shift (shielding) tensor and J would represent $\vec{B}_{loc}$. A general expression of the Hamiltonian for local interactions is:

$$\hat{H}_{loc} = -\gamma(\hat{I}_x \vec{B}_x^{loc} + \hat{I}_y \vec{B}_y^{loc} + \hat{I}_z \vec{B}_z^{loc}) \qquad (1.7)^7$$

where the subscripts designate Cartesian coordinate axes, $\hat{H}_{loc}$ and $\vec{B}^{loc}$ are the Hamiltion and magnetic field resulting from the local interaction, respectively.

In trying to understand an NMR interaction, the reference frame can be chosen such that only the diagonal elements of A are non-zero. This frame of reference is the principal axis frame (PAF) , and the non-zero diagonal elements are the principal values of the interaction tensor. For example, chemical shielding, σ, which can be depicted as an ellipsoid with the axes sizes indicative of the shielding strength in that direction (Figure 1.2), has principal components σ_{xx}, σ_{yy}, and σ_{zz}; these indicate the chemical shielding size when the PAF x, y, or z shielding axis, respectively, is aligned with $\vec{B}_0$. Chemical shielding is normally expressed in terms of the isotropic value (σ_{iso}) (Eq. 1.8), anisotropy (Δ) (Eq. 1.9), and asymmetry (η) (Eq. 1.10):

$$\sigma_{iso} = \frac{1}{3}(\sigma_{xx} + \sigma_{yy} + \sigma_{zz}) \tag{1.8}$$

$$\Delta = \sigma_{zz} - \sigma_{iso} \tag{1.9}$$

$$\eta = \frac{\sigma_{xx} - \sigma_{yy}}{\Delta} \tag{1.10}$$

To calculate an NMR spectrum, it is necessary perform a coordinate transformation from the PAF to the laboratory frame (the detection frame). Transformation can be achieved using passive rotation, where the reference frame is moved and tensor elements are redefined in the new frame. Assuming a (x, y, z) coordinate system and angles (ϕ, θ, ζ), a rotation about z by ϕ produces a new frame, (x_2,y_2, z_2). Next, rotating by θ about y_2 leads to (x_3,y_3, z_3). Finally, a rotation around z_3 by ζ leads to the final frame (i.e. laboratory). In some cases it is necessary to perform multiple frame transformations, (ref. Chapter 6). When the final frame is the laboratory frame, ζ = 0 since a rotation about $\vec{B}_0$ does not influence a signal's frequency position. As an example, by redefining σ in the laboratory frame, from the PAF, using the Euler angle set (ϕ, θ, 0º), the orientation-dependent chemical shift frequency (rad/s) can then be expressed as:

$$\omega_{CS}(\theta,\phi) = \omega_0 - (\sigma_{xx}\sin^2\theta\cos^2\phi + \sigma_{yy}\sin^2\theta\sin^2\phi + \sigma_{zz}\cos^2\theta) \tag{1.11}$$[7]

where ω_0 is the Larmor frequency, θ is the polar angle and ϕ is the azimuthal angle relating the PAF to the laboratory frame. The powder pattern NMR signal of chemical shielding (shift) anisotropy (CSA) is illustrated in Figure 1.2. The broad lineshpape observed in Figure 1.2 is unlike the sharp signals commonly observed in solution NMR spectra, and the reason for not seeing those types of features in solution NMR will be clarified in section 1.4.

1.3. RF Pulses and the Rotating Frame[8]

As previously mentioned, when a sample is placed in an NMR magnet, the spins align along $\vec{B}_0$ (longitudinal magnetization). Once the spins have reached equilibrium, RF irradiation (a pulse) applied 90° to the $\vec{B}_0$ direction (designated as $\vec{B}_1$) must be used to perturb the spin

system by rotating the spins into the x-y (tranverse) plane. Transverse magnetization is what is detected in NMR since the excitation/detection probe coil is in the transverse plane.

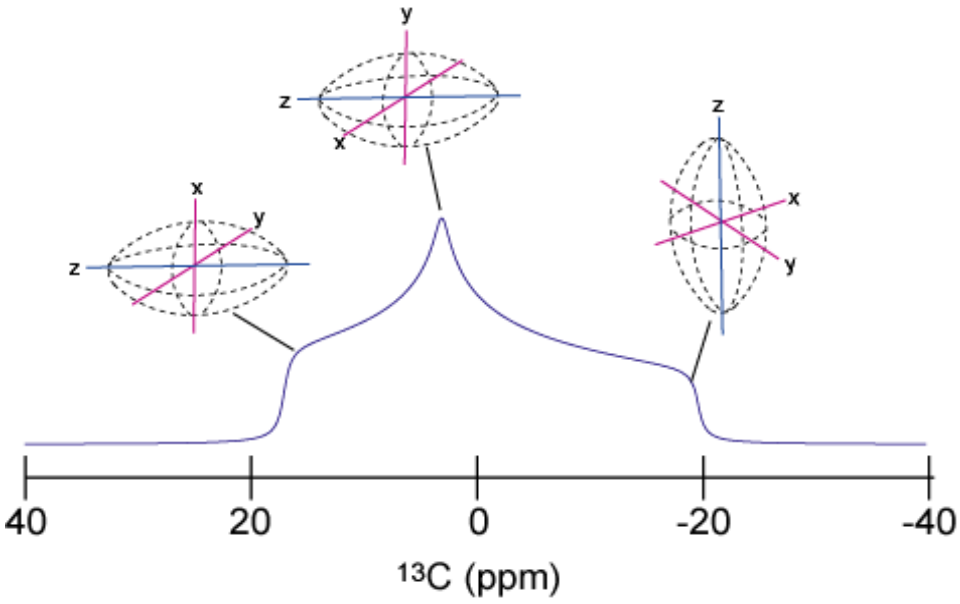

Figure 1.2. A simulated CSA powder pattern for different orientations of a ^{13}C site. Ellipsoids represent the electron distribution around the nucleus, which dictates the principal CSA values. Powder pattern positions are matched up with the corresponding ellipsoid orientations. The simulation considered $\sigma_{iso}=0$, $\eta=.7$, and $\Delta=-20$.

The spins will then precess in the transverse plane; in general the spin precession frequency around a $\vec{B}_1$ field is:

$$\omega_1 = -\gamma \vec{B}_1 \qquad \text{(rad/s)} \tag{1.12}$$

The Hamiltonian for an RF pulse in the rotating frame is:

$$H_{RF} = \omega_1 (I_x \cos\phi + I_z \sin\phi) \tag{1.13}$$

where ω_1 is the RF pulse strength and ϕ is the pulse phase angle. For spins precessing about $\vec{B}_0$,

$\omega = \omega_0$ (Larmor frequency) and $\vec{B} = \vec{B}_0$ in Eq. 1.12.

To better understand the effect of pulses and other spin dynamics, it is helpful to consider different ways of viewing the spin evolution. In an NMR experiment, $\vec{B}_1$ produces a linearly oscillating magnetic field along the x- or y-axis of the laboratory frame of reference, which is a reference frame where $\vec{B}_0$ is along the z-axis and the x- or y-axis is fixed in space. This linearly oscillating field can be decomposed into two magnetization vectors: one that rotates at the user-defined carrier frequency (which is at or near ω_0) in the same direction as the spin's magnetization (i.e. $-\omega_{car.}$), and one that rotates in the opposite sense at $\omega_{car.}$ (this vector doesn't affect the spins since it is at ~ $-2\omega_0$ and is not on resonance with the spins). As a simplification, a frame of reference can be chosen that is also at $-\omega_{car.}$, and in this case $\vec{B}_1$ is static; this is known as the rotating frame. In the rotating frame, the precession frequency of spins is now defined by an offset, Ω, which is the difference of ω_0 and the rotating frame frequency. Ω can be visualized in an NMR spectrum by separated peaks, which represent spins precessing faster/slower than $-\omega_{car}$ (i.e. the spins have different Ωs).

The rotating frame interpretation provides a means to understand how $\vec{B}_1$ can influence the equilibrium magnetization despite the fact that it is ~10^4 times smaller than $\vec{B}_0$. Considering that Ω is indicative of the magnetic field felt by the spins (ref. Eq.1.12), it is clear that a smaller Ω indicates a weaker magnetic field. So, the choice of $-\omega_{car}$ will produce an effective $\vec{B}_0$, with a strength proportional to the difference between ω_0 and $-\omega_{car}$. A close match between $-\omega_{car.}$ and ω_0 would then mean that the effective B_0 is incredibly small, thus making $\vec{B}$ more influential on the spins, and allowing it to rotate magnetization from the z-direction to the transverse plane.

1.4. Solid-State NMR: Anisotropic Interactions and Magic-Angle-Spinning

In section 1.2 was discussed how the chemical shift of an NMR signal depends on the molecular orientation to $\vec{B}_0$. Since molecules can change position, conformation, etc. over time, the NMR signal will be strongly dependent on how fast those changes occur relative to the NMR timescale. This is a key point in differentiating between 2 common types of NMR: solution and solid-state NMR (ssNMR). Small molecules (i.e. ≤10's of kDa)[9] in solution exhibit Brownian

Motion with rotational correlation times on the order of nano-/picoseconds, which motionally averages the anisotropic interactions, such as chemical shift anisotropy and dipolar interactions. Resulting spectra will then contain peaks at the isotropic frequency positions for the different sites in the molecule. In contrast, solid-state NMR experiments focus on sample systems with restricted molecular motion (i.e. correlation times of nanoseconds to seconds) such that on the NMR timescale, a large number of orientations are simultaneously present. This results in spectra exhibiting broad features, powder patterns, which consist of a superposition of signals from different orientations (i.e. Figure 1.2).

While powder patterns can provide a wealth of information, they lack the site-specific resolution necessary for operations like structural characterization. To obtain high resolution spectra in solid-state NMR, a coherent averaging of the anisotropic frequencies via mechanical rotation, magic-angle-spinning (MAS), is employed; MAS is illustrated in Figure 1.3.

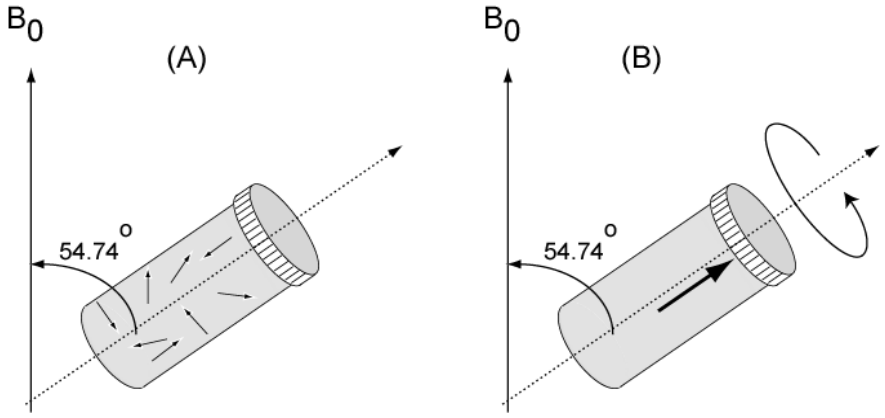

Figure 1.3. Depiction of the MAS process. Initially, the z-components of spin angular momentum for the spins, indicated by arrows, are aligned in random directions (A). Under sufficiently high MAS however, the average direction of the z-components will be along the rotor axis (B). In (B) a single bold arrow is used to represent the average orientation of the ensemble of spins.

To perform MAS the sample is packed into a rotor, which is inclined within a ssNMR MAS probe at an angle of $\beta = 54.74°$ ("magic angle") with respect to $\vec{B}_0$, and rotated at a rate, ω_r. Aligning the sample at the magic angle can cancel the anisotropy since this angle will make the

$P_2(\text{Cos}\theta)$ [= $.5(3\cos^2\beta\text{-}1)$] orientation dependence equal to 0. While the range of molecular orientations are still present for the sample packed in the rotor (Figure 1.3A), by spinning at a high rate (i.e. 3-4 times the frequency span of the anisotropic interaction)[7], an average tensor orientation will be produced along the rotor axis (Figure 1.3B), thereby reducing the powder pattern down to peaks at the isotropic frequency positions for the different sites in the molecule. To calculate the NMR spectrum, it is again necessary to perform coordinate transformations, as discussed in section 1.2. However, for MAS an extra step is needed; it is now necessary to transform from PAS to a reference frame centered on the rotor, and then from the rotor to the laboratory frame. With this multistep transformation in mind, the chemical shift, of a certain site under $\omega_r > \Delta/2$ can be found by:

$$\omega_{cs} = \omega_{iso} + (3\cos^2\beta - 1)(\Delta/2)[(3\cos^2\vartheta - 1) + \Delta\eta\sin^2\vartheta\cos 2\phi] \qquad (1.14)^{10}$$

where ϕ and θ are the orientation angles of σ_{zz} (PAF) to the rotor axis, β is the angle the rotor axis makes to the $\vec{B}_0$ direction, and ω_{iso} is the isotropic chemical shift.

1.5. Dipolar Coupling

When spins are near each other in a sample, the magnetic field generated by one nucleus can act through-space to influence a neighbor's spin energy. This spin interaction, dipolar coupling, can occur between identical types of nuclei (i.e. ^{13}C-^{13}C homonuclear dipolar coupling) or different nuclei (i.e. ^{13}C-^{1}H heteronuclear dipolar coupling). Dipolar coupling can be exploited for distance measurements and signal enhancement, though it can also lead to unfavorable effects such signal broadening and decay. Considering 2 spins, I and S, which could represent two different ^{1}Hs, or a ^{1}H and a ^{13}C, dipolar coupling can be described by:

$$\hat{H}_{DD}^{Hetero} = -d(3\cos^2\theta - 1)\hat{I}_z\hat{S}_z \qquad (1.15)$$

$$\hat{H}_{DD}^{Homo} = -\frac{d}{2}(3\cos^2\theta - 1)[3\hat{I}_z\hat{S}_z - (\hat{\mathbf{I}}\cdot\hat{\mathbf{S}})] \qquad (1.16)$$

with

$$\hat{\mathrm{I}} \cdot \hat{\mathrm{S}} = \hat{I}_x \hat{S}_x + \hat{I}_y \hat{S}_y + \hat{I}_z \hat{S}_z = \hat{I}_z \hat{S}_z + \frac{1}{2}(\hat{I}^+ \hat{S}^- + \hat{I}^+ \hat{S}^-) \tag{1.17}$$

and

$$d = (\frac{\mu_0}{4\pi}) \frac{\gamma_I \gamma_S \hbar}{r^3} \tag{1.18}$$

where Eq. 1.15 and Eq. 1.16 are the heteronuclear and homonuclear dipolar coupling Hamiltonians, respectively, which depend on the angle, θ, between the internuclear vector and and $\vec{B}_0$; $\hat{I}^{\pm}$ and $\hat{S}^{\pm}$ in Eq. 1.17 are the raising (+) and lowering (-) operators for the I and S spins, respectively. Eq. 1.18 is the dipolar coupling constant, which considers the permeability of free space, μ_0 (4π x 10^7 N A^{-2}),[11] and internuclear distance, r. Dipolar coupling can additionally be described by Eq. 1, with I being the detected spin, J would represent spin S, and A equates to the dipolar coupling tensor.

1.6. Cross-Polarization

In addition to MAS, another technique central to ssNMR is cross polarization (CP).[12] NMR-active nuclei are commonly classified as abundant spin nuclei (i.e. ^{1}H and ^{19}F) or dilute spin nuclei (i.e. ^{13}C or ^{15}N); the former designate nuclei with a high natural abundance and γ, and the latter have the opposite characteristics (i.e. ^{13}C : ~1.1% natural abundance and γ[^{13}C] = 0.25 γ[^{1}H]).[5] One difficulty in performing NMR experiments on dilute spin nuclei is the low natural abundance and γ lead to weak NMR signals with a long spin-lattice relaxation time (T_1), so for a direct polarization experiment, a large number of scans for signal averaging are necessary for adequate resolution and signal / noise ratios (which equates to long experiment times).

In solid state NMR, this problem is addressed using CP, which is a technique whereby transverse magnetization from an abundance spin nucleus is transferred to a dilute spin via their heteronuclear dipolar coupling interaction. CP serves to enhance the magnetization of the dilute spin, providing better signal intensity and signal/noise ratio, and reducing the experiment time by

way of necessitating less scans for signal averaging. Additionally, the recycle delay, the time provided between scans to allow the system to return to equilibrium with $\vec{B}_0$, is governed by the shorter spin-lattice relaxation time (T_1) of the abundant spin nucleus, which further serves to reduce experiment time.

For a CP transfer, using a ^{1}H-^{13}C dipolar spin pair as an example, the system is considered in a doubly rotating frame, which means that the ^{1}H and ^{13}C magnetization precesses about $\vec{B}_0$ at $\omega_0(^1\text{H})$ and $\omega_0(^{13}\text{C})$, respectively.[7] ^{1}H-^{13}C CP begins with creation of transverse ^{1}H magnetization, which is maintained along the rotating frame x- or y-axis (spin-locked) using a contact pulse for a given period of time (contact period). Spin- locking simply involves applying a continuous pulse along the axis to which the magnetization is directed (i.e. along the y-axis, for a 90° x-pulse to z-magnetization, which sends magnetization to the y-axis). Simultaneously, a contact pulse is also applied along the ^{13}C channel to maintain transverse ^{13}C magnetization along it's x or y rotating frame axis. In order for magnetization to transfer from ^{1}H to ^{13}C, the rotating frame energy level separation for the two nuclei must be equal; this is Hartmann-Hahn (HH) matching condition[13]:

$$\gamma_{^1H}\vec{B}_1^{\,^1H} = \gamma_{^{13}C}\vec{B}_1^{\,^{13}C} \tag{1.19}$$

1.7. Dipolar Decoupling

The dipolar coupling occurring between spins can cause line broadening and thus hinder high resolution in ssNMR. As mentioned, for MAS to average anisotropic spin interactions to zero, ω_r must be much greater than the anistropic frequency span, but this is not always possible with the current technology. In fact, the strong ^{1}H-^{1}H homonuclear dipolar coupling, which can exceed 100 kHz, is the big hurdle in performing high resolution ^{1}H ssNMR experiments. However, since the dipolar coupling Hamiltonians involve both spin and spatial terms (i.e. Eq.1.15 and 1.16), it is clear that MAS can be assisted in this case using RF irradiation. Many established pulse sequences are available for hetero- and homonuclear dipolar decoupling.[14-20] One caveat that must be considered in using these sequences, though, is that MAS rates comparable to the decoupling frequency can hinder the sequence's performance. The decoupling

discussed here will be in the context of ^{13}C-^{1}H and ^{1}H-^{1}H pairs.

1.7.1. Heteronuclear Decoupling

Heteronuclear dipolar decoupling is routinely used to remove the influence of ^{1}Hs on ^{13}Cs during ^{13}C MAS experiments of organic solids. To be effective, the radio frequency field strength, ω_1, applied on ^{1}Hs, should be much greater (i.e. 3x) than the strongest dipolar coupling interaction;[7] so for a directly bonded ^{13}C-^{1}H pair , with a dipolar coupling strength ~23 kHz, it would be necessary to use at least 69 kHz of decoupling. Typically ^{13}C magnetization is detected because it has a much wider spectral dispersion (i.e. ~200 ppm, compared to ~10 ppm for ^{1}H) and the low natural abundance of ^{13}C means that ^{13}C-^{13}C homonuclear dipolar coupling is weak and does not adversely affect the signals. Due to the strength of dipolar coupling among ^{1}Hs, irradiation at a particular resonance condition easily affects ^{1}Hs off resonance as well, thereby helping the efficiency of the procedure. The simplest type of heteronuclear decoupling is continuous wave (CW), which is simply an uninterrupted period of high power RF irradiation. This causes the spins to transition between the α and β states at a rate determined by ω_1. Since the ^{1}H influence on ^{13}C is determined by the z-component of the ^{1}H magnetization, if the $\alpha \leftrightarrow \beta$ transition is faster than the ^{13}C-^{1}H dipolar coupling frequency, the ^{13}C-^{1}H heteronucler dipolar coupling will be averaged to zero. A downfall of CW decoupling is residual line broadening due to interaction of the chemical shielding and heteronuclear dipolar coupling tensors.[21]

A more elaborate heteronuclear dipolar decoupling technique which reduces the line broadening seen for CW decoupling is the two-pulse phase modulation sequence (TPPM).[14] TPPM consists of a repeated block of 2 pulses with flip angle,θ, and phases, ϕ, which are out of phase which each other by $\Delta\phi$. The optimal θ and ϕ values depend on the spectrometer hardware, sample, ω_r, and ω_1.[14] However, in the original publication, for $\omega_1/2\pi$ = 75.8 kHz, the optimal ϕ is in the range of 10°-50°, and θ is near 150°, for $\omega_r/2\pi$ = 0 - 12 kHz.[14,21] TPPM was also found to be superior to CW as $\vec{B}_0$ and ω_r increased.[14]

Among others, an improvement on TPPM is the small phase incremental alternation with 64 steps (SPINAL-64) heteronuclear dipolar decoupling sequence.[16] SPINAL-64, which was introduced within the context of decoupling in liquid crystalline samples, is a supercycle of TPPM. A supercycle is a complex pulse sequence built by making many repetitions of a simpler

one, with phase shifts of the radiofrequency pulses.[11] Supercycles are less hindered by pulse imperfections and ^{1}H frequency offsets compared to their simpler counterparts.[11,16] To provide an idea on the makeup of SPINAL-64, the sequence first introduced consisted a block of sixteen 165° pulses with the following phase angles: [10°, -10°, 15°, -15°, 20°, -20°, 15°, -15°, -10°, 10°, -15°, 15°, -20°, 20°, -15°, 15°]; the block is then repeated 8 times to complete the 64 steps.[16] SPINAL-64 was shown to have better efficiency than TPPM or CW upon direct comparison, and it was also less hindered by ^{1}H chemical shift offsets compared to TPPM.[16]

1.7.2. Homonuclear Decoupling

Homonuclear dipolar decoupling can be achieved by causing the spins to uniformly experience all orientations in spin space over time (i.e. the magnetization spends an equal amount of time in each orientation). The earliest example is the Waugh-Huber-Haberlen (WAHUHA) sequence, which consists of a series of 90° ^{1}H pulses separated by time τ (Figure 1.4).[17] WAHUHA can be visualized by having the reference frame rotate in a manner dictated by the radio frequency pulse phases, but in the opposite direction (i.e. a 90° pulse along the rotating frame x-axis would produce a - 90° rotation of the reference frame); this is commonly referred to as the interaction representation and the frame is known as the toggling frame.[7] This process simplifies interpretation of WAHUHA because the effect of radiofrequency pulses on spin operators is removed. It is acceptable because, for instance, sending z magnetization onto the x-axis is equivalent to rotating the x-axis to meet the spins polarized perpendicular to it; in both instances the dipolar field is along the reference frame x-axis.[7,11] The homonuclear dipolar Hamiltonian (Eq. 1.16) acting on the spin system will then be $\hat{H}_{xx}$, $\hat{H}_{yy}$, or $\hat{H}_{zz}$ (subscripts defined for the toggling frame); the subscripts on the first term in the brackets of Eq. 1.16 then becomes x, y, or z, appropriately. Based on the definition of $\hat{\mathbf{I}}\cdot\hat{\mathbf{S}}$ in Eq. 1.16, if $\hat{H}_{xx}$, $\hat{H}_{yy}$, and $\hat{H}_{zz}$ act on the spin system for an equal amount of time, the total sum, and hence average homonuclear dipolar coupling interaction, over time will be zero.

One sophisticated method among modern state-of-the-art types of homonuclear dipolar decoupling methods is the frequency-switched Lee-Goldburg sequence (FSLG).[15,22] In FSLG, an effective magnetic field oriented at the magic angle in spin space is created by appropriately

setting Ω and ω_1 to satisfy the condition : $\tan^{-1}(54.7°) = \omega_1 / \Omega$.

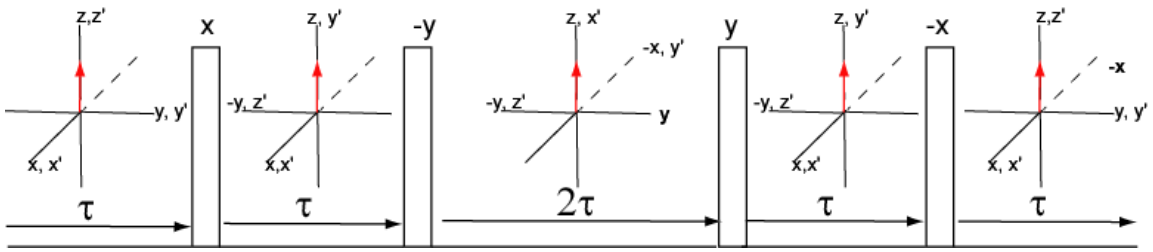

Figure 1.4. The WAHUHA sequence. 90° pulses are shown with phases indicated by letters above the pulses. Cartesian coordinate axes between pulses illustrate how the pulses reorient the Hamiltonian reference frame; x, y, and z represent the coordinates of the starting frame, and x', y', and z' mark the toggling frame. The red arrow signifies the net magnetization vector. For simplicity, only key axes labels are inidciated in each case

FSLG consists of a repeated block of two pulses which induce ~360° rotations and are 180° out of phase with each other. Unlike WAHUHA, where the magnetization can be imagined as making discrete jumps between different orientations, FSLG involves magnetization continuously precessing around the spin space magic angle. Alternating the phase compensates for off-resonance effects.[7]

1.8. Recoupling of Anistoropic Interactions

While MAS can average away anisotropic interactions for high resolution spectra, it costs the structural information inherent to the orientation dependence. Dipolar coupling, for instance, provides distance constraints because it is a factor of internuclear distance (Eq. 1.18). CSA can provide information on the electronic structure around the nucleus, molecular motion, and molecular conformations.[23] Hence, the development of MAS experiments that simultaneously provide good resolution and the reintroduce (recouple) anisotropic interactions has long been an active research area in ssNMR. Experiments of this nature normally incorporate RF pulse trains or careful selection of experiment parameters (i.e. MAS speed)[24] to interfere with MAS.

1.8.1. Dipolar Recoupling

Two pioneering dipolar recoupling methods are rotational-echo double-resonance (REDOR)[25] and dipolar recovery at the magic angle (DRAMA)[26], which achieve heteronuclear and homonuclear dipolar recoupling, respectively. The basic REDOR sequence, and its many elaborate variants, are some of the most heavily used ssNMR experiments. While DRAMA is no longer heavily used, it was instrumental in beginning the area of homonuclear dipolar recoupling techniques.DRAMA and REDOR will be discussed below, while Chapter 7 will introduce the Dipolar-coupling-mediated TOtal Correlation Spectroscopy (DTOCSY) technique,[27] a novel homonuclear dipolar recoupling technique.

1.8.1.1. REDOR

REDOR is one of the most widely used ssNMR techniques for structure determination of biomolecular samples,[28,29] The pulse sequence (Figure 1.5) starts with magnetization transfer from an abundant spin (i.e. ^{1}H) to the observed spin (i.e. ^{13}C) (S) using CP. Typically, two 180° pulses are applied along the indirect channel (I pulse) per rotor period, with a 180° pulse on the S channel at the central point to refocus the S-spin chemical shift. To understand how REDOR is able to reintroduce dipolar coupling under MAS, one can note the effect of the 180° pulses on the dipolar Hamiltonian. As shown in Eq. 1.15, the dipolar interaction Hamiltonian consists of the product of the spatial and spin parts of the interaction tensors. MAS provides a sinusoidal modulation of the spatial tensors so that integrations overtime are zero. However, the I pulses invert the sign of the spin part of the tensors, keeping the dipolar coupling from being refocused. As the reintroduced dipolar coupling will cause magnetization dephasing, it can be monitored through the reduced S signal intensity.

The REDOR experiment essentially consists of two parts. First, an experiment is performed without I pulses (S_0); this is the reference experiment since no dipolar dephasing occurs and the full signal intensity is obtained. Next, the experiment is repeated with the I pulses present, and the reduced signal intensity can be found (S). The S and S_0 experiments are repeated, with subsequent experiments having a longer dipolar recoupling period, thereby increasing the amount of time over which I and S interact. A plot can then be generated of S/S_0

or $\Delta S/ S_0$ vs. the number of rotor periods to obtain a dephasing curve, which can be fit with simulations to extract the dipolar coupling constant and internuclear distance. The dipolar coupling strength obtained under REDOR can be up to 70% of that observable in a static case.[11]

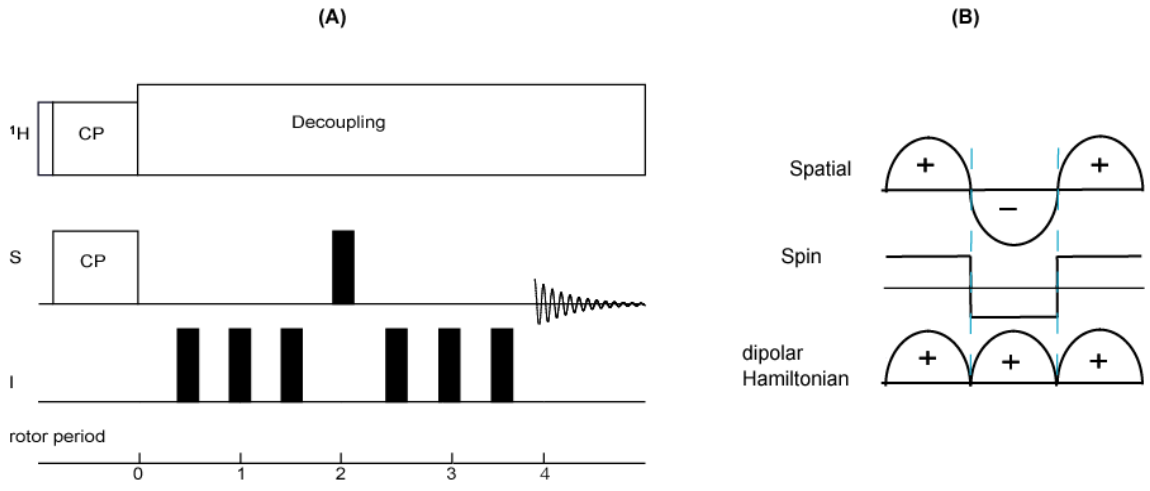

Figure 1.5. Schematic of the REDOR pulse sequence. The sequence is shown with 180° pulses at the full and half rotor period positions (4 rotor periods shown) (A) and also illustrated is its operation during an S experiment (1.5 rotor periods shown for simplicity) (B). In (B) 'spatial' and 'spin' designate the inversion of the spatial parts (by MAS) or spin parts (by pulses). Dashed blue lines designate the pulse positions. Since the sign of the spatial and spin parts of the Hamiltonian is the same in the presence of the 180° REDOR pulses, the product is positive and the dipolar Hamiltonian is maintained.

1.8.1.2. DRAMA[7,11,26]

RF pulses can also be used for homonuclear dipolar recoupling; but in a homonuclear case the nuclei have similar resonance frequencies, so simply applying 180° pulses as in REDOR would invert both spins and the Hamiltonian would cancel. Instead, DRAMA uses a series of 90° pulses in a manner analogous to WAHUHA; the experiment can be considered to involve a moving reference frame instead of rotated spins .[7,11] However, in DRAMA the reference frame only shifts between the y and z axes.With 90° pulses separated by a time,τ, the time dependence of Eq. 1.16 is:

$\hat{H}_{zz}^{Homo}$ for $0 \leq t < (\tau_r-\tau)/2$ and $(\tau_r+\tau)/2 < t \leq \tau_r$

(1.20)[30]

$\hat{H}_{yy}^{Homo}$ for $(\tau_r-\tau)/2 \leq t \leq (\tau_r+\tau)/2$

DRAMA can reintroduce 45 % of the dipolar coupling strength that would be obtained under a static case.[11] As an addition to the basic sequence, 180° pulses applied after every other τ_r can be used to cancel out the CSA and isotropic chemical shift offsets that is also recoupled under DRAMA.[7] Just like with REDOR, DRAMA can be split into S and S_0 experiments, where the recoupling pulses are present or absent, respectively.[11] The S and S_0 experiments are repeated for different recoupling time lengths, and the S/S_0 or $\Delta S/S_0$ values over the recoupling time range can be used to extract the dipolar coupling constant, and thereby distance.

1.8.2. CSA Recoupling

One of the early CSA recoupling techniques introduced was the two-dimensional (2D) MAS / CSA experiment.[31] Though a few methods had preceded it[32-34], in contrast to the MAS / CSA sequence, the CSA patterns obtained by those sequences were deformed compared to what would be observed in the static case. To reintroduce CSA, the MAS / CSA method uses four 180° pulses per τ_r to change the direction of spin precession at certain time points, thereby canceling the spatial modulation of MAS. The experiment is repeated with increasing periods of CSA recoupling to produce 2D spectra with the isotropic chemical shift spectrum along the direct acquisition frequency dimension, ω_2, and the undistorted CSA powder pattern along the indirect frequency dimension, ω_1. A CSA pattern can be obtained for each resolved site by taking a 1D slice along the ω_1 dimension at that site.

1.9. Separated Local Field ssNMR

A class of NMR experiments that have been beneficial for structural and dynamic studies are separated local field (SLF) techniques.[35-37] These are 2D NMR experiments that correlate heteronuclear (i.e. I-S, where S is detected) dipolar interactions with S spin chemical shifts. The

general makeup of a SLF sequence is shown in Figure 1.6. During the indirect time dimension, t_1, the S spin magnetization evolves under the heteronuclear dipolar coupling interaction, which is maintained by an absence of heteronuclear dipolar decoupling. Instead, a homonuclear dipolar decoupling sequence is applied to the I spins to prohibit any effect of I-I dipolar coupling on S magnetization. Following t_1, S magnetization evolves according to chemical shift under heteronuclear dipolar decoupling and is detected during t_2. Upon Fourier transformation a 2D spectrum with a pattern representative of I-S dipolar coupling (i.e. powder pattern, dephasing curve, etc.) is obtained in the indirect frequency domain, ω_1, and a normal S chemical-shift spectrum is produced in the direct acquisition domain, ω_2 .

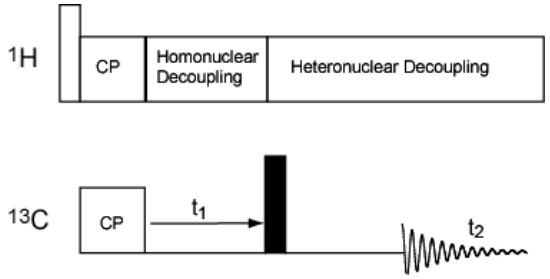

Figure 1.6. General illustration of a 2D SLF experiment on a ^{1}H-^{13}C system. Open and closed rectangles are 90° and 180° pulses, respectively.

An interaction pattern is obtained for each resolved S site; and since the interaction pattern is dependent on the dipolar coupling strength, which is a factor of the internuclear distance and vector orientation, structural information can be obtained for each of those sites.[38-40] Also, since the dipolar coupling strength can be modulated by molecular motion, it is possible to gain perspective on a system's dynamics.[41-44] Polymers are one of the many systems that have been investigated with SLF methods,[44-47] and Chapters 4-5 will briefly mention results from dipolar coupling-chemical shift correlation spectroscopy (DIPSHIFT) experiments that had been utilized to investigate aromatic ring flip motions in polymers .[48-51]

1.10. Nuclear Spin Relaxation

A key concept in NMR, with implications for experiment implementations and

elucidation of sample proprieties, is spin relaxation time; three forms are highlighted here. First, recall that when a sample is placed in $\vec{B}_0$ a net magnetization forms in the z-direction. Then, a $\vec{B}_1$ field can rotate the magnetization into the transverse plane where it precesses at ω_0; but at the same time the spins start to realign with $\vec{B}_0$ since $\vec{B}_0 >> \vec{B}_1$. The exponential rate of return of magnetization to equilibrium is characterized by the spin-lattice relaxation time, T_1. T_1 is sensitive to motions on the order of ω_0 (i.e. 300 MHz for ^{1}H with $B_0 = 7.05$ T), such as vibrations and librations. T_1 is important to keep in mind for planning NMR experiments because the time between transients must be long enough to adequately allow the magnetization to build back up along the $\vec{B}_0$ direction(typically ~5 T_1).

Another form of spin relaxation occurs when the net magnetization vector is rotated from the z-direction into the transverse plane and spin-locked along the rotating frame x- or y-axis; essentially it is precessing in a cone around the x- or y-axis analagous to how it precesses around $\vec{B}_0$ at equilibrium. Over time the magnetization will start to exponentially decay along the transverse axis, and this is described by the rotating frame spin-lattice relaxation time, $T_{1\rho}$. $T_{1\rho}$ is sensitive to motions on the order of the $\vec{B}_1$ frequency (~10's of kHz) and changes when intra-/intermolecular associations are modified.[52] $T_{1\rho}$ is also a consideration in performing CP.

The final spin relaxation to be considered surrounds the spins precessing in the transverse plane following a RF pulse. Initially the spins are aligned with one another as precession begins, but over time the magnetization vectors will get out of phase with each other and the net transverse magnetization will exponentially decay. This process, spin-spin relaxation, is characterized by the time constant T_2, which like $T_{1\rho}$ is sensitive to kHz range molecular motions. T_2 is reflected in the time domain NMR signal, the free induction decay (FID), where a longer FID represents a longer T_2, as well as in the spectral linewidth, as a shorter FID will produce a broader line due to uncertainty in the precessional frequency of the represented magnetization. Specifically, the full width at half maximum of the linewidth is $(\pi T_2)^{-1}$ (in Hz). It is also routine to use a "T_2 filter" in NMR experiments to obtain spectra of mobile components apart from more rigid ones. The rigid components will have a shorter T_2, so by inserting a free evolution delay (i.e. near the rigid component T_2) in a pulse sequence prior to acquisition, only the magnetization for the mobile components will remain for detection. T_2 must also be

accounted for in designing an NMR experiment that includes a delay period during which transverse magnetization is present; if T_2 is short compared to the delay period, the magnetization will dephase before it can be detected.

When measuring T_2 however, it is important to consider the effect of magnetic field inhomogeneity. Spins which experience dissimilar magnetic environments will precess at slightly different frequencies and thereby add to the transverse magnetization decay; this is usually indicated as T_2^*. To obtain a true value of T_2, an echo sequence can be employed[53,54].

A last important note to make about relaxation time measurements concerns the size of the probed area, which is a strong factor of detected nucleus. For instance, ssNMR ^{1}H experiments provide more of a "global view" of molecular motion, even up to 200 Å[55] distances, because strong ^{1}H-^{1}H homonuclear dipolar coupling, which allows spin diffusion and cross-relaxation among ^{1}Hs, influences the relaxation time. Conversely, ^{13}C experiments can provide information on localized dynamics since the low natural abundance prevents significant spin diffusion.

1.11. Conclusions

Hence, ssNMR serves as a powerful tool to study the structure and dynamics of systems on the molecular level. Using a suit of techniques it is possible to characterize a variety of motional modes (i.e. vibration, rotation), over a wide dynamic range, for distances up to a few hundred angstroms. Not to mention, structural information can be obtained for samples whether or not site-specific resolution can be obtained.

References

(1) Bloch, F.; Hansen, W. W.; Packard, M. D. *Phys Rev* **1946**, *69*, 127.

(2) Purcell, E. M.; Torrey, H. C.; Pound, R. V. *Physical Review* **1946**, *69*, 37.

(3) Parella, T.; BRUKER Analytik GmbH: 2000.

(4) Brown, S. P.; Spiess, H. W. *Chemical Reviews* **2001**, *101*, 4125.

(5) Levitt, M. H. *Spin Dynamics: Basics of Nuclear Magnetic Resonance*; John Wiley & Sons Ltd. : West Sussex, 2005.

(6) Homans, S. W. In *A Dictionary of Concepts in NMR*; Dwek, R. A., Ed.; Oxford University Press: Oxford, 1995, p 138.

(7) Duer, M. J. *Introduction to Solid-State NMR Spectroscopy*; Blackwell Publishing Ltd.: Malden, 2004.

(8) Keeler, J. *Understanding NMR Spectroscopy*; John Wiley & Sons Ltd.: West Sussex, 2005.

(9) Powers, R. *J. Struct. Funct. Genom.* **2002**, *2*, 113.

(10) Andrew, E. R. *Philos. Trans. R.Soc. London, Ser. A* **1981**, *299*, 505.

(11) Laws, D. D.; Bitter, H. M. L.; Jerschow, A. *Angew. Chem. Int. Ed.* **2002**, *41*, 3096.

(12) Pines, A.; Gibby, M. G.; Waugh, J. S. *J. Chem. Phys.* **1973**, *59*, 569.

(13) Hartmann, S. R.; Hahn, E. L. *Phys. Rev.* **1962**, *128*, 2042.

(14) Bennett, A. E.; Rienstra, C. M.; Auger, M.; Lakshmi, K.; Griffin, R. G. *J. Chem. Phys.* **1995**, *103*, 6951.

(15) Bielecki, A.; Kolbert, A. C.; Levitt, M. H. *Chem. Phys. Lett.* **1989**, *155*, 341.

(16) Fung, B. M.; Khitrin, A. K.; Ermolaev, K. *J. Magn. Reson.* **2000**, *142*, 97.

(17) Haeberlen, U.; Waugh, J. S. *Phys. Rev.* **1968**, *175*, 453.

(18) Sakellariou, D.; Lesage, A.; Hodgkinson, P.; Emsley, L. *Chem. Phys. Lett* **2000**, *319*, 253.

(19) Schenker, K. V.; Suter, D.; Pines, A. *J. Magn. Reson.* **1987**, *73*, 99.

(20) Rhim, W. K.; Elleman, D. D.; Vaughan, R. W. *J. Chem. Phys.* **1973**, *59*, 3740.

(21) Ernst, M. *J. Magn. Reson.* **2003**, *162*, 1.

(22) Bielecki, A.; Kolbert, A.; De Groot, H.; Griffin, R.; Levitt, M. *Adv. Magn. Reson* **1990**, *14*, 111.

(23) Wi, S.; Sun, H.; Oldfield, E.; Hong, M. *J. Am. Chem. Soc.* **2005**, *127*, 6451.

(24) Raleigh, D. P.; Levitt, M. H.; Griffin, R. G. *Chem. Phys. Lett.* **1988**, *146*, 71.

(25) Schaefer, J.; Gullion, T. *J. Magn. Reson.* **1989**, *81*, 196.

(26) Tycko, R.; Dabbagh, G. *Chem. Phys. Lett.* **1990**, *173*, 461.

(27) Spano, J.; Wi, S. *J. Magn. Reson.* **2010**, *204*, 314.

(28) Olsen, G. L.; Edwards, T. E.; Deka, P.; Varani, G.; Sigurdsson, S. T.; Drobny, G. P. *Nucleic acids research* **2005**, *33*, 3447.

(29) Wang, J.; Balazs, Y. S.; Thompson, L. K. *Biochemistry* **1997**, *36*, 1699.

(30) Tycko, R. Q. Rev. Biophys. **2006**, *39*, 1.

(31) Tycko, R.; Dabbagh, G.; Mirau, P. A. *J. Magn. Reson.* **1989**, *85*, 265.

(32) Alla, M. A.; Kundla, E. I.; Lippmaa, E. T. *Jetp Lett* **1978**, *27*.

(33) Yarim-Agaev, Y.; Tutunjian, P. N.; Waugh, J. S. *J. Magn. Reson.* **1982**, *47*, 51.

(34) Bax, A.; Szeverenyi, N. M.; Maciel, G. E. *J. Magn. Reson.* **1983**, *51*, 400.

(35) Dvinskikh, S. V.; Sandström, D.; Zimmermann, H.; Maliniak, A. *Chem. Phys. Lett.* **2003**, *382*, 410.

(36) Sergey, V. D.; Kazutoshi, Y.; Ayyalusamy, R. *J. Chem. Phys.* **2006**, *125*, 034507.

(37) Hester, R.; Ackerman, J.; Neff, B.; Waugh, J. *Phys. Rev. Lett.* **1976**, *36*, 1081.

(38) Schmidt Rohr, K.; Wilhelm, M.; Johansson, A.; Spiess, H. *Magn. Reson. Chem.* **1993**, *31*, 352.

(39) Schmidt-Rohr, K. *J. Am. Chem. Soc.* **1996**, *118*, 7601.

(40) Wu, C. H.; Ramamoorthy, A.; Opella, S. J. *J. Magn. Reson.* **1994**, *109*, 270.

(41) Xu, J.; Soong, R.; Im, S.-C.; Waskell, L.; Ramamoorthy, A. *J. Am. Chem. Soc.* **2010**, *132*, 9944.

(42) deAzevedo, E. R.; Saalwachter, K.; Pascui, O.; Souza, A. A. d.; Bonagamba, T. J.; Reichert, D. *J. Chem. Phys.* **2008**, *128*, 104505.

(43) Schmidt-Rohr, K.; Clauss, J.; Spiess, H. W. *Macromolecules* **1992**, *25*, 3273.

(44) Chen, Q.; Schmidt-Rohr, K. *Macromol. Chem. Phys.* **2007**, *208*, 2189.

(45) Schaefer, J.; Stejskal, E. O.; McKay, R. A.; Dixon, W. T. *Macromolecules* **1984**, *17*, 1479.

(46) Hu, J. Z.; Wang, W.; Bai, S.; Pugmire, R. J.; Taylor, C. M. V.; Grant, D. M. *Macromolecules* **2000**, *33*, 3359.

(47) Brus, J.; Urbanova, M.; Strachota, A. *Macromolecules* **2007**, *41*, 372.

(48) Munowitz, M. G.; Griffin, R. G.; Bodenhausen, G.; Huang, T. H. *J. Am. Chem. Soc.* **1981**, *103*, 2529.

(49) Hong, M.; Gross, J. D.; Griffin, R. G. *J. Phys. Chem. B* **1997**, *101*, 5869.

(50) Munowitz, M.; Aue, W. P.; Griffin, R. G. *J. Chem. Phys.* **1982**, *77*, 1686.

(51) Schaefer, J.; McKay, R. A.; Stejskal, E. O.; Dixon, W. T. *J. Magn. Reson.* **1983**, *52*, 123.

(52) Kimmich, R. *NMR Tomography, Diffusometry, Relaxometry.*; Springer: Berlin, 1997.

(53) Hahn, E. L. *Phys. Rev.* **1950**, *80*, 580.

(54) Meiboom, S.; Gill, D. *Rev. Sci. Instrum.* **1958**, *29*, 688.

(55) Schmidt-Rohr, K.; Spiess, H. W. *Multidimensional Solid-State NMR and Polymers*; Academic Press: San Diego, 1994.

Chapter 2
Introduction to Samples for Solid-State NMR Study

2.1. Biomembranes

Biological membranes play a critical role in maintaining the stability and health of cells because the membrane integrity is crucial for housing the cytosol and organelles, and its selective permeability helps maintain the proper balance of ions and allow nutrients, but not toxins, to pass through. A full understanding of the structures and functions related to biomembranes and their constituents is necessary for a thorough basic knowledge base that would provide the means to develop technologies focused on improving general well-being, such as disease therapies and injury repair.

A principle component of biomembranes is glycerophospholipid molecules. When amphipathic lipids are introduced into an aqueous environment, hydrophobic interactions between the lipids will provide a thermodynamic driving force for formation of lipid clusters.[1] For the two-tailed lipids that form organismal plasma membranes, where the cross-section of the head and tail regions is similar, bilayers are the preferred lipid aggregate because they reduce the hydrophobic surface-water interactions, and thereby impart the favorable case of an increase in entropy of the water. However, since in a pure bilayer there would be cases of acyl chain-water interactions at the bilayer edges, an even more stable structure is the liposome, which is a bilayer folded back on itself to form a lipid sphere with an aqueous core.

An established view of the structure/dynamics of a cell membrane is the fluid mosaic model.[2] In this representation, phospholipids form a two-dimensional (2D) bilayer, ~5-8 nm thick,[1] with the polar phosphate headgroups directed towards the outside aqueous environment, and the polar acyl chains forming the bilayer core. This organization evidences the ingenuity of nature, as a 2D arrangement is beneficial for enzymatic processes because it fosters frequent molecular interactions. Integral proteins are constrained in the bilayer via interactions between the hydrophobic portions of the protein and lipid. Lipids and proteins can move laterally in the membrane because protein-lipid interactions are noncovalent.

As has been alluded to, biological membranes are very complex, consisting not only of lipid molecules, but also proteins, peptides, and other macromolecules involved in all aspects of

cell functioning. This make-up can be reflective of the function of the cell; cells of myelin, which acts as an insulator, has a high lipid content, while cells involved in metabolism would have a high protein content.[1] The types of lipids present in the outer (exoplasmic) and inner (cytoplasmic) portions of the plasma membrane can differ, with distribution having a strong effect on biological functioning; for example phosphatidylserine must be in the exoplasmic space in order for platelets to take part in blood clotting.[1]

Membrane composition plays a major role in cellular interactions with an interesting class of cationic peripheral membrane molecule, antimicrobial peptides (AMPs). Biological organisms can be classified as eukaryotic or prokaryotic, and one of the differentiating characteristics is that eukaryotic membranes contain a significant portion of zwitterionic phospholipids and cholesterol, imparting an overall neutral charge, while prokaryotic cells have high anionic lipid content, making them negatively charged. Charge helps to provide a protective effect for eukaryotic organisms against the antimicrobial peptides innate to the organism, since cationic AMPs would have a preference for attack on prokaryotic membranes.

One of the major research efforts within the realm of biomembrane science is understanding the mode of action of AMPs which are innate to the immune systems of many different plants and animals and act as an initial defense against pathogenic organisms.[3-8] Research into the mechanism of action of AMPs can greatly benefit human health because understanding the intricacies of the immune response could aid in the development of new therapies, not to mention the peptides themselves may be useful in treating disease.[9] A curious aspect of AMPs that would instill hope in them as a novel type of therapy is that, in contrast to conventional drugs which act on specific cellular targets (i.e. a protein), AMPs are non-specific and attack the cell membrane.[10] Exploring novel treatments is crucial as presently there is a world-wide issue of drug-resistant pathogens.[11]

Since the initial discovery of AMPs ~30 years ago,[12] much experimental[8,13-20] and theoretical[21-24] efforts have been focused on better understanding their structure and function within a membrane environment, as these two aspects are important for developing novel therapies from AMPs. From a standpoint of characterizing their structure (i.e. α-helix), it is critical to study these molecules in a membrane-type environment because many AMP's only take on their active conformation in those cases; in their native, unbound form they will be in a random coil arrangement.[25] Of course, it is most ideal to study these peptides in an actual

membrane environment, which can be done with techniques such as microscopy[26] and florescence[27], but due to the fragile nature of the system it is not suitable for the methods like nuclear magnetic resonance spectroscopy (NMR), which can provide molecular-level information not accessible by other techniques. As an alternative, cell membrane-mimetic systems composed of phospholipids are made in the laboratory and are used in a variety of analytical measurements; these systems include oriented bilayers prepared between thin glass plates, a system that will be elaborated on later in Chapter 6, bicelles, and vesicles. Varying the composition (i.e. anionic and zwitterionic phospholipids, cholesterol, etc.) allows one to mimic membrane environments of prokaryotic (i.e. significant presence of anionic phospholipids) or eukaryotic organisms (i.e. outer membrane leaflets composed mainly of zwitterionic phospholipids, and only eukaryotic cell membranes contain cholesterol).[28] Exploring different compositions is key because whether the intention is to develop new therapies based on the peptides, or use the peptides themselves, it is only desireable for the AMPs and their derivatives to act on pathogens, while leaving AMP-host (i.e. human) cells unaffected. Clearly membrane mimetic systems are a very simplified environment compared to an actual cell membrane, but these models are a convenient way to study basic processes (i.e. lipid lateral diffusion) involved in peptide-membrane interactions.

One of the main focuses in this research area is understanding the details of the induced membrane dynamics/structure changes resulting from perturbation by AMPs. These interactions are likely initiated by the cationic nature of AMPs facilitating electrostatic binding to anionic lipids of pathogenic membranes.[17] Based on observations made in various AMP-lipid membrane studies, a few models have been developed to characterize possible interactions and resulting peptide-lipid supramolecular structures: the carpet model, barrel-stave model, and torroidal pore model. The latter two are depicted in Chapter 6, which will provide a view of the power of solid-state NMR for studying peptide-membrane interactions, [29-37] and the carpet model is shown in Figure 2.1 below.

In the barrel-stave model, a bundle of helical peptides create a pore in a bilayer with the hydrophobic portions of the peptides associated with the hydrophobic acyl chains of the phospholipids and the hydrophilic peptide regions comprising the pore lining.[7] Hence, peptides disrupting a membrane via this mechanism would need to be largely hydrophobic since there is a

notable interaction with the acyl chains.[25] The barrel-stave model is not ubiquitous though, as it has only been found for a few AMP's, including alamethicin.[25,38]

A second model, the carpet model, involves peptides initially lying parallel on the membrane surface.[39]

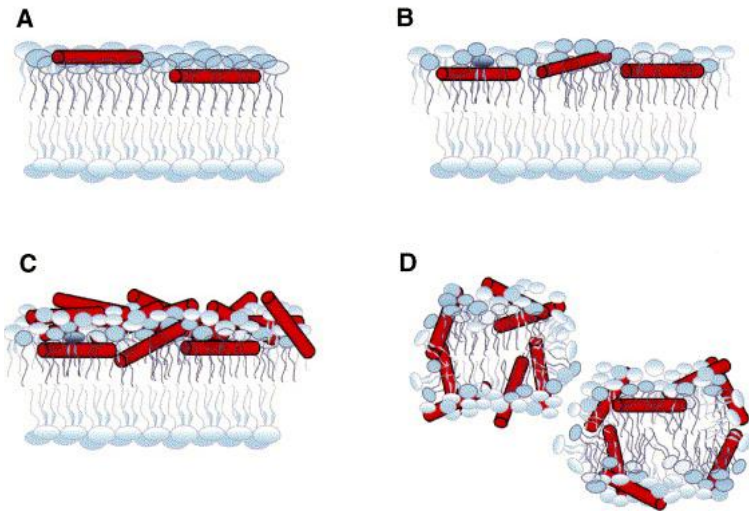

Figure 2.1.[40] Illustration of membrane disruption by the carpet mechanism. As in channel formation, peptide α-helices (cylinders) initially (A) bind and (B) accumulate in an orientation parallel to the membrane surface. (C) Continued accumulation of membrane-bound peptide associated with the phospholipid head-groups, eventually covering (i.e., carpeting) the bilayer.(D) Detergent-like membrane disintegration. Reproduced with permission from Sato, H.; Feix, J. B. *Biochimi. et Biophys. Acta, Biomembr.* **2006**, *1758*, 1245. Copyright 2006 Elsevier B.V.

The hydrophobic peptide portions interact with the acyl chain regions, and the hydrophilic portions interact with the lipid phosphate headgroups. At a critical peptide concentration, the bilayer can be compromised and fragmented into micelles by the AMPs.[7] The carpet mechanism is supported by AMP's such as dermaseptin,[41] and accounts for the efficacy of AMPs too short (i.e. < 22 amino acids[25]) to traverse a cell membrane and form a pore .[16,42]

A final possible mechanism that will be mentioned here is the torroidal pore model, where peptides are initially electrostatically bound parallel to the membrane surface, similar to the carpet mechanism, and a critical concentration aggregate with other peptides and start to

angle into the membrane.[17] A key feature of the torroidal-pore mechanism is that lipid headgroups angle in with the peptides so that the lipid molecules are forming a curved surface spanning the bilayer leaflets that is bordered by the AMPs. Unlike in the barrel-stave model, the pore surface consists of the hydrophilic portions of the peptide and the hydrophilic phosphate headgroups of the lipid.[7] The torroidal-pore model has been applied to membrane perturbation by AMPs such as protegrin-1(PG-1)[17], aurein-3.3 and magainin-2,[30] and MSI-78[8].

2.2. Reverse Osmosis Membranes

A key issue in global population wellbeing is the availability of clean water; though commonly associated with third-world nations, it is a problem for developed countries as well.[43] Billions of people do not have access to safe water supplies, leading to millions of related deaths a year, and around half of hospitalized patients.[44,45] Approximately 10% of diseases can be attributed to inadequate water supplies, and as the world's population increases, the majority will be born into areas with these types of poor conditions.[44,45] Both the issues of an inadequate amount of fresh water,[43] coupled with an increasing demand for that same freshwater which outpaces the growth of the population,[44] need to be considered in addressing the water shortage. A water crisis can also lead to a decreased supply, and hence increased price, of food, which is a further detriment to the world population. Not to mention, fresh water production requires a lot of energy, and the energy production processes (i.e. power plants) require water themselves.[43,46] However, even small efforts can reap great benefits, as demonstrated by an estimate that the economic growth of an affected country can be up to 1000s % when the water crisis is mediated,100's of millions more would be able to attend schooling, and billions in health costs would be saved per year.[45]

In order to meet the global demand, one approach has been the refining of salty/brackish water via the removal of salts - desalination. Current desalination methods include reverse osmosis (RO), electrodialysis, multi-stage flash photolysis, and evaporation; all are expensive due to the energy input required, but membrane processes (i.e. RO and electrodialysis) are the cheapest.[47] When considering water flow across a membrane, it is necessary to take osmotic pressure into account. Due to osmotic pressure, normally if two stores of water with an unequal solute concentration are joined by a semipermeable membrane, water will tend to move from the

hypotonic to the hypertonic store until a dynamic equilibrium is reached and the entropy gradient is zero. Osmotic pressure, π, is given as

$$\pi = -\frac{RT}{V_m} \ln a_{solv} \tag{2.1}$$

or under dilute conditions

$$\pi \equiv M_{solu} RT \tag{2.2}$$

where R is the ideal gas constant, T is absolute temperature (Kelvin), a_{solv} is the activity of the solvent, V_m is the molar volume of the solvent, and M_{solu} is the molar concentration of the solute. To produce fresh water from salty/brackish water, it is necessary to apply a force exceeding the osmotic pressure.

In reverse osmosis purification, water is forced through a semipermeable membrane at high pressure (i.e. MPa) to accumulate a reserve of fresh, contaminant-free water (Figure 2.2).

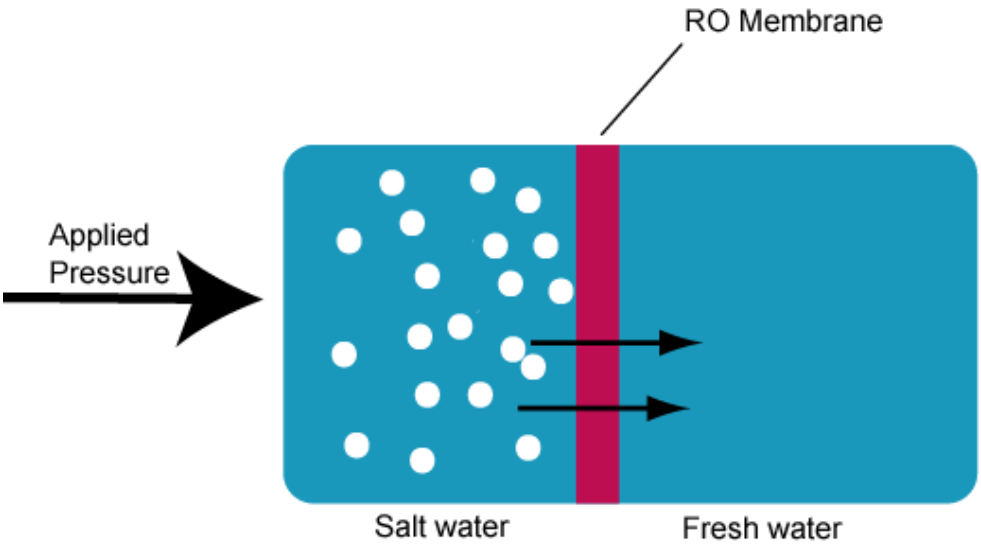

Figure 2.2. Illustration of desalination using RO membrane methodology.

In order to reduce costs much effort in the realm of RO methodology is focused on the development of more efficient polymer membranes.[44,47] RO membranes must be able to allow a high amount of water to flow through the membrane (high water flux) while simultaneously blocking salts, bacteria, and other contaminants. Also, accumulation of bio-organisms on the membrane surface (biofouling) can occur, which degrades the performance of the membranes. Thus, acceptable technology must be resistant to biofouling and anti-biofouling measures.

Transport in RO membranes takes place via a solution-diffusion process.[48,49] Ideally, the selective polymer membrane is dense and non-porous, so solutions can not simply flow through (which would be a pore-flow mechanism).[50] In solution diffusion, the molecules (i.e. water) dissolve into the membrane itself and travel through via stochastic jumps between transient pores that result from thermal motion of polymer chains.[51] Permeates are separated based on permeate-membrane solubility and diffusion rate differences.

The first RO membranes developed were made from cellulose acetate (CA), following the observation that CA had good salt rejection characteristics.[52,53] The major flaw of these membranes was that their thickness was detrimental to good water flux. Membrane preparation was improved by the introduction of a novel method which yielded anisotropic, asymmetric CA membranes. These membranes were made up of two CA layers: a nonporous selective layer (for water flux and salt rejection) over a thicker, porous support layer with non-uniform pore sizes.[47,54-56] Asymmetric membranes can be made by the phase inversion method; a polymer solution is coated on a substrate, and then exposed to a nonsolvent for the polymer, inducing pores in the membrane.[57] These membranes became commercially available in the 1970's.[47] CA membranes are resistant to chlorine degradation, but they are also susceptible to breakdown due to hydrolysis at high and low pH values (i.e. at pH 4-6 membranes can last years, while at pH 1 or 9 they are stable for only days), and they are mechanically weak to high pressures.[47] Since, CA is highly pH sensitive, using them is labor intensive because it necessitates close monitoring and maintenance efforts of the feed water.

Polyamide (PA) thin film composite (TFC) membranes are the current state-of-the-art technology.[58,59] TFCs consist of three layers: (layer 1: top/ outer layer) a very thin (i.e. $\leq .1$ μm)[60] layer of the selective membrane polymer which is the membrane portion facing the contaminated water (layer 2: middle) a thicker (i.e. polysulfone, ~50 μm) porous support layer (layer 3: bottom/ inner layer) a thick fabric layer for providing structural support (i.e. polyester,

~120 μm) .[44,61] The porous middle layer is formed on top of the bottom layer using phase-inversion[57], and the barrier layer can be formed on the porous layer via interfacial-polymerization.[62] With interfacial polymerization, an aqueous solution of one type of monomer is introduced on top of the middle layer, which is then exposed to a non-polar organic solution containing a second monomer; the two solutions are phase separated, but the monomers can react at the interface, which ensures a thin barrier layer.[44]Since TFC's are made in a step-by-step manner, a RO membrane can be tuned to different conditions by individually modifying the different layers. Furthermore, TFC's are also advantageous because the thin top/outer layer does not require a lot of material and can easily be crosslinked for tuning water flux/salt rejection.[63] PA has advantages over CA since it is not as susceptible to degradation from hydrolysis or marine organisms, and can withstand high pressures, compared to cellulose acetate, but it can easily be broken down by chlorine via attack of the amide moiety, [64] which is added to feed water as a biocide to prevent biofouling.[43,47] Chlorine sensitive membranes also make water treatment much more laborious and expensive because feed waters should be dechlorinated prior to meeting the membrane, and following membrane treatment the chlorine needs to be added again as a disinfectant. Despite the fact that some alternatives to the PA technology are commercially available, notably Nexar™ which was developed by Kraton Polymers LLC., much work is needed to upgrade the current technology to a point where it is feasible for producing fresh water on a large scale.

Many chemistry and materials research groups are presently focused on developing novel RO polymeric materials. Work discussed in Chapters 3-4 will focus on studies performed on various sulfonated poly(arylene ether sulfone) (also referred to as sulfonated polysulfone (SPS)) copolymers collaboratively developed by the McGrath Group (department of chemistry, Virginia Polytechnic Institute and Statue University) and the Freeman Group (department of chemical engineering, The University of Texas at Austin).[59,65-70] Polysulfones (PS) are versatile polymers with applictions in a wide array of areas such as proton exchange membranes (PEM),[71-74] vehicle components, food preparation and storage, and medical devices.[75] PSs could be useful as RO membranes as they are stable in the presence of chlorine due to the absence of an amide group, the target of attack in polyamide. Sulfonating PS is a desireable method for imparting a hydrophilic property to the hydrophobic PS, a requirement for allowing water flux.[76,77] Initially, even though these polymers showed good desalination membrane characteristics, they were not

heavily used because the chemistry for synthesizing SPSs, which involved post-polymerization sulfonation, was not optimal; reactions were difficult to control and sometimes detrimental to membrane performance .[76-80] However, interest in developing SPSs for RO applications reignited following the development of direct polymerization using disulfonated monomers.[59,78]

Briefly, in addition to SPSs, other avenues are being explored in developing new RO membranes. One idea has been to modify standard PA TFC membranes. For example, in one attempt a series of polyacyl chlorides were synthesized from polymerization of an acyl chloride monomer (trimesoyl chloride (TMC), 5-isocyanoto-isophthaloyl chloride (ICIC), or 5-chloroformyloxy-isophthaloyl chloride (CFCI)) with m-phenylenediamine.[81] The CFIC membrane had the highest salt rejection and lowest water permeability, followed by TMC, and the ICIC membrane had the highest water permeability and lowest salt rejection. In another instance, 3-monomethylol-5,5-dimethylhydantoin (MDMH) was grafted onto a PA membrane (MDMH-PA).[82] Prior to testing MDMH-PA and the PA for chlorine tolerance, MDMH-PA showed a comparably higher flux and lower salt rejection compared to PA. However, it also demonstrated better chlorine tolerance, as changes in water flux/salt rejection were greater for PA. Membranes composed of novel materials such as Si_3N_4 films with imbedded carbon nanotubes,[83,84] carbonaceous poly(furfuryl alcohol),[85] and liquid crytals[86] are also being investigated.

Once a desirable membrane material is found, research efforts can be focused on then optimizing the properties of the RO polymer by using additives; some examples are dimethylsulfoxide,[87] maleic acid,[88] and isopropyl alcohol[89]. A known way of increasing water flux in water purification membranes (i.e. RO and ultrafiltration (UF) membranes), is by incorporating polyethylene glycol (PEG), which acts as a plasticizer to soften the polymer matrix; details of the PEG-RO membrane interaction will be explained in Chapters 3-4. For instance, UF CA/ SPS membranes with PEG 600 (molecular weight is 600 kDA) showed increased water flux with increasing PEG content; for membranes of CA:SPS (85:15), flux was 85.5 $lm^{-2}h^{-1}$ for 2.5 % PEG and 141.5 $lm^{-2}h^{-1}$ for 10 % PEG.[90] Additionally, UF PS membranes containing PEG showed water flux changes that depended on the PEG size.[91] PEG 200,400, and 600, at 5-25 wt. % were explored, and it was seen that PEG-200 decreased water permeation, but PEG 400 and PEG 600 increased water flux, even up to ~6 times that for membranes not containing PEG (i.e. PEG 600 at 25 %). Increasing PEG 200 content continuously decreased

water permeation, while the opposite trend was noted for PEG 400 and PEG 600, with PEG 600 always producing the best flux enhancements. Finally, chitosan RO membranes containing PEG were studied, and it was observed that water flux increased 30 % upon adding 40 % PEG 200.[92]

The ability of solid-state NMR to elucidate molecular-level dynamics/structural parameters makes in a valuable tool for tuning the efficency of a RO membrane material since it is these that dictate the characteristics of the material as a whole.[87,93,94] Not to mention, solid-state NMR can selectively probe different polymer segments or domains (i.e. hydrophobic and hydrophilic polymer regions).

2.3. Hydrophobic Interactions and Fullerenes

Interactions of water with hydrophobic materials are ubiquitous in areas such as biology[95-99] and materials science.[100-105] Essentially, the nonpolar substances affect the randomly ordered water molecules and cause them to form a structured arrangement so that the water's entropy is maximized. A more complete understanding of hydrophobic hydration, which would provide insight into things like protein folding and clathrate formation, requires probing the water-hydrophobic material interface on the molecular level. One possible technique, solid-state NMR, has proven itself to be useful in surface studies.[8,30,106-108] As will be demonstrated in Chapter 8, it is especially helpful for water-hydrophobic material interfaces because cross-polarization (CP)[109] can exclude the bulk water influence from the measurement.

A class of hydrophobic materials of current interest, are carbon nanomaterials (fullerenes) (Chapter 8 will specifically focus on C_{60} in water; depicted in Figure 2.3). Fullerenes were first reported in 1985 in the form of the soccer-ball shaped C_{60}[110], and now other sphere-like allotropes[111], endohedral fullerenes[112-114], and carbon nanotubes[115] are also known. Fullerenes are now routinely made in the laboratory setting and are commercially available, but they have also recently been found in outer space[116] and are present in Earth's environment due to human processes.[103]

While the study described in Chapter 8 was not focused on a specific application or problem, there is interest in applications or occurrences of fullerenes in aqueous environments.[117] In terms of environmental health, there is much concern over what, if any, toxicity effects are

caused by anthropogenic fullerenes.[118-120] Practically, fullerenes could be of use in water transport[83] and purification by capturing bioorganisms[121,122] , metal ions[123], and pollutants[124].

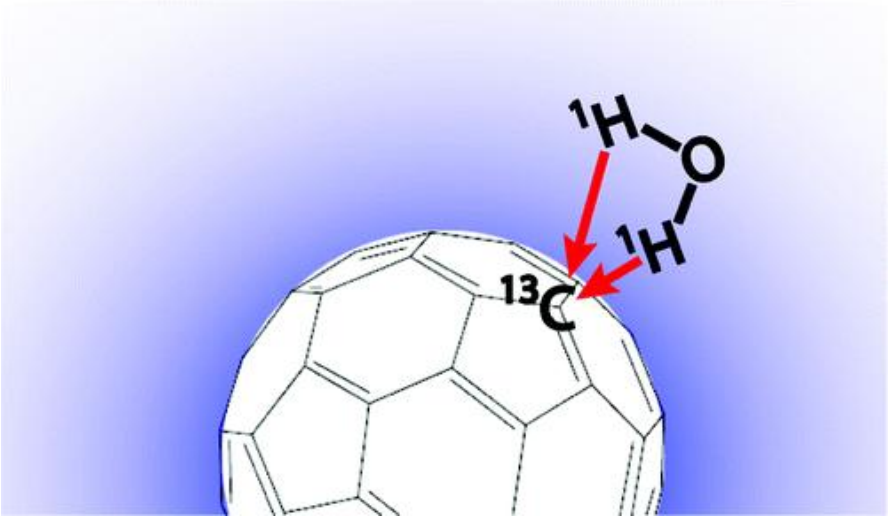

Figure 2.3.[125] Schematic of the experiment for C_{60} in water (only one molecule shown explicitly). The magnetic dipolar coupling between one ^{1}H in water and one ^{13}C site in C_{60} is strongly dependent on the separation between the ^{1}H and the ^{13}C, r, decaying as $1/r^3$. Hence, dipolar coupling is selective for the water immediately adjacent to the C_{60}, as represented schematically by a gradient in shading around the C_{60}. Multiple $^{13}C–^{1}H$ dipolar contacts are expected for each ^{13}C in a C_{60} molecule. Theoretical calculations are necessary to understand the structural arrangement of water around C_{60}. Reproduced with permission from Wi,S.; Spano, J.; Ducker, W.A. *J. Phys. Chem. C* **2010**, 114, 14986. Copyright 2010 American Chemical Society.

References

(1) Nelson, D. L.; Cox, M. M. In *Lehninger Principles of Biochemistry*; 4 ed.; W.H. Freeman and Company: New York, 2005.

(2) Singer, S. J.; Nicolson, G. L. *Science* **1972**, *175*, 720.

(3) Jenssen, H.; Hamill, P.; Hancock, R. E. W. *Clin. Microbiol. Rev.* **2006**, *19*, 491.

(4) Rozek, T.; Wegener, K. L.; Bowie, J. H.; Olver, I. N.; Carver, J. A.; Wallace, J. C.; Tyler, M. J. *Eur. J. Biochem.* **2000**, *267*, 5330.

(5) Alessandro, T.; Luca, S.; Anna, G. *Pept. Sci.* **2000**, *55*, 4.

(6) Ganz, T.; Selsted, M. E.; Szklarek, D.; Harwig, S. S.; Daher, K.; Bainton, D. F.; Lehrer, R. I. *J. Clin. Invest.* **1985**, *76*, 1427.

(7) Brogden, K. A. *Nat. Rev. Micro.* **2005**, *3*, 238.

(8) Hallock, K. J.; Lee, D. K.; Ramamoorthy, A. *Biophys. J.* **2003**, *84*, 3052.

(9) Hancock, R. E.; Chapple, D. S. *Antimicrob. Agents Chemother.* **1999**, *43*, 1317.

(10) Hancock, R. E. W.; Sahl, H.-G. *Nat. Biotech.* **2006**, *24*, 1551.

(11) Davies, J.; Davies, D. *Microbiol. Mol. Biol. Rev.* **2010**, *74*, 417.

(12) Hultmark, D.; Steiner, H.; Rasmuson, T.; Boman, H. G. *Eur. J. Biochem.* **1980**, *106*, 7.

(13) Dennison, S. R.; Harris, F.; Phoenix, D. A. *Biophys. Chem.* **2007**, *127*, 78.

(14) Huang, H. W. *Biochim. Biophys. Acta, Biomembr.* **2006**, *1758*, 1292.

(15) Marcotte, I.; Wegener, K. L.; Lam, Y.-H.; Chia, B. C. S.; de Planque, M. R. R.; Bowie, J. H.; Auger, M. e.; Separovic, F. *Chemistry and Physics of Lipids* **2003**, *122*, 107.

(16) Bechinger, B. *Biochim. Biophys. Acta, Biomembr.* **1999**, *1462*, 157.

(17) Kim, C.; Wi, S. *J. Phys. Chem. B.* **2008**, *112*, 11402.

(18) Roux, M.; Neumann, J. M.; Bloom, M.; Devaux, P. F. *Eur. Biophys. J.* **1988**, *16*, 267.

(19) Lai, Y.; Gallo, R. L. *Trends Immunol.* **2009**, *30*, 131.

(20) Mecke, A.; Lee, D. K.; Ramamoorthy, A.; Orr, B. G.; Banaszak Holl, M. M. *Biophys. J.* **2005**, *89*, 4043.

(21) Mandard, N.; Sy, D.; Maufrais, C.; Bonmatin, J. M.; Bulet, P.; Hetru, C.; Vovelle, F. *J. Biomol. Struct. Dyn.* **1999**, *17*, 367.

(22) Shepherd, C. M.; Vogel, H. J.; Tieleman, D. P. *Biochem. J.* **2003**, *370*, 233.

(23) La Rocca, P.; Biggin, P. C.; Tieleman, D. P.; Sansom, M. S. P. *Biochim. Biophys. Acta, Biomembr.* **1999**, *1462*, 185.

(24) Matyus, E.; Kandt, C.; Tieleman, D. P. *Curr. Med. Chem.* **2007**, *14*, 2789.

(25) Oren, Z.; Shai, Y. *Pept. Sci.* **1998**, *47*, 451.

(26) Matsuzaki, K.; Sugishita, K.-i.; Harada, M.; Fujii, N.; Miyajima, K. *Biochim. Biophys. Acta, Biomembr.* **1997**, *1327*, 119.

(27) Nizet, V.; Ohtake, T.; Lauth, X.; Trowbridge, J.; Rudisill, J.; Dorschner, R. A.; Pestonjamasp, V.; Piraino, J.; Huttner, K.; Gallo, R. L. *Nature* **2001**, *414*, 454.

(28) Zasloff, M. *Nature* **2002**, *415*, 389.

(29) Ouellet, M.; Auger, M. e.; Graham, A. W. In *Annu. Rep. NMR. Spectrosc.*; Academic Press: 2008; Vol. 63, p 1.

(30) Kim, C.; Spano, J.; Park, E.-K.; Wi, S. *Biochim. Biophys. Acta, Biomembr.* **2009**, *1788*, 1482.

(31) Gu, Z. T.; Opella, S. J. *J. Magn. Reson.* **1999**, *140*, 340.

(32) Ramamoorthy, A. *Solid State Nucl. Magn. Reson.* **2009**, *35*, 201.

(33) Bertelsen, K.; Paaske, B.; Thøgersen, L.; Tajkhorshid, E.; Schiøtt, B.; Skrydstrup, T.; Nielsen, N. C.; Vosegaard, T. *J. Am. Chem. Soc.* **2009**, *131*, 18335.

(34) Hong, M. *Acc. Chem. Res.* **2006**, *39*, 176.

(35) Strandberg, E.; Ulrich, A. S. *Concepts Magn. Reson.* **2004**, *23A*, 89.

(36) Marasinghe, P. A. B.; Buffy, J. J.; Schmidt-Rohr, K.; Hong, M. *J. Phys. Chem. B* **2005**, *109*, 22036.

(37) Webb, G. A.; Ouellet, M.; Auger, M. In *Modern Magnetic Resonance*; Springer Netherlands: 2006, p 271.

(38) Baumann, G.; Mueller, P. *J. Supramol. Struct.* **1974**, *2*, 538.

(39) Shai, Y. *Pept. Sci.* **2002**, *66*, 236.

(40) Sato, H.; Feix, J. B. *Biochim. Biophys. Acta, Biomembr.* **2006**, *1758*, 1245.

(41) Pouny, Y.; Rapaport, D.; Mor, A.; Nicolas, P.; Shai, Y. *Biochemistry* **1992**, *31*, 12416.

(42) Blondelle, S. E.; Houghten, R. A. *Biochemistry* **1992**, *31*, 12688.

(43) Service, R. *Science* **2006**, *313*, 1088.

(44) Geise, G. M.; Lee, H. S.; Miller, D. J.; Freeman, B. D.; McGrath, J. E.; Paul, D. R. *J. Polym. Sci., Part B: Polym. Phys.* **2010**, *48*, 1685.

(45) Water.org, http://water.org/learn-about-the-water-crisis/facts/.

(46) Webber, M. E. *Sci. Am. Sp. Ed.* **2008**, *18*, 34.

(47) Fritzmann, C.; Löwenberg, J.; Wintgens, T.; Melin, T. *Desalination* **2007**, *216*, 1.

(48) Wijmans, J. G.; Baker, R. W. *J. Membr. Sci.* **1995**, *107*, 1.

(49) Merten, U. *Ind. Eng. Chem. Fundam.* **1963**, *2*, 229.

(50) Koros, W. J.; Fleming, G. K.; Jordan, S. M.; Kim, T. H.; Hoehn, H. H. *Prog. Polym. Sci.* **1988**, *13*, 339.

(51) Baker, R. W. In *Membrane Technology and Applications*; 2 ed.; John Wiley & Sons: West Sussex, 2004.

(52) Reid, C. E.; Breton, E. J. *J. Appl. Polym. Sci.* **1959**, *1*, 133.

(53) Reid, C. E.; Kuppers, J. R. *J. Appl. Polym. Sci.* **1959**, *2*, 264.

(54) Riley, R.; Gardner, J. O.; Merten, U. *Science* **1964**, *143*, 801.

(55) Loeb, S.; Sourirajan, S. In *Saline Water Conversion-II*; American Chemical Society: 1963; Vol. 38, p 117.

(56) Loeb, S.; Sourirajan, S. US, 1964; Vol. 3,133,132.

(57) Kim, H. J.; Tyagi, R. K.; Fouda, A. E.; Ionasson, K. *J. Appl. Polym. Sci.* **1996**, *62*, 621.

(58) Riley, R. L.; Lonsdale, H. K.; Lyons, C. R.; Merten, U. *J. Appl. Polym. Sci.* **1967**, *11*, 2143.

(59) Park, H. B.; Freeman, B. D.; Zhang, Z. B.; Sankir, M.; McGrath, J. E. *Angew. Chem.* **2008**, *120*, 6108.

(60) Williams, M. E.; EET Corporation and Williams Engineering Services Company, Inc.: 2003, p 29.

(61) Petersen, R. J. *J. Membr. Sci.* **1993**, *83*, 81.

(62) Riley, P. L.; Milstead, C. E.; Lloyd, A. L.; Seroy, M. W.; Tagami, M. *Desalination* **1966**, *23*, 331.

(63) Cadottee, J. E. P., R.J. In *Handbook of Industrial Membrane Technology*; Porter, M. C., Ed.; William Andrew Publishing/Noyes: Westwood, 1990, p 307.

(64) Glater, J.; Hong, S.-k.; Elimelech, M. *Desalination* **1994**, *95*, 325.

(65) Wei, X.; Ho-Bum, P.; Cook, J.; Chang Hyun, L.; Gwangsu, B.; Freeman, B. D.; McGrath, J. E. *Water Sci. Technol.* **2010**, *61*, 619.

(66) Paul, M.; Park, H. B.; Freeman, B. D.; Roy, A.; McGrath, J. E.; Riffle, J. S. *Polymer* **2008**, *49*, 2243.

(67) Paul, M.; Roy, A.; Park, H. B.; Freeman, B. D.; Riffle, J. S.; McGrath, J. E. *Polym. Prepr.* **2007**, *48*.

(68) Wei, X; Park, H. B.; Cook, J.; Lee, C. H.; Byun, G.; Freeman, B. D.; McGrath, J. E. *Water Sci. Technol.* **2010**, *61*, 619.

(69) Park, H. B.; Freeman, B. D.; Zhang, Z. B.; Fan, G. Y.; Sankir, M.; McGrath, J. E. *PMSE Preprint* **2006**, *95*, 888.

(70) Geise, G. M.; Park, H. B.; Sagle, A. C.; Freeman, B. D.; McGrath, J. E. *J. Membr. Sci., In Press*.

(71) Li, Y.; Wang, F.; Yang, J.; Liu, D.; Roy, A.; Case, S.; Lesko, J.; McGrath, J. E. *Polymer* **2006**, *47*, 4210.

(72) Lee, H.-S.; Roy, A.; Lane, O.; Dunn, S.; McGrath, J. E. *Polymer* **2008**, *49*, 715.

(73) Wang, F.; Hickner, M.; Ji, Q.; Harrison, W.; Mecham, J.; Zawodzinski, T. A.; McGrath, J. E. *Macromolecular Symposia* **2001**, *175*, 387.

(74) Roy, A.; Lee, H.-S.; McGrath, J. E. *Polymer* **2008**, *49*, 5037.

(75) IDES; Vol. January 18,2011.

(76) Brousse, C.; Chapurlat, R.; Quentin, J. P. *Desalination* **1976**, *18*, 137.

(77) Noshay, A.; Robeson, L. M. *J. Appl. Polym. Sci.* **1976**, *20*, 1885.

(78) Ueda, M.; Toyota, H.; Ouchi, T.; Sugiyama, J.-I.; Yonetake, K.; Masuko, T.; Teramoto, T. *J. Polym. Sci., Part A: Polym. Chem.* **1993**, *31*, 853.

(79) Johnson, B. C.; Yilgör, İ.; Tran, C.; Iqbal, M.; Wightman, J. P.; Lloyd, D. R.; McGrath, J. E. *J. Polym. Sci. Pol. Chem.* **1984**, *22*, 721.

(80) Drzewinski, M.; MacKnight, W. J. *J. Appl. Polym. Sci.* **1985**, *30*, 4753.

(81) Liu, M.; Wu, D.; Yu, S.; Gao, C. *J. Membr. Sci.* **2009**, *326*, 205.

(82) Wei, X.; Wang, Z.; Chen, J.; Wang, J.; Wang, S. *J. Membr. Sci.* **2010**, *346*, 152.

(83) Holt, J. K.; Park, H. G.; Wang, Y.; Stadermann, M.; Artyukhin, A. B.; Grigoropoulos, C. P.; Noy, A.; Bakajin, O. *Science* **2006**, *312*, 1034.

(84) Fornasiero, F.; Park, H. G.; Holt, J. K.; Stadermann, M.; Grigoropoulos, C. P.; Noy, A.; Bakajin, O. *PNAS* **2008**, *105*, 17250.

(85) He, L.; Li, D.; Zhang, G.; Webley, P. A.; Zhao, D.; Wang, H. *Ind. Eng. Chem. Res.* **2010**, *49*, 4175.

(86) Hatakeyama, E. S.; Gabriel, C. J.; Wiesenauer, B. R.; Lohr, J. L.; Zhou, M.; Noble, R. D.; Gin, D. L. *J. Membr. Sci.* **2011**, *366*, 62.

(87) Kwak, S.-Y.; Jung, S. G.; Kim, S. H. *Environ. Sci. Technol.* **2001**, *35*, 4334.

(88) Vásárhelyi, K.; Ronner, J. A.; Mulder, M. H. V.; Smolders, C. A. *Desalination* **1987**, *61*, 211.

(89) Liu, M.; Yu, S.; Tao, J.; Gao, C. *J. Membr. Sci.* **2008**, *325*, 947.

(90) Malaisamy, R.; Mahendran, R.; Mohan, D.; Rajendran, M.; Mohan, V. *J. Appl. Polym. Sci.* **2002**, *86*, 1749.

(91) Idris, A.; Mat Zain, N.; Noordin, M. Y. *Desalination* **2007**, *207*, 324.

(92) Yang, T.; Zall, R. R. *J. Food Sci.* **1984**, *49*, 91.
(93) Kwak, S.-Y.; Woo Ihm, D. *J. Membr. Sci.* **1999**, *158*, 143.
(94) Xu, X.; Kirkpatrick, R. J. *J. Membr. Sci.* **2006**, *280*, 226.
(95) Modig, K.; Liepinsh, E.; Otting, G.; Halle, B. *J. Am. Chem. Soc.* **2003**, *126*, 102.
(96) Rodríguez-Cabello, J. C.; Alonso, M.; Pérez, T.; Herguedas, M. M. *Biopolymers* **2000**, *54*, 282.
(97) Cheng, Y.-K.; Rossky, P. J. *Nature* **1998**, *392*, 696.
(98) Cheng, Y.-K.; Sheu, W.-S.; Rossky, P. J. *Biophys. J.* **1999**, *76*, 1734.
(99) Sorenson, J. M.; Hura, G.; Soper, A. K.; Pertsemlidis, A.; Head-Gordon, T. *J. Phys. Chem. B* **1999**, *103*, 5413.
(100) Yaminsky, V. V.; Vogler, E. A. *Curr. Opin. Colloid Interface Sci.* **2001**, *6*, 342.
(101) Uchida, T.; Okabe, R.; Gohara, K.; Mae, S.; Seo, Y.; Lee, H.; Takeya, S.; Nagao, J.; Ebinuma, T.; Narita, H. *Can. J. Phys.* **2003**, *81*, 359.
(102) Satoh, M.; Yoda, E.; Komiyama, J. *Macromolecules* **1991**, *24*, 1123.
(103) Inomata, H.; Goto, S.; Otake, K.; Saito, S. *Langmuir* **1992**, *8*, 687.
(104) Burkett, S. L.; Davis, M. E. *Chem. Mater.* **1995**, *7*, 1453.
(105) Bowron, D. T.; Filipponi, A.; Roberts, M. A.; Finney, J. L. *Phys. Rev. Lett.* **1998**, *81*, 4164.
(106) Sindorf, D. W.; Maciel, G. E. *J. Am. Chem. Soc.* **1983**, *105*, 3767.
(107) Scolan, E.; Magnenet, C.; Massiot, D.; Sanchez, C. *J. Mater. Chem.* **1999**, *9*, 2467.
(108) Ladizhansky, V.; Hodes, G.; Vega, S. *J. Phys. Chem. B* **2000**, *104*, 1939.
(109) Pines, A.; Gibby, M. G.; Waugh, J. S. *J. Chem. Phys.* **1973**, *59*, 569.
(110) Smalley, R. E.; Kroto, H. W.; Heath, J. R. *Nature* **1985**, *318*, 162.
(111) Diederich, F.; Ettl, R.; Rubin, Y.; Whetten, R. L.; Beck, R.; Alvarez, M.; Anz, S.; Sensharma, D.; Wudl, F.; Khemani, K. C.; Koch, A. *Science* **1991**, *252*, 548.
(112) Jerzy, C.; Eugene, D. F. *J. Chem. Phys.* **1991**, *94*, 3730.
(113) Chai, Y.; Guo, T.; Jin, C.; Haufler, R. E.; Chibante, L. P. F.; Fure, J.; Wang, L.; Alford, J. M.; Smalley, R. E. *J. Phys. Chem.* **1991**, *95*, 7564.
(114) Dorn, H. C.; Stevenson, S.; Burbank, P.; Sun, Z.; Glass, T.; Harich, K.; Loosdrecht, P. H. M.; Johnson, R. D.; Beyers, R.; Salem, J. R.; Materials Research Society: 1995; Vol. 359, p 123.

(115) Iijima, S. *Nature* **1991**, *354*, 56.

(116) Cami, J.; Bernard-Salas, J.; Peeters, E.; Malek, S. E. *Science* **2010**, *329*, 1180.

(117) Labille, J.; Masion, A.; Ziarelli, F.; Rose, J.; Brant, J.; Villiéras, F.; Pelletier, M.; Borschneck, D.; Wiesner, M. R.; Bottero, J.-Y. *Langmuir* **2009**, *25*, 11232.

(118) Taurozzi, J. S.; Pandey, A. K.; Shan, W.; Miller, S. M.; Hashsham, S. A.; Tarabara, V. V. *Environ. Sci. Technol.y* **2006**, *40*, 7394.

(119) Tong, Z.; Bischoff, M.; Nies, L.; Applegate, B.; Turco, R. F. *Environ. Sci. Technol.* **2007**, *41*, 2985.

(120) Nowack, B.; Bucheli, T. D. *Environ. Pollut.* **2007**, *150*, 5.

(121) Lyon, D. Y.; Fortner, J. D.; Sayes, C. M.; Colvin, V. L.; Hughes, J. B. *Environ. Toxicol. Chem.* **2005**, *24*, 2757.

(122) Srivastava, A.; Srivastava, O. N.; Talapatra, S.; Vajtai, R.; Ajayan, P. M. *Nat. Mater.* **2004**, *3*, 610.

(123) Li, Y.-H.; Ding, J.; Luan, Z.; Di, Z.; Zhu, Y.; Xu, C.; Wu, D.; Wei, B. *Carbon* **2003**, *41*, 2787.

(124) Fugetsu, B.; Satoh, S.; Shiba, T.; Mizutani, T.; Lin, Y.-B.; Terui, N.; Nodasaka, Y.; Sasa, K.; Shimizu, K.; Akasaka, T.; Shindoh, M.; Shibata, K.-i.; Yokoyama, A.; Mori, M.; Tanaka, K.; Sato, Y.; Tohji, K.; Tanaka, S.; Nishi, N.; Watari, F. *Environ. Sci. Technol.* **2004**, *38*, 6890.

(125) Wi, S.; Spano, J.; Ducker, W. A. *J. Phys. Chem. C* **2010**, *114*, 14986.

Chapter 3

Disulfonated Poly(Arylene Ether Sulfone) Random Copolymer Blends Tuned for Rapid Water Permeation via Cation Complexation with Poly(Ethylene Glycol) Oligomers

Reproduced in part with permission from Lee, C.H.; VanHouten, D; Lane, O; McGrath, J.E.; Hou, J; Madsen, L.A.; Spano, J.; Wi, S; Cook, J.; Xie, W.; Oh, H.J.; Geise, G.M.; Freeman, B.D. *Chem. Matter.*, **2011**, 23, 1039. Solid-state NMR experiments were performed by the Wi Group at Virginia Tech. Diffusion measurements were performed by the Madsen Group at Virginia Tech. Polymer processing and characterization was performed by the McGrath Group at Virginia Tech and the Freeman Group at the University of Texas at Austin.

3.1. Introduction

The ability to efficiently and economically produce fresh water from brackish and seawater is critical to addressing the growing global water shortage.[1] Reverse osmosis (RO) processes can be used to effectively remove salts and large solutes, including bacteria, from natural water using membranes with high flux and high salt rejection characteristics.[2,3] Currently, interfacially polymerized aromatic polyamide (PA) thin film composite membranes are the state-of-the-art RO technology because they offer high water flux and salt rejection (>99%) over a wide pH range.[4] PA membranes, however, can be degradaded by chlorine-based chemicals such as sodium hypochlorite, which is used to disinfect water, and membrane performance suffers after continuous exposure to even low concentrations of available chlorine.[5,6]

Disulfonated poly(arylene ether sulfone) copolymers, now being developed for desalination membrane applications, are more stable in chlorinated solution than commercial PA membranes.[7,8] This chlorine tolerance may be due to the absence of amide bonds in the sulfonated polysulfone; amide bonds, such as those found in commercial PA RO membranes, are vulnerable to attack by chlorine-based chemicals.[9,10] Figure 3.1 presents the chemical structure of 20 mol % disulfonated poly(arylene ether sulfone) random copolymer (BPS-20). BPS-20, when studied as a cast film, exhibits stable RO performance, i.e., no substantial decrease in salt rejection or increase in water flux, after continuous exposure to chlorinated water at both high

and low pH, i.e., >40 h at 500 ppm available chlorine.[8] A commercial PA membrane (SW30HR, Dow Film-Tec) experienced a 20% decrease in salt rejection within 20 h of exposure to the same chlorinated conditions.[8]

The water flux and salt rejection of BPS random copolymers exhibit a trade-off relationship;[2,11] highly water-permeable BPS materials tend to exhibit relatively low NaCl rejection and vice versa. BPS-20 has been identified as a candidate for desalination membrane applications because the NaCl rejection of BPS-20 is 99%.

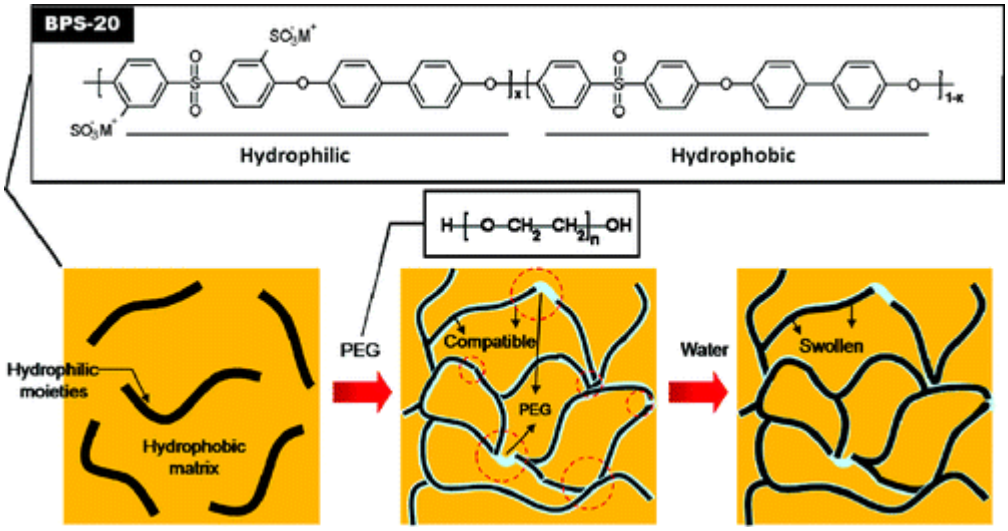

Figure 3.1. Pseudoimmobilization of PEG molecules with BPS-XX. Here, $M^+ = Na^+$ or K^+ and XX = degree of sulfonation in mol %. In BPS-20, *x* is 0.2.

The BPS-20 water permeability (0.033 L μm m^{-2} h^{-1} bar^{-1}),[8] however, is low. For example, considering a BPS-20 material with a 100 nm thick active layer in a composite membrane structure, similar to the accepted structure of commercially available PA RO membranes, the water permeance would be expected to be 0.33 L m^{-2} h^{-1} bar^{-1} (2000 ppm NaCl feed at 27.6 bar and pH 8).[8,12] This is much less than commercially available PA RO membranes, DOW BW30 and SW30HR, whose water permeance is 3.3 L m^{-2} h^{-1} bar^{-1} (2 000 ppm NaCl feed at 15.5 bar and pH 8)[13] and 1.1 L m^{-2} h^{-1} bar^{-1} (32 000 ppm NaCl feed at 55.2 bar and pH 8),[14] respectively.[15]

This chapter describes a new approach to increase the water permeability of BPS-20 and

thus improve the material's desalination performance, via addition of poly(ethylene glycol) (PEG, Figure 3.1), a hydrophilic cation complexing agent. PEG oligomers were blended with BPS-20 to vary the resulting material's water permeability without changing the BPS material's degree of sulfonation (DS) because 20 % disulfonation was found to be optimal for salt rejection. PEG systems are ubiquitous in self-assembly,[16,17] gas separation,[18]water purification,[19-23] and biomedical applications.[24,25] For example, PEG can be coated or grafted on ultrafiltration membranes to reduce fouling by oil−water mixtures[23] and to reduce blood coagulation in clinical hemodialysis.[21]

The water-soluble PEG is often immiscible in many polymers because it does not interact favorably with many polymer matrices, allowing its extraction in aqueous environments. To prevent such leaching, PEG chains can be immobilized via chemical modification (i.e., cross-linking[23] or grafting[21,22]) or hydrogen bonding with acidic polymers (e.g., poly(acrylic acid)[26] and poly(methacrylic acid)[27]). There are, however, applications for PEG (i.e., pore forming agents)[19,20] where blending has been successfully employed.

Ether oxygen atoms of PEG form complexes with a variety of metal cations (Li^+, Na^+, K^+, Cs^+, and Rb^+) via ion−dipole interactions[28,29] similar to the behavior of cyclic ethers (e.g., crown ethers).[30-32] Such interactions in aqueous environments[33] have been suggested to explain the miscibility of PEG molecules and salt form sulfonated polymers, which are composed of sulfonate anions and metal cations ($-SO_3M$, where M is a cation of an alkali metal element such as Na or K). If PEG does complex with metal cations in sulfonated polymers, physical enthalpic interactions might effectively immobilize PEG in the sulfonated polymer matrix without the use of covalent bonds (pseudoimmobilization, Figure 3.1). These interactions could prevent PEG from leaching out of the polymer matrix upon exposure to water provided that the interactions are strong and sustained. Additionally, as will be shown by results of experiments discussed herein, PEG may increase the water permeability of the sulfonated polymer matrix. This study seeks to understand the nature of the interaction between PEG and the disulfonated copolymer, BPS-20. The main objective is to systematically investigate the influence of PEG complexing agents, with different molecular weights and concentrations, on the physicochemical characteristics of the salt form of sulfonated polymer membranes. To probe these polymer blends, we employed pulsed-field gradient stimulated echo (PGSTE) NMR spectroscopy, which can track the diffusion of water molecules in mixed matrixes over time using magnetic field

gradients to label nuclear spins with NMR frequencies based on their locations.[34,35] Another major objective is to verify the efficacy of our pseudoimmobilization approach for forming fast water transport pathways for desalination applications. Finally, the chlorine resistance of the blend films was compared to a PA membrane by using solid-state NMR to evidence structural changes occurring in the polymers following exposure under different chlorine conditions (variations in time of exposure, and chlorine concentration).

3.2. Experimental Methods

3.2.1. Materials

BPS-20 in the potassium salt form ($-SO_3K$) was synthesized by Akron Polymer Systems (Akron, OH) following published procedures.[36-40] The material used in this study, BPS-20 (the exact degree of sulfonation was 20.1 mol % measured using ^{1}H NMR) has an intrinsic viscosity of 0.82 dL g^{-1} in NMP with 0.05 M LiBr at 25 °C. PEG oligomers (molecular weight M_n = 600 (0.6k), 1000 (1k), and 2000 (2k) Da) with two −OH groups at their terminal ends (Figure 3.1) were purchased from Aldrich Chemical Co. and used as received. Dimethyl acetamide (DMAc) (Aldrich Chemical Co.) was used as a casting solvent without additional purification.

3.2.2. BPS-20_PEG Blends

After 2 g of BPS-20 was completely dissolved in DMAc at 30 °C, a PEG oligomer of the desired molecular weight was added to the BPS-20 solutions in two different concentrations: 5 wt % and 10 wt % (relative to the mass of BPS-20 in the solution). The resulting solutions were mixed for 1 day. Each solution (total solids concentration, 10 wt % in DMAc) was degassed under vacuum at 25 °C for at least 1 day and cast on a clean glass plate. Then, the cast solution was dried for 4 h at 90 °C and heated to 150 °C for 1 day under vacuum. The resulting films were easily peeled off of the glass plate and stored in deionized (DI) water at 30 °C for 2 days to further remove residual solvent. The nominal thickness of all films was approximately 30−40 μm, except those used for Fourier transform infrared spectroscopy (FT-IR) measurement (20 μm). Transparent, ductile, and light-yellow BPS-20_PEG blend films were obtained. The yellow

color increased with increasing PEG molecular weight and concentration. The BPS-20_PEG films are denoted as BPS-20_PEG molecular weight-PEG concentration (wt %). For instance, BPS-20_PEG0.6k-5 denotes a BPS-20 film containing 5 wt % of 0.6 kDa PEG.

3.2.3. Characterization

The thermal decomposition behavior of BPS-20_PEG films was investigated using a thermogravimetric analyzer (TGA) (TA Instruments Q500 TGA) operated at a heating rate of 10 °C min^{-1} from 50 to 600 °C in a 60 mL min^{-1} nitrogen sweep gas. Prior to the thermal decomposition measurements, all films were preheated in the TGA furnace at 110 °C for 15 min. Transmission FT-IR was used to study the interactions between BPS-20 and PEG. FT-IR spectra in the range of 4000−900 cm^{-1} were obtained using a Tensor 27 spectrometer (Bruker Optics).

Cross-polarization magic-angle spinning (CPMAS) ^{13}C solid-state NMR (ssNMR) spectra were taken with a Bruker Avance II 300 MHz wide-bore spectrometer operating at Larmor frequencies of 75.47 MHz for ^{13}C and 300.13 MHz for ^{1}H nuclei. Thin film samples (50−60 mg) were cut into small pieces and packed into 4 mm magic-angle spinning (MAS) rotors. CP for 1 ms mixing time was achieved at 50 kHz rf-field at the ^{13}C channel with the ^{1}H rf field ramped linearly over a 25% range centered at 38 kHz. Ramped CP compensates for the MAS attenuation of the ^{1}H-^{13}C heteronuclear dipolar coupling and complication of matching the Hartman-Hahn[41] condition, both of which are necessary for efficient polarization transfer.[42-44] A pulse technique known as total suppression of spinning side bands (TOSS)[45] was combined with a CP sequence to obtain sideband-free ^{13}C MAS spectra at a 6 kHz spinning speed (ν_r). The NMR signal averaging was achieved by coadding 2048 transients with a 4 s acquisition delay time. ^{1}H and ^{13}C $\pi/2$ pulse lengths were 4 and 5 μs, respectively. Small phase incremental alternation with 64 steps (SPINAL-64)[46] decoupling sequence at 63 kHz power was used for proton decoupling during ^{13}C signal detection.

To determine the glass transition temperature (T_g) of BPS-20 and BPS-20_PEG films, dynamic mechanical analysis (DMA) was conducted using a TA DMA 2980 (TA Instruments) in multifrequency tension mode; the temperature range was 0 to 300 °C with a ramp of 5 °C min^{-1} in a nitrogen atmosphere. The film samples were 4 mm in width, and each was subjected to a preload force of 0.025 N with an amplitude of 25 μm at a frequency of 1 Hz.

Water uptake (%) was calculated using the following equation:

$$Uptake(\%) = \frac{W_w - W_d}{W_d} \times 100$$

where W_d and W_w are the measured masses of dry and fully hydrated film samples, respectively. Each sample, approximately 5 × 5 cm^2, was dried in a vacuum oven at 110 °C for 1 day before measuring W_d and immersed in DI water at 25 °C for 1 day before measuring W_w.

Surface morphologies were examined via tapping mode atomic force microscopy (AFM), using a Digital Instruments MultiMode scanning probe microscope with a NanoScope Iva controller. A silicon probe (Veeco, end radius <10 nm, with a force constant = 5 N m^{-1}) was used to image the samples, and the set-point ratio was 0.82. Prior to measurement, all samples were equilibrated at 30 °C and 40% relative humidity (RH) for at least 12 h.

For pulsed-field gradient NMR spectroscopy (PFG NMR), each film was cut into 5.5 × 5 mm^2 pieces and stacked together to a total mass of about 40 mg in a custom-built Teflon cell that was sealed to maintain water content during diffusion measurements. The test cell was loaded into a Bruker Avance III WB 400 MHz NMR spectrometer equipped with both a Micro5 triple-axis-gradient (maximum 300 G cm^{-1}) microimaging probe and an 8 mm double resonance ($^1H/^2H$) rf coil. The pulsed-gradient stimulated echo pulse sequence (PGSTE) was applied with a $\pi/2$ pulse time of 32 μs, a gradient pulse duration (δ) ranging from 1 to 3 ms, and diffusion time (Δ) ranging from 20 to 800 ms.[35] Each measurement was repeated with 32 gradient steps, and the maximum gradient strength was chosen to achieve 70−90% NMR signal attenuation.

The water permeability (P_w, L μm m^{-2} h^{-1} bar^{-1}) of BPS-20 and BPS-20_PEG films was evaluated at 25 °C using a dead-end cell apparatus with a feed of 2000 ppm NaCl in DI water. P_w was defined as the volume of water (V) permeated per unit time (t) through a membrane sample of area (A) and thickness (l) at a pressure difference (ΔP = 400 psig or 27.6 bar):

$$P_w = \frac{Vl}{At\Delta P}$$

Salt rejection (R, %) was measured using a dead-end cell filtration apparatus with an

aqueous feed solution containing 2000 ppm NaCl at pH 6.5−7.5 and a pressure of 400 psig. Salt rejection (R) was calculated as follows:

$$R = \frac{C_f - C_p}{C_f} \times 100$$

Here, C_f and C_p are the NaCl concentrations in the feed and permeate, respectively. Salt concentration was measured with a NIST-traceable expanded digital conductivity meter (Oakton Con 110 conductivity and TDS meter).

Tensile properties of the films were determined using an Instron 5500R universal testing machine equipped with a 200 lb load cell at 30 °C and 44−54% RH. Crosshead displacement speed and gauge length were set to 5 mm min^{-1} and 25 mm, respectively. Dogbone specimens (50 mm long and at least 4 mm wide) were cut from a single film. Prior to the measurement, each specimen was dried under vacuum at 110 °C for at least 12 h and then equilibrated at 30 °C and 4% RH. At least 5 measurements were collected, and the average of these measurements is reported.

3.3. Results and Discussion

Because PEG is water-soluble and these materials are being evaluated for desalination applications, the stability of the hydrated films was explored. To determine whether PEG leached from the blend films, samples were stored in 30 °C DI water for 150 days. After the 150 day soaking period, PEG content in the blend films was investigated using TGA, FT-IR, and NMR spectroscopy.

Figure 3.2 presents dynamic TGA thermograms of BPS-20 and BPS-20_PEG films. All of the materials exhibit three distinct thermal decomposition steps: (I) thermal evaporation of water molecules [<~215 °C], (III) thermal desulfonation of BPS-20 [375−420 °C], and (IV) thermo-oxidation of BPS-20 [>~420 °C].[40,47] The initial weight loss, ascribed to desorption of water from the samples, increased with PEG concentration, suggesting that water hydrates both the PEG molecules and BPS-20 sulfonate groups.

An additional thermal decomposition step (II), ascribed to thermo-oxidation of PEG

[215−375 °C], was observed for the BPS-20_PEG blend samples. Thermal decomposition of PEG began around 215 °C, which is higher than the initial thermal decomposition temperature (T_d) of pure PEG (~175 °C)[48] and similar to T_d of the ester bridge grafted PEG.[49] This increase in the initial T_d suggests that PEG interacts with BPS-20. Interactions of this nature may have bond energies similar to a weak covalent bond,[49]e.g., ester bond. PEG decomposition was quantified and compared to the amount of PEG initially added to the BPS-20 polymer matrix. The mass of PEG in the blend matrix after the water soaking step was essentially equal to that of the initial blend, evidencing no leaching from the matrix under our test conditions. We believe that the physical interaction between PEG and BPS-20 may arise from two sources: bonding interaction between the BPS-20 sulfonate groups and PEG −OH groups and ion−dipole interactions between PEG and the metal cation (K^+) associated with the BPS-20 sulfonate groups.

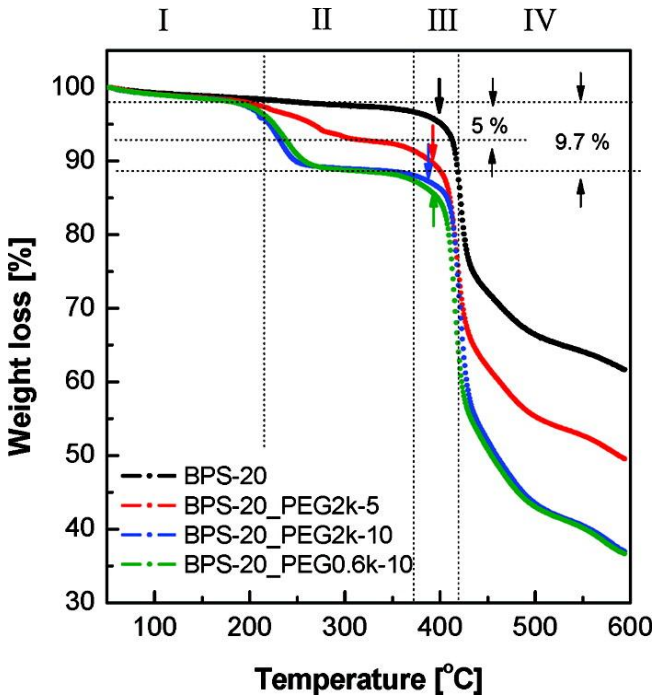

Figure 3.2. TGA thermograms of BPS-20 and BPS-20_PEG materials after soaking in deionized water at 30°C for 150 days. Work was performed by the McGrath Group at Virginia Tech.

The maximum BPS-20 thermal desulfonation temperature (T_{ds} ~398 °C) decreases by 5−12 °C upon addition of PEG. The reduction of T_{ds} was more significant for the BPS-20_PEG blends

containing higher molecular weight PEG and higher PEG concentration.

Figure 3.3 shows FT-IR spectra of BPS-20 and BPS-20_PEG samples over the relevant range of vibration frequencies to identify the interactions between PEG and BPS-20.

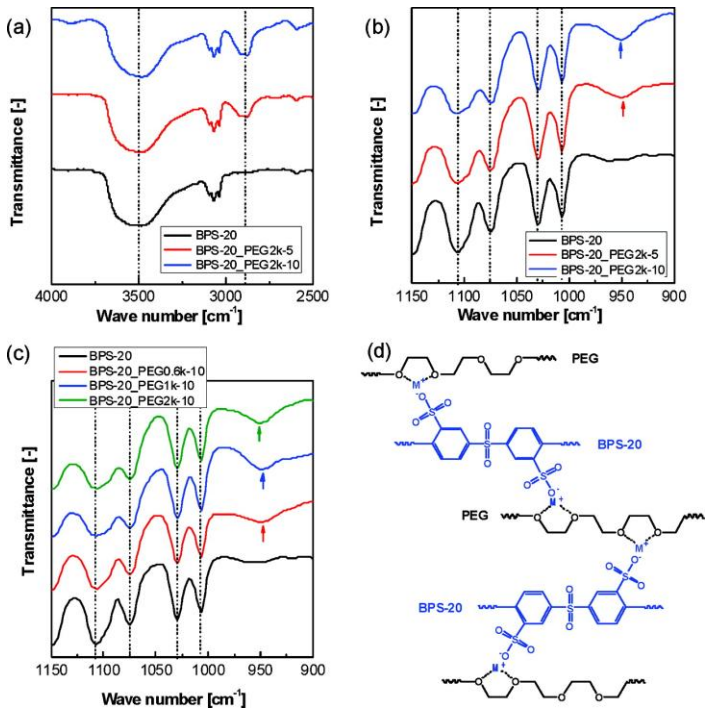

Figure 3.3. FT-IR spectra of BPS-20 and BPS-20_PEG materials. Spectra are shown for blends with different concentrations (a and b) and molecular weights (c) of PEG. (d) Simulated cation binding with PEG molecules ($M^+ = Na^+$, K^+, and other metal cations). Work was performed by the McGrath Group at Virginia Tech.

To ensure that peak intensities were normalized, dry films of equivalent thicknesses (20 μm) were analyzed. The strong band at 2850 cm^{-1} in Figure 3.3a is assigned to the stretching vibration of the aliphatic alkyl ($-CH_2-$) PEG groups. The peak intensity of the $-CH_2-$ groups increased with PEG concentration, but the peak position did not shift. The bands at 1075 and 1030 cm^{-1} in Figure 3.3b are attributed to the symmetric stretching vibration of SO_3^- in BPS-20. The absorption band at 1107 cm^{-1} is associated with the $-SO_3K$ asymmetric stretching vibration. Its frequency is higher than the frequency (1098 cm^{-1}) of the corresponding vibration for the$-SO_3Na$ form of the same BPS-20 polymer. The observed frequency difference between the

Na^+ and K^+ form of the BPS-20 material may be due to the polarization difference between the ionic bonds in the $-SO_3K$ group and the $-SO_3Na$ group.[50] After addition of PEG, most of the peaks, including a stretching vibration band of diphenyl ether (−O−) at 1006 cm^{-1}, did not shift. This result indicates that hydrogen bonding between BPS-20 and PEG is not significant when the sample is in the dry state. In this discussion, the relative intensity changes in the SO_3^- bands were excluded because of the presence of a strong characteristic PEG band occurring between 1020 and 1200 cm^{-1}.[51]

In contrast, the absorption band (~950 cm^{-1}) in Figure 3.3b, assigned to the PEG aliphatic ether (−C−O−C−), became more distinct and shifted to higher frequency as PEG concentration increased. An analogous band shift was observed in BPS-20_PEG samples containing high molecular weight PEG (Figure 3.3c). The peak's shift suggests that a chemical species exists in the vicinity of the PEG molecules and physically interacts with the PEG aliphatic ether groups. Free alkali metal cations, such as Na^+ and K^+, form complexes with PEG $-CH_2CH_2O-$ groups in both aqueous and nonaqueous solvents.[28,29,52,53] Furthermore, the ion−dipole interaction of PEG with the free metal cations is strengthened when long PEG chains (>9 repeat units) are used.[29] In particular, the selectivity of long PEG chains to K^+ ions are promoted to the equivalent level of crown ethers (e.g., 18-crown-6).[33] PEG (>14 units of $-CH_2CH_2O-$) used in this study may interact strongly with the K^+ ions that are associated with the BPS-20 $-SO_3^-$ groups (Figure 3.3d) because the ionic bond strength of the potassium sulfonate groups is theoretically stronger than the ion−dipole interaction between PEG and the sulfonate group metal cations,[54] and the PEG $-CH_2CH_2O-$ groups have higher K^+ coordination numbers (6−7) compared to Na^+ (2−4).[28,55]

^{13}C ssNMR spectra of BPS-20_PEG, Figure 3.4, provided information about the interaction of BPS-20 and PEG, and allowed monitoring of changes in the environment of the fully hydrated polymer system. Characteristic peaks for hydrated BPS-20 were consistently observed at the same chemical shifts regardless of PEG addition. Therefore, hydrogen bonding is not significant in hydrated BPS-20, and the ion−dipole interaction governs the macroscopic properties of both the dry and hydrated BPS-20_PEG system.

We believe that the ability of PEG to complex with metal cations affected the BPS-20_PEG glass transition temperature (T_g). Generally, the T_g of sulfonated polymers increases as the degree of sulfonation increases due to the bulky and ionic nature of the sulfonate groups.[56]

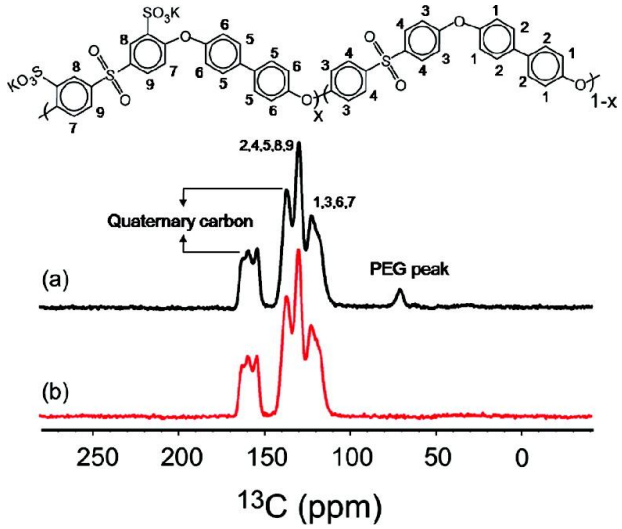

Figure 3.4. ^{13}C ssNMR spectra of (a) BPS-20_PEG0.6k-5 and (b) BPS-20. Work was performed by the Wi group at Virginia Tech.

For example, the BPS-20 T_g (270 °C, Figure 3.5) is higher than that of BPS-00 (Radel, T_g = 220 °C).[57] Also, BPS-20 displays a broad T_g range, since the sulfonate groups are randomly distributed and may form ionic domains of different sizes within the hydrophobic matrix. When incorporated in BPS-20, PEG may disrupt the inter- and/or intramolecular ionic interactions between the sulfonate groups in the BPS-20 ionic domains (entropic effect); a decrease in T_g could indicate this disruption. A broad tan δ peak between 150 and 200 °C, observed using DMA, can be attributed to sulfonated ionic domain dilution that occurs when PEG is introduced to BPS-20. T_g depression behavior was especially significant in BPS-20_PEG samples containing long PEG chains and higher, i.e., 10 wt %, PEG concentration. For example, the T_g of BPS-20_PEG2k-10 dropped by 43 °C, comparable to the T_g of nonsulfonated BPS-00. The T_g of BPS-20_PEG samples decreased linearly with a slope that depended on PEG molecular weight, which makes it possible to estimate the theoretical T_g change in BPS-20 upon PEG addition.

BPS-20_PEG samples are binary systems composed of BPS-20 and PEG (T_g = ~−60 °C). The PEG homopolymer T_g is effectively constant over the molecular weights chosen for this study (0.6k, 1k, and 2k).[58,59] Unlike immiscible systems that show distinct and constant T_g for each component, the T_g of the BPS-20_PEG binary system depended on PEG concentration.

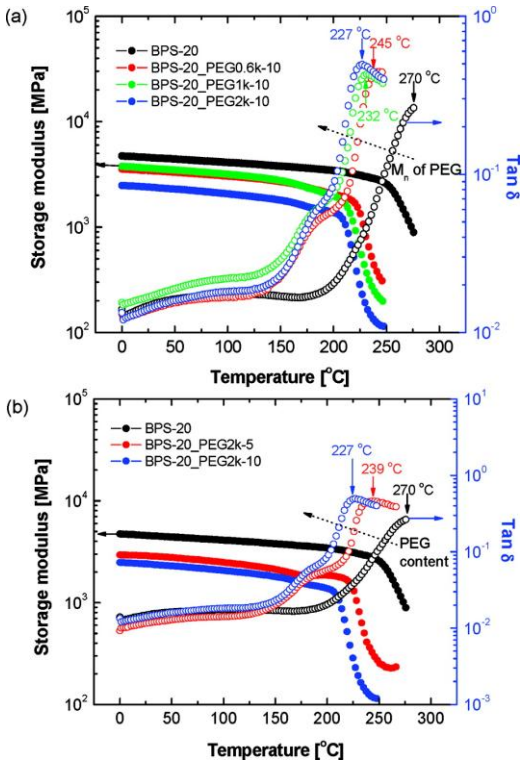

Figure 3.5. DMA profiles of BPS-20_PEG membranes with different (a) molecular weights and (b) concentration of PEG. Work was performed by the McGrath Group at Virginia Tech.

The measured T_gs of BPS-20_PEG samples are very similar to theoretical predictions (202−232 °C) made using the Flory−Fox equation.[60] Comparison to theoretical predictions based on the Flory-Fox equation is commonly used to determine whether binary systems are miscible, compatible, or not at all miscible. In the following equation, $T_{g,i}$ and W_i represent the T_g and weight fraction of component *i*, respectively,

$$\frac{1}{T_{g,BPS-20PEG}} = \frac{W_{BPS-20}}{T_{g,BPS-20}} + \frac{W_{PEG}}{T_{g,PEG}}$$

On the basis of the agreement between the measured BPS-20_PEG T_g data and predictions made using the Flory−Fox equation, we conclude that BPS-20 and PEG form a compatible system as a result of ion−dipole interactions between PEG and the BPS-20 sulfonate groups.

As the DS increases, the density of the BPS copolymer increases relative to unsulfonated

BPS-00 (1.30 g cm^{-3}).[57] When PEG is incorporated into BPS-20, the density of the blend material decreases, as shown in Figure 3.6a. This decrease in density occurs because PEG acts as a plasticizer that increases BPS-20 chain spacing and free volume.

The BPS-20_PEG density, when compared to the density calculated by assuming volume additivity (Figure 3.6a), suggests that blending PEG with BPS-20 results in free volume changes that extend beyond what would be expected from simple mixing. Dry BPS-20_PEG samples exhibit higher densities than wet samples. Density measurements also suggest that the free volume of BPS-20_PEG increased as PEG chains became longer and more concentrated.

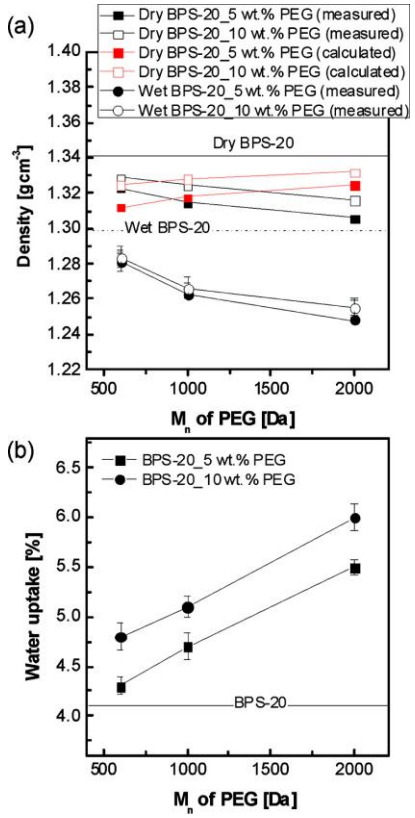

Figure 3.6. (a) Density and (b) water uptake of BPS-20_PEG. Calculated density of BPS-20_PEG was obtained from volume additivity: $1/\rho_{BPS\text{-}20\_PEG} = \varphi_{BPS\text{-}20}/\rho_{BPS\text{-}20} + \varphi_{PEG}/\rho_{PEG}$. Here, ρ[62] and φ are the density and volume fractions, respectively, of each component in the blend. Work was performed by the Freeman Group at the University of Texas at Austin.

The water uptake of BPS-20_PEG (Figure 3.6b) correlated inversely with density. Water

uptake increased as hydrophilic PEG was incorporated into BPS-20. Figure 3.6 indicates that low density BPS-20_PEG samples (i.e., high free volume samples) showed greater water uptake than samples of higher density (i.e., low free volume samples). Free volume is expected to influence water and salt transport properties in these polymers.[61]

In addition to water uptake, the surface morphology of sulfonated polymers can influence water permeability. AFM images, shown in Figure 3.7, indicate that the strong ion−dipole interaction of PEG with K^+ ions in BPS-20 sulfonate groups can induce a hydrophilic−hydrophobic nanophase separation even though BPS-20 is a random copolymer.

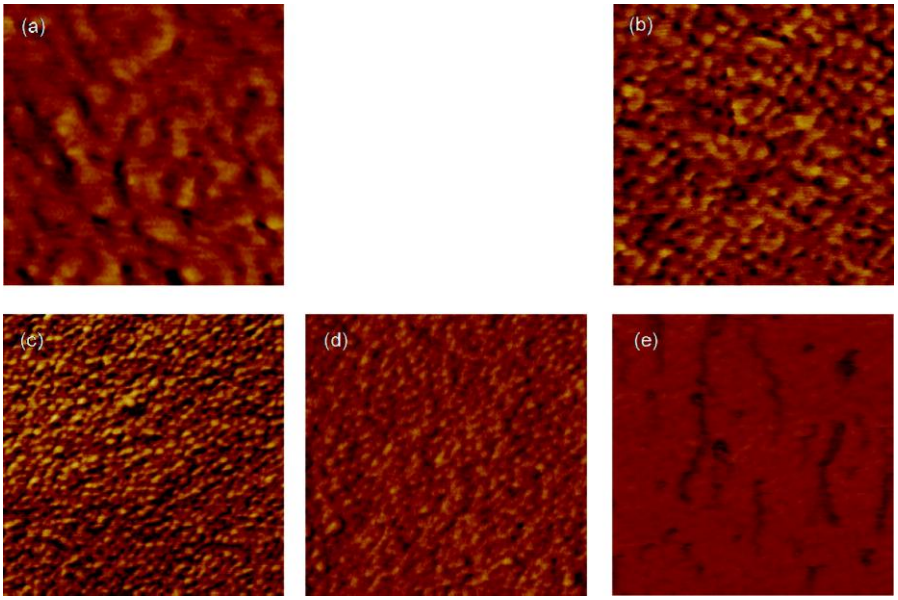

Figure 3.7. AFM images of BPS-20 and BPS-20_PEG blends. Images shown for: (a) BPS-20, (b) BPS-20_PEG2k-5, (c) BPS-20_PEG0.6k-10, (d) BPS-20_PEG1k-10, and (e) BPS-20_PEG2k-10 materials in tapping mode. The dimensions of the images are 250 × 250 nm^2. The phase scale is 0−20°. The measurement was conducted at 35% RH**.** Work was performed by the McGrath Group at Virginia Tech.

In BPS-20 (Figure 3.7a), hydrophilic rod-like structures (darker regions) with average diameters of 9−12 nm are randomly distributed, yet connected, throughout the hydrophobic copolymer matrix (lighter regions).[40] When PEG was added to BPS-20, the morphology of the matrix changed. In BPS-20_PEG2k-5 (Figure 3.7b), the hydrophilic ionic domain size decreased to an

average diameter of 3−6 nm and hydrophilic phase connectivity appeared to improve. The decrease in domain size and improved connectivity may be related to strong ion−dipole interactions and the high coordination number of PEG $-CH_2CH_2O-$ units to K^+ ions in the BPS-20 sulfonate groups.[27,55] PEG (>9 units of $-CH_2CH_2O-$) typically prefers a meander conformation (e.g., helical coil structure) when exposed to free alkali metal cations.[29] The observed hydrophilic−hydrophobic phase separation depends on both PEG chain length and concentration. As PEG chain length increased, at a constant concentration (10 wt %, Figure 3.7c−e), the hydrophilic domains became more interconnected but generally decreased in size. Another morphological change was observed as the PEG concentration in BPS-20_PEG2k was varied from 5 to 10 wt % (Figure 3.7b,e). Unlike BPS-20_PEG2k-5, BPS-20_PEG2k-10 appears to have two different kinds of ionic domains: irregularly distributed ionic domains, with sizes similar to BPS-20_PEG2k-5, and capillary-shape ionic domains, with sizes less than 1 nm. The ionic domains appear to be interconnected by long, tortuous hydrophilic pathways. The unevenly developed morphology may cause BPS-20_PEG2k-10 to have a lower water permeability than BPS-20_PEG2k-5.

PGSTE-NMR provides information about the diffusion of molecules in materials (i.e., the self-diffusion coefficient, *D*, of water in the polymer matrix, which depends strongly on water uptake, morphology, and temperature). PGSTE-NMR is sensitive to the identity of the mobile species (e.g., water) and changes in sample environment, such as water content. All samples exhibited reduced *D* values at long diffusion times (Δ), indicating the existence of tortuous hydrophilic pathways, similar to those observed in the AFM images of Figure 3.7. However, interpreting the water permeation behavior in these blend materials is not trivial since the PEG influences the hydrophilicity and ionic domain structure of the material. In this study, we used the Mitra equation[63] for porous media to assess diffusive restrictions (related to the surface-to-volume ratio of diffusion pathways, *S*/*V*) that result from the material's morphology.

$$D = D_0\left(1 - \frac{4}{9\sqrt{\pi}}\frac{S}{V}\sqrt{D_0\Delta}\right)$$

Here, *S*/*V* (meter^{-1}) is a factor associated with the internal roughness in the mixed matrix. An increase in *S*/*V* is expected to enhance water diffusion. By fitting *D* vs Δ, we extracted values for

the effective "free" water diffusion coefficient D_0 (that expected at very small Δ) and S/V. Here, D_0 is interpreted as the effective intradomain diffusion coefficient of "free" water through the polymer's hydrophilic domain structure. Figure 3.8 shows the change in $D_0 \times S/V$ as a function of PEG molecular weight. $D_0 \times S/V$ values appear to correlate with water permeability data in Figure 3.9. This scaled water diffusion behavior in the mixed matrix materials decreased with increasing PEG chain length. However, the $D_0 \times S/V$ values for the BPS-20_PEG samples were greater than that for BPS-20. This finding indicates that S/V plays an important role in the diffusion and permeation of water through these samples.

Figure 3.9 presents water permeability and salt rejection data for BPS-20_PEG films. Water permeability increased relative to BPS-20 films, with a dependence, on both PEG concentration and chain length. Water permeability was greater in samples that contained higher concentration of PEG; these samples, with 10 wt % PEG, also exhibited higher water uptake.

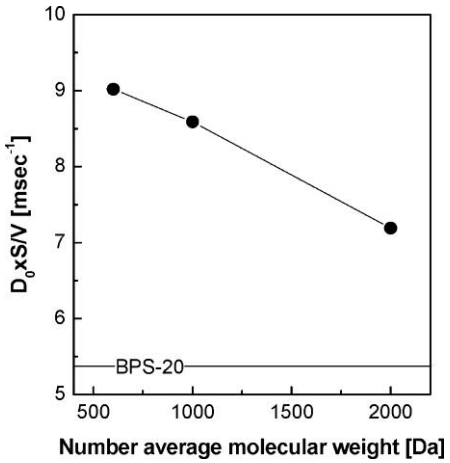

Figure 3.8. Diffusion behavior through tortuous water pathways in BPS-20_PEG 10% materials. Error is ~ ± 5 %. Work was performed by the Madsen Group at Virginia Tech.

Water permeability of BPS-20_PEG, however, decreased as PEG chain length increased. Water permeability is likely affected by the morphological changes that occur upon adding PEG, as indicated by AFM and scaled PGSTE-NMR (Mitra analysis[63]). We believe that the morphological contribution was particularly significant in BPS-20_PEG2k, which contained the highest PEG molecular weight.

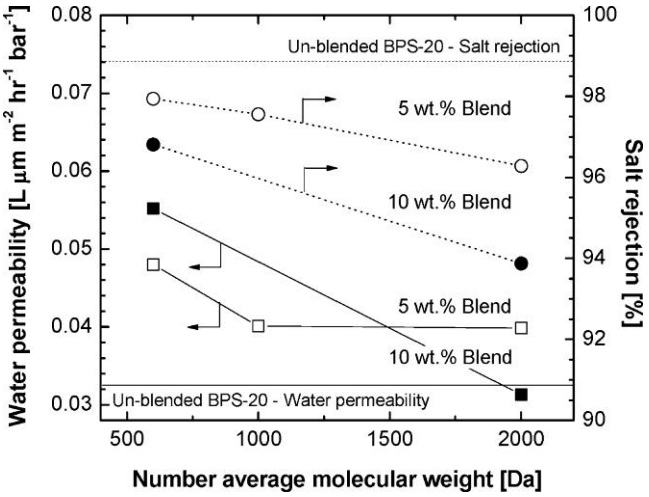

Figure 3.9. Water permeability (squares; right) and salt rejection (circles;left) of BPS-20_PEG films. Work was performed by the Freeman Group at the University of Texas at Austin. Error was not calculated by Lee because only a single measurement was performed for each sample.

The long and tortuous channels in BPS-20_PEG2k-10 may restrict water diffusion and cause the water permeability to decrease even though the water uptake increased relative to that of BPS-20_PEG1k-10. Unlike other 10 wt % blends, the water permeability of BPS-20_PEG2k-10 was lower than BPS-20_PEG2k-5.

The water permeability of the blend materials may also be influenced by hydrogen bonding between water molecules and hydrophilic functional groups in the blend materials: BPS-20 sulfonate, PEG −OH, and PEG −O− groups. A constant amount of BPS-20 was used in BPS-20_PEG. Because the number of sulfonate groups was fixed, the difference in hydrogen bonding activity within different BPS-20_PEG samples is theoretically derived from the number of nonionic −OH and −O− PEG groups.[64] As was shown in Table 1 of the published manuscript[65], the relative number of −OH groups increased as the PEG molecular weight decreased. Furthermore, the relative number of −OH groups increased when PEG concentration increased from 5 to 10 wt %. These results are similar to the water permeability results in Figure 3.9, suggesting the −OH groups may contribute more to water permeability than the −O− groups.

On the basis of the results shown in Figure 3.9, salt rejection decreases substantially with increases in PEG concentration and molecular weight. For example, in BPS-20_PEG2k-10, the rejection was 93.9% (98.9% for pure BPS-20). We speculate that the ion−dipole interaction

between K^+ ions and PEG oxyethylene units may weaken the electrostatic interaction of $-SO_3^-$ groups that would typically form physically cross-linked, ion-selective domains. Additionally, PEG incorporation into BPS-20 increases the material's water uptake. This increase in swelling reduces the concentration of sulfonate groups in the polymer matrix, which may result in decreased ion exclusion and, thus, decreased salt rejection.[2,66] Both the disruption of ion-selective domains and the dilution of sulfonate group concentration could result in reduced salt rejection as PEG concentration increases, which is consistent with the experimental observations. The reduced salt rejection was more significant in BPS-20_PEG samples prepared with higher molecular weight PEG. Longer PEG chains are associated with the formation of stronger ion−dipole interactions with K^+ ions in the BPS-20 sulfonate groups and highly water-swollen polymer matrixes.

Plasticizers increase the free volume of a polymer matrix and weaken the inter- and intramolecular interactions between the polymer chains, which can result in reduced mechanical properties. Though the stress and strain of BPS-20_PEG samples decreased, there was no significant effect on toughness ,ductility, tensile modulus, or strength.[65]

Resistance to degradation by chlorine-based disinfectants is critical for the long-term performance of RO membranes. An accelerated chlorine stability test was conducted by immersing each sample in a sealed vial containing a pH 4.0 ± 0.3 buffered aqueous solution of sodium hypochlorite (NaOCl) at concentrations of 100, 1000, and 10,000 ppm[67] for 2 time periods: 1 day and 1 week. Structural changes were monitored with ^{13}C ssNMR (Figure 3.10). ssNMR is a powerful technique for characterizing such changes because, as different molecular components have unique spectral frequencies, it is easy to notice the loss/formation of new features; not to mention, a rough estimation of concentration can be made. A reference PA film was obtained from the interfacial polymerization of *m*-phenylenediamine (3 wt % in water) and trimesoyl chloride (5 mM). The aromatic ring in the PA was vulnerable to electrophilic chlorine attack as reported in the literature.[68,69] The phenyl ring C−H peaks of the PA film decreased with exposure to chlorine due to the formation of C−Cl bonds (Figure 3.10a). Also, the intensity of the C' peak for the PA film decreased as PA chains were degraded by chlorine attack at the C' sites. In contrast, none of the BPS-20 peaks showed changes in position or intensity after exposure at 10,000 ppm chlorine at pH 4.0 ± 0.3 for 1 week (Figure 3.10b). However, PEG concentration in the blends decreases as chlorine concentration or exposure time increases.

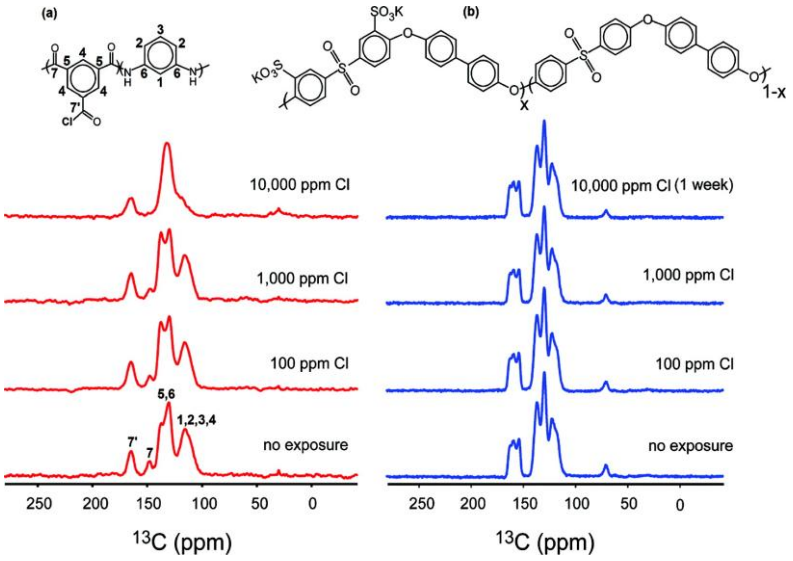

Figure 3.10. ^{13}C ssNMR spectra of (a) PA and (b) BPS-20_PEG0.6k-5 after exposure to different chlorine concentrations.[67] Work was performed by the Wi Group at Virginia Tech.

For example, in BPS-20_PEG0.6k-5, which is shown as a representative example of the blends, the PEG content obtained from relative peak integration with respect to the BPS-20 peaks fell to about 60% of its initial value after 1 day of immersion in 1000 ppm of chlorine. PEG loss may be related to oxidative degradation of PEG.[70] No additional PEG was lost when the films were exposed to highly concentrated solutions of chlorine for a long time. A similar trend was observed for BPS-20_PEG0.6k-10. This suggests that the ion−dipole interaction between PEG and BPS-20 is stable under harsh conditions, although exposure to chlorinated water may weaken the interaction.

3.4. Conclusion

Blends of PEG with BPS-20, a potassium salt form sulfonated random copolymer, gave rise to strong ion−dipole interactions between K^+ ions in the BPS-20 sulfonate groups and PEG. These interactions are similar to the behavior of crown ethers and alkali metal cations,[30-32] and resulted in high compatibility between BPS-20 and PEG , preventing PEG leaching from exposure to water for long periods of time (pseudoimmobilization). The strength of the ion−dipole interaction was similar to a weak covalent bond, as shown in the thermal

decomposition behavior of PEG in the blend materials. The cation complexing capability of PEG molecules weakened the inter- or intramolecular hydrogen bonding between sulfonate groups, which typically form physically cross-linked ionic domains. Increases in PEG molecular weight and concentration resulted in a reduction of the blend's T_g. This plasticization led to increased free volume and water uptake. The ion−dipole interaction and the high coordination number of the PEG $-CH_2CH_2O-$ units to K^+ ion in the BPS-20 sulfonate groups converted the sample surface morphology from a random distribution of hydrophilic domains in the hydrophobic polymer matrix into a more defined hydrophilic−hydrophobic nanophase separated morphology. This trend was more pronounced in BPS-20_PEG samples containing high concentrations of PEG. Increased water uptake and interconnected hydrophilic domains, resulting from the addition of PEG, increased the water permeability of BPS-20_PEG compared to BPS-20. Long PEG chains formed long and tortuous hydrophilic channels that decreased water diffusion (D_0 S/V) and, thus, water permeation. Furthermore, NaCl rejection decreased upon the addition of PEG likely because of weakened electrostatic interactions between K^+ ions and $-SO_3^-$ groups and reduced ionic exclusion due to dilution of the BPS-20 sulfonate groups caused by increased water uptake. The decrease in NaCl rejection was minimized when short PEG chains (e.g., 0.6k) were used. With the addition of PEG, water permeability increased to about 200% compared to the unblended BPS-20 starting material. The influence of PEG addition on sample toughness and ductility was negligible. Unlike PA membranes, which degrade when exposed to chlorinated solutions, BPS-20_PEG resisted breakdown after prolonged exposure to high chlorine concentrations, as was was illustrated using ^{13}C MAS ssNMR spectra of PA and BPS-20_PEG0.6k-5 exposed to exposed to various NaOCl concentrations for extended periods of time. For the PA sample, polymer degradation was evidenced by decreasing intensity for aromatic methine peaks, as well as C'. In contrast, for the BPS-20 sample, polymer integrity was exhibited by relatively constant spectra; the major difference observed, a decrease in peak intensity for the oxyethylene CH_2 of PEG, stabilized after an initial loss and was unaffected by longer periods of exposure to high NaOCl concentrations.

Incorporating PEG molecules into low disulfonated salt form random copolymers offers an effective and economical avenue to increase the material's water permeability, and because it is highly resistant to NaOCl, it is stable to the routine anti-biofouling measures.[15,23] However, the BPS-20 polymer matrix and hydroxyl-terminated PEG blends may not exhibit the necessary

water permeability and salt rejection to be an attractive RO membrane material. Therefore, our ongoing studies are focusing on random copolymers with higher degrees of sulfonation and ion-selective PEG. Finally, we will attempt to synthesize multiblock copolymers containing PEG moieties to improve the hydrophilic and hydrophobic phase-separation of these chemically stable materials.

References

(1) Service, R. F. *Science* **2006**, *313*, 1088.

(2) Geise, G. M.; Lee, H. S.; Miller, D. J.; Freeman, B. D.; McGrath, J. E.; Paul, D. R. *J. Polym. Sci., Part B Polym. Phys.* **2010**, *48*, 1685.

(3) Baker, R. W. *Membrane Technology and Applications*; 2 ed.; John Wiely & Sons Ltd.: Chichester, U.K,, 2004.

(4) Cadotte, J. E. U.S., 1981; Vol. 4,277,344.

(5) Petersen, R. J.; Codotte, J. E.; Porter, M. C. *Handbook of Industrial Membrane Technology*; Noyes Publications: Park Ridge, NJ, 1990.

(6) Knoell, T. *Ultrapure Water* **2006**, *23*, 24.

(7) Paul, M.; Park, H. B.; Freeman, B. D.; Roy, A.; McGrath, J. E.; Riffle, J. S. *Polymer* **2008**, *49*, 2243.

(8) Park, H. B.; Freeman, B. D.; Zhang, Z. B.; Sankir, M.; McGrath, J. E. *Angew. Chem., Int. Ed.* **2008**, *47*, 6019.

(9) Drzewinski, M.; Macknight, W. J. *J. Appl. Polym. Sci.* **1985**, *30*, 4753.

(10) Brousse, C. L.; Chapurlat, R.; Quentin, J. P. *Desalination* **1976**, *18*, 137.

(11) Geise, G. M.; Park, H. B.; Sagle, A. C.; Freeman, B. D.; McGrath, J. E. *J. Membr. Sci.* **2010**, *369*, 130.

(12) Xie, W.; Cook, J.; Chen, C.; Park, H. B.; Freeman, B. D.; Lee, C. H.; McGrath, J. E. *J. Membr. Sci.* **2010**, submitted for publication.

(13) DOW. Water Solutions BW30-400 Product Specification, http://www.dow.com/liquidseps/prod/bw30_400.htm.

(14) Water Solutions SW30HR-380 Product Specification, http://www.dow.com/liquidseps/prod/sw30hr_380.htmDOW. .

(15) Van Wagner, E. M.; Sagle, A. C.; Sharma, M. M.; Freeman, B. D. *J. Membr. Sci.* **2009**, *345*, 97.

(16) Lee, M.; Jang, C. J.; Ryu, J. H. *J. Am. Chem. Soc.* **2004**, *126*, 8082.

(17) Mao, G.; Castner, D. G.; Grainger, D. W. *Chem. Mater.* **1997**, *9*, 1741.

(18) Chakrabarty, B.; Ghoshal, A. K.; Purkait, M. K. *J. Colloid Interface Sci.* **2008**, *320*, 245.

(19) Chakrabarty, B.; Ghoshal, A. K.; Purkait, M. K. *J. Membr. Sci.* **2008**, *309*, 209.

(20) Chou, W. L.; Yu, D. G.; Yang, M. C.; Jou, C. H. *Sep. Purif. Technol.* **2007**, *57*, 209.

(21) Wang, P.; Tan, K. L.; Kang, E. T.; Neoh, K. G. *J. Mater. Chem.* **2001**, *11*, 783.

(22) Revanur, R.; McCloskey, B. D.; Breitenkamp, J.; Freeman, B. D.; Emrick, T. *Macromolecules* **2007**, *40*, 3624.

(23) Ju, H.; McCloskey, B. D.; Sagle, A. C.; Wu, Y. H.; Kusuma, V. A.; Freeman, B. D. *J. Membr. Sci.* **2008**, *307*, 260.

(24) Lazzara, G.; Milioto, S. *J. Phys. Chem. B* **2008**, *112*, 11887.

(25) Van Alstine, J. M.; Malmsten, M. *Langmuir* **1997**, *13*, 4044.

(26) Nishi, S.; Kotaka, T. *Macromolecules* **1985**, *18*, 1519.

(27) Philippova, O. E.; Karibyants, N. S.; Starodubtzev, S. G. *Macromolecules* **1994**, *27*, 2398.

(28) Okada, T. *Macromolecules* **1990**, *23*, 4216.

(29) Chan, K. W. S.; Cook, K. D. *Macromolecules* **1983**, *16*, 1736.

(30) Doan, K. E.; Heyen, B. J.; Ratner, M. A.; Shriver, D. F. *Chem. Mater.* **1990**, *2*, 539.

(31) Gokel, G. W. *Crown Ethers and Cryptands*; The Royal Society of Chemistry: Cambridge, U.K., 1991.

(32) Pedersen, C. J. *J. Am. Chem. Soc.* **1967**, *89*, 2495.

(33) Yanagida, S.; Takahasi, K.; Okahara, M. *Bull. Chem. Soc. Jpn.* **1977**, *50*, 1386.

(34) Stejskal, E. O.; Tanner, J. E. *J. Chem. Phys.* **1965**, *42*, 288.

(35) Li, J.; Wilmsmeyer, K. G.; Madsen, L. A. *Macromolecules* **2009**, *42*, 255.

(36) Li, Y.; VanHouten, R. A.; Brink, A. E.; McGrath, J. E. *Polymer* **2008**, *49*, 3014.

(37) Li, Y.; Wang, F.; Yang, J.; Liu, D.; Roy, A.; Case, S.; Lesko, J.; McGrath, J. E. *Polymer* **2006**, *47*, 4210.

(38) Kim, Y. S.; Dong, L.; Hickner, M. A.; Glass, T. E.; Webb, V.; McGrath, J. E. *Macromolecules* **2003**, *36*, 6281.

(39) Sumner, M. J.; Harrison, W. L.; Weyers, R. M.; Kim, Y. S.; McGrath, J. E.; Riffle, J. S.; Brink, A.; Brink, M. H. *J. Membr. Sci.* **2004**, *239*, 199.

(40) Wang, F.; Hickner, M.; Kim, Y. S.; Zawodzinski, T. A.; McGrath, J. E. *J. Membr. Sci.* **2002**, *197*, 231.

(41) Hartmann, S. R.; Hahn, E. L. *Phys. Rev.* **1962**, *128*, 2042.

(42) Duer, M. J. *Introduction to Solid-State NMR Spectroscopy*; Blackwell Publishing Ltd.: Malden, 2004.

(43) Peersen, O. B.; Wu, X. L.; Kustanovich, I.; Smith, S. O. *J. Magn. Reson., Ser. A* **1993**, *104*, 334.

(44) Metz, G.; Wu, X. L.; Smith, S. O. *J. Magn. Reson., Ser. A* **1994**, *110*, 219.

(45) Dixon, W. T. *J. Chem. Phys.* **1982**, *77*, 1800.

(46) Fung, B. M.; Khitrin, A. K.; Ermolaev, K. *J. Magn. Reson.* **2000**, *142*, 97.

(47) Lee, C. H.; Park, H. B.; Chung, Y. S.; Lee, Y. M.; Freeman, B. D. *Macromolecules* **2006**, *39*, 755.

(48) Hechavarria, L.; Mendoza, N.; Altuzer, P.; Hu, H. *J. Solid State Electrochem.* **2010**, *14*, 323.

(49) Cappelli, A.; Galeazzi, S.; Giuliani, G.; Anzini, M.; Grassi, M.; Lapasin, R.; Grassi, G.; Farra, R.; Depas, B.; Aggravi, M.; Donati, A.; Zetta, L.; Boccia, A. C.; Bertini, F.; Samperi, F.; Vomero, S. *Macromolecules* **2009**, *42*, 2368.

(50) Zundel, G. *Hydration and Intermolecular Interaction*; Academic Press: New York, 1969.

(51) Kim, C. H.; Kim, D. W.; Cho, K. Y. *Polym. Bull.* **2009**, *63*, 91.

(52) Izatt, R. M.; Bradshaw, J. S.; Nielsen, S. A.; Lamb, J. D.; Christensen, J. J.; Sen, D. *Chem. Rev.* **1985**, *85*, 271.

(53) Izatt, R. M.; Pawlak, K.; Bradshaw, J. S.; Bruening, R. L. *Chem. Rev.* **1991**, *91*, 1721.

(54) Kerres, J. A. *Fuel Cells* **2005**, *5*, 230.

(55) Besner, S.; Vallee, A.; Bouchard, G.; Prud'homme, J. *Macromolecules* **1992**, *25*, 6480.

(56) Xu, K.; Li, K.; Khanchaitit, P.; Wang, Q. *Chem. Mater.* **2007**, *19*, 5937.

(57) Solvay Advanced Polymers, www.Solvayadvancedpolymers.com.

(58) Read, B. E. *Polymer* **1962**, *3*, 529.

(59) Back, D. M.; Schmitt, R. L. *Kirk-Othmer Encyclopedia of Chemical Technology*; John Wiley & Sons Ltd.: New York, 2004; Vol. 10.

(60) Fox, T. G. *Bull. Am. Phys. Soc.* **1956**, *1*, 123.

(61) Yasuda, H.; Lamaze, C. E.; Ikenberry, L. D. *Die Makromol. Chem.* **1968**, *118*, 19.

(62) Zoller, P.; Walsh, D. J. *Standard Pressure-Volume-Temperature Data for Polymers*; Technomic Publishing Co., Inc: Lancaster, PA, 1995.

(63) Mitra, P. P. *Physica A* **1997**, *241*, 122.

(64) Porter, M. R. *Handbook of Surfactants*; 2 ed.; Blackie Academic and Professional, an imprint of Chapman & Hall: London, 1994.

(65) Lee, C. H.; VanHouten, D.; Lane, O.; McGrath, J. E.; Hou, J.; Madsen, L. A.; Spano, J.; Wi, S.; Cook, J.; Xie, W.; Oh, H. J.; Geise, G. M.; Freeman, B. D. *Chem. Mater.* **2011**, *23*, 1039.

(66) Helfferich, F. *Ion Exchange*; Dover Publications: New York, 1995.

(67) Jayarani, M. M.; Rajmohanan, P. R.; Kulkarni, S. S.; Kharul, U. K. *Desalination* **2000**, *130*, 1.

(68) Bieron, J. F.; Dinan, F. J.; Zabicky, J. *The Chemistry of Amides*; Wiley Interscience: New York, 1970.

(69) March, J. *Advanced Organic Chemistry: Reactions, Mechanisms, and Structure*; John Wiley: New York, 1992.

(70) Chen, S. F.; Zheng, J.; Li, L. Y.; Jiang, S. Y. *J. Am. Chem. Soc.* **2005**, *127*, 14473.

Chapter 4

Solid-state NMR Molecular Dynamics Characterization of a Highly Chlorine-Resistant Disulfonated Poly(Arylene Ether Sulfone) Random Copolymer Blended with Poly(Ethylene Glycol) Oligomers for Reverse Osmosis Applications

Reproduced in part from Lee, C.H.; Spano, J.; McGrath, J.E.; Cook, J.; Freeman, B.D.; Wi, S. *J. Phys. Chem. B,* **accepted.** Sold-state NMR experiments were performed by the Wi Group at Virginia Tech. Polymer processing and characterization was performed by the McGrath Group at Virginia Tech and the Freeman Group at the University of Texas at Austin.

4.1. Introduction

The production of fresh water from brackish water or seawater has been considered as an energy-efficient and cost-effective way to cope with global water shortage.[1] Reverse osmosis (RO) water purification has been applied to produce pure water by effectively removing hydrated salt ions and microorganisms through a semipermeable membrane with high flux/rejection characteristics.[2] Up to now, aromatic polyamides (PAs) have been widely used as a RO membrane material because of their high water flux and excellent NaCl rejection (> 99%) at a broad range of pH values.[3] However, PAs show a critical weakness to chlorine (e.g., NaOCl) that is added as an oxidizing biocide to remove microorganisms that accumulate on the membrane surface, blocking water flux.[4,5] PAs lose their salt rejection easily after a continuous exposure even at a low concentration of chlorine (~ a few ppb).[5]

Aromatic polysulfone, an engineering plastic with high mechanical strength, has excellent tolerance to chorine owing to the absence of an amide bond, which is vulnerable to chlorine attack.[6] By introducing sulfonate ($-SO_3^-M^+$; M = Na or K) groups in aromatic polysulfone, which provides a necessary hydrophilic character, one can obtain an excellent membrane material with selective ionic transport, fast water permeation, and extended lifetime under aqueous chlorine condition.[7,8] Polycondensation using a very reactive, disulfonated halide monomer is an effective way to introduce sulfonate groups into the skeleton of aromatic polysulfone.[6,9] Disulfonated poly(arylene ether sulfone) random copolymers (BPS-XXK, where K means that the counter-ion of SO_3^- groups is K^+ ion and XX indicates degree of sulfonation

[DS] in mol%; Figure 4.1) thus obtained exhibit excellent chlorine-resistance, even under a continuous chlorine exposure (e.g., over 40 hours at 500 ppm).[6] However, the BPS-XXK system shows a trade-off relationship between water permeability and salt rejection in that a BPS-XXK system with a higher DS produces a greater water flux, but a higher NaCl passage.[6,10,11] Hence, BPS-20K, a relatively low DS material, was considered as an alternative RO membrane material owing to its excellent NaCl separation property being similar to that of commercial PA (> 99%).[6] Yet, its water permeability property (0.03 L μm m^{-2} hr^{-1} bar^{-1}) should be improved further because its polymeric matrix is still dominated by the hydrophobic nature of aromatic polysulfone.

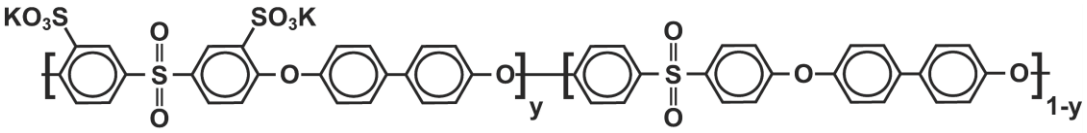

Figure 4.1. Disulfonated poly(arylene ether sulfone) random copolymers (BPS-XXK, XX= 100y).

Nonionic poly(ethylene glycol) (PEG) molecules have been widely used in self-assembly,[12,13] gas separation,[14] water purification,[15-18] and biomedical applications.[19,20] Nanophase separated hydrophilic-hydrophobic domains were identified on atomic force microscopy (AFM) images of BPS-20K membrane surfaces blended with PEG molecules even though BPS-20K is a random copolymer.[21] The distribution, size, and shape of hydrophobic-hydrophilic domains observed were strongly dependent on the amount and molecular weight of PEGs added. In the mixed matrices PEG possesses high compatibility with BPS-20K due to the formation of ion-dipole interactions between the oxyethylene ($–CH_2CH_2O–$) units in PEG and K^+ ion in sulfonate group ($–SO_3K^+$) in BPS-20K. The resultant BPS-20K/PEG membranes demonstrated a lower glass transition temperature (T_g), smaller density, and higher water uptake as the molecular weight and the amounts of PEG molecules increased.[21] When PEG molecules were blended with BPS-20K, the resulting BPS-20K/PEG membranes showed improved water permeability compared to the pure BPS-20K, though with a somewhat reduced salt rejection.[21] The water permeability increase could be attributed to the domain separation, as just discussed,

and a poorer salt rejection may be due to the ion-dipole interactions may hinder the ionic domain's ability to repel salt molecules. Unexpectedly, the highest water permeability was found at a BPS-20K/PEG sample employing the lowest molecular weight of PEG (M_n = 600 Da) we tested. An understanding of this peculiar behavior on the molecular level and the dynamics-transport correlations observed in this binary system were still not established in detail. A fundamental understanding of these correlations would enable the design of a RO membrane material with enhanced water permeability, while retaining the original salt rejection property of BPS-20K.

In this study we have investigated the dynamic characteristics of BPS-20K/PEG blended systems by using solid-state NMR spectroscopy. Because the macroscopic properties of the polymeric materials have their origins in molecular dynamics, elucidating the motional characteristics of polymeric materials on the molecular level is critical for understanding membrane morphology. Spin-lattice relaxation time (T_1) and spin-lattice relaxation time at the rotating frame ($T_1\rho$) measurements have been employed to study the dynamic characteristics of BPS-20K/PEG systems. We have also examined the motionally averaged, apparent ^{1}H-^{13}C heteronuclear dipolar couplings of aromatic methine groups of BPS-20K to monitor the influence of PEGs on the local segmental mobility of the polymeric backbone, which would be correlated to the free volume and packing order in the hydrophobic domains.

4.2. Experimental

4.2.1. Materials

BPS-20K was synthesized at Akron Polymer Systems (Akron, OH, USA) via polycondensation based on 3,3'-disulfonate-4,4'-dichlorodiphenylsufone (SDCDPS, 20 mol%), 4,4'-dichlorodiphenyl-sulfone (DCDPS, 80 mol%), and 4,4'-biphenyl (BP, 100 mol%).[21,22] The intrinsic viscosity of BPS-20K determined in NMP with 0.05M LiBr at 25 °C was 0.82 dLg^{-1} and its degree of sulfonation (DS), determined by ^{1}H NMR measurement was 20.6. PEG oligomers with number average molecular weight M_n = 600 (0.6k), 1,000 (1k), and 2,000 (2k) Da possessing two hydroxyl (-OH) groups at their terminal ends were purchased from Aldrich Chemical Co. (WI, USA). Dimethyl acetamide (DMAc) and di(ethylene glycol) (Di[EG])

obtained from Aldrich Chemical Co. was used as casting solvents without additional purification.

4.2.2. Fabrication of BPS-20K/PEG Blend Membranes

2 g of fiber-like BPS-20K was dissolved in DMAc at room temperature (solution concentration = 10 wt.%). Then a constant amount (e.g., 0.2 g) of PEG molecules (M_n = 0.6, 1.0, and 2.0 kDa) was added to the solution and mixed for 4 hours until a homogeneous solution was obtained. After degassing, the viscous solution was cast on a glass plate and dried at 90 ^oC for 6 hours, and 150 ^oC for 12 hours under vacuum. Finally, a tough, ductile, and transparent BPS-20K/PEG blend film was obtained after soaking in deionized water at 25 ^oC. A heterogeneous membrane thus obtained was denoted as BPS-20K_PEGx-y, which means that BPS-20K contains y wt% of PEG whose M_n is x kilodalton (kDa). The nominal thicknesses of membranes were in the range of 25-35 μm. Pure BPS-20K films were made from both DMAc and Di(EG) solutions and used as references in our experiments. BPS-20H, where H represents $–SO_3^-H^+$, was made by treating a BPS-20K film in boiling H_2SO_4 solution (0.5 M) for 2 hours and, subsequently, in boiling pure water for 2 hours.

4.2.3. Solid-State NMR spectroscopy

50-60 mg of membrane samples in thin film form were chopped into small pieces for packing into 4 mm magic-angle spinning (MAS) rotors for stable spinning at a speed, ν_r. Solid-state NMR (ssNMR) experiments were carried out on a Bruker Avance II-300 wide-bore spectrometer operating at 300.13 MHz for ^1H and 75.47 MHz for ^{13}C nuclei, using a Bruker 4 mm MAS NMR probe.

All experiments in this work utilize the Hartman-Hahn ^1H-^{13}C cross-polarization (CP) mixing scheme[23,24] for obtaining enhanced signal intensity and wider spectral dispersion in ^{13}C, utilizing a short acquisition delay (2-3 s) (Figure 4.2). The typical CP mixing time for obtaining a basic CPMAS spectrum was 1 ms. ^1H T_1 relaxation measurements were carried out by employing the inversion recovery method,[25] which is combined with CP (Figure 4.2B). A variable delay time τ following the initial ^1H 180° inversion pulse was combined with a ^1H-^{13}C CP scheme employing a short mixing time (~150 μs) to transfer ^1H magnetizations to the directly

attached ^{13}Cs. An indirect detection scheme is necessary because a direct, site-specific detection of ^{1}H is still not obtainable in solid state.

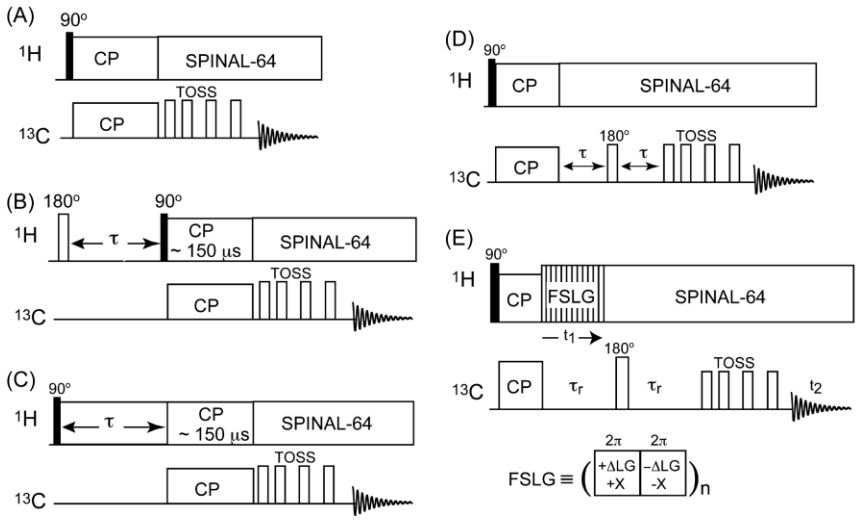

Figure 4.2. Pulse sequences used in the experiments. Shown are basic CP under MAS (A); inversion recovery for ^{1}H T_1 measurement (B); ^{1}H $T_1\rho$ measurement (C); ^{13}C T_2 measurement (D); s ^{1}H-^{13}C dipolar separated local field NMR spectroscopy (E). In each case the TOSS pulse sequence was attached before the signal detection to remove spinning sidebands. The CP mixing time used in Fig. 2B and 2C was 150 μs for choosing only directly bonded ^{1}H-^{13}C pairs for signal transfer. The CP mixing time used in the ^{13}C T_2 sequence was 1 ms for maximizing ^{13}C signal intensity. A filled bar represents a 90° pulse and an open bar a 180° pulse for both ^{1}H and ^{13}C channels. The MAS spinning speeds were 6 kHz (A, B, C, and D) and 2.74 kHz (E). The spin-lock rf pulse power along the ^{13}C and ^{1}H channels was 50 kHz. An optimal CP condition was found by readjusting the proton spin-lock pulse power during CP according to the optimizations at a certain ν_r. 62.5 kHz of SPINAL-64 was used for proton decoupling during t_2 in each sequence.

Figure 4.2C demonstrates our adapted ^{1}H $T_1\rho$ measurement sequence. Transverse ^{1}H magnetizations created by a 90° pulse are spin-locked by a variable rf-pulse block that is 90° out of phase from the excitation pulse. This locked magnetization undergoes signal decay with a relaxation parameter $T_1\rho$, which is sensitive over intermolecular or interchain associations via

hydrogen bonding or cross-linking.[26-28] An indirect CP detection scheme is also required in this case to monitor ^{1}H magnetizations along the ^{13}C channel by employing a short ^{1}H-^{13}C CP scheme. Finally, for ^{13}C T_2 measurements, ^{13}C echo signals created by a ^{1}H-^{13}C CP scheme are allowed to evolve as a function of variable delay time τ that is placed along both sides of a 180º pulse (Figure 4.2D).

A separated local field experiment was carried out to investigate the ring-flip motions of aromatic phenylene rings in the polymeric backbone by monitoring the local ^{1}H-^{13}C dipolar interactions of methine groups (Figure 4.2E). Carbon magnetizations prepared by a ^{1}H-^{13}C CP was allowed to evolve under the influence of the ^{1}H-^{13}C dipolar interaction for the indirect time, t_1, that is implemented by the frequency switching Lee-Goldburg (FSLG) scheme[29] to suppress ^{1}H-^{1}H homonuclear dipolar couplings. A t_1-modulatd ^{13}C magnetization that is dephased by a ^{13}C-^{1}H dipolar interaction within a rotor period, τ_r, is refocused by a 180° pulse and is subsequently detected during the direct acquisition time, t_2 ,on a two-dimensional (2D) dipolar-chemical shift (DIPSHIFT)[30-32] correlation scheme. The maximum duration of t_1 was $1\tau_r$, (364.8 μs; ν_r = 2741 Hz), which is 21 times a t_1-increment that corresponds to a basic FSLG unit, $(8.69\ \mu s)_0(8.69\ \mu s)_{180}$, where 0 and 180 designate the phase angles (in degree) of a rf-pulse (power (ν_1) = 94 kHz; offset = ±66.45 kHz). The CP mixing time used in the ^{13}C T_2 and DIPSHIFT sequence is 1.0 ms for obtaining strong ^{13}C signal intensity. The total suppression of spinning side bands (TOSS)[33] pulse sequence, which consists of a train of four π-pulses with appropriate delay times, was combined with each NMR sequence to obtain sideband free ^{13}C MAS spectra. The NMR signal averaging of each experiment was achieved by co-adding 2048 scans with a 4 s acquisition delay time. ^{1}H and ^{13}C 90° pulse lengths were 4 μs and 5 μs, respectively. Small phase incremental alternation with 64 steps (SPINAL-64)[34] decoupling sequence at 63 kHz power was used for proton decoupling during the direct ^{13}C signal detection.

4.2.4. Analysis of Dynamic ^{1}H-^{13}C Dipolar Coupling

For extracting the information of the ring-flip dynamics of aromatic phenylene rings in the backbone of the BPS-20K polymer, the experimentally obtained, apparent ^{1}H-^{13}C dipolar coupling interaction of a methine group on a phenylene ring has been analyzed based on a two-site jump model, incorporating a semiclassical exchange formalism.[35] We developed an in-house

Metlab program to calculate stochastic two-site jumps of an aromatic phenylene ring that would influence the NMR spectral frequencies via a kinetic modification of the Bloch equation.[36] Simulations were carried out by fixing the C-H dipolar coupling to 23 kHz, the strength of a directly bonded ^{1}H-^{13}C (r_{H-C} = 1.09 Å) segment, and by varying the flip rate (κ) and amplitude (β) of the ring-flip motion. A three-angle set of 1154 orientations generated by the Conroy method[37], which accounts for the segments being aligned at different orientations to the applied magnetic field, was employed for powder averaging. Best-fit simulations were found by comparing the experimental data and trial simulation data.

4.3. Results and Discussion

Figure 4.3 shows a solid-state ^{13}C CPMAS spectrum of BPS-20K (ν_r = 6 kHz) (A) and a ^{13}C solution-state spectrum of the same type of polymer dissolved in DMSO-d_6 (B). The solution-state spectrum and the polymer structure drawn are provided to aid peak assignments of the solid-state spectrum. Despite the obvious broad peaks, it is clear that there is still the possibility to distinguish certain sites (here, as a group with similar sites), so the broadening does not totally hinder data analysis. For example, it is noteworthy that despite the poor resolution, the methine sites are not clustered under just one peak. Peak assignments given for methine groups in the solution-state spectrum with letters *a*-*i* are extended to the solid-state MAS spectrum with color-coded dashed lines as guides. Methine carbon sites assigned at 119, 122, 129, and 131 ppm were chosen for ^{1}H T_1, ^{1}H $T_1\rho$, and ^{13}C T_2 relaxation measurements as well as ^{1}H-^{13}C dipolar separated local field experiments.[38-40]

The signal overlap in the ^{13}C NMR spectral region of aromatic phenylene rings, due in part to there actually being a distribution of a certain site (i.e. b; there are b sites along various positions of the chain, chains can have different proximities to their neighbors, etc.), imposes a limitation for an unambiguous peak assignment for each site. Occasionally, this limitation can be alleviated in a multi-dimensional correlation spectroscopy, where on a multidimensional map it is possible to better observe the spectral components making up a broad peak, or a technique that does not require a fully resolved spectral resolution. For instance, the 2D ^{1}H-^{13}C/^{13}C DIPSHIFT experiment introduced in Figure 4.2E takes a 1D slice at a site-specific frequency position of ^{13}C, after Fourier transforming the 2D (t_1, t_2) data set along t_2, to extract the time

evolution of an apparent ^{1}H-^{13}C dipolar coupling along t_1. Therefore, it substantially alleviates the peak overlapping problem of the ^{13}C MAS spectrum acquired along the direct acquisition domain. Moreover, ^{1}H T_1 measurements do not necessarily require a site-specific resolution.

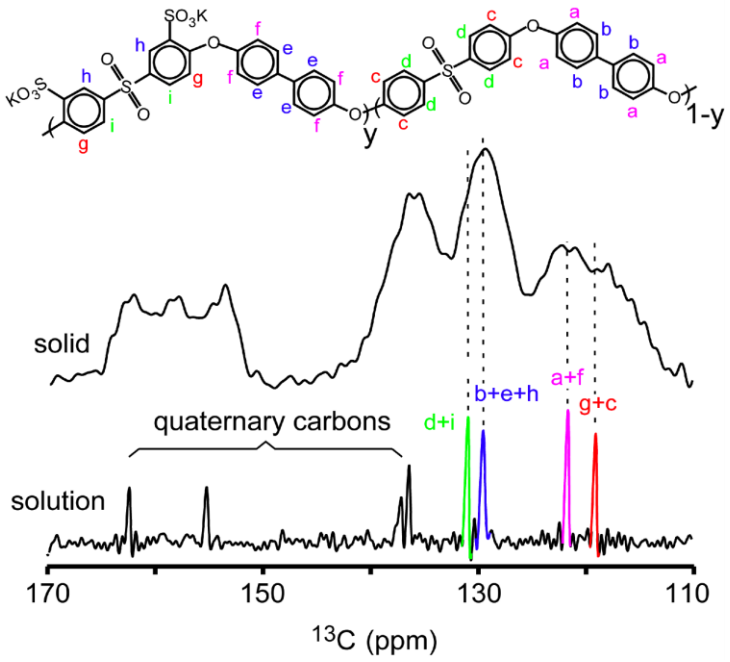

Figure 4.3. ^{13}C solid-state CPMAS spectrum and the assigned ^{13}C solution-state spectrum of BPS-20K. Work was performed by the Wi Group at Virginia Tech.

Protons in a bulk polymeric sample system in the solid state form a strongly dipolar coupled spin network, in which proton spins communicate with one another via ^{1}H-^{1}H spin diffusion, forming a shared equilibrium state. Since these protons will then share a uniform T_1 value, one does not necessarily require resolved signals for ^{1}H T_1 measurements (vide infra).

Figure 4.4 shows T_1 relaxation data of methine protons on aromatic phenylene rings in ^{1}H form BPS-20H and K^{+}-salt form BPS-20K (A), and BPS-20K/PEG blends (B). We used the ^{13}C peak at 129 ppm for our data analysis. By normalizing the intensity of the initial magnetization, M(0), to -1, the observed signal decay in each data set was correlated to the variable delay time, τ, in a plot according to $\ln[1-M(\tau)] = \ln 2 - \tau/T_1$, where $M(\tau)$ is the measured signal intensity at a time point τ. A straight line yielding a slope, $-1/T_1$, was used to extract the T_1 parameter in each data set in Figure 4.4A and B.

The T_1 value of BPS-20H is 0.070 s, while those of BPS-20K cast from DMAc and Di(EG) solutions are 0.69 s and 0.63 s, respectively (Figure 4.4A and Table 4.1). A big difference in T_1s between the ^1H and K^+ salt forms can be attributed to the difference in water uptake (BPS-20H: 19.2 wt%; BPS-20K: 4.1 wt%), and the presence or absence of labile acidic protons and strong electrostatic interactions due to the $-SO_3^-K^+$ groups in the ionic domains. Water molecules behave as a plasticizers in the polymer matrix, resulting in a shorter T_1 in the solid state. Moreover, the mobility of the labile acid protons would have been increased by water molecules present in hydrophilic domains; the faster correlation time would produce a shorter T_1. The linear regression coefficient (r^2) associated with the best curve-fitting was ≥ 0.99 for each data set. T_1 relaxation data thus obtained are listed in Table 4.1.

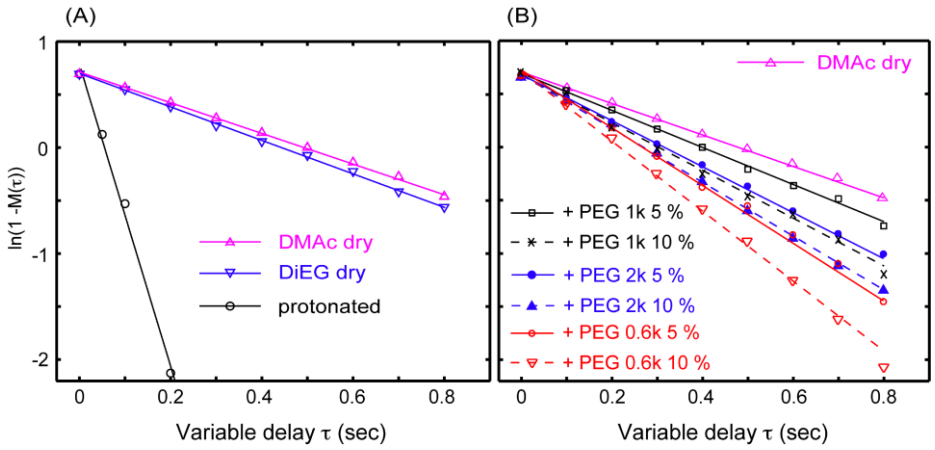

Figure 4.4. ^1H T_1 relaxation times measured on methine protons of aromatic phenylene rings in BPS-20 derivatives. Experiments employed the pulse sequence shown in Figure 4.2B. Samples considered are BPS-20H, BPS-20Ks [casting solvents: DMAc and Di(EG)], and BPS-20K/PEG blends. Error in T_1 is ~± .02 s for all samples except BPS-20H (~± .002 s). Displacement of protons in the sulfonic acid groups by potassium ions accompanies a dramatic increase in ^1H T_1 relaxation time. BPS-20K cast from DMAC and Di(EG) solutions show slightly different ^1H T_1 relaxation times. An unexpectedly shorter T_1 relaxation time is obtained with the smallest molecular weight of PEGs (M_n: 600). Work was performed by the Wi Group at Virginia Tech.

^1H T_1 relaxation data separately obtained by analyzing other peaks at 119, 122, and 131 ppm also produced an identical T_1 value in each data set (not shown). ^1Hs from aromatic methine groups,

bound water molecules, and sulfonic acid groups are coupled via ^1H-^1H homonuclear dipolar interactions. Thus, when proton spins undergo T_1 relaxation processes, magnetizations decay via self-relaxations within individual protons as well as cross-relaxations among different protons. Methine protons coupled to water protons and labile acid protons therefore undergo faster T_1 decay due to the cross-relaxations to those protons.

A K+-salt form produces a longer ^1H T_1 value because it has less amounts of water uptake and does not possess any labile acidic protons.

Table 4.1. ^1H T_1 and ^1H $T_{1\rho}$ Relaxation Parameters Measured at 25° C on Disulfonated Poly(Arylene Ether Sulfone) Random Copolymers Blended with Poly(Ethylene Glycol)s[a]

Sample	^1H T1 (s)[b] (methine)	$^1HT_{1\rho}$ (ms)[c] (methine)	$^1HT_{1\rho}$ (ms)[d] (-OCH_2CH_20-)	τ_C ($T_{1\rho}$) (μs) (-OCH_2CH_20-)
BPS-20K_PEG0.6k-5	.37	4.8	2.4	360
BPS-20K_PEG0.6k-10	.29	5.3	1.4	210
BPS-20K_PEG1k-5	.57	5.2	3.8	570
BPS-20K_PEG1k-10	.44	4.5	2.3	340
BPS-20K_PEG2k-5	.48	4.5	3.0	450
BPS-20K_PEG2k-10	.39	4.7	1.8	270
BPS-20K (DMAc)	.69	5.5	-	-
BPS-20K (Di[EG])	.63	-	-	-
BPS-20H	.070	5.3	-	-

a. Work was performed by the Wi Group at Virginia Tech.
b. Error is ~ ± .02 s for all samples except BPS-20H (~± .002 s).
c. Error is ~ ± .5 ms.
d. Error is ~ ± .2 ms.

The hydrodynamic radius of a K^+ ion is smaller than that of H^+, providing stronger electrostatic interactions between K^+ ions and sulfonate anions. If interactions involve -$SO_3^-K^+$ groups from nearby polymer chains, the chains can become tied together, inducing a more rigid polymer matrix.[41,42] Atoms or small molecular segments in this environment undergo slower motions, resulting in a longer correlation time and therefore a longer T_1 relaxation time.

Figure 4.4B and Table 4.1 show ^1H T_1 relaxation data and their corresponding best-fit curves of BPS-20K/PEG blends. T_1 values extracted from these curves are 0.37 s (5 %) and 0.29 s (10 %) for BPS20K_PEG0.6k; 0.57 s (5 %) and 0.44 s (10 %) for BPS20K_PEG1k; and 0.48 s (5 %) and 0.39 s (10 %) for BPS20K_PEG2k (Table 4.1). As can be seen from these data, BPS-20K/PEG blends provide generally a shorter T_1 value as compared to the non-blended sample.

In BPS-20K/PEG blends, similar to the case with crown ether compounds, ion-dipole interactions occur between the oxyethylene units of PEG and K^+ ions of sulfonate groups.[21,43,44] A K^+ can associate with 6 or 7 oxyethylene units,[44] thereby weakening the electrostatic interactions between K^+ ions and sulfonate anions. This decreases the T_g and density, leading to greater free volume elements in the polymer matrix (Table 4.2), which would increase the water uptake because there would then be more spaces that water could occupy (Table 4.2). This effect would become more significant as the amounts and/or the M_n of PEG molecules increase. PEG molecules behave as a plasticizers, softening the BPS-20K polymer matrix.

Table 4.2. Water Uptake/Permeation, Salt Rejection, T_g, and Density of BPS-20 and BPS-20_PEG Films.[21,a]

Sample	Water Uptake[b] [%]	Water Permeability[c] [L μm m^{-2} hr^{-1} bar^{-1}]	NaCl Rejection[d] [%]	Glass transition temperature[e] (T_g, ^oC)	Density[f] (g cm^{-3})
BPS-20K	4.1	0.032	98.9	270	1.340
BPS-20K_PEG0.6k-5	4.3	0.048	97.9	256	1.218
BPS-20K_PEG0.6k-10	4.8	0.055	96.8	245	1.197
BPS-20K-PEG1k-5	4.7	0.040	97.6	250	1.164
BPS-20K_PEG1k-10	5.1	0.047	95.9	232	1.156
BPS-20K_PEG2k-5	5.5	0.040	96.3	239	1.128
BPS-20K_PEG2k-10	6.0	0.033	93.9	227	1.112

a. Work was performed by the McGrath Group at Virginia Tech and the Freeman Group at the University of Texas at Austin.
b.Water uptake = $(W_s-W_d)/W_d\times100$. W_s = wet film (dimension = 5×5 cm^2) weight after soaking in deionized water at 25 ^oC for one day. W_d = dry film weight after drying at 110 ^oC under vacuum for one day. Error is ~± .3 %.[21]
c. Measured at 25 ^oC using dead-end filtration; Feed pressure = 400 psig. Error was not calculated by Lee[21] because only one measurement was performed for each sample.
d. Measured at 25 ^oC using dead-end filtration. NaCl concentration = 2000 ppm. pH = 6.5-7.5. Feed pressure = 400 psig. Error was not calculated by Lee[21] because only one measurement was performed for each sample.
e. Measured by dynamic mechanical analysis (DMA) of dried samples (4 mm in width). Error is ~ ± 2°C.
f. Measured based on the mass and volume of dried polymer membrane samples. Error is ~ ± .001.

The increase of free volume and water uptake in the polymer matrix would provide a softer environment for an atom or small molecular segment to vibrate with a faster correlation time, resulting in weaker ^1H-^1H homonucelar dipolar interactions. Therefore, the presence of PEGs in the BPS-20K matrix would result in a shorter T_1 time. PEG's terminal –OH groups may also

play a role in determining the mobility of PEGs in the polymer matrix, although its overall effect is minor. Terminal –OH groups will predominantly interact with water in the matrix, increasing the mobility of PEGs. The number of terminal –OH groups per a unit amount (g) of PEG increases as the M_n of PEG decreases since for a constant mass amount, using chains of lower M_n allows more chains to be present.

The decrease in T_1 time would be more significant as the amount of blended PEG increases because the water uptake and the number of oxyethylene units available for forming K^+-oxyethylene ion-dipole interactions increase when the weight percentage of PEGs increases. Interestingly however, a nonlinear chain length-dependent trend in T_1 (0.6 kDa < 2 kDa < 1 kDa) was observed when the molecular weight of PEGs is varied while fixing the weight percentage of PEGs. The pattern observed in our T_1 data indicates that the morphology of a BPS-20K/PEG blended system is a function of many different variables, including, not exclusively, the water uptake, the number of terminal –OH groups, and the number and spatial distribution of oxyethylene groups in the matrix. Since the water uptake increases as the molecular weight of PEG increases (Table 4.2), we expect that the T_1 time of the sample with PEG-2k is the shortest. However, the T_1 time from the sample blended with PEG-0.6k is the shortest as indicated previously. First of all, this peculiar behavior can be attributed to the increase of the moles of terminal –OH groups as the chain length of PEG decreases. The terminal –OH groups may interact predominantly with water molecules thereby increasing the overall mobility of PEG molecules in the polymeric matrix.

However, the distribution of oxyethylene units throughout the polymeric matrix, which is governed by the molecular weight of PEGs, is a key factor to determine the nano-miscibility of PEG oligomers with BPS-XXK. A thoroughly mixed, uniformly distributed state of K^+-oxyethylene ion-dipole interactions throughout the polymeric matrix is required to maximize the plasticization effect of PEG oligomers. The nanoscale distribution of K^+-oxyethylene interactions in the polymeric matrix is determined by the molar ratios between the K^+ ions and PEG oligomers (Table 4.3). The mole of oxyethylene units varies when a weight percentage of PEGs changes since adding a higher amount of PEG is also including more oxyethylene units, but is invariant when the chain length of PEGs increases under a specified weight percentage. The molar ratio between K^+ ions and oxyethylene units is about 1.0:1.3 and 1.0:2.7 for samples with 5 wt% and 10 wt% PEGs added, respectively, regardless of M_n. The number of oxyethylene

units per PEG molecule is 13, 22, and 45 for PEG0.6k, -1k, and -2k, respectively. Thus, the molar ratio, PEG/K^+, decreases considerably when the M_n of PEGs increases under a fixed weight percentage. Therefore, for a fixed weight percent, blends of longer PEG chains may provide more localized, less thoroughly mixed oxyethylene units throughout the polymer matrix because more oxyethylene units are confined within the space that a single PEG strand spans.

Table 4.3. The Molar Ratio of Oxyethyelene Unit/K^+ Depending on the Amount and Molecular Weight of PEGs Added

Sample	Oxyethylene unit/K^+ ratio	PEG/K^+ ratio
BPS-20K_PEG0.6k-5	1.3	0.10
BPS-20K_PEG0.6k-10	2.7	0.21
BPS-20K_PEG1k-5	1.3	0.060
BPS-20K_PEG1k-10	2.7	0.12
BPS-20K_PEG2k-5	1.3	0.030
BPS-20K_PEG2k-10	2.7	0.060

Therefore, a blended system with a lower M_n of PEGs would provide an improved plasticization effect in the polymer matrix because the K^+-oxyethylene ion-dipole interactions are more dispersed, resulting in a shorter T_1 time.

Indeed, the BPS-20K_PEG0.6k-10 system provides the shortest T_1 relaxation time (Table 4.1) as expected, and surprisingly the highest water permeability (Table 4.2). However, the high water permeability can be accounted for by considering that the transport of water molecules in glassy membranes would depend on the motional dynamics of polymeric chains, as they may alter the position and shape of nano-separated hydrophilic-hydrophobic domains over time. Since water molecules captured in hydrophilic domains diffuse in the polymeric matrix due to the thermal motion of polymeric chains, the rate of water diffusion would increase when the motional frequency (or correlation time) of polymeric chains increases.

A T_1 relaxation time is sensitive to changes occurring in a long distance, up to 200 nm, via multistep ^1H-^1H spin diffusion.[45,46] Therefore a measured T_1 value may reveal various molecular parameters determining the miscibility and morphology of polymeric blends (i.e. the ^1H T_1 of methine groups in the hydrophobic backbone is influenced by the K^+-oxyethylene ion-

dipole interactions in the hydrophilic domains). Thus, ^{1}H T_1 measurements can diagnose the size, distribution, and miscibility of hydrophobic and hydrophilic domains on the molecular level.

The temperature dependence of ^{1}H T_1 times was also investigated over the range of 25-70 °C. Pure BPS-20K (red filled triangles connected by red solid line), BPS-20K_PEG2k-5 (blue crosses connected by blue dashed line), BPS-20K_PEG2k-10 (blue open circles connected by blue solid line), and BPS-20K_PEG1k-5 (pink open squares connected by pink dashed line) showed a considerable increase in T_1 with temperature (category A; Figure 4.5).

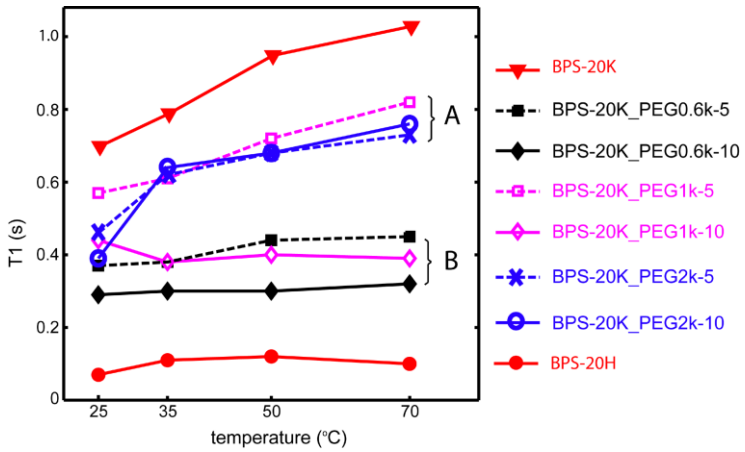

Figure 4.5. Temperature dependence of ^{1}H T_1 of aromatic methine sites in BPS-20K/PEG blends. Error in T_1 is ~ ± .02 s. Work was done by the Wi Group at Virginia Tech.

Meanwhile, the data observed from BPS-20H (red filled circles connected by red solid line), BPS-20K_PEG0.6k-5 (black filled squares connected with black dashed line), BPS-20K_PEG0.6k-10 (black filled diamonds connected with black solid line), and BPS-20K_PEG1k-10 (pink open diamonds connected by pink solid line) demonstrated virtually non-increasing T_1 values over the temperature range (category B; Figure 4.5). A notable observation is that while both 2k samples take category A, and both 0.6k samples take B, the 1k sample is split: the 10% weight takes B and the 5% weight sample is in category A. Overall, the T_1 value of a BPS-20K/PEG blend is placed between the T_1 values of BPS-20K and BPS-20H.

The observed temperature dependence in T_1 is abnormal since T_1 values generally increase with temperature for sample systems like ours, which are on the slow motional side of T_1 curve (Bloembergen-Purcell-Pound theory).[47] This is temporarily attributed to a thermal

annealing effect that is induced in the polymer matrix. A few nearby sulfonate groups, including K^+ ions, may form more closely associated (ordered) states due to the thermal annealing effect. Using this idea then, it would indicate that the effect has more of a dependence on PEG amount for blends incorporating PEG1k. The presence of more ordered sulfonate groups provide stronger electrostatic cross-linking among different polymer chains, resulting in slower polymeric chain motions. Slower chain motions with a longer correlation time, in turn, provide an increase in T_1 value on the slow motional side of the T_1 curve. The presence of PEGs hinders this thermal annealing effect due to the weakened electrostatic interaction between K^+ ions and sulfonate anions. This hindrance is bigger when the molar ratio of PEGs increases. A similar phenomenon was observed in the T_1 behavior of the thermally annealed tetraalkylammonium ions of perfluorosulfonate ionomers.[48]

The categories A and B observed in Figure 4.5 can be correlated to the relative molar ratio, PEG/K^+ (Table 4.3). When PEG/K^+ < 0.10, the observed T_1 behavior of a sample over the temperature range incorporated takes the category A. Meanwhile, when the ratio is larger than 0.10, then the observed T_1 behavior takes the category B (Figure 4.5). This observation indicates that the miscibility of PEGs with BPS-XXK on the molecular level may take a crucial role in determining the temperature-dependent T_1 behavior. The category A, which involves longer PEG molecules that possess more oxyethylene units confined to a single PEG strand, has more localized, less efficiently dispersed oxyethylene units throughout the polymer matrix. The category B, which involves smaller PEG molecules, therefore forms more thoroughly dispersed K^+-oxyethylene ion-dipole interactions in the polymeric matrix due to the larger PEG/K^+ molar ratio. More thoroughly mixed PEG molecules in the BPS-20K matrix would enhance the plasticization effect, weakening more effectively the electrostatic interactions between K^+ ions and $–SO_3^-$ groups in ionic domains. Weakened electrostatic interactions between K^+ ions and sulfonate anions may provide weaker intra- and interchain associations of polymers, resulting in faster motions of atoms or small molecular segments, which leads to shorter T_1 values over the temperature range tested.

One complementary experiment to the ^1H T_1 experiment that can be used to diagnose ion-dipole interactions between K^+ ions and oxyethylene units in ionic domains is the ^1H $T_{1\rho}$ experiment (Figure 4.2C). $T_{1\rho}$ responds to the motional rates on the order of tens or hundreds of kHz, which are sensitive over the molecular motions in polymeric molecules that are influenced

by the presence of intra- or intermolecular associations, such as cross-linking or hydrogen bonding networks.[49] We monitored the ^{1}H $T_{1\rho}$ times of both methine and oxyethylene units via indirect ^{13}C detection at 127 ppm and 70 ppm, respectively, but only the oxyethylene units of PEG demonstrated a meaningful variation in $T_{1\rho}$ data. As shown in Figure 4.6**,** the ^{13}C peak of oxyethylene units does not provide a peak overlap problem because it is isolated at 70 ppm. Figure 4.6 also shows plots of ln(M(τ)) over the variation of the delay time τ, where M(τ) is the signal intensity of ethylene ^{1}Hs. An experimental $T_{1\rho}$ relaxation parameter can be extracted from the slope of this plot, -1/ $T_{1\rho}$. The range of measured $T_{1\rho}$ parameters is 1.4-3.8 ms depending on the specific BPS-20K/PEG sample (Table 4.1). The trend observed in $T_{1\rho}$ values matches that of T_1 (0.6 kDa < 2 kDa < 1 kDa), with the shortest $T_{1\rho}$ value observed for oxyethylene units of PEG0.6k blended at 10 wt%.

The driving mechanism of ^{1}H $T_{1\rho}$ relaxation in our sample system is ^{1}H-^{1}H homonuclear dipolar couplings because the contribution of proton's small chemical shift anisotropy can be neglected. The low natural abundance of ^{13}C (~ 1%) also makes the contribution of ^{1}H-^{13}C dipolar interaction negligible in our $T_{1\rho}$ data analysis.

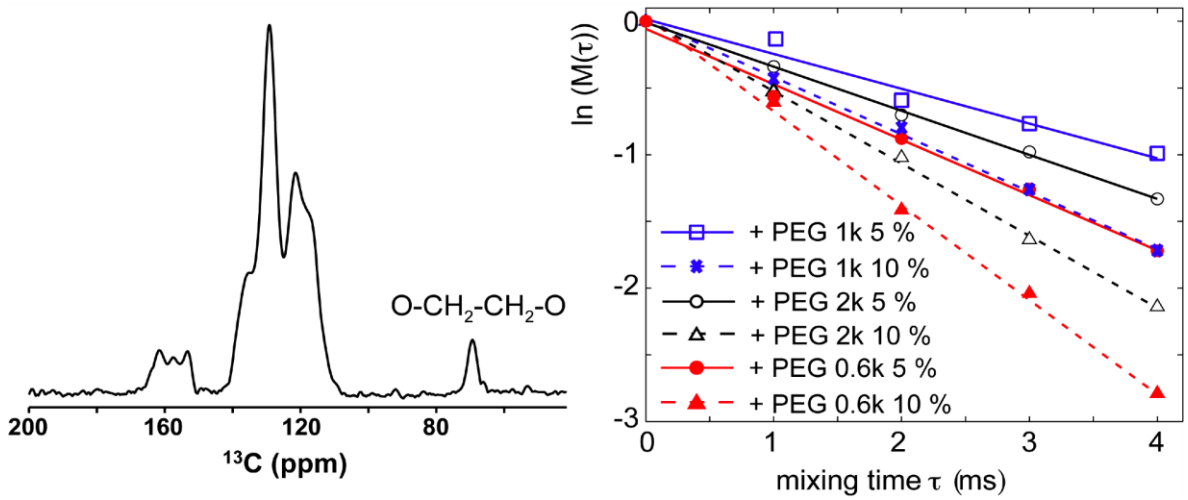

Figure 4.6. ^{1}H $T_{1\rho}$ relaxation data measured on oxyethylene units of PEG. The minimum T_1 time was observed at BPS-20K_PEG0.6k. Error in $T_{1\rho}$ is ~ ± .2 s. Work was performed by the Wi Group at Virginia Tech.

Thus, the motional correlation time, τ_c, involved in the measured $T_{1\rho}$ relaxation time can be

extracted from the following equation:[50,51]

$$\frac{1}{T_1\rho} = \frac{3}{2}\delta_{HH}^2\left[\frac{3\tau_c}{1+4\omega_1^2\tau_c^2} + \frac{5\tau_c}{1+\omega_H^2\tau_c^2} + \frac{2\tau_c}{1+4\omega_H^2\tau_c^2}\right]. \quad (4.1)$$

Here, δ_{HH}^2 is an effective ^{1}H-^{1}H dipolar coupling strength experienced by the protons at the measurement site, which is found to be 23 kHz for methylene protons in oxyethylene units and 20 kHz for methine protons in pheneylene rings, as extracted from separate experiments employing ^{1}H-wideline separation (WISE) NMR spectroscopy.[52] Frequencies defined by ω_1 and ω_H are the radiofrequency field strength of the spin-lock pulse (63 kHz) in the pulse sequence (Figure 4.2C) and the Larmor frequency of ^{1}H (300.1 MHz), respectively. When Eq. 4.1 was used to analyze our $T_{1\rho}$ data, the shortest τ_c (210 μs) was observed at the oxyethylene units in BPS-20K_PEG0.6k-10. The ranges of τ_cs extracted from the experimental $T_{1\rho}$ times are 210 ~ 570 μs for methylene protons in oxyethylene units (Table 4.1) and 540 ~ 620 μs for aromatic methine groups.

Unlike the aromatic methine groups which show insignificant changes in $T_{1\rho}$s or τ_cs over the variations of PEGs, the methylene protons in the oxyethylene unit of PEG accompany a noticeable amount of variations in both $T_{1\rho}$ and τ_c, as the weight percentage and molecular weight of PEGs change. As in the case of T_1 (data not provided), a shorter $T_{1\rho}$ value leads to a shorter τ_c value. This implies that the oxyethylene units of PEGs bound to the sulfonate groups in the hydrophilic domains undergo faster segmental motions in the milli-to-microseconds regime. But the $T_{1\rho}$ time measured at the hydrophobic methine sites (127 ppm) didn't show any meaningful variations to the blending of PEGs.

Changes in $T_{1\rho}$ times measured at the oxyethylene units of PEG indicate that PEG oligomers make ion-dipole interactions with K^+ ions, providing interconnections among randomly separated, hydrophilic domains that are composed of sulfonate groups in BPS-20K.[21] Smaller PEGs are advantageous to provide more homogenously mixed BPS-20K/PEG blends, but again an optimal blending condition of PEGs in the BPS-20K matrix is determined by considering a balance between the molar ratios of oxyethylene/ K^+ and PEG/K^+. This balancing effect is justified by the trend observed in our T_1 and $T_{1\rho}$ data (0.6 kDa < 2 kDa < 1 kDa). Increased interconnections among different hydrophilic regions may behave as channels for

water transport. Indeed, BPS-20K_PEG-0.6k-10, which provides the shortest T_1 and $T_{1\rho}$, does provide the largest water permeability.

Ring-flip motions of aromatic phenylene rings were also investigated to study the local segmental mobility of the main chain of BPS-20K by monitoring the apparent coupling strength of local ^{1}H-^{13}C dipolar interactions (results not shown here). This piece of information would be useful for estimating the packing density of the polymeric chains in the hydrophobic domains because the ability and extent to which the rings could flip would depend on the proximity of it's neighbors and the void volume. Results showed that the amplitude and frequency of the ring-flip motions of aromatic phenylene groups in the hydrophobic regions are invariant to the blending of PEGs in the hydrophilic domains. The observed amplitude and τ_c of the ring-flip motion of aromatic phenylene groups in the BPS-20K sample system are $\beta = 70 \pm 10^{o}$ and $\kappa \leq 10^{-7}$ s, respectively, regardless of the sample type. It can be justified that the measured ^{1}H-^{13}C dipolar coupling strength is a localized property confined in the hydrophobic domain, and changes occurring in the hydrophilic domains are remote from this local coupling. The results evidence that the size of the free volume elements around pheneylene rings is largely invariant to the formation of K^{+}-oxyethylene ion-dipole interactions in the hydrophilic domains.

4.4. Conclusion

We conclude that PEGs blended in the BPS-20K matrix form multivalent K^{+}-oxyethylene ion-dipole interactions, weakening the electrostatic interactions involving sulfonate ions. This interaction produces greater free volume in the ionic domains and enhances interconnectivity between hydrophilic domains, leading to improved water permeability.[21] Among six BPS-20K/PEG samples obtained by adding 5 or 10 wt% of PEGs with variable molecular weights (0.6 kDa, 1 kDa, and 2 kDa), a blended BPS-20K sample with 10 wt% of 0.6 kDa of PEG, which yielded the shortest ^{1}H T_1 and $T_1\rho$ times, has provided the best water permeability with the least compromise in the salt rejection property. Trends observed in our T_1 and $T_1\rho$ data also showed *ad hoc* correlations with other types of macroscopic properties, such as the T_g, density, and water uptake. These correlations are key factors needed to wisely tune the materials on the molecular level to achieve desired bulk properties. Our observations may suggest that NMR T_1 and $T_1\rho$ relaxation measurements can be utilized for monitoring the dynamics-transport correlations on

the molecular level of the polymeric membranes developed for RO applications. Furthermore, their capability to probe global and local properties of a polymer, respectively, over a wide dynamic range, allows an understanding of how different polymer regions effect those correlations.

^{1}H T_1 data measured on the methine sites on aromatic phenylene rings indicate that high-frequency motions, such as vibrations involving atoms or small segments in hydrophobic domains, become more prominent as the amount of PEGs increases or the mixing of oxyethylene units becomes more homogeneous on the molecular level. The strength of ^{1}H-^{1}H homonuclear dipolar interactions among methine protons becomes weaker as the segmental mobility of atoms or molecular segments increases due to the binding of PEGs, which thereby impairs electrostatic interactions involving sulfonate groups. The network size of ^{1}H-^{1}H homonuclear dipolar interactions also contracts as the size of hydrophobic domains becomes smaller. The presence of more flexible oxyethylene protons also produces an overall, weaker ^{1}H-^{1}H dipolar network. These effects explain why the ^{1}H T_1 times of methine sites become shorter as PEG molecules are blended into the BPS-20K matrix.

Our ^{1}H $T_1\rho$ measurement data indicate that the interaction of oxyethylene units of PEGs with sulfonate groups improves the interconnectivity between BPS-20K chains. Increased intermolecular associations between BPS-20Ks via PEG blending would provide better interwoven hydrophilic domains that form channels for improved water transport in the ionic domains. The motional correlation time of oxyethylene units participating in K^{+}-oxyethylene ion-dipole interactions becomes shorter when smaller PEGs are used.

The ring-flip motions of aromatic phenylene rings, diagnosed by the apparent dipolar coupling strengths of ^{1}H-^{13}C sites, provided an identical amplitude ($70 \pm 10°$) and correlation time ($\leq 10^{-7}$ s) regardless of the morphological changes that occurred due to the PEG complexation with sulfonate groups in the ionic domains. This observation suggests that the lower frequency components (< MHz) of the molecular motions of aromatic pheneylene rings in the BPS-20K polymer are localized in the hydrophobic domains, and that PEG molecules exist only in the ionic domains. Invariance of the local ring-flip motions agrees with the theoretically calculated van der Waals volume of BPS-20K (data not shown), which is unaffected by the inclusion of PEG or water molecules in the calculations.

References

(1) Service, R. F. *Science* **2006**, *313*, 1088.

(2) Baker, R. W. *Membrane Technology and Applications*; 2nd ed.; John Wiely & Sons, Ltd., 2004.

(3) Cadotte, J. E.; Patent, U., Ed. 1981; Vol. 4, p 344.

(4) Burbano, A. A.; Adham, S. S.; Pearce, W. R. *J. AWWA* **2007**, *99*, 116

(5) Petersen, R. J.; Cadotte, J. E. In *Handbook of Industrial Membrane Technology*; Porter, M. C., Ed.; Noyes, Park Ridge: 1996, p 307.

(6) Park, H. B.; Freeman, B. D.; Zhang, Z. B.; Sankir, M.; McGrath, J. E. *Angew. Chem. Int. Ed.* **2008**, *47*, 6019

(7) Brousse, C. L.; Chapurlat, R.; Quentin, J. P., 1976; Vol. 18.

(8) Drzewinski, M.; Macknight, W. J. *J. Appl. Polym. Sci.* **1985**, *30*, 4753.

(9) Paul, M.; Park, H. B.; Freeman, B. D.; Roy, A.; McGrath, J. E.; Riffle, J. S. *Polymer* **2008**, *49*, 2243.

(10) Geise, G. M.; Lee, H.-S.; Miller, D. J.; Freeman, B. D.; McGrath, J. E.; Paul, D. R. *J. Polym. Sci. Pol. Phys.* **2010**, *48*, 1685.

(11) Geise, G. M.; Park, H. B.; Sagle, A. C.; Freeman, B. D.; McGrath, J. E. *J. Membr. Sci.* **2011**, *369*, 130.

(12) Mao, G.; Castner, D. G.; Grainger, D. W. *Chem. Mater.* **1997**, *9*, 1741.

(13) Lee, M.; Jang, C. J.; Ryu, J. H. *J. Am. Chem. Soc.* **2004**, *126*, 8082.

(14) Chakrabarty, B.; Ghoshal, A. K.; Purkait, M. K. *J. Colloid Interf. Sci.* **2008**, *320*, 245.

(15) Ju, H.; McCloskey, B. D.; Sagle, A. C.; Wu, Y. H.; Kusuma, V. A.; Freeman, B. D. *J. Membr. Sci.* **2008**, *307*, 260.

(16) Chou, W. L.; Yu, D. G.; Yang, M. C.; Jou, C. H. *Sep. Purif. Technol.* **2007**, *57*, 209.

(17) Revanur, R.; McCloskey, B. D.; Breitenkamp, J.; Freeman, B. D.; Emrick, T. *Macromolecules* **2007**, *40*, 3624.

(18) Chakrabarty, B.; Ghoshal, A. K.; Purkait, M. K. *J. Membr. Sci.* **2008**, *309*, 209.

(19) Van Alstine, J. M.; Malmsten, M. *Langmuir* **1997**, *13*, 4044.

(20) Lazzara, G.; Milioto, S. *J. Phys. Chem. B.* **2008**, *112*, 11887.

(21) Lee, C. H.; VanHouten, D.; Lane, O.; McGrath, J. E.; Hou, J.; Madsen, L.; Spano, J.; Wi, S.; Cook, J.; Xie, W.; Oh, H. J.; Freeman, B. D. *Chem. Mater.* **2011**, *23*, 1039.

(22) Wang, F.; Hickner, M.; Kim, Y. S.; Zawodzinski, T. A.; McGrath, J. E. *J. Membr. Sci.* **2002**, *197*, 231.

(23) Hartmann, S. R.; Hahn, E. L. *Phys. Rev.* **1962**, *128*, 2042.

(24) Pines, A.; Gibby, M. G.; Waugh, J. S. *J. Chem. Phys.* **1973**, *59*, 569.

(25) Harris, R. K. *Nuclear Magnetic Resonance Spectroscopy*; Pitman: London, 1983.

(26) Scheler, U. In *Solid-state NMR spectroscopy, Principles and Applications*; Duer, M. J., Ed.; Blackwell Science Ltd.: 2002, p 483.

(27) Virta, A.; Komu, M.; Kormano, M. *Magn. Reson. Red.* **1997**, *37*, 53.

(28) Kwak, S. Y.; Jung, S. G.; Kim, S. H. *Envirn. Sci. Technol.* **2001**, *35*, 4334.

(29) Bielecki, A.; C., K. A.; Levitt, M. H. *Chem. Phys. Lett.* **1989**, *155*, 341.

(30) Schaefer, J.; Stejskal, E. O.; McKay, R. A.; Dixon, W. T. *Macromolecules* **1984**, *17*, 1479.

(31) Munowitz, M. G.; Griffin, R. G.; Bodenhausen, G.; Huang, T. H. *J. Am. Chem. Soc.* **1981**, *103*, 2529.

(32) Hong, M.; Gross, J.; Griffin, R. *J. Phys. Chem. B* **1997**, *101*, 5869.

(33) Dixon, W. T. *J. Chem. Phys.* **1982**, *77*, 1800.

(34) Fung, B. M.; Khitrin, A. K.; Ermolaev, K. *J. Magn. Reson.* **2000**, *142*, 97.

(35) McConnell, H. M. *J. Chem. Phys.* **1958**, *28*, 430.

(36) Bloch, F. *Phys. Rev.* **1946**, *70*, 460.

(37) <http://www.mhl.soton.ac.uk/public/software/Ori-entations/index.html>, A. f.

(38) Webb, G. G.; Zilm, K. W. *J. Am. Chem. Soc.* **1989**, *111*, 2455.

(39) Burum, D. P.; Bielecki, A. *J. Magn. Reson.* **1991**, *95*, 184.

(40) Sethi, N. K. *J. Magn. Reson.* **1991**, *94*, 352.

(41) Moore, R. B.; Cable, K. M.; Croley, T. L. *J. Membr. Sci.* **1992**, *75*, 7.

(42) Eisenberg, A.; Hird, B.; Moore, R. B. *Macromolecules* **1990**, *23*, 4098.

(43) Chan, K. W. S.; Kelsey D. Cook, K. D. *Macromolecules* **1983**, *16*, 1736.

(44) Okada, T. *Macromolecules* **1990**, *23*, 4216.

(45) Schmidt-Rohr, K.; Spiess, H. W. *Multidimensional Solid-State NMR and Polymers*; Academic Press: San Diego, 1994.

(46) Bloembergen, N. *Physica* **1949**, *15*, 386.

(47) Bloembergen, N.; Purcell, E. M.; Pound, R. V. *Phys. Rev.* **1948**, *73*, 679.

(48) Park, J. K.; Spano, J.; Moore, R. B.; Wi, S. *Polymer* **2009**, *50*, 5720.

(49) Kimmich, R. *NMR Tomography, Diffusometry, Relaxometry*; Springer: Berlin, 1997.

(50) Abragam, A. *The Principles of Nuclear Magnetism*; Clarendon Press: Oxford, 1983.

(51) Huster, D.; Xiao, L.; Hong, M. *Biochemistry* **2001**, *40*, 7662.

(52) Schmidt-Rohr, K.; Clauss, J.; Spiess, H. W. *Macromolecules* **1992**, *25*, 3273.

Chapter 5

Investigation of the Molecular Dynamics in a Series of Poly(Arylene Ether Sulfone) Segmented Copolymer Analogues using Solid-State NMR

Reproduced in part with permission from Spano, J.; Zhang, B.; Chen, Y.; Turner, S.; Wi, S. *J. Polym. Sci. B: Polym. Phys.*, **submitted**. Solid-state NMR experiments were carried about by the Wi Group, and polymer synthesis and characterization were carried out by the Turner Group, at Virginia Tech.

5.1. Introduction

One polymer system of industrial importance that has been highly researched is thermoplastic polyarylethers.[1,2] In particular, poly(arylene ether sulfone)s (PAES) are known to have excellent thermal and mechanical properties.[3,4] Due to the amorphous nature, however, some applications of PAES are limited by poor solvent resistance and unacceptable thermal dimensional changes near their glass transition temperature, T_g.

One way that these disadvantages can be addressed is by incorporating 1,4-cyclohexylene ring units into the polymer backbone to enhance the mechanical properties and improve crystallization rate.[5] Cyclohexylene ring containing polyesters, such as poly(1,4-cyclohexylenedimethylene 1,4-cyclohexanedicarboxylate) (PCCD), poly(butylene 1,4-cyclohexanedicarboxylate) (PBCHD) and Poly(1,4-cyclohexane dimethylene terephthalate) (PCT) (Figure 5.1), has been widely reported in the literature;[6-8] however, to the best of our knowledge, little effort has been done with cyclohexylene ring containing PAESs.

This chapter describes the investigation of the molecular dynamics of a series of PAES polymer analogues modified with 1,4-cyclohexylene ring units. The dynamics of the four differently modified polymers was investigated using magic-angle-spinning (MAS) solid-state NMR (ssNMR) methods, which provide a wealth of information complementary to the conventional macroscopic characterization tools. The motional dynamics characterization of synthetic polymeric materials is crucial for correlating observable macroscopic phenomena, such as T_g, melting temperature, T_m, free volume, etc., to the corresponding molecular segmental mobility on the atomic level.[9] These efforts provide valuable information for understanding and

controlling polymeric materials. Depending on the type of experiments, ssNMR spectroscopy provides information on polymer motion that spans over distances ranging from a few nanometers up to even a few hundreds of nanometers, as well as dynamics of local segments whose time scales range from a few nanoseconds to seconds.

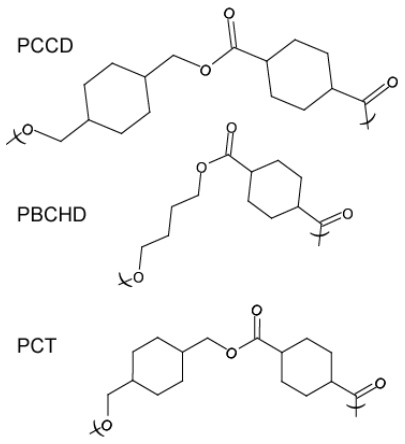

Figure 5.1. Repeating units of select cyclohexylene ring containing polyesters.

A suit of ssNMR techniques have been employed in this study for investigating polymer dynamics. One method is relaxation time measurements: spin-lattice relaxation time ,T_1,[10-13] rotating frame spin-lattice relaxation time,$T_1\rho$,[11-15] and spin-spin relaxation time, T_2.[15,16] T_1 is affected by motions in the MHz regime, while $T_{1\rho}$ and T_2 are sensitive to dynamic processes on the order of kHz, so together the measurements help to understand a polymer's mobility over a wide dynamics range. Also employed for studying polymer mobility are the ^{1}H-^{13}C/^{13}C *dip*olar coupling–chemical *shift* correlation spectroscopy (DIPSHIFT)[17-19] and the *c*enterband-*o*nly *d*etection of *ex*change (CODEX) experiment.[20,21] The ^{1}H-^{13}C/^{13}C DIPSHIFT experiment can characterize the local ring-flip dynamics of aromatic rings by exploiting the molecular motional attenuation of the heteronuclear dipolar coupling strength of a certain ^{1}H-^{13}C bond (~23 kHz for a rigid ^{1}H- ^{13}C bond), and is particularly useful to detect motions that occur within an intermediate time scale (milli-to microseconds).[22] The CODEX experiment is a powerful technique to investigate slow backbone conformational dynamics (correlation time,τ_c = 0.1/s–3000/s) with high sensitivity and resolution under MAS conditions. CODEX experiments can elucidate the amplitude and correlation time of segmental reorientation dynamics, as well as the

geometry and number of exchanging sites involved in the motion. These studies discussed herein provide insight on how different second monomers affect the mobility and packing of the polymer chains as well as the sizes, distributions, and miscibility of domains the aromatic PAES and aliphatic 1,4-cyclohexylene units constitute.

5.2. Experimental

5.2.1. Polymer Synthesis

The detailed synthesis of the monomers, the hydroxyl-terminated PAES oligomers with controlled molecular weight and cyclohexylene ring containing PAES polymer is described elsewhere.[23] The polymer acronyms and structures of PAES block copolymers, incorporating aliphatic segments, investigated in this study are shown in Figure 5.2. The polymers are composed of biphenol based polysulfone (BPPAES) oligomer and ester components.

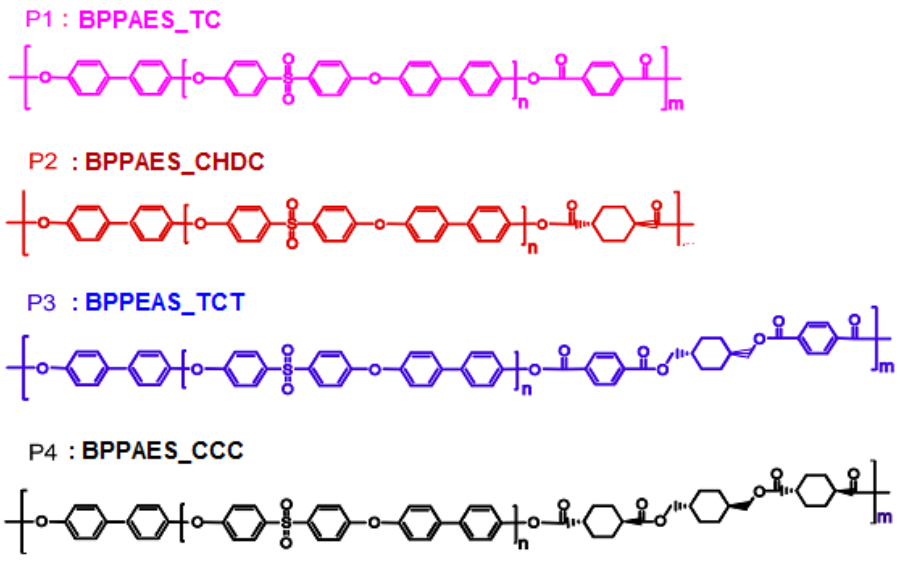

Figure 5.2. Structures of the four cyclohexylene ring containing PAES samples investigated. Synthesis was performed in the Turner Group at Virginia Tech.

TC, CHDC, TCT, and CCC monomers were used in the synthesis of P_1, P_2, P_3, and P_4 respectively as indicated by the acronyms listed. These block copolymers have the same "n"

repeat unit, but differ in the "m" repeat unit block; this m-block may contain cyclic alkyl groups (i.e. P_2, P_4), aromatic rings (i.e. P_1), or a combination of the two (i.e. P_3).

5.2.2. Characterization of the Synthesized Polymer

^{1}H and ^{13}C NMR spectra were obtained on a JEOL 500 (500 MHz) spectrometer at room temperature with chemical shifts relative to tetramethylsilane (TMS). T_gs and T_ms were determined by Differential Scanning Calorimetry (DSC). Data were obtained by using a TA Q2000. Nitrogen was used as the carrying gas with a sample flow rate of 20 ml/min and a heating rate of 10 ^{o}C/min. T_gs was determined in the second heating cycle. Thermogravimetric analysis (TGA) was carried out by a TA Instruments TGA 1000 from 25 ^{o}C to 800 ^{o}C under nitrogen at a heating rate of 60 ^{o}C /min. Size Exclusion Chromatography (SEC) was used to determine molecular weights and molecular weight distributions. Data were obtained in SEC solvent (chloroform, N,N-dimethylformamide (DMF) and N-methyl-2-pyrrolidone (NMP)) at 30 ^{o}C on a Waters Alliance model 2690 chromatograph equipped with a Waters HR 0.5+ HR 2+ HR 3+ HR 4 styragel column set. A Viscotek refractive index detector and a viscometer were used for molecular weight determination. Polystyrene standards were utilized to construct a universal molecular weight calibration curve.

5.2.3. Solid-State NMR Spectroscopy

Unlabeled (i.e. natural abundance ^{13}C) polymer samples in powder form were packed into 4 mm rotors for MAS experiments. ssNMR experiments were performed on a Bruker Avance II-300 wide bore NMR spectrometer (7.05 T) operating at ^{13}C and ^{1}H Larmor frequencies of 75.47 MHz and 300.13 MHz, respectively, using a Bruker 4 mm MAS NMR probe; pulse sequences are show in Figure 5.3. All experiments utilize the Hartman-Hahn ^{1}H-^{13}C cross-polarization (CP) mixing scheme[24,25] for obtaining enhanced signal intensity and wider spectral dispersion in ^{13}C, utilizing a short acquisition delay (2-3 s) which is governed by the shorter ^{1}H T_1 relaxation time rather than by the longer ^{13}C T_1 relaxation time. The total suppression of spinning side bands (TOSS)[26] sequence, which consists of a train of four π-pulses with appropriate delay times, was combined with each NMR sequence to obtain side-band free ^{13}C MAS spectra.

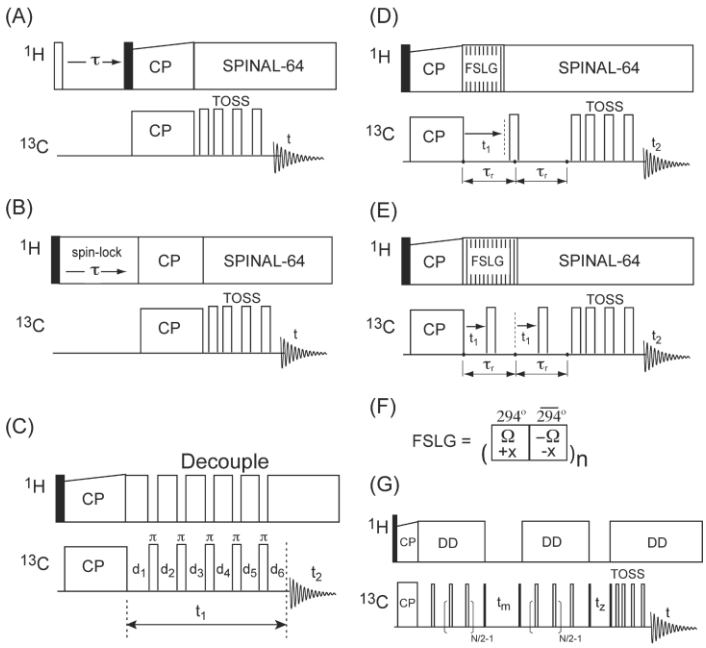

Figure 5.3. NMR pulse sequences employed in this work. Sequences are shown for: (A) ^{1}H T_1, (B) ^{1}H $T_{1\rho}$, (C) 2D-PASS, (D) DIPSHIFT-1X, (E) DIPSHIFT-2X, (F) basic FSLG unit, and (G) CODEX. Open and closed rectangles represent 180° and 90° pulses, respectively. Each sequence employs a TOSS sequence block for obtaining a sideband free ^{13}C spectrum along the direct signal acquisition domain.Additionally, for the T_2 measurement, 83 kHz of proton decoupling power was applied during the spin echo period under the SPINAL-64 sequence. These experiments were performed by the Wi Group at Virginia Tech.

The NMR signal averaging of each experiment was achieved by co-adding 2048 scans with a 4 s acquisition delay time. ^{1}H and ^{13}C $\pi/2$ pulse lengths were 4 μs and 5 μs, respectively. Small phase incremental alternation with 64 steps (SPINAL-64)[27] decoupling sequence at 63 kHz power was used for proton decoupling during the direct ^{13}C signal detection in each experiment.

5.2.3.1. NMR Relaxation Measurements

^{1}H T_1, ^{13}C T_2 and ^{1}H $T_{1\rho}$ were performed at $\nu_r = \omega_r /2\pi = 6$ kHz , where ν_r is the MAS spinning speed, employing a CP scheme for signal detection. ^{1}H T_1 relaxation measurements were made via the inversion recovery method[28] (Figure 5.3A). A variable delay time, τ,

following the initial ^{1}H 180° inversion pulse was combined with a ^{1}H-^{13}C CP scheme employing a short mixing time (~ 150 μs) to transfer ^{1}H magnetizations to the directly attached ^{13}C atoms. This indirect detection scheme is necessary because a direct, site-specific detection of proton resonances is not permissible for solid state hydrocarbon-based polymer samples due to the extensive line broadening produced by ^{1}H-^{1}H homonuclear dipolar coupling. Figure 5.3B demonstrates our ^{1}H $T_{1\rho}$ sequence modified with the same indirect detection scheme. ^{1}H magnetizations created by a 90° pulse are spin-locked by a variable rf-pulse block that is 90° out of phase from the initial 90° pulse. ^{1}H transverse magnetization that is locked by the spin-lock pulse undergoes signal decay with a relaxation parameter $T_{1\rho}$, which is sensitive over segmental molecular motions with time scales of a few milliseconds or microseconds.[29] ^{13}C T_2 relaxation times were measured by monitoring the decay of ^{13}C echo signals as a function of a variable delay time, τ, that is placed along both sides of a 180° Hahn-echo pulse (the pulse sequence is not shown). A 1 ms CP mixing time was used to maximize ^{1}H-^{13}C signal transfer. By comparison to the other two relaxation experiments, it can be understood that with a longer mixing time, the magnetization of a given ^{1}H will be transferred to distant ^{13}Cs in the sample, in addition to the directly bonded ^{13}C.

For the ^{1}H T_1, ^{1}H $T_{1\rho}$, and ^{13}C T_2 measurements, the variable delay time, τ, was extended from 0 to 1 s in 10 increments of .1 s each (T_1), from 0 to 10 ms in 10 increments of 1 ms each ($T_{1\rho}$), and from 0 to 5 ms in 10 increments of .5 ms each (T_2). Relative intensities were found by comparing peak intensities for slices from the different delay times to the intensity of the first slice. Relaxation times were then extracted based on linear regression of the experimental points in plots.

5.2.3.2. Measurement of Chemical Shift Anisotropy of Aromatic Carbon Sites

The chemical shift anisotropy (CSA) of individual ^{13}C sites was investigated by obtaining spinning sideband patterns, which are separated by order, employing the two-dimensional *p*hase *a*djusted *s*pinning *s*ideband (2D PASS) experiment[30,31] under a slow MAS condition. The pulse sequence (Figure 5.3C) was used to encode spinning sidebands of ^{13}C peaks on a full 2D ^{13}C spectrum. Carbon magnetizations prepared by a standard CP method evolved during a single rotor period, τ_r (= $1/\nu_r$), that consists of five π-pulses and 6 delay times (d_1-d_6) placed at

appropriate time intervals. The positions of π-pulses and delay times placed in the indirect time, t_1, were varied accordingly to separate sidebands of ^{13}C sites by order (ν_r = 1.5 kHz). Then, ^{13}C magnetizations are encoded during the signal acquisition time, t_2, under ^1H decoupling.

Successive rows of the 2D PASS spectrum were sheared along the indirect frequency domain so as to align all sidebands at the same frequency position. A slice obtained at a specific frequency position along the direct frequency domain provides a CSA sideband pattern for the ^{13}C site at that position. Numerical simulations were carried out employing a home-built program written in the Matlab programming language. The convention of CSA tensor parameters[32] used in our study is:

$$\left|\delta_{zz} - \delta_{iso}\right| \geq \left|\delta_{xx} - \delta_{iso}\right| \geq \left|\delta_{yy} - \delta_{iso}\right| \tag{5.1}$$

where δ_{ii} (ii = xx, yy, and zz) are the diagonal CSA tensor elements at the PAF and δ_{iso} is the isotropic chemical shift (ppm) defined by

$$\delta_{iso} = \left(\delta_{xx} + \delta_{yy} + \delta_{zz}\right)/3 \tag{5.2}$$

The chemical shift anisotropy (CSA), δ (ppm), and asymmetry parameter, η, are defined by:

$$\delta = \left(\delta_{zz} - \delta_{iso}\right) \tag{5.3}$$

$$\eta = \left(\delta_{yy} - \delta_{xx}\right)/\delta \tag{5.4}$$

MAS sideband spectral simulations were carried out to find the best-fit CSA parameters by varying both δ and η.

5.2.3.3. ^1H-^{13}C Dipolar Local Field Measurements

Changes in the local free volume elements around aromatic phenylene rings due to the incorporation of aliphatic 1,4-cyclohexylene units into the polymer sequence have been

investigated by investigating aromatic ring-flip motions of phenylene rings. For this purpose, the ^{1}H-^{13}C dipolar local field strength[32,33] of aromatic methine groups was examined by utilizing 2D ^{1}H-^{13}C/^{13}C *dip*olar coupling chemical *shift* (DIPSHIFT) correlation experiments (Figure 5.3D and E). When a phenylene ring in the polymer backbone undergoes a ring-flip motion, which is governed by the free volume element around the phenylene ring, the apparent dipolar coupling strength of a ^{1}H-^{13}C bond in the ring will be scaled down. The full 23 kHz of ^{1}H-^{13}C dipolar coupling strength at the static environment decreases as the ring-flip motion undergoes due to the thermal motion. Then, by analyzing the magnitude of the apparent dipolar coupling of a ^{1}H-^{13}C group, the magnitude of relative free volume elements around the common aromatic PAES block can be estimated.

5.2.3.4. Slow Segmental Reorientations of Polymer Backbones Studied by CODEX

The *c*enterband-*o*nly *d*etection of *ex*change (CODEX) experiment was used to probe slow segmental reorientations of polymer backbones with rates in the ranges of 1 – 3000 Hz in solids. CODEX has a special advantage in signal sensitivity and resolution because it utilizes only the centerband of a MAS spectrum. The CODEX experiment monitors the signal dephasing resulting from the segmental reorientations of polymer chains that induce changes in the orientation-dependent chemical shift frequencies. The timescale of molecular motions that is sensitive in the CODEX experiment is complementary to the those available from T_1 (a few nanoseconds), $T_1\rho$ (milliseconds to microseconds), or T_2 (a few milliseconds) relaxation measurements.

The CODEX pulse sequence (Figure 5.3G) begins with a ^{1}H/^{13}C CP (mixing time = 1 ms), followed by a series of two π pulses per τ_r, applied for, $\frac{N}{2}\tau_r$ (t_{csa}; N is an even integer), in order to recouple CSA. A ^{13}C transverse magnetization evolves under this CSA. Then, the ^{13}C signal is converted into a longitudinal magnetization that is allowed to mix during t_m (= $n\tau_r$, where *n* is an integer), after which the magnetization is converted back into the transverse mode and the transverse ^{13}C magnetization is exposed to a second CSA recoupling pulse block for another $\frac{N}{2}\tau_r$. If no molecular motions are involved during t_m, the chemical-shift evolution during the first CSA recoupling block is refocused by the second CSA recoupling block. If a

molecule undergoes segmental reorientations during t_m, the signal evolution by the first CSA recoupling block is not completely refocused by the second CSA block, due to the changes in the orientation-dependent frequencies, resulting in signal dephasing. Therefore, segmental reorientations occurring in the polymer chains can be studied by the CODEX experiment under an experimental condition that provides sideband-free, high-resolution CPMAS signals. In particular, sideband-free spectra are desirable because sidebands can crowd spectra, leading to confusing spectra and possible interference of the interesting isotropic peaks.

The second longitudinal mixing time, a short z-filter time t_z ($t_z = k\tau_r$, where k is an integer; $k << n$), is introduced in the pulse sequence to remove any signal loss due to T_1/T_2 relaxation and ^{13}C-^{13}C dipolar spin diffusion. Essentially, a z-filter cancels extraneous z-magnetization that was created during the transverse evolution period by using a 90° pulse to send the unwanted z-magnetization into the transverse plane, and the desired transverse magnetization (from the evolution period) is stored along the longitudinal direction. The unwanted magnetization will then dephase according to T_2, and following a second 90° pulse, the signal due the desired CSA-modulated ^{13}C magnetization (stored magnetization) will be obtained. To compensate any potential signal loss in the CODEX experiment (S), a reference spectrum, S_0, is recorded by switching τ_m and τ_z in the pulse sequence and a ratio S/S_0 is calculated. A pure-exchange CODEX NMR signal is then obtained by calculating $1\text{-}S/S_0$. Signals under detection are exposed to TOSS to aid in removing spinning sidebands, and finally ^{13}C magnetization is detected under SPINAL-64 for proton decoupling.

An isotropic rotational diffusion model was employed to simulate experimental CODEX data, assuming a finite set of conformational sites (30 discrete sites as conformer populations) that undergo mutual reorientational exchanges among them. Simulations were carried out by varying both t_m and t_{CSA} to find out the reorientational correlation time (τ_c) of the segmental reorientations in polymer chain. A single τ_c, as well as a distribution, were employed in our data analysis for obtaining the best-fit simulations. For considering a distribution in τ_c, a log-Gaussian weighting function provided by[37-39]

$$G(\tau, \tau_c) = \frac{1}{\sigma\sqrt{2\pi}} \exp\left[-(\ln\tau - \ln\tau_c)/2\sigma^2\right] \tag{5.5}$$

where σ is the half-height full-width (HHFW) in decades, was employed by considering arbitrarily 17 logarithmically spaced τ values between 0.002 $\tau_c < \tau < 400\ \tau_c$. CODEX signal intensities were obtained by plotting the normalized pure exchange signal, $1\text{-}S/S_0$, as a function of t_m or t_{CSA}. A home-built simulation program written in the Matlab programming language according to the known algorithm was utilized in our data analysis. A τ_c associated with the segmental reorientations of polymer chains was extracted based on the best-fit simulations.

5.3. Results and Discussion

5.3.1. The T_g and T_m of Polymers

Table 5.1. Molecular Weight, T_g, and T_m of a Series of Poly(Arylene Ether Sulfone) Segmented Copolymer Analogues[a]

BP-based Polymer	Molar Mass		Polydispersity	T_g (^oC)	T_m (^oC)	ΔT (^oC)
	M_n	M_w	M_w/M_n			
P_1	6.2K	9.2K	1.5	200	247	47
P_2	5.2 K	8.4 K	1.6	186	244	58
P_3	14.0 K	19.3 K	1.4	177	241	64
P_4	12.2 K	15.9 K	1.3	167	244	77

a. Work was performed by the Turner Group at Virginia Tech. Error values were not calcuted by Zhang.

With BP PAES oligomers, all four polymer samples showed crystallinity. Independent of the acid chloride monomers, the T_ms of the polymers were all in the vicinity of 240 ^oC. Decreasing T_gs in the monomer sequence of CHDC (P_2) > TCT (P_3) > CCC (P_4) were found. Because of the structure independency of T_m, the decreasing T_gs enlarged the crystallization window ($\Delta T = T_m\text{-}T_g$, Table 5.1). For all polymers no recrystallization or melting transition were observed in either the cooling cycle or the second heating cycle of the DSC, indicating that the semi-crystallinity was a result of solvent-induced crystallization with relatively low molecular weight samples. A slow crystallization rate in the melt inhibits polymer recrystallization.

5.3.2. ^{13}C CPMAS Spectra of Polymer Samples

The ^{13}C spectra of the polymers investigated in this study are shown in Figure 5.4A.

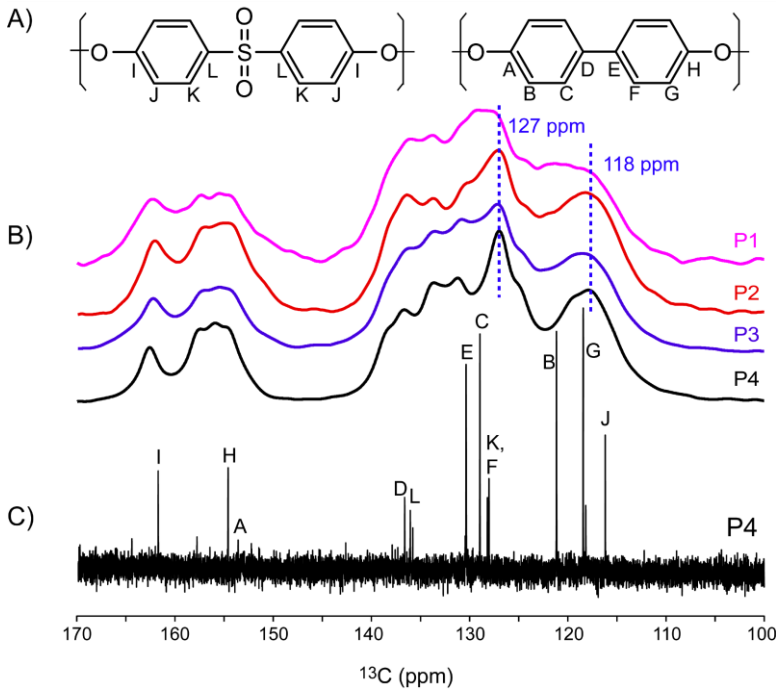

Figure 5.4. Details of spectroscopic backgrounds for the present experiments. The aromatic segments from the polymers focused on in our ssNMR experiments are exhibited, with different ^{13}C sites labeled by letters (A). Example ^{13}C MAS spectra for each of the polymer samples (B) are shown atop a solution ^{13}C spectrum of P_4 (C). The letter-labeled peaks in the solution spectrum (C) correspond to the ^{13}C sites of the aromatic rings (A). Dashed vertical lines lines in B represents frequency positions employed for T_1, $T_1\rho$, T_2, CODEX, and ^1H-^{13}C dipolar local field experiments and show how the broad peaks in the MAS spectra at 127 ppm and 118 ppm match up to the peaks in the solution spectrum. Additionally, a quaternary peak located at position H (136 ppm) is considered for CODEX experiments. Work was performed by the Wi Group at Virginia Tech.

In the experiments mentioned herein, methine groups on the aromatic phenylene rings indicated at B, C, F, G, J, and K sites (Figure 5.4A) were utilized for various types of ssNMR experiments for monitoring molecular motions. Example ^{13}C MAS ssNMR spectra for P_1-P_4 (Figure 5.4B) are shown above a solution ^{13}C NMR spectrum of P_4 (Figure 5.4C). This solution ^{13}C NMR spectrum had been assigned for sites A-L, and served to aid in identifying peaks in the ssNMR spectrum. The broad ssNMR peaks centered at 127 ppm and 118 ppm were chosen for analysis

since these covered the frequency range of CH signals observed in the solution state spectrum. Aided by the dashed blue vertical lines, the broad ssNMR peaks at 127 ppm and 118 ppm are shown to correspond to methine ^{13}C sites: C, F, and K (127 ppm), and B, G, and J (118 ppm). Sites B, G, and J correspond to ^{13}C sites adjacent to the ^{13}C bonded to oxygen, sites C and F are ^{13}C sites 2 atoms away from the ether oxygen, and K is the ^{13}C site adjacent to the ^{13}C bonded to the sulfone group.

The frequency regions of 127 ppm and 118 ppm are crowded in solid state by signal overlaps of many different methine sites in aromatic phenylene rings. Signal overlaps impose a limitation for an unambiguous peak assignment for each site in ssNMR spectra. In many cases, however, this limitation can be alleviated in a multi-dimensional correlation spectroscopy or in a technique that doe not require a fully resolved 1D spectrum. For instance, a fully resolved, site-specific NMR spectrum is not necessary for measuring ^{1}H T_1 relaxation time of protons in solid state (*vide infra*). Protons in a bulk polymeric sample system in solid state form a strongly dipolar coupled spin network, in which proton spins communicate with one another via strong ^{1}H-^{1}H dipolar interactions, forming an equilibrium state that is shared among these spins. Therefore, protons involved in a common spin network share a uniform T_1 value, thus, one does not necessarily require fully resolved peaks for ^{1}H T_1 measurements.

5.3.3. ^{1}H T_1, ^{1}H $T_{1\rho}$, and ^{13}C T_2 Relaxation Times

Figure 5.5 summarizes experimental data obtained from ^{1}H T_1 and ^{1}H $T_{1\rho}$ relaxation studies by utilizing the pulse sequences shown in Figure 5.3A and B. Color-coded experimental points (open circles) and linear fittings (solid lines) for P_1 (pink), P_2 (red), P_3 (blue), and P_4 (black), detected by ^{13}C ssNMR signals at 127 ppm (Figure 5.5A and C) or 118 ppm (Figure 5.5A and D) are displayed. For extracting ^{1}H T_1 relaxation times according to the time-frame of the pulse sequence shown in Figure 5.3A, the longitudinal magnetization present after delay time τ, $M_z(\tau)$, is related to the equilibrium ^{1}H magnetization, M_0:

$$\ln(M_0 - M_z(\tau)) = \ln 2 - \tau / T_1 \tag{5.6}$$

where M_0 is normalized to be 1 and ln designates a natural logarithm. Eq. 5.6 was plotted

(Figure 5.5A and B) to extract T_1values from the slopes of the lines (Table 5.2).

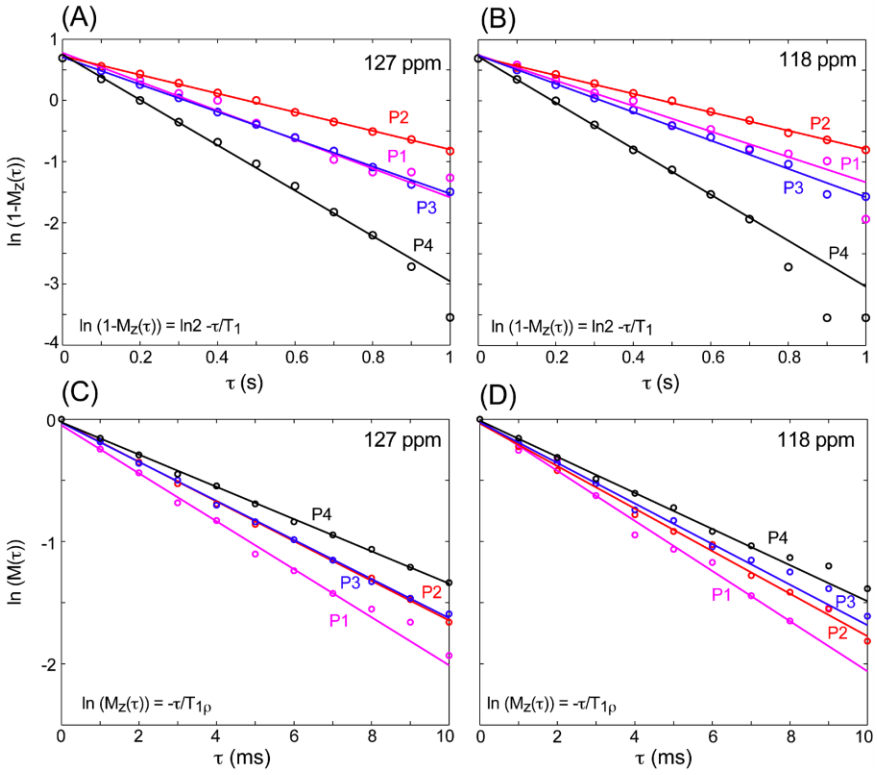

Figure 5.5. Least-squares best-fit plots for ^{1}H T_1 (A,B) and ^{1}H $T_{1\rho}$ (C, D) relaxation time measurements on the four polymer samples. Analysis was performed for ^{13}C ssNMR signals at 127 ppm (A, C) and 118 ppm (B,D). The experimental data shown as open circles and the best-fit results shown as solid lines are overlaid; these are color coded to represent P_1 (pink), P_2 (red), P_3 (blue) and P_4 (black). Error in T_1 is ~ ± .01 s and error in $T_{1\rho}$ is ~ ± .3 ms. Work was performed by the Wi Group at Virginia Tech.

As shown in Table 5.2, ^{1}H T_1s found from analysis of the peaks at 127 ppm and 118 ppm were similar for a given polymer because protons in a dipolar coupled network form a common equilibrium state due to cross-relaxations.

Using the 127 ppm signal, P_4 had the shortest ^{1}H T_1 (0.27 s), P_1 and P_3 were similar (0.42-0.48 s), and P_2 had the longest (0.66 s). The observed ^{1}H T_1 times demonstrated a rough correlation to the T_g of polymers in that they both decreased in the order P_2, P_3, P_4. A shorter T_1 value corresponds to a shorter τ_c of atomic or segmental vibrations in the solid polymer matrix,[29]

with frequencies that are close to the ^{1}H Larmor frequency.

Table 5.2. ^{1}H T_1 and ^{13}C T_2 Relaxation Times[a]

Polymer	^{1}H T_1 (127 ppm)	^{1}H T_1 (118 ppm)	^{13}C T_2 (127 ppm)	^{13}C T_2 (118 ppm)
P_1	0.42 ± .02 s	0.48 ± .02 s	7.2 ± .5 ms	5.0 ± .5 ms
P_2	0.66 ± .01 s	0.66 ± .01 s	8.0 ± .5 ms	5.7 ± .5 ms
P_3	0.45 ± .01 s	0.43 ± .01 s	6.6 ± .3 ms	5.1 ± .2 ms
P_4	0.27 ± .01 s	0.27 ± .01 s	7.9 ± .2 ms	5.3 ± .1 ms

a. ^{1}H T_1 relaxation times are detected indirectly via ^{13}C peaks at 127 ppm and 118 ppm. Work was performed by the Wi Group at VirginiaTech.

Thus, it can be understood that as we incorporate more flexible aliphatic copolymer blocks, the conformational freedom of the copolymer as a whole would improve. The resultant polymer matrix would then become more flexible with a lower T_g, resulting in faster segmental motions that lead to shorter T_1 times. The lowest T_g and shortest ^{1}H T_1 are observed from the copolymer structure P_4, which would possess the highest conformational flexibility in its segmented block. The observed ^{1}H T_1 times also show a correlation to the polydispersity of copolymers in that the trend in the magnitude of ^{1}H T_1 time is also the trend in the magnitude of polydispersity (M_w/M_n) values; $P_2 > P_1 \geq P_3 > P_4$ (Table 5.1 and 5.2). Polydispersity indicates the distribution in polymer chain sizes, with a higher polydispersity indicating that more higher molecular weight chains are present. It makes sense that polydispersity and T_1 trends would follow each other then, since a bigger chain would have a longer motional correlation time. Thus, the rate of vibrational motions seem to be a factor of the polymer formation characteristics, which shows a relationship to the aliphatic character of the segmented block.

While not proven, the trend may also be related to polymer packing. If only a dependence on aliphatic character of the segmented block is considered, an curious observation would be the longer T_1 time observed from P_2 than from P_1, even though P_1 contains purely aromatic segmented blocks. First, this point can be reconciled by noticing that the polydispersity of P_2 is actually higher than that of P_1 (Table 5.1). Additonally, by considering the conformational/configurational structures of the segmented parts in P_1 and P_2 as shown in Figure 5.6, a packing difference is also possible. P_1 contains an aromatic 1,4-phenylene dicarboxylate ring while P_2 contains aliphatic trans-1,4-cyclohexane dicarboxylate in the segmented block.

While the segmented block of P_1 could take cis or trans configurational structures, the trans-1,4-cyclohexane dicarboxylate segment in P_2 would only take the energetically favorable chair form with dicarboxylic substituents in equatorial positions at room temperature. Therefore, the polymer matrix of P_1 would be more disordered in its packing state than P_2. Protons in a more disordered packing state would possess a softer polymer matrix due to the decrease in the sample density, leading to a shorter correlation time.

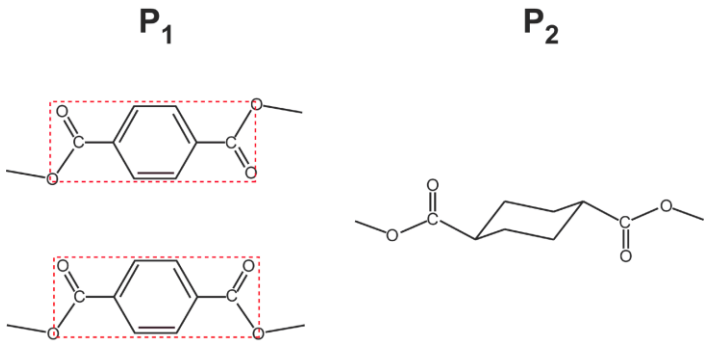

Figure 5.6. Configurational structures of P_1 and P_2 in the segmented block. While the phenylene dicaboxylate group in copolymer P_1 possesses equally probable, two configurational structures, the trans-1,4-cyclohexane dicarboxylate groups in copolymer P_2 possesses take predominantly the more stable equatorial positions.

It is also interesting that P_1 and P_3 take almost an identical T_1 value although P_3 takes additionally trans-1,4-cyclohexane dimethanol and trans-1,4-cyclohexane dicarboxylate in the segmented block. P_1 has a higher polydispersity than P_3, so it might be expected that it would have a longer T_1. Further investigation is needed to understand this trend.

^{1}H T_1 relaxation measurements can be used to characterize the miscibility and domain sizes of segmented block copolymers, within nanoscopic-to-mesoscopic dimensions, because it is mediated by multistep ^{1}H-^{1}H spin-diffusions, allowing communication between two protons separated by even several tens of nanometers in space. Therefore, an alternative interpretation of our ^{1}H T_1 data is to correlate the measured T_1 values to the domain sizes and miscibility of segmented blocks in the copolymer matrix. An aliphatic copolymer segment may provide kinks in the polymeric chain, due to its flexible nature, that can penetrate into the domains formed by aromatic segments in the copolymer structure, reducing the size of domains. It may also improve

the miscibility between domains made from aromatic and aliphatic segments.

Introduction of an aliphatic block into the segmented structure also influenced the $T_{1\rho}$ relaxation time measured at the common copolymer block, albeit the observed trend is somewhat different from that of T_1. Because $T_1\rho$ is a factor of the spin-lock pulse power, it responds to the segmental motions that move in the tens of kHz regime, making it sensitive over molecular events within a few nanometers scale—a more localized probe than ^{1}H T_1. Figure 5.5C and D show the plots and least-square fits of ^{1}H $T_1\rho$ data measured via ^{13}C sites at 127 ppm and 118 ppm, respectively. The $T_1\rho$ relaxation parameter can be found from a linear equation

$$\ln(M_{xy}(\tau)) = \ln(M_{xy}(0)) - \frac{\tau}{T_1\rho} \tag{5.7}$$

where $M_{xy}(0)$ is the size of the spin-locked transverse magnetization at the initial point (i.e. immediately after the CP; normalized to 1) and $M_{xy}(\tau)$ is the transverse magnetization present after a spin-lock period, τ. Eq. 5.7 was employed for obtaining $T_1\rho$s from the line slopes of the least-square fits. The range of ^{1}H $T_{1\rho}$s for P_1-P_4 is 4.9-7.2 ms as listed in Table 5.3.

Table 5.3. ^{1}H $T_{1\rho}$ Relaxation Times[a]

Polymer	$\delta(^1H\text{-}^1H)$[b]	127 ppm		118 ppm	
		$T_{1\rho}$ (ms)	τ_c (ms)	$T_{1\rho}$ (ms)	τ_c (ms)
P_1	20 kHz	5.1 ± 0.2	0.19	4.9 ± 0.4	0.18
P_2	16 kHz	6.2 ± 0.1	0.15	5.8 ± 0.1	0.14
P_3	18 kHz	6.3 ± 0.1	0.19	6.0 ± 0.2	0.18
P_4	18 kHz	7.2 ± 0.1	0.22	6.8 ± 0.2	0.21

[a] ^{1}H $T_{1\rho}$ values are detected indirectly via ^{13}C peaks at 127 ppm and 118 ppm. Work was performed by the Wi Group at Virginia Tech.
[b] Effective ^{1}H-^{1}H dipolar coupling strength measured by ^{1}H 2D WISE experiments. Error is ± 1 kHz.

The ^{1}H $T_1\rho$ relaxation time is governed by ^{1}H-^{1}H homonuclear dipolar coupling because the contribution of proton's small chemical shift anisotropy (CSA) can be neglected. The contribution of ^{1}H-^{13}C dipolar interactions is also negligible because of the low natural abundance of ^{13}C (~1%). If an on-resonance spin-lock pulse irradiation is assumed, the motional

correlation time (τ_c) can be extracted from a measured $T_1\rho$ relaxation parameter according to the following equation:[40-42]

$$\frac{1}{T_1\rho} = \frac{1}{2}\langle \delta_{HH} \rangle^2 \left[\frac{3\tau_c}{1+4\omega_1^2\tau_c^2} + \frac{5\tau_c}{1+\omega_H^2\tau_c^2} + \frac{2\tau_c}{1+4\omega_H^2\tau_c^2} \right]. \quad (5.8)$$

Here, $\langle \delta_{HH} \rangle$ is an effective ^{1}H-^{1}H dipolar coupling strength experienced by the protons at the measurement site, and ω_1 and ω_H are the radiofrequency field strength of the spin-lock pulse (63 kHz) and the Larmor frequency of ^{1}H (301 MHz), respectively.

The effective ^{1}H-^{1}H dipolar coupling strength will reflect the size of ^{1}H-^{1}H homonuclear dipolar network that may reflect the flexibility and packing order of molecular segments as well as the average domain size of aromatic PAES blocks. Figure 5.6 shows 1D ^{1}H MAS spectra extracted from 2D wideline separation (WISE) NMR spectra[43] measured indirectly along ^{13}C at 127 ppm of P_1 (A), P_2 (B), P_3 (C), and P_4 (D) that had been utilized to measure $\langle \delta_{HH} \rangle$. An observation of characteristic broad spinning sidebands in a 2D PASS spectrum evidences ring flip motions of aromatic phenylene rings.[43] Ring-flip motions of aromatic pheneylene rings would provide motionally averaged, weakened intermolecular dipolar interactions. Dipolar interactions formed along the flip axes are however unchanged, resulting in relatively isolated proton pairs. The presence of these relatively isolated proton spin pairs provides a spectrum with spinning sidebands.

Spectral simulations employing a home-built program, which calculates the relative MAS sideband intensities of an effective ^{1}H-^{1}H dipolar coupling interaction, had yielded the $\langle \delta_{HH} \rangle$s of the methine sites at 127 ppm as 20 kHz (P_1), 16 kHz (P_2), 18 kHz (P_3), 18 kHz (P_4), respectively. Nearby aromatic methine protons in each polymer would have a similar range of ^{1}H-^{1}H dipolar coupling strength. As these data indicate, an introduction of aliphatic, segmented copolymer block slightly reduces the magnitude of $\langle \delta_{HH} \rangle$, indicating that the presence of aliphatic segments in the polymer matrix results in a less strongly coupled protons at the aromatic methine sites due to the increased chain motions or due to the decreased molecular packing order. It is noticeable that P_2 sample produces the smallest $\langle \delta_{HH} \rangle$, while P_3 and P_4 samples result in the same amount of $\langle \delta_{HH} \rangle$. Given $T_1\rho$ and $\langle \delta_{HH} \rangle$ data, we utilized the Newton-Raphson algorithm[44] to find the

solution of Eq.5.8 to find τ_c. The motional correlation times (τ_cs) thus obtained from the measured $T_1\rho$ and $\langle \delta_{HH} \rangle$ are 0.14-0.21 ms for 118 ppm and 0.15-0.22 ms for 127 ppm, respectively, as summarized in Table 5.3.

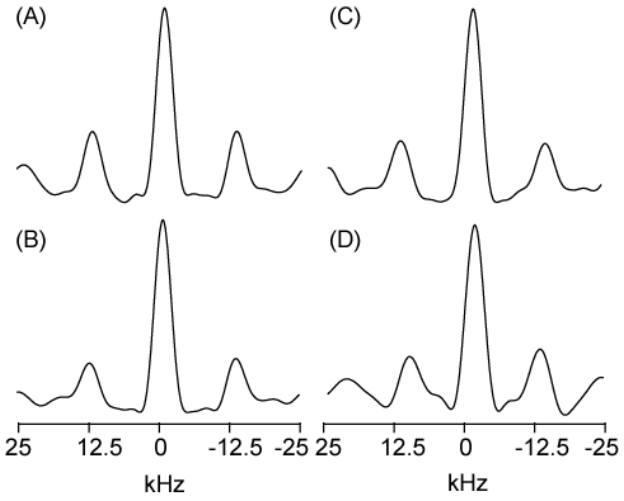

Figure 5.7. ^{1}H WISE spectra of P_1 (A), P_2 (B), P_3 (C), and P_4 (D) measured indirectly via the ^{13}C peak at 127 ppm. Simulation of each spectrum utilizing a single ^{1}H-^{1}H dipolar pair provided an effective dipolar coupling strength as 20 kHz (P_1), 16 KHz (P_2), 18 kHz (P_3), and 18 kHz (P_4), respectively. Error is ± 1 kHz. Work was performed by the Wi Group at Virginia Tech.

As can be noticed from Table 5.3, ^{1}H $T_1\rho$ increased, for both 127 ppm and 118 ppm, in the order: P_1, $P_2 \approx P_3$, P_4. This trend is roughly opposite that of ^{1}H T_1, but the trend in correlation times is exactly opposite the trend of ^{1}H T_1. This evidences that the time scale of segmental motions in PAES in a few tens kHz regime becomes slower as the portion of the aliphatic structures in the segmented block increases. Motion is slower because a bigger aliphatic hydrocarbon segment possesses a greater barrier for a segmental rotation in the polymer matrix.

Finally, ^{13}C T_2s have been measured by employing a standard spin-echo sequence to record echo signals at 127 ppm and 118 ppm. A least-squares data analysis employing the same equation form as Eq. 5.2, replacing $T_1\rho$ and ^{1}H transverse magnetization under spin-lock into T_2 and ^{13}C transverse magnetization, respectively, provided ^{13}C T_2s as summarized in Table 5.2. The trend observed in ^{13}C T_2 times measured at 127 ppm and 118 ppm is similar to that of $T_1\rho$.

Overall, P_1 and P_3 had the shorter ^{13}C T_2 times, and P_2 and P_4 the longer. Unlike ^1H T_1 and ^1H $T_1\rho$ data that are mainly governed by ^1H-^1H homonuclear dipolar interactions, ^{13}C T_2 data measured on a natural abundance ^{13}C sample would be governed by ^{13}C's chemical shift, a local property of a site of interest. T_2 relaxation is modulated by a process with τ_c around 10^{-3} - 10^{-6} s. Thus, a longer T_2 time indicates an increased mobility with a few kilohertz frequency, and the results seem to indicate that the 127 ppm and 118 ppm regions for a given polymer are different in this respect, in contrast to the ^1H T_1 and $T_1\rho$ values. Differences between ^{13}C T_2 and ^1H $T_1\rho$ shows that even though they are sensitive to similar motional frequencies, there is value in exploring both parameters.

5.3.4. CSA Measurement

CSAs of aromatic phenylene ^{13}C sites in PAES block were analyzed site-specifically to investigate the influence of the segmented aliphatic blocks. Figure 5.8A shows the 2D PASS spectrum of P_2 acquired employing a timetable that consists of 16 t_1 slices, with $\boldsymbol{\nu_r}$ = 1.5 kHz; this rate provides spinning sidebands because it is too slow to average the orientation dependence of the CSA tensor. A central band and spinning sidebands originating from an identical ^{13}C site are separated by order along the indirect frequency domain in such a way that the frequency position of a band is shifted by TD x ν_r/SW from the band that is located a step below it, where TD and SW are the number of spectral data points and the spectral width, respectively. The central band and sidebands from an identical site must be aligned at the same frequency position to extract a 1D projection of a MAS sideband spectrum. For this purpose, a shearing transformation was applied to the 2D PASS spectrum (e.g., Figure 5.8A) by shifting each row by -k(TD x ν_r/SW), where k = 1, 2, …, 16 are the sideband orders.

An experimental 1D MAS sideband pattern extracted from the sheared 2D PASS spectrum and a simulated 1D MAS spectrum obtained from a trial tensor parameter set were normalized in such a way that the intensity of the biggest line is set to 1 and the intensities of other lines are adjusted according to the relative ratios with respect to the biggest line. Numerical simulations were carried out to find the best-fit spectrum and tensor parameters for each data set by employing a home-built program written in Matlab programming language. The root mean

square variance, $\sqrt{\sum(E_i - S_i)^2}$, where E_i and S_i are the line intensity of experimental and simulated 1D MAS spectra of order i, was calculated for each data point on a 2D grid map formed by varying δ and η. Figure 5.8B (P_2) and C (P_4) are the contour maps that show the calculated variances thus obtained, considering the 1D MAS spectrum taken at 127 ppm of each 2D PASS data set.

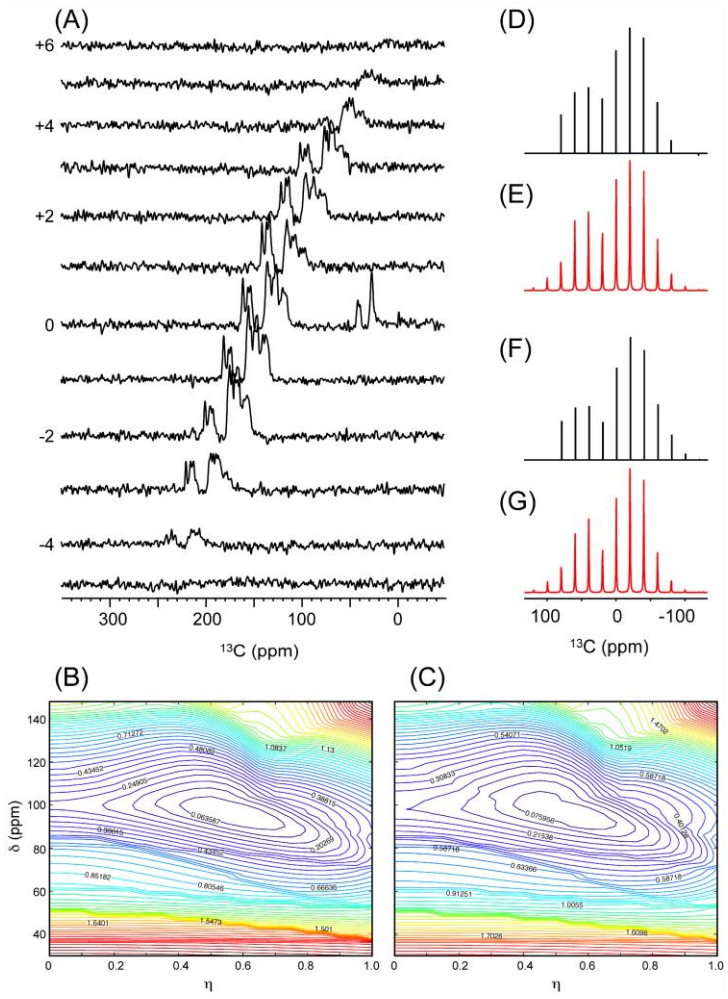

Figure 5.8. 2D ^{13}C PASS experiments on P_2 and P_4. The ω_1 slices from P_2 spectra are sorted according to the order of the sidebands (A) (ν_r = 1500 Hz). RMS statistic as a function of the CSA parameters η and δ of P_2 (B) and P_4 (C) measured on the ^{13}C peak at 127 ppm. Experimental (D, F) and simulated (E, G) CSA spinning sideband bars obtained for P_2 (D, E) and P_4 (F, G) are shown. Work was performed by the Wi Group at Virginia Tech.

Regions of the minimum variance are visible in both contour maps. The position of the minimum variance corresponds to the δ and η parameters that provide the best-fit simulation. Figure 5.8D and F are the experimental 1D MAS sideband spectra of P_2 and P_4, respectively, that are taken at 127 ppm. Figure 5.8E and G are the corresponding best-fit simulations of P_2 and P_4, employing CSA tensor parameters found from Figure 5.8B and C (δ = 94 ± 5 ppm; η = 0.6 ± 0.1). Table 5.4 summarizes CSA values of the P_1-P_4 samples obtained from ^{13}C sites at 136 and 127 ppm. CSA values measured at the common, aromatic carbon sites are largely invariant to the modification of the segmented blocks in the copolymer structures. This invariance implies that the CSA interaction of aromatic carbon sites, a relatively isolated local interaction, is determined by the molecular environment of aromatic PAES segments that may form local structural domains that are isolated from the aliphatic segments on the nanoscopic scale.

Table 5.4. CSA Parameters of ^{13}C Sites at 127 ppm and 136 ppm[a]

Peak position	P_1		P_2		P_3		P_4	
	δ[b]	η[c]	δ	η	δ	η	δ	η
136 ppm	88	0.7	88	0.6	90	0.6	92	0.5
127 ppm	92	0.5	94	0.6	88	0.6	94	0.6

a. Work was performed by the Wi Group at Virginia Tech.
b. The CSA, δ, is defined by $\delta_{33} - \delta_{iso}$, where $\delta_{iso} = (\delta_{11}+\delta_{22}+\delta_{33})/3$. δ_{ii} (i = 1, 2, or 3) is a tensor element defined in the principal axes frame (PAS). The error bound of CSA is ± 5 ppm.
c. The asymmetry parameter η is $(\delta_{11}-\delta_{22})/\delta$. The error bound of η is ± 0.1.

5.3.5. Slow Segmental Reorientation Dynamics of Polymers

Figure 5.9 shows ^{13}C CODEX NMR data and the corresponding best-fit simulation results measured on P_2 (A, B) and P_4 (C, D) samples detected at 136 and 127 ppm to monitor the slow reorientational dynamics of polymer chains. Figure 5.9A and C show the pure exchange CODEX spectra ($\Delta S = S_0$-S) recorded by increasing the exchange mixing time t_m under a fixed CSA recoupling time, t_{CSA}, to 0.32 ms. The CODEX exchange signal intensities were normalized by calculating $(S_0\text{-}S)/S_0$, where S_0 is the signal intensity recorded by switching t_m and t_z in the CODEX sequence to compensate signal loss due to ^{13}C-^{13}C spin diffusion as well as T_1 and T_2

relaxations. As the mixing time t_m increases, the spectral intensity of ΔS increases as expected.

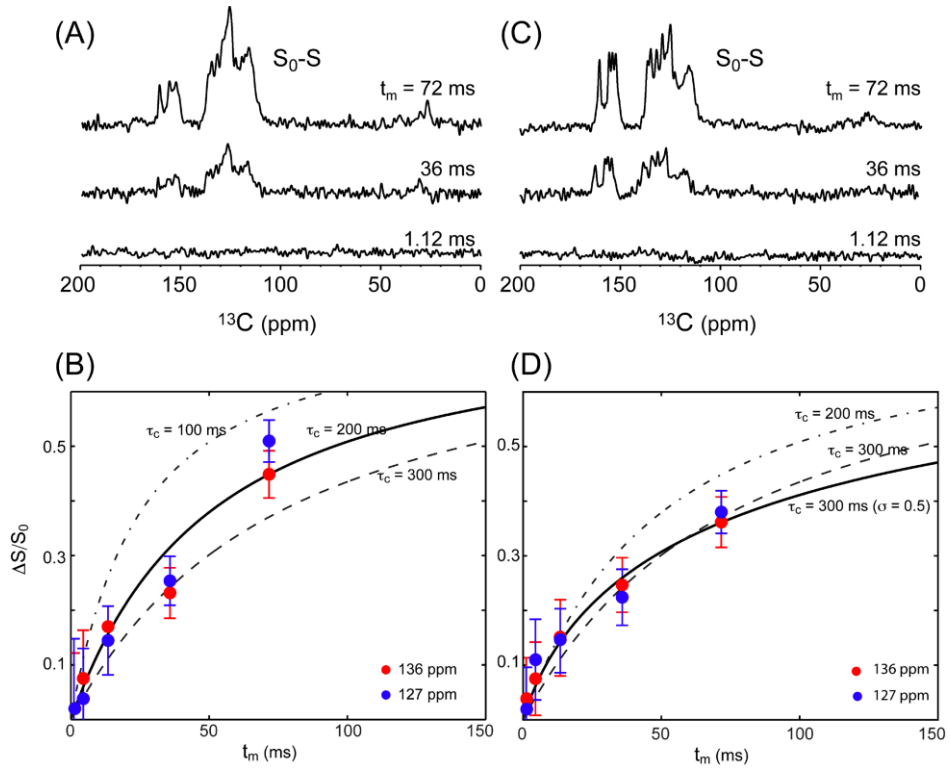

Figure 5.9. CODEX results of P_2 and P_4. Pure exchange CODEX spectra of P_2 (A) and P_4 (C) recorded by varying t_m with t_{CSA} = 0.32 ms and t_z = 1.12 ms. The normalized t_m-dependent CODEX dephasing intensities (B: P_2 and D: P_4) measured on ^{13}C peaks at 136 ppm (red circles) and 127 ppm (blue circles). Error bars are obtained by calculating the signal-to-noise ratio of both signal and reference spectra. The MAS spinning speed incorporated was 6250 Hz. Aromatic methine groups in the P_2 and P_4 samples with different aliphatic, segmented copolymer blocks demonstrate different motional correlation times in CODEX experiments. The P_4 sample, with a longer aliphatic copolymer block resulted in multiple, slower motional correlation times with a distribution. Work was performed by the Wi Group at Virginia Tech.

Red and blue filled circles with error bars were used to designate the peak intensity profiles recorded at 136 ppm and 127 ppm, respectively. Within experimental errors, different measurements at the 136 and 127 ppm positions have demonstrated an identical trend for the chain segmental motions. The best-fit CODEX simulation data obtained employing an isotropic

rotational diffusion model have provided a correlation time within a range of 0.2-0.3 s, by employing a single correlation time (B; P_2) or multiple correlation times with a log-Gaussian distribution (D; P_4). CSA tensor parameters measured by 2D PASS experiments as shown in Table 5.4 were used as the input parameters of CSA tensors required in our CODEX simulations. Data shown in Figure 5.9B provided a single correlation time, t_m = 200 ms, while data shown Figure 5.9D provided multiple correlation times with a log-Gaussian distribution ($\langle t_m \rangle$ = 300 ms; σ = 0.5). The average correlation time, $\langle t_m \rangle$, extracted from P_4 sample is longer than the t_m value from P_2 sample. Moreover, an assumption of a log-Gaussian distribution in the correlation time was required for analyzing the P_4 data, while a single correlation time was enough for the data analysis of P_2. This implies that an incorporation of a longer aliphatic, segmented copolymer block may result in slower rotational reorientations of polymer chains due to the increased rotational barriers. An increased conformational flexibility in P_4 chain may also lead to multiple reorientational modes with a distribution in the correlation time.

5.4. Conclusions

The dynamics of four PAES segmented copolymer analogues were investigated in the time scales covering from nanoseconds to seconds through a suit of MAS ssNMR methods. By measuring ^{1}H T_1 and ^{1}H $T_1\rho$, it was possible to obtain motional information of the common PAES block, within a few tenths or hundreds of nanoseconds or microseconds regimes. Generally, as a conformationally or configurationally more flexible copolymer segment is incorporated into the copolymer sequence, the resultant polymer matrix becomes softer with lower glass transition and melting temperatures as well as shorter T_1 time, as the atomic or segmental vibrations in a softer polymer matrix become faster. The observed magnitude in the ^{1}H T_1 relaxation times ($P_2 > P_1 > P_3 > P_4$) follows exactly the trend observed in the polydispersity (M_w/M_n) of each sample (Table 5.1 and 5.2), which is related to the distribution of polymer chain sizes. As a softer aliphatic segment is incorporated into the copolymer structure, chain motions involving bigger segments within a time scale within 10^{-3}-10^{-6}s range detected by ^{1}H T_1 relaxation become slower because a longer aliphatic segment may accompany higher barriers for segmental rotations in the polymer matrix.

CODEX experiments carried out on methine sites of aromatic pheneylene rings indicated that slow segmental reorientations occur within 100-300 ms range. When an isotropic rotational diffusion model was incorporated with a log-Gaussian distribution of correlation times, an increased conformational flexibility in the segmented block leads to a longer average correlation time with a larger distribution. This is because rotational reorientations of bigger aliphatic segments with increased rotational barriers would accompany multiple motional modes with different correlation times due to the increased conformational flexibility.

Aromatic ring-flip motions exhibited by the PAES portion of the polymer were evidenced through the DIPSHIFT (not shown) and 2D WISE experiments. Through DIPSHIFT, it was found that the ring-flip motions detected by the apparent ^{1}H-^{13}C local dipolar interactions of aromatic methine sites had produced essentially the same result for all polymer samples. The effective ^{1}H-^{13}C dipolar coupling strength (14.5 kHz) and the correlation time ($< 10^{-7}$ s) and amplitude (60º) of ring-flip motions involved in aromatic pheneylene rings were invariant to the changes provided in the aliphatic segmented block. The similar result for all samples may imply that the free volume element around the aromatic PAES block is invariant to the modification of aliphatic segments in the copolymer sequence. The observed invariance in the ^{13}C CSAs measured on methine carbon sites on aromatic PAES blocks also confirms domain separations made of aromatic blocks and aliphatic blocks. Combined, these studies provided insight on how the different segmented blocks affect the physical characteristics of the polymer chains, which can provide valuable directions for future polymer design and synthetic efforts.

References

(1) Hale, W. F.; Farnham, A. G.; Johnson, R. N.; Clendinning, R. A. *J. Polym. Sci. A1* **1967**, *5*, 2399.

(2) Johnson, R. N.; Farnham, A. G.; Clendinning, R. A.; Hale, W. F.; Merriam, C. N. *J. Polym. Sci. A1* **1967**, *5*, 2375.

(3) Rose, J. B. *Polymer* **1974**, *15*, 456.

(4) Robeson, L. M.; Farnham, A. G.; McGrath, J. E. *Applied Poly. Symp.* **1975**, *1975*, 373.

(5) Turner, S. R. *J. Polym. Sci. A1* **2004**, *42*, 5847.

(6) Corrado, B.; Annamaria, C.; Paola, M.; Elisabetta, M.; Giancarlo, B.; Francesco Di, C. *Macromol. Chem. Physic.* **2008**, *209*, 1333.

(7) Charles, J. K.; Alan, B.; James, G. S. *J. Polym. Sci. Part A* **1964**, *2*, 2115.

(8) Scheirs, J.; Long, T. E. *Modern Polyesters: Chemistry and Technology of Polyesters and Copolyesters*; John wiley & Sons, Inc: New York, 2003.

(9) Schmidt-Rohr, K.; Spiess, H. W. *Multidimensional Solid-State NMR and Polymers*; Academic Press: San Diego, 1994.

(10) Kishore, A. I.; Herberstein, M. E.; Craig, C. L.; Separovic, F. *Biopolymers* **2002**, *61*, 287.

(11) Wang, J.; Cheung, M. K.; Mi, Y. *Polymer* **2002**, *43*, 1357.

(12) Masson, J. F.; Manley, R. S. J. *Macromolecules* **1992**, *25*, 589.

(13) Zhang, X.; Takegoshi, K.; Hikichi, K. *Macromolecules* **1992**, *25*, 2336.

(14) Simmons, A.; Natansohn, A. *Macromolecules* **1991**, *24*, 3651.

(15) Huijgen, T. P.; Gaur, H. A.; Weeding, T. L.; Jenneskens, L. W.; Schuurs, H. E. C.; Huysmans, W. G. B.; Veeman, W. S. *Macromolecules* **1990**, *23*, 3063.

(16) Chen, Q.; Kurosu, H. *Ann. R. NMR S.* **2007**, *61*, 247-282.

(17) Schaefer, J.; Stejskal, E. O.; McKay, R. A.; Dixon, W. T. *Macromolecules* **1984**, *17*, 1479.

(18) Munowitz, M. G.; Griffin, R. G.; Bodenhausen, G.; Huang, T. H. *J. Am. Chem. Soc.* **1981**, *103*, 2529.

(19) Kolbert, A. C.; de Groot, H. J. M.; Levitt, M. H.; Munowitz, M. G.; Roberts, J. E.; Harbison, G. S.; Herzfeld, J.; Griffin, R. G. *Multinuclear Magnetic Resonance in Liquids and Solids--Chemical Applications*; Kluwer Academic Publishers: Dordrecht, 1990.

(20) deAzevedo, E. R.; Hu, W.-G.; Bonagamba, T. J.; Schmidt-Rohr, K. *J. Am. Chem. Soc.* **1999**, *121*, 8411.

(21) deAzevedo, E. R.; Hu, W.-G.; Tito J. Bonagamba, T. J.; Schmidt-Rohr, K. *J. Chem. Phys.* **2000**, *112*, 8988.

(22) deAzevedo, E. R.; Saalwachter, K.; Pascui, O.; de Souza, A. A.; Bonagamba, T. J.; Reichert, D. *J. Chem. Phys.* **2008**, *128*, 104505.

(23) Zhang, B.; Turner, R. S. *J. Polym. Sci. A1* **2011**, *submitted*.

(24) Pines, A.; Gibby, M. G.; Waugh, J. S. *J. Chem. Phys.* **1973**, *59*, 569.

(25) Stejskal, E. O.; Schaefer, J.; Waugh, J. S. *J. Magn. Reson.* **1977**, *28*, 105.

(26) Dixon, W. T. *J. Chem. Phys.* **1982**, *77*, 1800.
(27) Fung, B. M.; Khitrin, A. K.; Ermolaev, K. *J. Magn. Reson.* **2000**, *142*, 97.
(28) Harris, R. K. *Nuclear Magnetic Resonance Spectroscopy*; Pitman, 1983.
(29) Kimmich, R. *NMR Tomography, Diffusometry, Relaxometry*.; Springer: Berlin, 1997.
(30) Antzutkin, O. N.; Shekar, S. C.; Levitt, M. H. *J. Magn. Reson. A* **1995**, *115*, 7.
(31) Antzutkin, O. N.; Lee, Y. K.; Levitt, M. H. **1998**, *135*, 144.
(32) Jameson, C. *J. Solid State NMR* **1998**, *11*, 265.
(33) Munowitz, M.; Aue, W. P.; Griffin, R. G. *J. Chem. Phys.* **1982**, *77*, 1686.
(34) Munowitz, M. G.; Griffin, R. G.; Bodenhausen, G.; Huang, T. H. *J. Am. Chem. Soc.* **1981**, *103*, 2529.
(35) Hong, M.; Gross, J. D.; Rienstra, C. M.; Griffin, R. G.; Kumashiro, K. K.; Schmidt-Rohr, K. *J. Magn. Reson.* **1997**, *129*, 85.
(36) Bielecki, A.; C., K. A.; Levitt, M. H. *Chem. Phys. Lett.* **1989**, *155*, 341-346.
(37) O'Connor, R. D.; Ginsburg, E. J.; Blum, F. D. *J. Chem. Phys.* **2000**, *112*, 7247.
(38) deAzevedo, E. R.; Reichert, D.; Vidoto, E. L. G.; Dahmouche, K.; Judeinstein, P.; Bonagamba, T. J. *Chem. Mater.* **2003**, *15*, 2070.
(39) Wachowicz, M.; White, J. L. *Macromolecules* **2007**, *40*, 5433.
(40) Mehring, M. *High Resolution NMR in Solids*; Springer-Verlag: Berlin, 1983.
(41) Kimmich, R. *NMR Tomography Diffusometry Relaxometry*; Springer-Verlag: Berlin, 1997.
(42) Huster, D.; Xiao, L.; Hong, M. *Biochemistry* **2001**, *40*, 7662.
(43) Schmidt-Rohr, K.; Clauss, J.; Spiess, H. W. *Macromolecules* **1992**, *25*, 3273.
(44) Press, W. H.; Teukolsky, S. A.; Vetterling, W. T.; Flannery, B. P. *Numerical Recipes in C: The Art of Scientific Computing (2nd)*; Cambridge University Press: Cambridge, 1992.

Chapter 6

Evidence of Pores and Thinned Lipid Bilayers Induced In Oriented Lipid Membranes Interacting with the Antimicrobial Peptides, Magainin-2 and Aurein-3.3

6.1. Introduction

Membrane-acting antimicrobial peptides (AMPs), which are produced by many tissues and cell types in a variety of invertebrate, plant, and animal species, destroy the cell membranes of invaded microorganisms, such as bacteria, fungi, protozoa, and enveloped viruses, as well as malignant cells and parasites.[1-10] Because D- and L-amino acid versions of antimicrobial peptides generally show little selectivity in binding, the antimicrobial action of AMPs appears to involve direct attacks on the cell membrane rather than accompanying any of the protein-based receptors and transporters on the cell surface of microbes, resulting in depolarization, permeabilization, and lysis;[11-14] though some receptor-mediated AMP binding effects were also reported.[15,16] AMPs, which consist of 5–50 amino acid residues, can be categorized into five major classes: α-helical, defensin-like (cystein-rich), β-sheet, peptides with an unusual composition of regular amino acids, and bacterial and fungal peptides containing modified amino acids.[17] Despite their diverse types of membrane-induced secondary structures, all AMPs display an amphiphilic structure, with one surface highly positive (hence, hydrophilic) and the other hydrophobic.

For AMPs forming membrane-acting secondary structures upon binding to lipid membranes, two commonly reported modes are the "*S*-state", in which the peptide is bound approximately parallel to the membrane surface, and the "*I*-state", in which the peptide is inserted in the membrane approximately parallel to the membrane normal.[18-21] A surface-bound *S*-state[22] would be favorable when the peptide concentration is low because cationic AMPs can bind electrostatically to the anioinic headgroups of lipid bilayers. If the peptide concentration reaches a threshold value, a few closely placed AMP molecules may insert into bilayers after forming an intermolecular peptide bundle, leading to a transition from a *S*-state to an *I*-state.

Molecules and ions can transport across the cell membranes through this pore, resulting in the lysis of a cell due to the destruction of an osmotic pressure gradient existing across the cell membranes. A transition from a *S*-state to an *I*-state has a sigmoidal peptide concentration dependence, suggesting cooperativeness in the peptide–membrane interactions.[23-26] In addition to these is the "*T*-state", in which the peptide inserts into the membrane with the helix axis approximately 120° to the membrane normal. The "*T*-state" was initially reported for PGLa, [27-30] but has also been seen for MSI-103[29] and MAP[31]. Also reported are the barrel-stave model,[32] peptide-induced inverted hexagonal phases and,[33,34] and detergent-type micelles[35] involving certain lipids and peptides.

This chapter discusses an investigation of the membrane binding properties of a known AMP, magainin-2[18,36], and an unknown AMP, from the aurein family, aurein-3.3[5,9,37-39] Both magainin-2, an α-helical structured 23-residue peptide found on the skin of the African clawed frog *Xenopus laevis*, and aurein-3.3, an unknown structured 17-residue AMP present in the secretion from the granular dorsal glands of the Green and Golden Bell Frog *Litoria aurea*, possess a broad-spectrum of antimicrobial activity against various types of bacteria, virus, and fungi. Moreover, magainin-2 and aurein-3.3 receive our particular attention because they possess potential drug activities against diabetic foot ulcers and cancer cells, respectively.

Reportedly, magainin-2 forms a *S*-state at a low peptide concentration and transitions to an *I*-state after a critical peptide concentration in phospholipids bilayers.[18,26,40-42] In contrast, the behavior of aurein-3.3 is still unknown. We investigated the membrane-disrupting characteristics of magainin-2 and aurein-3.3 in oriented phospholipid bilayers by investigating ^{31}P and ^{2}H ssNMR spectra of lipids. Various compositions of oriented lipid bilayers were studied, including zwitterionic phosphatidylcholine (PC), anionic phosphatidylglycerol (PG), and cholesterol. We have evidenced the existence of peptide-induced supramolecular lipid organizations (i.e. toroidal pores and thinned membrane bilayers) that are under the influence of dynamic lateral diffusions of lipids in cell membrane mimetic media, as exemplified in ^{31}P and ^{2}H ssNMR spectra. A spectral analysis protocol[43] recently developed was applied for simulating the spectral characteristics of such AMP-induced supramolecular lipid assemblies; this provides a means to extract the lateral diffusion coefficients of lipids located on curved membrane surfaces, on a few nanometers scale, which may hitherto have been difficult to characterize.

6.2. Experimental Methods

6.2.1. Materials

All phospholipids were purchased from Avanti Polar Lipids (Alabaster, AL). These include 1-palmitoyl-2-oleoyl-*sn*-glycero-3-phosphotidylcholine (POPC), 1-palmitoyl-d_{31}-2-oleoyl-*sn*-glycero-3-phosphotidylcholine (POPC-d_{31}), and 1-palmitoyl-2-oleoyl-*sn*-glycero-3-phosphotidylglycerol (POPG). Antimicrobial peptides, magainin-2 (GIGKFL HSAK KFG KAFVGEIMNS; HPLC purity: 98.9%; MW: 2466.90) and aurein-3.3 (GLFDI VKK IAG HIVSSI-$CONH_2$; HPLC purity: 98.3%; MW: 1796.20), were purchased from GL Biochem (Shanghai, China) and EZBiolab Inc. (Westfield, IN), respectively, and used without further purification. Trifluoroethanol (TFE), naphthalene, chloroform and sodium phosphate dibasic were purchased from the Aldrich Chemicals (Milwaukee, WI). Thin cover-glass plates ($\sim$ 80 μm in thickness) cut into rectangles of 10 mm × 5 mm in width were obtained from the Marienfeld Laboratory Glassware (Bad Mergentheim, Germany).

6.2.2. Preparation of Oriented Phospholipid Bilayers

A known, standard procedure[44,45] was used to prepare mechanically oriented lipid bilayers between thin cover-glass plates. Peptides and phospholipids dissolved in TFE and chloroform, respectively, were mixed to produce peptide-to-lipid (P:L) molar ratios of 0:100, 1:80, 1:50, and 1:20. The solution was air-dried and redissolved in a chloroform/TFE (2/1) solution containing a 5-fold excess amount of naphthalene. The solution was deposited onto thin cover-glass plates at a surface concentration of 0.01–0.04 mg/mm^2, air-dried, and then vacuum-dried overnight to remove residual organic solvents and naphthalene. The dried sample was directly hydrated with 2 μl of water and placed in a chamber containing a saturated solution of Na_2HPO_4, which provides about 95% relative humidity, for 2 days.[46,47] The full hydration condition of the lipids used in our study was confirmed by Yamaguchi et al. previously by FT-IR measurements: the amount of water was 50 ± 3 wt.%.[48] 10 – 15 glass plates were stacked together, wrapped with parafilm, and sealed in a polyethylene bag to prevent dehydration during ssNMR measurements. For a fully hydrated condition, an additional 2–4 μl of water was applied

to the plates along the sides of the stack before wrapping.[47,49] Extreme care was taken in handling the plates, as inadvertently applying force by pressing or moving the plates could disrupt a perfect bilayer structure. Disruption would be evident in spectra of pure bilayers or bilayers with very low peptide concentration .

6.2.3. Solid-State ^{31}P and ^{2}H NMR Spectroscopy

^{31}P and ^{2}H ssNMR experiments were performed on a Bruker (Karlsruhe, Germany) Avance II 300 MHz spectrometer operating at the resonance frequencies of 300.12 MHz for ^{1}H, 121.49 MHz for ^{31}P, and 46.07 MHz for ^{2}H. A static double-resonance probe, equipping a rectangular, flat coil with inner dimension of 18 × 10 × 5 mm, was used for measuring static ^{31}P and ^{2}H ssNMR spectra of oriented phospholipid bilayers confined between thin cover-glass plates that are interacting with AMPs. The temperature of the sample compartment in the NMR probe was maintained at 20 °C by using the BCU-X temperature control unit. The ^{31}P chemical shift was referenced to 85% H_3PO_4 at 0 ppm. The pulse power calibrations of ^{31}P and ^{2}H channels were carried out by using 85% H_3PO_4 and D_2O solutions, respectively. The 90°-pulse durations of ^{31}P and ^{2}H pulses incorporated in our NMR experiments were both 5 μs. ^{31}P spectra were acquired with a single 90° pulse with a ^{1}H decoupling power of 45 kHz and a recycle delay of 2 s. The ^{2}H spectra were acquired using a quadrupolar echo sequence, 90° (or 45°)–τ_{echo}–90°–detection,[50] with an echo delay time τ_{echo} = 30 μs, while incorporating a short recycle delay of 0.3 s. The spectral widths of ^{31}P and ^{2}H ssNMR spectra were 20 and 100 kHz, respectively. ^{31}P and ^{2}H spectra were typically averaged over 2048 and 12000 scans, respectively. ^{31}P two-dimensional (2D) exchange spectra were obtained by using a conventional three pulse sequence, 90°–t_1–90°–τ_m–90°–detection (t_2) ,[51] with τ_m = 5–200 ms, to examine lateral diffusive motions of lipids in a slow motional regime by correlating orientation-dependent frequencies at two different measurement times, t_1 and t_2, that are separated by a mixing period τ_m.

6.3. Theoretical Considerations

6.3.1. Calculations of Anisotropic ^{31}P and ^{2}H NMR Spectra of Lipids

Anisotropic ^{31}P and ^{2}H ssNMR spectra can readily be used to characterize disordered

structures of lipids in membrane bilayers.[52-55] Anisotropic ssNMR lineshapes of ^{31}P chemical shift anisotropy (CSA) and ^{2}H quadrupolar coupling (QC) interactions would reveal the angular distributions of ^{31}P and ^{2}H sites in lipids, and therefore, the orientation of lipids with respect to an applied magnetic field, B_0. When a two-tailed phospholipid in a bilayer is considered under a sufficiently hydrated condition, a fast uniaxial rotation of the lipid within a few nanoseconds around its chain axis, which is collinear to the direction of the local bilayer normal, forms a motionally averaged, axially symmetric CSA tensor of the ^{31}P nucleus in the lipid .[56] Figure 6.1A explains how a rapid, uniaxial rotation of a phospholipid around its chain axis, which is collinear to the principal axis component δ_{22} of the ^{31}P's CSA, provides motionally averaged CSA tensor elements $\delta_{//}$ (= δ_{22}) and $\delta\perp$ (= (δ_{11} + δ_{33})/2) (Figure6.1B).

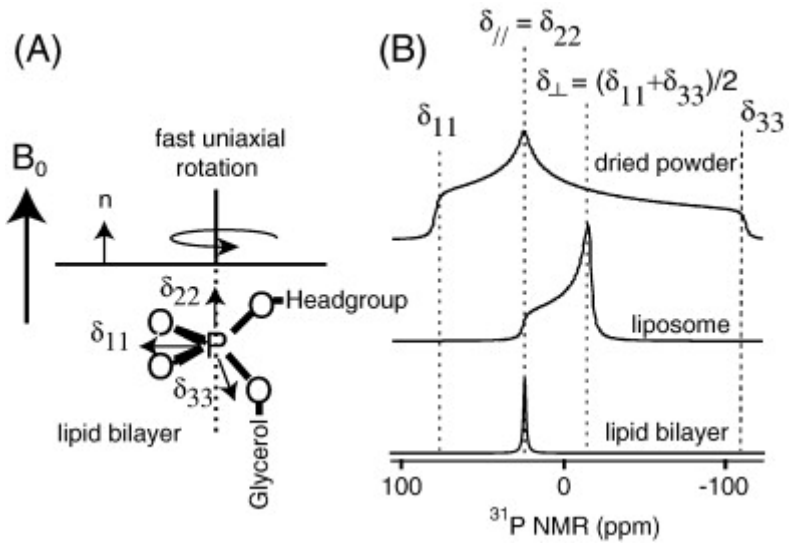

Figure 6.1. Background for ^{31}P NMR of lipids. (A) A fast, uniaxial rotation of a phospholipid in a lipid bilayer around its chain axis, which is collinear to the intrinsic δ_{22} component of the ^{31}P CSA of the phosphate group, makes motionally averaged, uniaxial ^{31}P CSA tensor components: $\delta_{//} = \delta_{22}$; $\delta\perp = (\delta_{11} + \delta_{33})/2$. (B) The ^{31}P CSA powder pattern measured on dried powders (top row) decreases into a motionally averaged, narrower CSA pattern for lipids distributed on a liposome (middle row) due to the fast uniaxial rotations of lipids. When the bilayer normal *n* of a lipid bilayer is collinear to the applied magnetic field, B_0, phospholipids aligned in an oriented lipid bilayer provide a sharp line at the 0° position (the $\delta_{//}$ direction, bottom row).

Thus, lipids involved in, for instance, a liposome provide a narrower ^{31}P NMR CSA powder pattern, specified by motionally averaged tensor elements, $\delta_{//}$ and $\delta_{\perp}$, with the highest signal intensity being present at $\delta_{\perp}$. Lipids in a uniformly aligned bilayer would provide a single sharp peak at the $\delta_{//}$ position because lipids are aligning uniformly along a single direction that is parallel to the membrane normal direction. QC tensor parameters of deuterons located in the hydrophobic acyl chains of a perdeuterated lipid, such as POPC-d_{31}, also follow the same motional averaging mechanism as the CSA tensor parameters in the ^{31}P nucleus of the hydrophilic headgroup, resulting in motionally averaged, axially symmetric QC tensor parameters.

An observed anisotropic frequency of a site in a lipid in either a ^{31}P or ^{2}H ssNMR spectrum depends on the spatial position of the site with respect to B_0. The observed anisotropic NMR frequencies of lipids distributed on a curved membrane surface can therefore be determined by a surface integral over an Euler angle set, $\Omega(0°, \theta, \phi)$, as:[43]

$$\nu_{\lambda}(\Omega) = \int_{\Omega} \nu_{\lambda}(0°, \theta_i, \phi_i)\, p(\Omega) d\Omega \tag{6.1}$$

where $p(\Omega)$, a probability density function that is directly proportional to an infinitesimal surface area at Ω, is called an anisotropic NMR lineshape factor. For lipids distributed on a liposome, the ssNMR lineshape factor, $p(\Omega)$, is $sin\theta$. For lipids possessing a cylindrical or planar distribution, it is 1. The ν_{λ} term is an anisotropic ssNMR frequency measured at the laboratory frame (rotating frame in the usual sense) provided by:

$$\nu_{\lambda} = \frac{1}{h} R^{\lambda}_{2,0} T^{\lambda}_{2,0} \qquad (\lambda = \text{CSA or QC}) \tag{6.2}$$

where h is the Plank constant and $R_{2,0}$ and $T_{2,0}$ are the spatial part and the spin part of NMR tensor parameters, respectively. The spin part tensors, $T_{2,0}$ terms, that commute with the dominant Zeeman Hamiltonian are $\sqrt{\frac{2}{3}} I_z$ for ^{31}P CSA and $\frac{(3I_z^2 - 2)}{\sqrt{6}}$ for ^{2}H QC interactions, respectively. The spatial tensors, $R^{\lambda}_{2,0}$ terms, defined at the laboratory frame can be related to the same tensors defined in the motionally averaged PAS frame by coordinate transformations via a

common reference frame, a frame defined by the glass plate normal direction.[43,47]

6.3.2. Anisotropic ^{31}P and ^{2}H ssNMR Spectral Lineshapes on a Thinned Bilayer

According to the so-called "carpet" model,[22] cationic AMPs would bind preferentially to the headgroups of phospholipids before inserting into membrane bilayers, resulting in thinned membrane bilayers, particularly when peptide concentration is low.[20,57] This surface-bound mode, known as a *S*-state, would produce a curved, thinned dimple in a membrane bilayer. If lipids distributed on a thinned surface of a membrane bilayer make fast lateral diffusions, the anisotropic frequency dispersion in either the ^{31}P or ^{2}H spectrum would produce a motionally averaged sharp line(s) at the center-of-mass position of the anisotropic linewidth, resulting in a decrease in the apparent frequency span in the NMR spectrum.[43]

To simulate the spectral features of a membrane thinning effect, we approximated the thinned portion in a lipid bilayer to a dimple produced by the rotation of a period of the sinusoidal cosine function, which is defined on the *x*–*z* plane, around the *z*-axis by ϕ, as demonstrated in Figure 6.2A. A portion of a peptide-bound thinned bilayer provides a curved membrane surface whose bilayer normal direction deviates from B_0. A fast uniaxial rotation of a lipid along its chain axis makes a lipid align orthogonal to the tangential line drawn on the thinned dimple where a lipid is positioning. A thinned membrane surface thus obtained would therefore result in the increase of anisotropies in ^{31}P and ^{2}H spectra. A NMR lineshape factor governed by this geometry is provided as

$$\frac{a}{\pi}\sec\theta\sin^{-1}[\frac{a}{\pi}\tan\theta] \tag{6.3}$$

where d and a are the depth and the radius of a dimple, respectively, and θ is an angle between the alignment axis of a lipid, which is perpendicular to the tangential line drawn on the curved spot, and the mechanical alignment direction *z*-axis; its range θ varies from 0 to $\tan^{-1}(\pi d/a)$. The relative sizes of a and d are arbitrary, but a reported d on a cell surface due to AMP binding is in the 1–2 Å range.[58] However, on the oriented lipid bilayers interacting with an AMP, MSI-78, well-defined domains of thinned bilayers possessing d up to 1.1 nm have been observed by

AFM.[57] It is convenient to use the relative ratio, *d/a*, for lineshape simulations. Due to a plane of symmetry at $x = 0.5a$, the range of x required for calculating θ is $0 \leq x \leq 0.5a$.

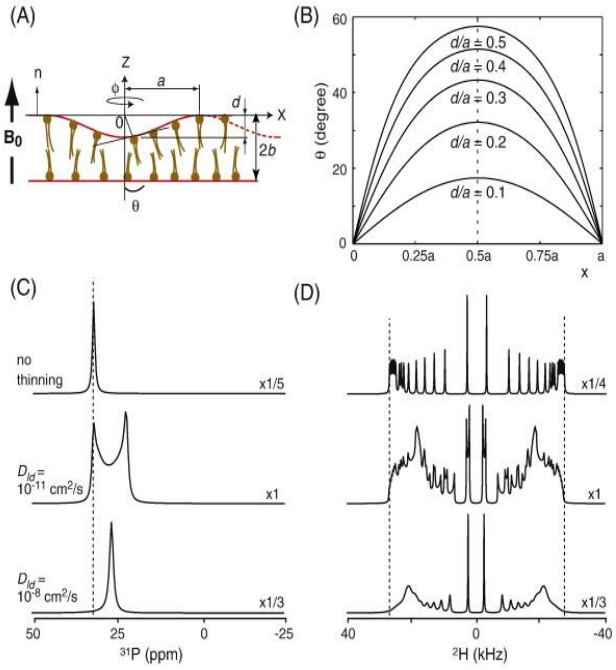

Figure 6.2. Spectral and geometrical details for membrane dimples. (A) Geometrical details of dimples. Depth and the radius are defined by *d* and *a*, respectively. Lipid molecules would align orthogonal to the tangential line drawn on the curved surface of the membrane. The extent of membrane thinning is described by a *d/a* ratio. (B) The θ angle, which specifies the position and anisotropic frequency of a lipid on a thinned surface, varies in the range of 0° to $\tan^{-1}(\pi d/a)$. Ranges of θ values, depending on the *d/a* ratios, are shown. Expected ^{31}P (C) and ^{2}H (D) anisotropic ssNMR spectral lineshapes of POPC-d_{31} lipids distributed on a thinned membrane bilayer, specified by b = 20 Å, a = 24 Å, and d = 4 Å, with $D_{ld} = 10^{-11}$ cm^2/s and 10^{-8} cm^2/s. A fast lateral diffusive rate ($D_{ld} = 10^{-8}$ cm^2/s) of lipids makes a motionally averaged sharp line(s) (bottom row) at the center-of-mass position of an anisotropically broadened lineshape with a slow lateral diffusive rate ($D_{ld} = 10^{-11}$ cm^2/s) for either a ^{31}P or ^{2}H site (middle row), resulting in an apparently narrower anisotropic frequency span in the spectrum. ^{31}P and ^{2}H ssNMR spectra from a perfect bilayer are provided as a reference (top row). Dashed lines are eye-guides for comparing the sizes of frequency spans.

Figure 6.2B demonstrates the dependence of θ on the ratio *d/a*. As d increases, one observes an increase in the anisotropy of lipids distributed on a thinned membrane surface.

6.3.3. Anisotropic ^{31}P and ^{2}H ssNMR Spectral Lineshapes of Lipids Forming Toroidal Pores

It is widely accepted that insertions of membrane-acting AMPs into membrane bilayers induce toroidal pores.[19,45,46] Previously, we introduced a general elliptic toroidal pore model to simulate the experimental anisotropic ^{31}P and ^{2}H ssNMR spectra of lipids interacting with the AMP protegrin-1.[43] Anisotropic ^{31}P or ^{2}H ssNMR spectra of lipids located on the inner surface of an elliptic toroidal pore (Figure 6.3A) can be calculated by a lineshape factor provided by

$$\frac{bd}{\sqrt{d^2\cos^2\theta + b^2\sin^2\theta}}\left(a + d - \frac{bd\sin\theta}{\sqrt{d^2\cos^2\theta + b^2\sin^2\theta}}\right) \tag{6.4}$$

where *b*, *a*, and *d* are the monolayer thickness of the lipid bilayer, the radius of a pore at its narrowest location, and the semiminor (or semimajor if $d > b$) distance of the generator ellipse defined on the *x*–*z* plane, respectively. The angle θ is considered between the *z*-axis defined in Figure 6.3A and a line drawn from the center of the generator ellipse to the position of a lipid located on the toroidal inner surface ($0° \leq \theta \leq 180°$). For such a lipid, a fast uniaxial rotation along its chain axis would orient the chain axis orthogonal to the tangential line drawn on the surface. Then, a modified angle (θ'), specifying the orientation of the chain axis of a lipid with respect to B_0 ($z \,//\, B_0$), can be identified as

$$\theta' = \tan^{-1}\left(\frac{b^2\sin\theta}{d^2\cos\theta}\right) \tag{6.5}$$

For an elipse, since a position orthogonal to a tangential line drawn on the surface may not match up to a line drawn from the center of the elipse to a spot on the surface, θ and θ' may not be equal. When $d = b$ however, $\theta = \theta'$ and Eq. 6.4 becomes $b(a + b - b\sin\theta)$, which is the case for a circular toroidal pore model reported by Ramamoorthy et al.[45]

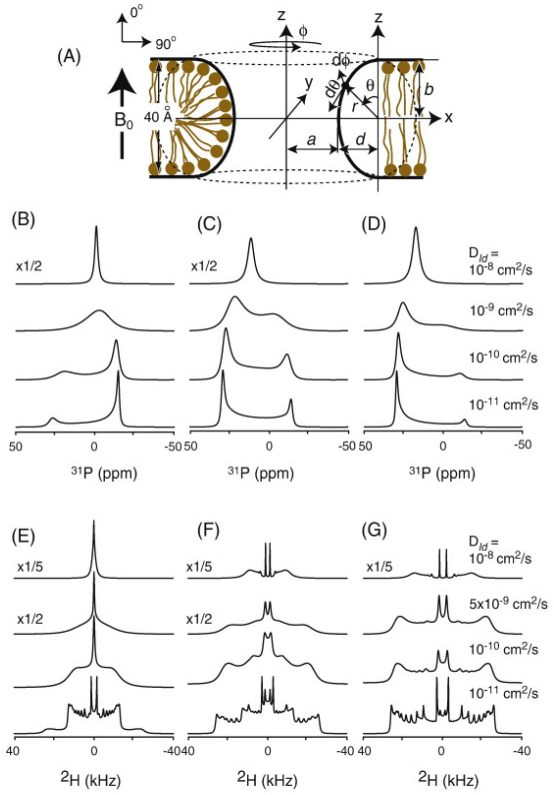

Figure 6.3. An elliptic toroidal pore model describing a lipid pore formed in a flat membrane bilayer. An elliptic ring torus is characterized by the rotation of an elliptic circle in the *x*–*z* plane, with parameters *r* and θ, by angle ϕ about the *z*-axis, which is separated by the distance, $a + d$, from the center of the ellipse. Pore geometric parameters are *a*, the radius of a pore at its narrowest location, *b*, the monolayer thickness of a lipid bilayer (≈ 20 Å), and *d*, the elliptic semiminor (or semimajor if $d > b$) axis. Only the inner surface of the ring torus is considered for lipid distributions. The ranges of *r*, θ, and ϕ are: $d \leq r \leq a + d$; $0 \leq \theta \leq \pi$; $0 \leq \phi \leq 2\pi$. The influence of a lateral diffusive rate on the anisotropic ^{31}P (B–D) and ^{2}H (E–G) ssNMR spectra of lipids in an elliptic toroidal pore with $a = b$ and $d = 0.5b$ (B, E), b (C, F), and $1.4b$ (D, G) is indicated. The range of lateral diffusion coefficients considered is 10^{-8}–10^{-11} cm^2/s. Broadened lineshapes are clearly visible in the ^{31}P and ^{2}H spectra at $D_{ld} > 10^{-11}$ cm^2/s. $D_{ld} = 10^{-8}$ cm^2/s provides a motionally averaged sharp peak at the center-of-mass position of the anisotropic powder pattern of each site in either ^{31}P or ^{2}H spectra. Unlike the ^{31}P cases, a coalesced sharp peak was provided only at $d = 0.5b$ in the ^{2}H spectra because the center-of-mass positions of two anisotropic powder patterns of each ^{2}H site do not coincide at other *d*/*b* ratios.

6.3.4. Lateral Diffusive Dynamics of Lipids on the Curved Surface of a Membrane

Lateral diffusive motions of lipids occurring on the 2D surface of a cell membrane play a crucial role for the transportation of surface molecules (i.e. nutrients, metabolites, and drugs). Upon binding to AMPs, lipids on cell membranes may readjust their diffusive rates due to the favorable, electrostatic peptide–lipid interactions. To better understand the dynamic nature of AMP-induced membrane assemblies (i.e. pores) it will be important to consider how the lateral diffusive motions of lipids are exemplified in the lineshapes of ^{31}P and ^{2}H ssNMR spectra.

A classical diffusion model had been incorporated previously to describe the lateral diffusions of lipids distributed on the curved surfaces of pores and thinned bilayers.[43] We assume that lipid molecules containing ^{31}P or ^{2}H sites migrate from one region to another on a curved membrane surface with a certain diffusive rate. The relative position and orientation of either a ^{31}P or ^{2}H site in the *i*th lipid on the curved surface of either a pore or thinned bilayer under the influence of B_0 can be represented by an angular point, (θ_i, ϕ_i), in a grid coordinate defined on a surface.[43] A position of a lipid, (θ_i, ϕ_i), specifies the anisotropic frequency of a site with respect to the B_0 direction. If a lateral diffusive motion is considered among a discrete set of grids, ($n\Delta\theta$, $m\Delta\phi$), where *n* and *m* are integers, the orientation of either a ^{31}P or ^{2}H site in a lipid will then be encoded by an anisotropic frequency $\Omega(\theta_i, \phi_i)$. We assume that a lipid in a position, (θ_i, ϕ_i), migrates into its adjacent lattice points, ($\theta_{i\pm1}$, $\phi_{i\pm1}$), according to

$$(\theta_i,\phi_{i\pm1}) \xleftrightarrow{\Pi^{\phi}_{i,i\pm1}} (\theta_i,\phi_i) \xleftrightarrow{\Pi^{\theta}_{i,i\pm1}} (\theta_{i\pm1},\phi_i) \tag{6.6}$$

thus, mimicking the lateral diffusion as a series of successive random walks. Because oriented lipid bilayers are confined between glass plates, we can safely ignore random translational or rotational tumbling motions of lipids or lipid assemblies.[51] The geometry dependent first-order exchange rate constants ($\Pi^{\phi}_{i,i\pm1}, \Pi^{\theta}_{i\pm1,i}$) can be related to the diffusion coefficient, D_{ld}, in the standard diffusion equation defined as:[54,59]

$$\frac{d}{dt}M = D_{ld}\nabla^2 \cdot M = \Pi M \tag{6.7}$$

where, M, D_{ld}, Π, and ∇^2 are the column matrix that reflects the intensity of magnetization of each anisotropic frequency site in a lipid, the lateral diffusion coefficient, the first-order exchange rate constant, and a coordinate-dependent *Laplacian*, respectively. A more detailed description to solve this differential equation on the curved surface of either an elliptic pore or thinned membrane bilayer is provided in the previous publication.[43] By assuming angular increments ($\Delta\theta$, $\Delta\phi$) to separate sites in the lattice, the rate constants defined along the θ and ϕ variables can be provided as:

$$\Pi^{\theta}_{i,i\pm1} = \frac{D_{ld}}{h_2(\theta)h_3(\theta)}\frac{h_3(\vartheta \pm \Delta\theta/2)}{h_2(\vartheta \pm \Delta\theta/2)}\frac{1}{(\Delta\theta)^2}; \Pi^{\varphi}_{i,i\pm1} = \frac{D_{ld}}{h_3(\theta)^2}\frac{1}{(\Delta\phi)^2} \tag{6.8}$$

where

$$h_2(\theta) = \frac{bd}{\sqrt{d^2\cos^2\theta + b^2\sin^2\theta}}; h_3(\theta) = a + d - h_2(\theta)\sin(\theta) \tag{6.9}$$

for an elliptic toroidal pore model and

$$h_2(\theta) = \sec\theta; h_3(\theta) = \frac{a}{\pi}\sin^{-1}[\frac{a}{\pi d}\tan\theta] \tag{6.10}$$

for a thinned membrane dimple. Then, the time evolution of anisotropic magnetizations of either ^{31}P or ^{2}H sites in lipids, distributed on a curved membrane surface, can be calculated by solving the Bloch–McConnell differential equation[60,61] that requires setting up a standard tri-diagonal NMR exchange matrix for molecular diffusions. The model suggested by Kim and Wi[43] generally considers any arbitrary orientation of the glassplate normal with respect to B_0.

Figure 6.2C and D shows lineshape variations introduced in the ^{31}P (A) and ^{2}H (B) solid-state NMR spectra, respectively, of POPC-d_{31} lipids forming thinned lipid bilayers with d/a = 0 (top row) and d/a = 0.167 with $D_{ld} = 10^{-10}$ cm^2/s (middle row) and $D_{ld} = 5 \times 10^{-7}$ cm^2/s (bottom row), while assuming d = 4 Å, z // B_0, and b = 20 Å. When d/a = 0, the magnitude of D_{ld} is irrelevant to the lineshape variations. The range of the θ angle with d/a = 0.167 is $0° \le \theta \le 27.7°$,

and we arbitrarily considered 100 lipid molecules over the range of θ. The CSA of ^{31}P, the B_0 strength, the QC parameters of ^{2}H sites in a palmitoyl chain, and the line broadening factors considered for the spectral simulations are 32 ppm, 7.05 T, 4–32 kHz, and 50–200 Hz, respectively. Distorted peaks are visible in both ^{31}P and ^{2}H ssNMR spectra at $d/a \neq 0$ when a slow lateral diffusive rate ($D_{ld} = 10^{-10}$ cm^2/s) is considered (middle row). Distortion occurs because a single sharp peak (^{31}P) or a pair of sharp peaks (^{2}H) resulting from a site in a perfectly aligned lipid bilayer ($d/a = 0$; top row) is deformed by the disorder in a thinned dimple. If lipids migrate from one region to another by a fast lateral diffusion, ca., $D_{ld} = 5 \times 10^{-7}$ cm^2/s, a motionally averaged single sharp peak (^{31}P) or pair of sharp peaks (^{2}H) per site will be obtained at the center-of-mass position of an anisotropic frequency span of a site, resulting in apparently reduced ^{31}P CSA and ^{2}H QC tensor parameters (bottom row). Therefore, the magnitudes of the apparent ^{31}P CSA and ^{2}H QC tensor parameters obtained from the spectra of lipids, distributed on a thinned surface with a fast lateral diffusion coefficient, decrease as the d/a ratio increases. In many cases, thinned membrane bilayers would be formed prior to the formation of pores in lipid membranes (carpet model). Thus, in actual AMP–lipid interaction systems, lipid pores formed by the insertion of AMPs in membranes would be located in membrane bilayers that are already thinned.

Figure 6.3 shows ^{31}P (B–D) and ^{2}H (E–G) ssNMR spectral lineshapes of POPC-d_{31} lipid bilayers forming toroidal pores of $d = 0.5b$ (B, E), $d = b$ (C, F), and $d = 1.4b$ (D, G), with $D_{ld} = 10^{-8}$ cm^2/s, 10^{-9} cm^2/s, 10^{-10} cm^2/s, and 10^{-11} cm^2/s. The peak intensity is greater along the 0° orientation than the 90° orientation in both ^{31}P and ^{2}H spectra when $d/b > 1$ (D and G), while the opposite is true when $d/b < 1$ (B and E). This intensity variation can be understood by considering that $d/b > 1$ represents a more gradual transition of lipid orientations in going from parallel to the membrane normal, to the curved surface of the pore; a more gradual transition would mean that more lipids stay parallel to the membrane normal. Conversely, $d/b < 1$ is the case for a more abrupt orientation change, and the opposite argument would hold. The pore radius, a, was fixed to the monolayer thickness, b (= 20 Å), of a lipid bilayer.[19,62,63] It has been reported that about 90 POPC lipids are involved in a pore induced by magainin-2.[19,45] In the simulations however, we arbitrarily used 100 anisotropic orientations of lipid molecules with the same tensor values and spectral processing parameters as used in Figure 6.2. The line broadening factors (50–200 Hz) used for the spectral processing cannot explain the extent of peak

broadening/coalescent effects introduced in the simulated ^{31}P and ^{2}H spectra.

A simple line broadening effect is visible when $D_{ld} < 10^{-10}$ cm^2/s. Most of the detailed fine structures of ^{31}P and ^{2}H spectra are washed away when D_{ld} is about 10^{-9} cm^2/s. When D_{ld} reaches the 10^{-8} cm^2/s regime, characteristic of pure lipids, motionally averaged ^{31}P and ^{2}H NMR spectra, with shifted center-of-mass positions depending on the ratio of *d/b*, result. The center-of-mass positions of two anisotropic ^{2}H spectra of lipids on an elliptic pore per each ^{2}H site do not coincide in general, and the gap between the center-of-mass positions of two transitions widens as the QC tensor parameter or the *d/b* ratio increases (Figure 6.3F and G). At $d = 0.5b$, however, all ^{2}H peaks provide a coinciding center-of-mass position regardless of the magnitude of QC parameters, resulting in a single sharp peak at the center with $D_{ld} = 10^{-8}$ cm^2/s (Figure 6.3E). At this condition, both ^{31}P and ^{2}H anisotropic spectra are similar to those from lipids that take a random, a micellar, or a liposomal distribution. However, unlike spectra from a random or a spherical distribution, anisotropic lineshapes of ^{31}P and ^{2}H NMR spectra of lipids distributed on an elliptic pore with $d/b = 0.5$ that are simulated at $z \parallel B_0$ and $z \perp B_0$ orientations are distinctive.[43] These motionally averaged, spectral broadening/
coalescent effects are evidenced experimentally in ^{31}P and ^{2}H ssNMR spectra measured on oriented POPC membranes interacting with the AMP protegrin-1.[43,46]

Anisotropic ^{31}P and ^{2}H ssNMR lineshapes based on a toroidal pore model are unlike those expected from lipid bilayers spread discontinuously by the mosaic distribution.[64] In a fluid mosaic model, the bulk of the phospholipids are in discontinuous, fluid bilayers, whose membrane normal directions are scattered around an average value. As a perfect bilayer is distorted, anisotropic disorders will be reflected in decreasing signal intensity at the 0° frequency position, and increasing intensity at the 90° position, which are at the leftmost and rightmost in the frequency span, respectively. This signal variation is because only a change in the polar angle, not the azimuthal angle (for $\eta = 0$) and the positional rotation around B_0, contributes to a frequency shift. An asymmetric resonance line would result from discontinuous bilayers whose membrane normal directions are taking a Gaussian distribution, with a standard deviation σ, around an average direction (parallel to B_0) (Figure 6.4). An accepted σ for lipid bilayers prepared between cover-glass plates is 5–15°.[47,64] Figure 6.4 shows ^{31}P and ^{2}H ssNMR lineshapes expected for lipid bilayers having mosaic spreads of σ = 5–70°. As can be seen in either ^{31}P or ^{2}H spectra (Figure 6.4), even a very broad, asymmetrical lineshape with σ = 30°

does not provide anisotropic frequencies near 90°. When the $\sigma > 40°$, the distorted lineshapes (Figure 6.4) approach that of a random distribution. Thus, the fact that the mosaic distribution needed to produce intensity at the 90° position is almost 3 times the maximum known mosaic spread in oriented lipid bilayers supports ascribing signals at the 90° position to pores.

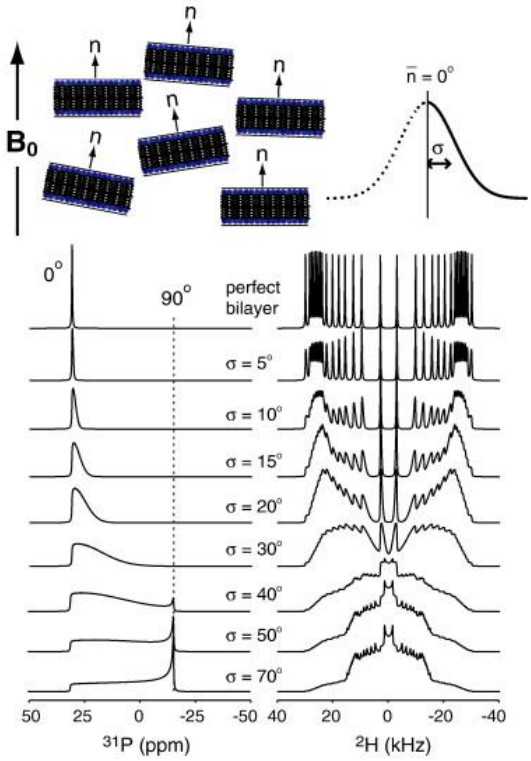

Figure 6.4. ^{31}P and ^{2}H lineshapes expected from lipid bilayers whose normal directions have a mosaic distribution (σ = 5–70°). When the average normal direction is parallel to B_0, the rotational invariance around B_0 makes the resulting lineshapes resulting half-Gaussians. The known range, σ = 5–15°, of mosaic spread still provides relatively narrow, asymmetrically broadened lines in ^{31}P and ^{2}H spectra around the 0° position, the average bilayer normal direction. Even with ca. σ = 30°, non-realistically broadened lines in ^{31}P and ^{2}H spectra still lack peak intensities around the 90° position. When $\sigma > 50°$, both ^{31}P and ^{2}H spectra resemble those of a random lipid distribution.

6.4. Experimental Results

6.4.1. Interaction of Magainin-2 and Aurein-3.3 with POPC Bilayers

A zwitterioninc type of membrane lipid, POPC, has a hydrophilic headroup and hydrophobic palmitoyl- and oleyl acyl chains. Zwitterionic lipids are common in membranes of *eukaryotic* cells, so POPE or POPC can be used as a reference for mixed membrane systems. Using ^{31}P and ^{2}H ssNMR spectroscopy, we studied oriented POPC-d_{31} bilayers binding with magainin-2 and aurein-3.3 at various peptide:lipid (P:L) ratios. Figure 6.5 shows experimental (A, C, E, and G) and simulated (B, D, F, and H) ^{31}P (A, B, E, and F) and ^{2}H (C, D, G, and H) ssNMR spectra of oriented POPC-d_{31} bilayers interacting with magainin-2 (A–D) and aurein-3.3 (E–H), at P:L = 0:100, 1:80, 1:50, and 1:20. A stack of glass plates is placed in the external magnetic field B_0 so that the glass plate normal is parallel to the external magnetic field B_0 (z // B_0). An ideal lipid bilayer would provide peaks only along the 0° orientation in the absence of AMPs. An asymmetrical lineshape in ^{31}P spectrum at P:L = 0:100 would exemplify potentially possible mosaic spreads of lipid bilayers with $\sigma \approx 10°$. As AMPs perturb membrane structures, we observe distorted lineshapes spanning over the entire frequency range, from the 0° to 90° position, in ^{31}P and ^{2}H ssNMR spectra, even at P:L = 1:80. Interestingly, the observed ^{31}P and ^{2}H spectral lineshapes cannot be explained by considering a mosaic spread model because a mosaic distribution model does not generate frequencies spanning over all the anisotropic frequency positions, including the frequency around the 90° position, without providing a significantly broadened lineshape along the 0° position (Figure 6.4). Lineshapes are also not congruent with a random model (Figure 6.1B). However, these lineshapes can be simulated well by a toroidal pore model with variable *d* values (Figure 6.3) as shown in Figure 6.5. The observed NMR tensor parameters agree with the known values for phospholipids in liquid crystalline states[45-47]: δ_{csa} = 30 ppm, η_{csa} = 0 for the ^{31}P CSA, and e^2qQ/h = 3.0–36 kHz and η_{QC} = 0 for ^{2}H QC parameters.[65] Quadrupolar splittings are characterized by the mobility of the CD_2 groups in the acyl chains of lipids. The formation of a lipid pore imposes anisotropic line broadenings in both ^{31}P and ^{2}H spectra without modifying tensor parameters that are determined in pure lipid bilayers.[46,48] ^{31}P CSA and ^{2}H QC tensor parameters associated with various types of lipid topologies can be extracted by direct spectral simulations or signal dePaking.[66]

The best-fit simulations in Figure 6.5 (B, D, F, and H), incorporating a pore model over P:L from 1:80 to 1:20, were provided by ranges of *d* values from 1.5*b*–1.8*b* to 1.0*b*–1.2*b*, respectively, with $a = b$. We used $a = b$ in our simulations based on the experimental observation that the range of pore diameters induced in the cell membranes of *Escherichia coli* interacting

with cecropin is about the monolayer thickness *b* of bilayers.[67]

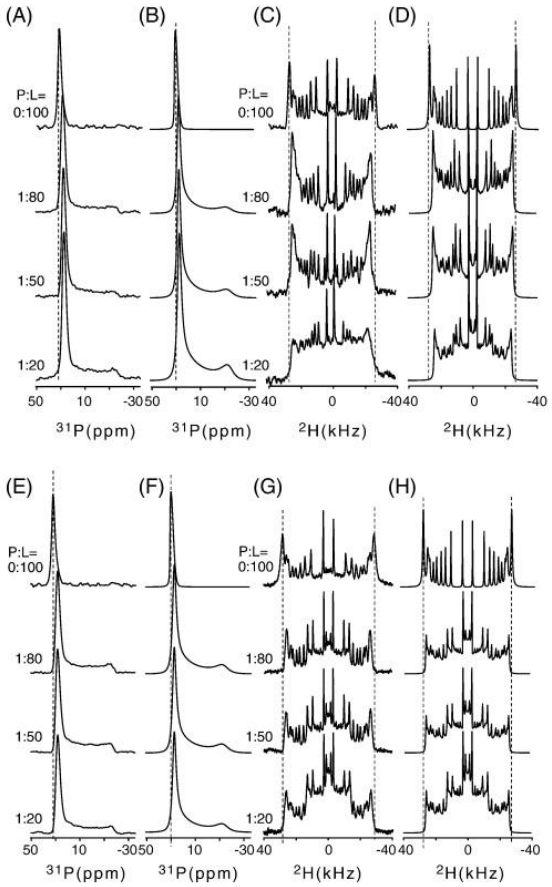

Figure 6.5 Results from experiments of magainin-2 and aurein-3.3 interacting with oriented POPC-d_{31} bilayers. Shown are experimental (A, C, E, G) and simulated (B, D, F, H) ^{31}P (A, B, E, F) and ^{2}H (C, D, G, H) ssNMR spectra for the cases of magainin-2 (A–D) and aurein-3.3 (E–H), at P:L = 0:100, 1:80, 1:50, and 1:20. The glassplate normal was parallel to B_0 for NMR measurements. Eye-guides (dashed lines) along the 0° orientation of lipids in the pure POPC-d_{31} spectra show a decreasing line width as peptide concentration increases. All spectra shown conform to the spectral simulations based on an elliptic toroidal pore model with variable d/b ratios. The decreasing frequency spans of ^{31}P and ^{2}H ssNMR spectra evidence thinned membrane bilayers with $D_{ld} = 10^{-8}$–10^{-9} cm^2/s. The ^{2}H spectra of aurein-3.3 showed elliptic pores with shorter d (perhaps due to deeper peptide insertions) than those cases involving maginin-2, while providing less prominent thinning effects, even at P:L = 1:20.

D_{ld} cannot be assessed from these 1D spectra because they do not exemplify the influence of lateral diffusive motions of lipids. By comparing to the simulated spectra, however, we can be assured that $D_{ld} < 10^{-11}$ cm^2/s since sharp features are observable, but there are no signals at the isotropic frequency position (Figure 6.3). The observed spin–spin relaxation time, T_2, of ^{31}P in phospholipids is in the 0.5–1.4 ms range over the peptide concentrations we tested. Although not explicitly included in the simulated spectra, a flat portion of lipid bilayers with some degree of mosaic spread would add to the signal intensity along the 0° position of the pore lineshape. As the peptide concentration increases, the observed trend in the spectra, particularly in ^{2}H spectra is the spectral feature of a pore model with shorter *d* length, increasing intensity at the 90° positions. However, the trend in the ^{31}P spectra is not as prominent as that of the ^{2}H spectra, evidencing a stronger interaction with the lipid chains than with the headgroups. Aurein-3.3 produces pores with somewhat shorter *d* lengths than magainin-2, as can be seen in the spectra. Based on the best-fit simulation data, the simulated *d* values that agree with the features of experimental spectra are 1.8*b* (P:L = 1:80), 1.7*b* (P:L = 1:50), and 1.5*b* (P:L = 1:20) for magainin-2/POPC-d_{31} and 1.2*b* (P:L = 1:80), 1.1*b* (P:L = 1:50), and 1.0*b* (P:L = 1:20) for aurein-3.3/POPC-d_{31}.

Another feature observed is decreaseing frequency spans in both ^{31}P and ^{2}H ssNMR spectra in Figure 6.5 as the peptide concentrations increase. This decrease is more prominent in ^{2}H spectra, which measure the hydrophobic environment of peptide–lipid complexes. Although several groups have correlated the decrease in peak splitting with changes in membrane thickness,[48,68] no existing theoretical model except our membrane thinning model considered with a fast D_{ld} successfully explains this property (Figure 6.2). The magnitudes of apparent ^{2}H QC tensor parameters observed in Figure 6.5 are clearly less than those observed from pure lipid bilayers, particularly at high P:L. According to the best-fit simulation data obtained from the membrane thinning model, the observed decreases in the anisotropic frequency spans of ^{2}H ssNMR spectra of POPC-d_{31}/magainin-2 and POPC-d_{31}/aurein-3.3 produced d/a = 0.1–0.2 and $D_{ld} = 10^{-7}$–10^{-8} cm^2/s. In our experimental spectra, the relative portions of lipids that are involved in pores and thinned membranes are unclear.

6.4.2. Interaction of AMPs with Anionic Membranes.

Anionic lipids, which are abundant in *prokaryotic* cell membranes, are crucial for the mode of interaction for cationic AMPs to selectively bind on the bacterial cell membrane. An electrostatic interaction between anionic lipids and cationic AMPs plays a central role for antimicrobial action. We incorporated a lipid system consisting of a POPC and POPG mixture with a molar ratio of 3:1 to mimic the non-neutral lipid composition of the bacterial cell membranes in a simple way. Figure 6.6 shows experimental (A, C, E, G) and simulated (B, D, F, H) ^{31}P (A, B, E, F) and ^{2}H (C, D, G, H) ssNMR spectra of POPC-d_{31}(3)/POPG(1) lipids interacting with magainin-2 (A, B, C, D) and aurein-3.3 (E, F, G, H), at P:L ratios 0:100, 1:80, 1:50, and 1:20. In these peptide–lipid systems containing anionic lipids the frequency span of ^{2}H spectra decreases prominently, as can be identified clearly from the samples with P:L = 1:20, as the peptide concentration increases. The observed ^{31}P CSA tensor parameters, however, are still very similar to those obtained without anionic POPG lipids.[65]

When a toroidal pore model is incorporated, the anisotropic ^{31}P and ^{2}H ssNMR spectra of POPC-d_{31}(3)/POPG(1) lipids interacting with magainin-2 and aurein-3.3 peptides again provide lineshape characteristics that are consistent with toroidal pores with $a \approx b$ and d = 1.6–1.8b. The potential contribution from the flat portions of lipid bilayers is not explicitly included in the simulated spectra. Except for the prominent linewidth decrease observed in ^{2}H spectra, magainin-2 does not provide much difference in the shape of pores induced in the POPC-d_{31} lipids, both with and without the presence of POPG lipids, at all three P:L ratios. However, a dramatic increase in d, from 1.0–1.2b to 1.6–1.8b, is observed in the lipids interacting with aurein-3.3 as the lipid composition changed from pure POPC-d_{31} to POPC(3)/POPG(1). Both peptides, however, show very similar spectral characteristics in ^{31}P NMR spectra for both POPC and POPC(3)/POPG(1) lipid systems even at P:L = 1:20. The D_{ld}s incorporated in the pore lineshape simulations for the experimental ^{31}P and ^{2}H ssNMR spectra of both peptide systems are $D_{ld} \leq 10^{-11}$ cm^2/s because we do not observe any motionally averaged lineshapes.

6.4.3. Interaction of AMPs with POPC/Cholesterol

Cholesterol, an important constituent of *eukaryotic* cell membranes, is generally absent from bacterial membranes. It largely hydrophobic, but it has a polar hydroxyl group, making it amphipathic, allowing its insertion into a membrane bilayer with the hydroxyl group oriented

toward the aqueous phase and the hydrophobic ring system facing the phospholipid acyl chains. However, $D_{ld} = 10^{-7}$–10^{-8} cm^2/s is required for explaining the membrane thinning phenomenon, as explained previously. This immobilizes the first few acyl chains, making lipid bilayers less deformable and less permeable to small water soluble molecules including AMPs.[69-71]

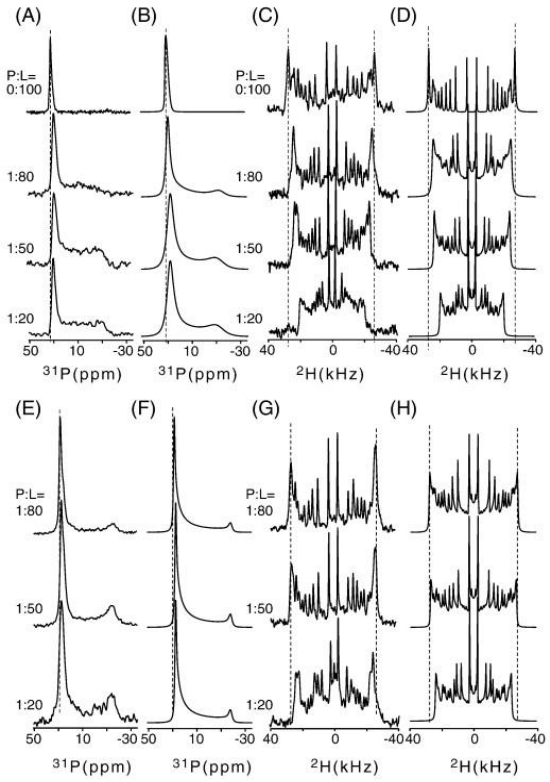

Figure 6.6. Results from experiments on magainin-2-bound and aurein-3.3-bound oriented POPC-d_{31}/POPG membrane bilayers, measured at z // B_0. The POPC-d_{31}/POPG molar ratio was 3:1. Shown are experimental (A, C, E, G) and simulated (B, D, F, H) ^{31}P (A, B, E, F) and ^{2}H (C, D, G, H) ssNMR spectra of cases with magainin-2 (A–D) and aurein-3.3 (E–H) for P:L = 0:100, 1:80, 1:50, and 1:20. The presence of anionic POPG lipids provides a significantly prominent membrane thinning effect in the ^{2}H spectra at high P:L, especially in magainin-2. The shoulder peak near the 0° orientation in the ^{31}P spectra of the aurein-3.3 system at all P:L ratios might indicate a portion of thinned membranes with a slower lateral diffusive rate that maintains the same geometrical feature, or a portion of thinned surfaces with a bigger d/a ratio that maintains the same lateral diffusive rate.

We prepared a mixture of POPC-d_{31} /cholesterol (1:1 molar ratio) to investigate the influence of cholesterol in AMP–lipid interactions. Figure 6.7 shows experimental (A, C, E, G), and simulated (B, D, F, H) ^{31}P (A, B, E, F) and ^{2}H (C, D, G, H) ssNMR spectra of POPC-d_{31}/cholesterol interacting with magainin-2 (A, B, C, D) and aurein-3.3 (E, F, G, H) at P:L ratios of 0:100, 1:80, 1:50, and 1:20. Observed decreasing linewidth in ^{2}H spectra with increasing peptide concentration may be due to the membrane thinning effect. Based on our simulation, the lineshapes of both ^{2}H and ^{31}P spectra evidence the induction of lipid pores with $d > b$ in oriented membranes of both sample systems. The pore parameters obtained from the best-fit simulations are $d = 1.5b$ (P:L = 1:80), $d = 1.2b$ (P:L = 1:50), and $d = 1.1b$ (P:L = 1:20) for POPC-d_{31} /cholesterol/magainin-2 and $d = 1.6b$ (P:L = 1:80), $d = 1.5b$ (P:L = 1:50), and $d = 1.0b$ (P:L = 1:20) for POPC-d_{31}/cholesterol/aurein-3.3, assuming $a = b$.

^{2}H spectra from both peptide systems demonstrate increases of the QC parameters of all ^{2}H sites, [65] which agrees with the fact that cholesterol molecules in membranes freeze the segmental motion of hydrophobic acyl chains of lipids. The QC parameters obtained from both sample systems were in the range of 7.2–65 kHz depending on the position of the ^{2}H site in the palmitoyl chain. However, the CSA parameters of ^{31}P nuclei are in the range of 27–28 ppm, which are actually less than the value observed at the pure POPC lipid system, indicating that cholesterol does not deter the rates of uniaxial rotations of POPC lipids.

6.5. Discussion

Maganinin-2, an AMP with 23 amino acid residues, forms an α-helical structure in lipid membranes.[72] In a helical wheel representation, it makes an amphipathic helix with well-defined hydrophobic (red) and hydrophilic (blue) faces, (Figure 6.8A). The secondary structure of the aurein-3.3 peptide in lipid membranes is still unknown. In a helical wheel representation (Figure 6.8B), however, aurein-3.3 also reveals well-separated hydrophobic and hydrophilic faces, suggesting that aurein-3.3 would form an α-helical structure in lipid membranes.

The positively charged residues located on the hydrophilic face of a helix would be faced-up, allowing favorable electrostatic interactions with the anionic headgroups of lipids, while the hydrophobic residues on the opposite side would be faced-down and buried into the membrane, contacting the hydrophobic tail groups of lipids (Figure 6.9A).[73]

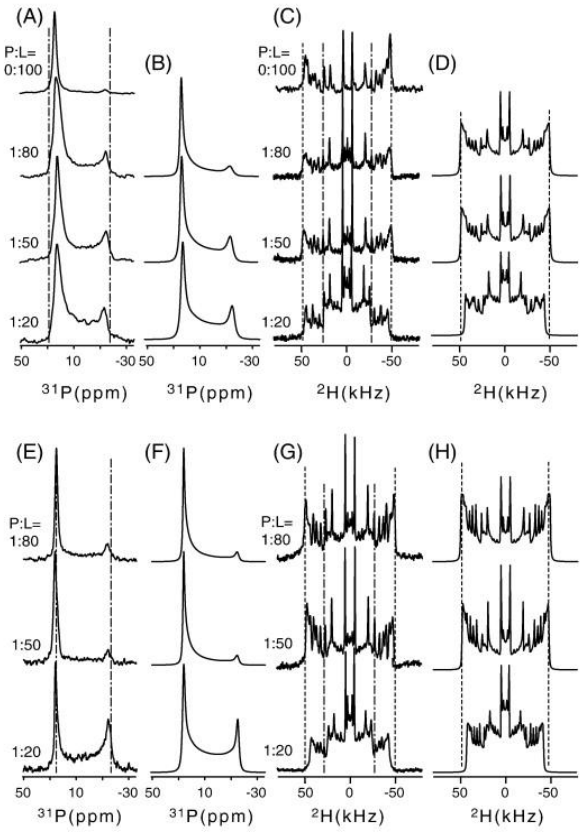

Figure 6.7. Results from experiments on magainin-2-bound and aurein-3.3-bound POPC-d_{31}/cholesterol membrane bilayers, measured at z // B_0. Shown are experimental (A, C, E, F) and simulated (B, D, F, H) ^{31}P (A, B, E, F) and ^{2}H (C, D, G, H) ssNMR spectra for cases of magainin-2 (A–D) and aurein-3.3, for P:L = 0:100, 1:80, 1:50, and 1:20. Pore forming and thinning phenomena are visible in both ^{31}P and ^{2}H spectra. Dashed and dashed-dot lines (eye-guides) compare frequency spans at different P:L ratios, and indicate the frequency spans of peptides with POPC-d_{31} lipids without cholesterol, respectively. Unlike the ^{31}P spectra, the frequency spans of ^{2}H spectra of POPC-d_{31} lipids involving cholesterol increased significantly, revealing decreased segmental motions of hydrophobic acyl chains. The length d of the simulated pore geometry decreases as the peptide concentration increases. The spectral features of ^{2}H spectra of aurein-3.3 system are quite similar to those from magainin-2, except that pores induced in membranes possess somewhat longer d. The linewidth of ^{31}P spectra decreases at all P:L ratios.

This mode of AMP–lipid interaction would facilitate thinned membrane bilayers, a common

feature when the peptide concentration is low. After reaching a critical AMP concentration, a few closely placed AMP molecules would self-assemble into a bundle while angling and inserting into the membrane to form a toroidal wormhole (Figure 6.9B).[74]

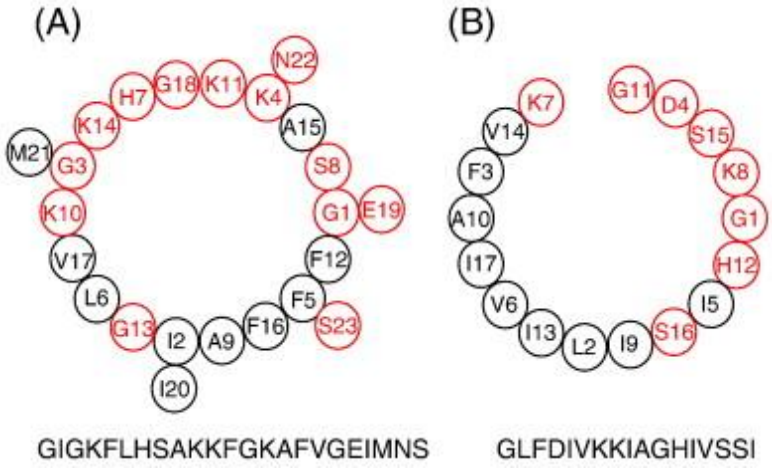

Figure 6.8. Helical wheel representations of magainin-2 and aurein-3.3. Both peptides demonstrate well-separated hydrophobic and hydrophilic faces, suggesting a potential amphipathic helical structure of aurein-3.3 in lipids, as in the case of magainin-2.

This mechanism explains reasonably well the formation of a toroidal pore with variable length *d* with respect to *b* (Figure 6.3), which is required to explain most of our ^{31}P and ^{2}H ssNMR spectra measured on lipids interacting with magainin-2 and aurein-3.3. By forming a deeply inserted bundle in the membrane, cationic AMPs would find a favorable way to coexist with amphiphilic lipids and water molecules as shown in Figure 6.9C. It allows water molecules inside of the pore to transport molecules and ions across the membrane. ^{31}P and ^{2}H ssNMR spectra with variable 0°/90° intensities satisfying a toroidal pore model with variable length *d* were frequently observed at various P:L ratios when β-hairpin shaped, defensin-like (cystein-rich) AMPs or α-helical structured AMPs were interacting with oriented phospholipids.[43,46] A toroidal pore model considering different *d* lengths (Figure 6.3B–G) successfully explains different types of experimental ^{31}P and ^{2}H ssNMR lineshapes exhibiting variable intensities between the 0° and 90° positions of lipids.[43,46]

The model shown in Figure 6.9D could also explain the insertion of a bundle of self-assembled AMPs in the membrane. In this case, peptides hide hydrophobic residues (black)

inside of the bundle, while exhibiting hydrophilic residues (red) outside, to favor interactions with hydrophilic headgroups of lipids and water. In this model, lipids located on the inner surface of a pore would be more flexible for lateral diffusivity than the case shown in Figure 6.9C because peptides are not intermingled with lipid molecules on the pore wall by penetration.

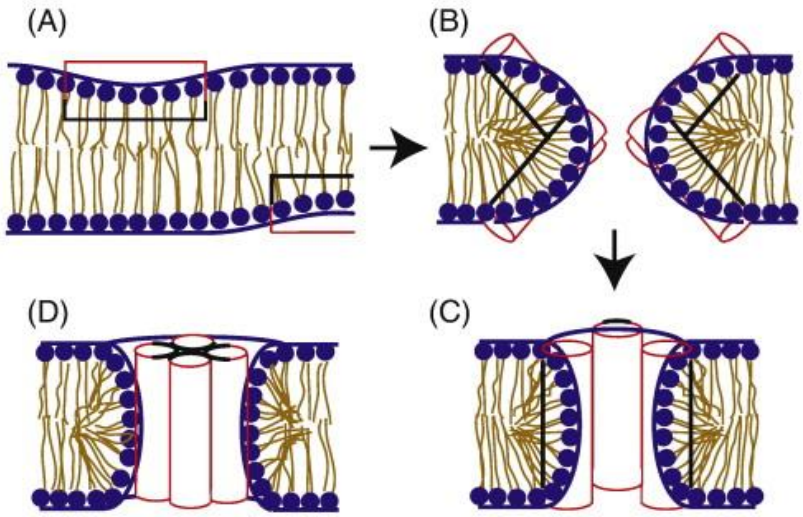

Figure 6.9. Models suggested for explaining the gradual insertion of peptides and the formation of elliptic toroidal pores with variable *d* length. AMPs bound on the membrane surface (A) self-assemble and tilt in order to insert into the membrane (B). AMPs insert deeper into the membrane to form a well-defined pore and accommodate molecular/ionic transportations across the membrane through this pore (C). Also plausible is a model assuming a self-assembled peptide bundle, with hydrophobic faces buried inside of the bundle, which can be inserted into a bilayer to form a pore (D). The outward-facing hydrophilic faces of the peptide bundle make favorable interactions with the hydrophilic headgroups of lipids.

However, Figure 6.9D would be less favorable for an efficient transportation of molecules or ions through the pore compared to the other type shown in Figure 6.9C because the inside part of the pore that is occupied by AMPs is hydrophobic. For cationic AMPs to interact with zwitterionic and neutral lipids, such as POPC or POPC/cholesterol, AMPs would self-assemble into a bundle more readily even at lower AMP concentration to minimize the accumulation of overall charge density. In this case, the critical peptide concentration for the formation of a

peptide bundle will be lower than the case involving anionic lipids. On the molecular level, cationic AMPs are readily miscible with anionic lipids but not with zwitterionic lipids.

^{31}P and ^{2}H ssNMR spectroscopic techniques are optimal for diagnosing the structural perturbations in lipid bilayers induced by membrane-acting peptides. Within our knowledge, without incorporating a toroidal pore model with variable length in *d*, it is not possible to explain the lineshape patterns of ^{31}P and ^{2}H ssNMR spectra we obtained experimentally, particularly the intensity profiles along the 90° position with respect to the applied magnetic field direction (z // B_0). As can be seen in Figure 6.5, the best-fit simulations for the experimentally observed ^{31}P and ^{2}H ssNMR spectra originating from magainin-2/POPC-d_{31} and aurein-3.3/ POPC-d_{31} systems were provided by a toroidal pore model with $a \approx b$, $d > b$, and lateral diffusion coefficients in the range of $\leq 10^{-11}$ cm^2/s—lineshape characteristics that are motionally averaged by lateral diffusions are not visible. The observed pore lineshape characteristics are evident even at the lowest peptide concentration (P:L = 1:80) we considered, indicating that the critical peptide concentration for membrane insertion is very low. However, as the peptide concentration increases, the *d* parameter changes from 1.8*b* (P:L = 1:80) to 1.3*b* (P:L = 1:20) for magainin-2/POPC-d_{31}, and from 1.2*b* (P:L = 1:80) to 1.0*b* (P:L = 1:20) for aurein-3.3/POPC-d_{31}. It is not clear why the *d* parameter of a toroidal pore shows stronger peptide concentration dependence in ^{2}H spectra. We hypothesize however that the insertion of a peptide bundle into a lipid bilayer would result in a more perturbed environment along the hydrophobic tail parts that exist inside of the bilayer than along the hydrophilic headgroups that face outward. We observed that pore lineshapes show time-dependent drift over several days or weeks depending on the composition of membranes (data not shown). Ramamoorthy and coworkers reported that pores initially formed can be converted into micelles or even into inverted hexagonal phases over time.[33-35]

In usual cases, thinned membrane bilayers would form before pores in anionic lipid membranes when interacting with cationic AMPs because the presence of anionic lipids favors an *S*-bound state over an inserted *I*-state. The helical axis of an α-helical AMP, which takes on a parallel orientation with respect to the surface of a membrane bilayer at low peptide concentrations,[18] would need to tilt to insert into membranes after a critical concentration has been reached (Figure 6.9B). This mechanism would explain how a pore with a shallower peptide insertion — an elliptic pore with a longer *d* value — is more probable for the interaction of a helical AMP with anionic membrane bilayers than with zwitterionic membrane bilayers.

The linewidths of ^{31}P and ^{2}H spectra had decreased prominently in lipid bilayers involving anionic lipids that are interacting with AMPs. The magnitudes of observed coupling parameters of ^{31}P CSA and ^{2}H QC interactions in the presence of AMP molecules are less than those from pure lipid bilayers. [65] Although the linewidth decrease effect is evident both in the ^{31}P CSA and ^{2}H spectra, a more prominent effect was observed in the ^{2}H spectra, which contain local structural and dynamic information of hydrophobic alkyl chains. A synergistic effect between the lateral diffusive motion and the segmental wobbling of the acyl chains would provide a more prominent linewidth decrease effect. Interestingly, an increase in the peptide concentration decreased the linewidth of both ^{31}P and ^{2}H ssNMR spectra for both peptide cases,[57] which can readily be simulated based on our membrane thinning model with a fast lateral diffusive rate of lipids (D_{ld} = 10^{-7}–10^{-9} cm^2/s) (Figure 6.2). According to our thinning simulation scheme, the observed linewidth decreases in both ^{31}P and ^{2}H anisotropic spectra provide the best-fit simulation with d/a = 0.2–0.3 and D_{ld} = 10^{-8}–10^{-9} cm^2/s. If we adopt an average thin depth of membranes on the order of 11 Å,[57] the diameter of the thinned membrane dimple would be in the range of 36–55 Å.

In general, the lateral diffusive rate of lipids on a membrane surface is a function of the membrane composition, the concentration of an obstacle, temperature, and the hydration level. The lateral diffusion coefficient of lipids in a pure lipid bilayer is 10^{-7}–10^{-8} cm^2/s.[75] In the presence of membrane-acting peptides, the rate of lateral diffusions of lipids in membranes would be slowed down due to the electrostatic, hydrophilic, and/or hydrophobic peptide–lipid interactions. Therefore, membrane surfaces binding with AMPs would have significantly lower rates of lateral diffusions. Less obvious is why lipids involved in the holes of toroidal pores move more slowly (< 10^{-11} cm^2/s) than lipids involved on thinned membrane bilayers (10^{-8}–10^{-9} cm^2/s) if we incorporate our model to explain the linewidth decrease effect. We hypothesize that the lateral diffusive motion of lipids involved in a toroidal pore would be significantly slower than that of pure bilayers because the lipid motion must accompany somewhat unfavorable transbilayer motions involving both up- and down-leaflets (when z // B_0, the lateral diffusive motion around ϕ angle is not observable in NMR), while those occurring on a thinned membrane surface would still maintain a reasonably fast diffusive rate because the mechanism involved is the typical lateral diffusive motion of lipids on a single surface. This reasoning matches well with the observation by Opella and coworkers that membrane proteins incorporated

in bicelles undergoes fast axial diffusion ($D_{rot} \geq 10^5$ s^{-1}) on the bicelle surface, providing narrow line widths along ^{15}N chemical shift (< 2 ppm) and ^{1}H–^{15}N dipolar couplings ($\sim$ 250 Hz).[76]

The range of transverse relaxation time, T_2, measured on POPC, POPC(3)/POPG(1), and POPC(1)/Chol(1) systems interacting with magainin-2 and aurein-3.3 at P:L = 1:80, 1:50, and 1:20 was 0.6–1.5 ms, with shorter T_2 times at higher peptide concentrations (data not shown). Because of these moderate to short T_2 times and the slow lateral diffusive rates of lipids, we cannot attribute the apparent line broadening effect in 1D NMR spectra sorely to the lateral diffusive dynamic motions of lipids. A 2D exchange spectroscopic technique was incorporated to investigate slow lateral diffusive rates of lipids. Figure 6.10 shows 2D ^{31}P exchange spectra measured on a POPC(3)/POPG(1) system interacting with aurein-3.3 at P:L = 1:20, with mixing times of 5, 50, and 200 ms. At 50 and 200 ms, peak intensities of experimental spectra centered along the diagonal frequency positions in spectra measured with 5 ms mixing time smeared out to the off-diagonal positions on both sides, demonstrating exchanges among different nuclear sites, generating different anisotropic frequencies. This might indicate that nuclear sites possessing different anisotropic frequencies are on the same curved membrane surface. Major peak intensity patterns on the experimental spectra with different mixing times were reasonably well simulated by assuming two-dimensional lateral diffusive motions of lipids located on the curved surface of a pore with $a = b$, $d = 1.6b$, and $D_{ld} = 10^{-11}$ cm^2/s, as shown in Figure 6.10D–F. Thus, our postulation to assume mobile lipids on pore surfaces can be justified. Moreover, the order of lateral diffusion coefficients extracted from our lineshape analysis agrees well with other experimental data.[77-79] Even though we consider a potential distribution in the bilayers' normal directions with respect to the glass plate normal direction (n // B_0) and assume a few degrees (10–15°) of a typical mosaic spread of lipid bilayers prepared between glass plates,[64] which results in an asymmetrical half-Gaussian peak pattern along the frequency position of 0° orientation of lipids, the observed anisotropic frequencies spanning over all the anisotropic frequency regions, including the frequency positions close to and along the 90° orientation (− 18 ppm in a ^{31}P spectrum), cannot be explained by this simple mosaic distribution model (Figure 6.4). Moreover, if anisotropic frequencies spanning over the whole spectral range are from discontinuous bilayers that are spread by mosaic distribution, nuclear sites with different anisotropic frequencies would not provide lateral diffusive exchange among different nuclear sites because they are physically separated.

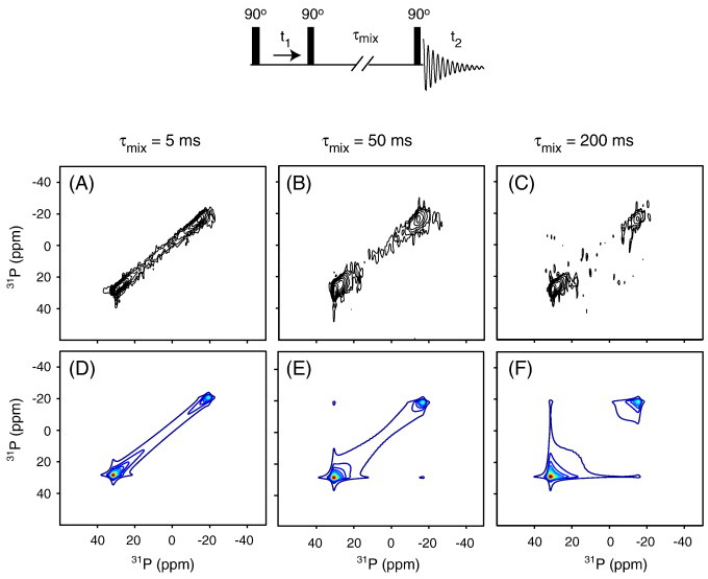

Figure 6.10. 2D ^{31}P exchange NMR spectra of POPC (3)/POPG(1) interacting with aurein-3.3 at P:L = 1:20. Spectra shown for mixing times of 5 ms (A), 50 ms (B), and 200 ms (C). The main features of the experimental 2D spectra were reproduced reasonably well by incorporating a pore geometry model with $a = b$, $d = 1.6b$, and $D_{ld} = 10^{-11}$ cm^2/s.

Several different sizes and shapes of pores and thinned membrane "dimples" would coexist in membranes, and therefore it is more plausible to postulate an ensemble average of these lipid assmblies. AMP-induced lipid pores forming in membranes which are already thinned might explain why we observe the lineshape characteristics of pores and thinned bilayers simultaneously from the experimental spectra. It is natural to assume that AMPs produce various sizes of pores; however, a significant portion of AMP molecules still maintains *S*-binding states, even at a high peptide concentration, because not all of the AMP molecules are allowed to form peptide bundles. Our experimental spectra measured on POPC, POPC/POPG, and POPC/ cholesterol lipids, interacting with magainin-2 and aurein-3.3, support the coexistence of pores with thinned membranes. The relative portions of lipids that are involved in pores and thinned membranes are unclear.

The frequency spans of ^{31}P spectra of POPC/cholesterol lipids interacting with magainin-2 and aurein-3.3 are comparable to those observed without cholesterol, indicating that the presence of cholesterol does not deter the rate of the uniaxial rotation of a lipid around its chain

axis. Actually, the frequency spans of ^{31}P spectra of POPC under the interaction of cholesterol show even narrower widths than those spectra without cholesterol at all P:L ratios. Narrower widths might be explained by considering the increased disorder in lipid bilayers owing to the cholesterol insertion. However, the frequency spans observed in the ^{2}H spectra at all P:L ratios provide dramatic increases in QC parameters at all ^{2}H sites (from 4.0–36.5 kHz without cholesterol to 7.2–65.5 kHz with cholesterol), as shown in Figure 6.7. This result satisfies our general expectation that cholesterol molecules that are inserted into membranes freeze the segmental wobbling motions of hydrophobic acyl chains of lipids, resulting in the increase of ^{2}H's QC tensor parameters. Thus, the magnitudes of site-specific QC couplings in a perdeuterated acyl chain of a phospholipid that is confined in a lipid bilayer are determined not only by the uniaxial rotation of the lipid around its chain axis, but also by the segmental wobbling motion of its acyl chains. As the peptide concentrations increased, the apparent QC parameters decreased, satisfying our prediction based on the thinning model while demonstrating the formation of elliptic toroidal pores with shorter *d* values. For both sample systems, simulations of ^{2}H spectra for all 15 ^{2}H sites in the perdeuterated palmitoyl chain required a lateral diffusion coefficient, $D_{ld} \leq 10^{-11}$ cm^2/s, which is similar to the value obtained from POPC(3)/POPG(1) systems. Based on this observation, we can conclude that cholesterol molecules inserted into membranes do not significantly alter either the rate of either uniaxial rotations or the lateral diffusive rates of lipids, although it freezes the segmental motions of hydrophobic acyl chains.

As a final note, an additional model that was briefly mentioned in the introduction, but not explicitly addressed in the work, is the barrel-stave model.[32] Like the toroidal pore model discussed herein, the barrel-stave mechanism involves peptides inserted vertically into the membrane. A key difference, and one that can be used to differentiate resulting ssNMR lineshapes, is that the barrel-stave model applies to hydrophobic peptides, and it proposes that the lipids basically maintain their positions parallel to the membrane normal direction, which in a ^{31}P or ^{2}H ssNMR spectrum, would add to the intensity at the O° orientation frequency position. Since the barrel-stave model does not involve lipids oriented perpendicular to the membrane normal, it would not account for the lineshapes that were observed in our studies, and so it would not be a fitting model to explain the interactions between magainin-2 or aurein-3.3 and the membrane systems studied here.

6.6. Conclusions

The main goal of the present study was to investigate the AMP-induced structures and dynamics of supramolecular lipid assemblies induced in oriented bilayers on the molecular level by ssNMR spectroscopy. Anisotropic ^{31}P and ^{2}H ssNMR spectra measured on oriented bilayers of POPC-d_{31}, POPC-d_{31}/POPG, and POPC-d_{31}/cholesterol that are interacting with magainin-2 and aurein-3.3 peptides evidenced the presence of elliptic toroidal pores and thinned membrane bilayers. When combined with lateral diffusive dynamics of lipids, these supramolecular lipid assemblies explain well the spectral characteristics of experimental ^{31}P and ^{2}H ssNMR spectra measured on the various lipid systems interacting with magainin-2 and aurein-3.3 at variable P:L ratios. The spectral analysis protocol[43] introduced provides a convenient means to extract the lateral diffusion coefficients of lipids involved on the curved surface of either an AMP-induced pore or a thinned dimple from the lineshape characteristics of motionally averaged ^{31}P and ^{2}H ssNMR spectra that may hitherto have been difficult to characterize. We expect that this protocol would enhance understanding of the cell membrane disruptive mechanisms of various types of membrane-acting AMPs.

References

(1) Papagianni, M. *Biotechnol. Adv.* **2003**, *21*, 465.

(2) Bachére, E. *Aquaculture* **2003**, *227*, 427.

(3) Thomma, B. P. H. J.; Cammue, B. P. A.; Thevissen, K. *Curr. Drug Target Infect. Disord.* **2003**, *3*, 1.

(4) Hancock, R. E. W.; Lehrer, R. *Trends Biotechnol.* **1998**, *16*, 82.

(5) Rozek, T.; Bowie, J. H.; Wallace, J. C.; Tyler, M. J. *Rapid Commu. Mass Spectrom.* **2000**, *14*, 2002.

(6) Cole, A. M. *Protein and Peptide Lett.* **2005**, *12*, 41.

(7) Conlon, J. M. *Rev. in Medical Microbiol.* **2004**, *15*, 17.

(8) Yount, N. Y.; Yeaman, M. R. *Protein and Peptide Lett.* **2005**, *12*, 49.

(9) Rozek, T.; Wegener, K. L.; Bowie, J. H.; Olver, I. N.; Carver, J. A.; Wallace, J. C.; Tyler, M. J. *Eur. J. Biochem.* **2000**, *267*, 5330.

(10) Hoskin, D. W.; Ramamoorthy, A. *Biochim. Biophys. Acta* **2008**, *1778*, 357.

(11) Saberwal, G.; Nagaraj, R. *Biochim. Biophys. Acta* **1994**, *1197*, 109.

(12) Hancock, R. E. W.; Falla, T.; Brown, M. *Adv. Microb. Physiol.* **1995**, *37*, 135.

(13) Nicolas, P.; Mor, A. *Annu. Rev. Microbiol.* **1995**, *49*, 277.

(14) Nissen-Meyer, J.; Nes, I. F. *Archi. Microbiol.* **1997**, *167*, 67.

(15) Edgerton, M.; Koshlukova, S. E.; Lo, T. E.; Chrzan, B. G.; Straubinger, R. M.; Raj, P. A. *J. Biol. Chem.* **1998**, *273*, 20438.

(16) Teuber, M.; Bader, J. *Archi. Microbiol.* **1976**, *109*, 51.

(17) Hwang, P. M.; Vogel, H. J. *Biochem. Cell Biol.* **1998**, *76*, 235.

(18) Matsuzaki, K. *Biochim. Biophys. Acta Biomembr.* **1998**, *1376*, 391-400.

(19) Matsuzaki, K.; Sugishita, K.; Ishibe, N.; Ueha, M.; Nakata, S.; Miyajima, K.; Epands, R. M. *Biochemistry* **1998**, *37*, 11856-11863.

(20) Chen, F. Y.; Lee, M. T.; Huang, H. W. *Biophys. J.* **2003**, *84*, 3751.

(21) Bechinger, B. *Biochim. Biophys. Acta* **1999**, *1462*, 157.

(22) Pouny, Y.; Rapaport, D.; Mor, A.; Nicolas, P.; Shai, Y. *Biochemistry* **1992**, *31*, 12416.

(23) Mazzuca, C.; Stella, L.; Venanzi, M.; Formaggio, F.; Toniolo, C.; Pispisa, B. *Biophys. J.* **2005**, *88*, 3411.

(24) Heller, W. T.; Waring, A. J.; Lehrer, R. I.; Huang, H. W. *Biochemistry* **1998**, *37*, 17331.

(25) He, K.; Ludtke, S. J.; Huang, H. W.; Worcester, D. L. *Biochemistry* **1995**, *34*, 15614.

(26) Wu, Y.; He, K.; Ludtke, S. J.; Huang, H. W. *Biophys. J.* **1995**, *68*, 2361.

(27) Glaser, R. W.; Sachse, C.; Dürr, U. H. N.; Wadhwani, P.; Afonin, S.; Strandberg, E.; Ulrich, A. S. *Biophys. J.* **2005**, *88*, 3392.

(28) Afonin, S.; Grage, S. L.; Ieronimo, M.; Wadhwani, P.; Ulrich, A. S. *J. Am. Chem. Soc.* **2008**, *130*, 16512.

(29) Strandberg, E.; Kanithasen, N.; Tiltak, D.; Burck, J.; Wadhwani, P.; Zwernemann, O.; Ulrich, A. S. *Biochemistry* **2008**, *47*, 2601.

(30) Tremouilhac, P.; Strandberg, E.; Wadhwani, P.; Ulrich, A. S. *Biochim. Biophys. Acta Biomembr.* **2006**, *1758*, 1330.

(31) Wadhwani, P.; Bu rck, J.; Strandberg, E.; Mink, C.; Afonin, S.; Ulrich, A. S. *J. Am. Chem. Soc.* **2008**, *130*, 16515.

(32) He, K.; Ludtke, S. J.; Heller, W. T.; Huang, H. W. *Biophys. J.* **1996**, *71*, 2669.

(33) Ramamoorthy, A.; Thennarasu, S.; Lee, D. K.; Tan, A.; Maloy, L. *Biophys. J.* **2006**, *91*, 206.

(34) Thennarasu, S.; Lee, D. K.; Tan, A.; Prasad Kari, U.; Ramamoorthy, A. *Biochim. Biophys. Acta Biomembr.* **2005**, *1711*, 49.

(35) Porcelli, F.; Buck, B.; Lee, D. K.; Hallock, K. J.; Ramamoorthy, A.; Veglia, G. *J. Biol. Chem.* **2004**, *279*, 45815.

(36) Zasloff, M. *Proc. Natl. Acad. Sci.* **1987**, *84*, 5449.

(37) Apponyi, M. A.; Pukala, T. L.; Brinkworth, C. S.; Maselli, V. M.; Bowie, J. H.; Tyler, M. J.; Booker, G. W.; Wallace, J. C.; Carver, J. A.; Separovic, F. *Peptides* **2004**, *25*, 1035.

(38) Pan, Y. L.; Cheng, J. T. J.; Hale, J.; Pan, J.; Hancock, R. E. W.; Straus, S. K. *Biophys. J.* **2007**, *92*, 2854.

(39) Marcotte, I.; Wegener, K. L.; Lam, Y. H.; Chia, B.; de Planque, M. R. R.; Bowie, J. H.; Auger, M.; Separovic, F. *Chem. Phys. Lipids* **2003**, *122*, 107.

(40) Hirsh, D. J.; Hammer, J.; Maloy, W. L.; Blazyk, J.; Schaefer, J. *Biochemistry* **1996**, *35*, 12733.

(41) Bechinger, B.; Zasloff, M.; Opella, S. J. *Protein Sci.* **1993**, *2*, 2077.

(42) Bechinger, B.; Gierasch, L.; Montal, M.; Zasloff, M.; Opella, S. *Solid State Nucl. Magn. Reson.* **1996**, *7*, 185.

(43) Wi, S.; Kim, C. *J. Phys. Chem. B* **2008**, *112*, 11402.

(44) Cornell, B. A.; Separovic, F.; Baldassi, A. J.; Smith, R. *Biophys. J.* **1988**, *53*, 67.

(45) Hallock, K. J.; Lee, D. K.; Ramamoorthy, A. *Biophys. J.* **2003**, *84*, 3052-3060.

(46) Yamaguchi, S.; Hong, T.; Waring, A.; Lehrer, R. I.; Hong, M. *Biochemistry* **2002**, *41*, 9852-9862.

(47) Buffy, J. J.; McCormick, M. J.; Wi, S.; Waring, A.; Lehrer, R. I.; Hong, M. *Biochemistry* **2004**, *43*, 9800.

(48) Yamaguchi, S.; Huster, D.; Waring, A.; Lehrer, R. I.; Kearney, W.; Tack, B. F.; Hong,
M. *Biophys. J.* **2001**, *81*, 2203.

(49) Yang, L.; Weiss, T. M.; Lehrer, R. I.; Huang, H. W. *Biophys. J.* **2000**, *79*, 2002.

(50) Butterworth, J. *Proc. Phys. Soc.* **1965**, *86*, 297.

(51) Fenske, D. B.; Jarrell, H. C. *Biophys. J.* **1991**, *59*, 55.

(52) Auger, M.; Smith, I.; Jarrell, H. C. *Biophys. J.* **1991**, *59*, 31.

(53) Macquaire, F.; Bloom, M. *Phys. Rev. E* **1995**, *51*, 4735.

(54) Dolainsky, C.; Unger, M.; Bloom, M.; Bayerl, T. *Phys. Rev. E* **1995**, *51*, 4743.

(55) Marasinghe, P.; Buffy, J.; Schmidt-Rohr, K.; Hong, M. *J. Phys. Chem. B* **2005**, *109*, 22036.

(56) Gorenstein, D. G. *Phosphorus-31 NMR: Principles and Applications*; Academic Press: Orlando, 1984.

(57) Mecke, A.; Lee, D. K.; Ramamoorthy, A.; Orr, B. G.; Banaszak Holl, M. M. *Biophys. J.* **2005**, *89*, 4043.

(58) Janshoff, A.; Bong, D. T.; Steinem, C.; Johnson, J. E.; Ghadiri, M. R. *Biochemistry* **1999**, *38*, 5328.

(59) Dolainsky, C.; Karakatsanis, P.; Bayerl, T. *Phys. Rev. E* **1997**, *55*, 4512.

(60) Kaplan, J. I.; Fraenkel, G. *NMR of Chemically Exchanging Systems*; Academic Press: New York, 1980.

(61) Jackman, J. L.; Cotton, F. A. *Dynamic Nuclear Magnetic Resonance Spectroscopy*; Academic Press: New York, 1975.

(62) Yang, L.; Harroun, T. A.; Weiss, T. M.; Ding, L.; Huang, H. W. *Biophys. J.* **2001**, *81*, 1475.

(63) Matsuzaki, K.; Sugishita, K.; Harada, M.; Fujii, N.; Miyajima, K. *Biochim. Biophys. Acta Biomembr.* **1997**, *1327*, 119-130.

(64) Moll, F.; Cross, T. A. *Biophys. J.* **1990**, *57*, 351.

(65) Kim, C.; Spano, J.; Park, E.-K.; Wi, S. *Biochim. Biophys. Acta Biomembr.* **2009**, *1788*, 1482.

(66) Sternin, E.; Fine, B.; Bloom, M.; Tilcock, C.; Wong, K.; Cullis, P. *Biophys. J.* **1988**, *54*, 689-694.

(67) Christensen, B.; Fink, J.; Merrifield, R.; Mauzerall, D. *Proc. Natl. Acad. Sci.* **1988**, *85*, 5072.

(68) Nagle, J. *Biophys. J.* **1993**, *64*, 1476.

(69) Yeagle, P.; Albert, A.; Boesze-Battaglia, K.; Young, J.; Frye, J. *Biophys. J.* **1990**, *57*, 413.

(70) Kessel, A.; Ben-Tal, N.; May, S. *Biophys. J.* **2001**, *81*, 643.

(71) Reyesmateo, C.; Ulises Acuna, A.; Brochon, J. C. *Biophys. J.* **1995**, *68*, 978.

(72) Segrest, J. P.; De Loof, H.; Dohlman, J. G.; Brouillette, C. G.; Anantharamaiah, G. *Proteins: Struct. Funct. Bioinform.* **1990**, *8*, 103-117.

(73) Matsuzaki, K.; Nakamura, A.; Murase, O.; Sugishita, K.-i.; Fujii, N.; Miyajima, K. *Biochemistry* **1997**, *36*, 2104.

(74) Fernandez, D. I.; Gehman, J. D.; Separovic, F. *Biochim. Biophys. Acta Biomembr.* **2009**, *1788*, 1630.

(75) Gennis, R. B. *Biomembranes: Molecular Structure and Function*; Springer: New York, 1989.

(76) De Angelis, A. A.; Nevzorov, A. A.; Park, S. H.; Howell, S. C.; Mrse, A. A.; Opella, S. J. *J. Am. Chem. Soc* **2004**, *126*, 15340.

(77) Saxton, M. J. *Biophys. J.* **1987**, *52*, 989.

(78) Eisinger, J.; Flores, J.; Petersen, W. P. *Biophys. J.* **1986**, *49*, 987.

(79) Lindblom, G.; Orädd, G.; Rilfors, L.; Morein, S. *Biochemistry* **2002**, *41*, 11512.

Chapter 7

Dipolar-Coupling-Mediated Total Correlation Spectroscopy in Solid-State ^{13}C NMR: Selection of Individual ^{13}C-^{13}C Dipolar Interactions

Reproduced in part with permission from Spano, J.; Wi, S. *J. Magn. Reson.*, **2010**, 204, 314.
 All work was performed in the Wi Group at Virginia Tech.

7.1. Introduction

Solid-state NMR (ssNMR) spectroscopy has evolved as a suitable technique for structure determination of a wide variety of sample systems including biomolecules, regardless of the sample's morphology.[1-9] Many techniques developed for structural investigation in ssNMR spectroscopy exploit heteronuclear or homonuclear dipolar couplings between spins to measure internuclear distances, while performing magic-angle-spinning (MAS) to obtain well resolved spectra.[10-16] These techniques provide distance information quantitatively when applied to a selectively labeled spin system that provides isolated dipolar interactions.

When applied on an extensively or uniformly labeled sample system, these techniques normally have limited accuracies for distance measurements. One difficulty that arises in performing such experiments is the dipolar truncation effect; the more informative long-range, weaker dipolar couplings are masked by the less informative short-range, stronger dipolar couplings.[17-19] As a preface, within the context of a correlation experiment, this means that correlations between short-range pairs are more easily detected because the strong dipolar interaction between them is more favorable for magnetization transfer. For an experiment in which dipolar coupling is used to quantitatively measure distances, which is achieved by observing the decay of magnetization of a detected spin, the dipolar truncation effect will lead to the detected spin's dephasing being dictated by the short range interactions. In this case, short-range interactions would cause faster dephasing than long-range, so in essence, the magnetization of the detected spin dephases before it can feel the effect of the long-range interaction. Another type of complication arising from a uniformly labeled sample system is the relayed signal transfer; a signal transfer between two uncoupled nuclei via a third spin that is coupled to both spins.[20] Relayed transfer is undesirable because it provides a false impression of

a correlation, which would then lead to an erroneous structure determination. While these problems may be alleviated by preparing selectively labeled samples, these preparations are time consuming and expensive compared to using uniformly labeled samples; not to mention, much more structural information can be gained from a uniformly labeled sample since many dipolar pairs, hence many geometrical constraints, are available.

Selective heteronuclear distance measurements were implemented in uniformly or extensively labeled samples in the platform of the rotational-echo double resonance (REDOR) technique[10] by incorporating frequency selective pulses to isolate a certain *I*–*S* spin interaction from a complicated I_mS_n spin system.[21] Moreover, multiple, simultaneous ^{13}C–^{15}N distance measurements that were free from any ^{13}C peak broadening effect due to ^{13}C–^{13}C homonuclear *J*-coupling interactions were accomplished in uniformly ^{13}C–^{15}N-labeled samples by employing the three-dimensional (3D) transferred echo double resonance (TEDOR) method, combined with a z-filtering or a selective π-pulse inversion scheme.[22]

Various types of frequency selective techniques have also been developed to accurately measure homonuclear dipolar interactions by curing problems associated with extensively or uniformly labeled samples. The first generation of these techniques includes the rotational resonance (RR)[11,23] and rotational resonance in tilted frame (RRTR)[24,25] which reintroduce the homonuclear dipolar interaction when the chemical shift difference of two spins under consideration matches the MAS spinning frequency. A more elaborate extension of this approach, performed under constant-time mode combined with a selective irradiation scheme, is the rotational resonance width (R^2W) technique,[26-29] that satisfactorily isolates longer range ^{13}C–^{13}C dipolar interactions in uniformly labeled sample systems by varying the spinning speed. These techniques work under moderate-to-slow spinning conditions with spin pairs of relatively big isotropic chemical shift differences.

Recently, chemical shift assisted homonuclear dipolar recoupling methods that produce secularized zero-quantum (ZQ) dipolar Hamiltonians have been introduced. These include the truncated dipolar recoupling (TDR),[30] triple oscillating field technique (TOFU),[31] and zero-quantum shift evolution assisted selective homonuclear recoupling (ZQ-SEASHORE)[32] methods; these have been demonstrated to be useful for selectively measuring distances between homonuclear spin pairs in a weak coupling regime if the difference in chemical shifts between the nuclei in a certain spin pair is greater than the dipolar coupling between them. The TDR

method utilizes a symmetry-based $C3_3^1$ technique[15,16,33,34] that reintroduces ZQ-homonuclear dipolar interactions, as well as the isotropic and anisotropic chemical shift interactions. The TOFU method uses triply oscillating rf fields that allow simultaneous recoupling of isotropic chemical shifts and ZQ-homonuclear dipolar interactions. The ZQ-SEASHORE method consists of alternating blocks of the radio-frequency-driven recoupling (RFDR) sequence[35,36] and free evolution time for chemical shift evolution. Here, the RFDR sequence reintroduces ZQ homonuclear interactions under a high MAS spinning speed (>30 kHz). Chemical shift interactions in the ZQ-SEASHORE, TOFU, and TDR methods truncate the flip-flop terms of ZQ-homonuclear dipolar interactions under a weak coupling regime, resulting in the secularized ZQ-homonuclear dipolar interactions that commute with one another. When combined with a selective irradiation scheme incorporating a Gaussian pulse for frequency selection under a constant-time mode, these methods are very promising for obtaining long-range distance information with minimal dipolar truncation effects. However, a secularized ZQ dipolar Hamiltonian requires a mixing mode along transverse magnetizations, which is less favorable than a mixing mode along longitudinal magnetizations, because of the unfavorable signal loss due to a T_2-relaxation, particularly when NMR signals possess short T_2-relaxation times or the proton decoupling power is not sufficient. A related technique to the ZQ-SEASHORE is the double-quantum shift evolution assisted selective homonuclear recoupling (DQ-SEASHORE) method.[37] This sequence includes alternating blocks of C7,[12] a symmetry-based DQ recoupling sequence, and chemical shift evolution period under a slow-to-moderate spinning condition. The frequency selectivity of DQ-SEASHORE is achieved by adjusting the lengths of the free precession periods.

One detriment of the original implementation of the TDR approach was that the desired ^{13}C–^{13}C homonuclear dipolar recouplings were hindered largely by ^{13}C–^{1}H heteronuclear dipolar couplings that were also reintroduced by the sequence.[30] Magnetizations in transverse mode are quickly attenuated during the mixing period when the mixing scheme is under residual ^{13}C–^{1}H dipolar couplings. This unfavorable signal attenuation effect persists even under a high power proton decoupling. As a result, Levitt and coworkers applied the sequence on a deuterated model compound. A deuterated compound would not require high power decoupling because $\gamma(^1H) \sim 6.5\ \gamma(^2H)$, meaning that ^{13}C-^{2}H heteronuclear dipolar coupling is much weaker than ^{13}C-^{1}H dipolar coupling, and the interaction can more readily be removed by MAS.

This chapter describes an attempt to implement the $C3_3^1$ sequence as a longitudinal mixing block in the scheme of a standard two-dimensional (2D) NMR exchange experiment at the expense of the direct secularization effect. However, this approach obtains the selection of ^{13}C–^{13}C dipolar interactions by incorporating a Gaussian or a cosine-modulated Gaussian pulse[38-40] into the center of the 2D mixing block to partially remove relayed signal transfers as well as dipolar truncation effects from the complicated spin network in the sample system. Furthermore, the removal of the devastating requirement of extreme proton decoupling power required for the original TDR approach, which can burden the probe and damage a sample sensitive to heating, makes this new approach a practical method within the normal decoupling condition for a protonated organic solid. In this scheme, the flip-flop terms of the ZQ-homonuclear dipolar Hamiltonian are utilized for in-phase signal transfers in the strong coupling regime when the isotropic and anisotropic chemical shift terms are refocused at the end of the basic $C3_3^1$ unit in the mixing sequence. So, the essential feature of this approach is to suppress the offset and anisotropic chemical shift terms by π-pulses (composite π-pulses here) placed synchronously in the mixing pulse block. The major gain of this approach is the removal of the devastating requirement of the original TDR approach for an extreme proton decoupling power, which is impractical within the normal experimental condition for a protonated organic solid. Simplification or individualization of ^{13}C–^{13}C dipolar interactions are achieved by incorporating a Gaussian or a cosine-modulated Gaussian pulse[38-40] into the 2D mixing block to remove relayed signal transfers as well as dipolar truncation effects in some favorable conditions. Our approach is reminiscent of the TOCSY experiment,[41] a solution state NMR spectroscopic technique that utilizes the flip-flop terms of *J*-coupling interactions in a strong coupling regime, because our approach utilizes the flip-flop terms of ZQ-homonuclear dipolar couplings for the mixing of longitudinal magnetizations in a strong coupling regime. Hence, we named our approach as the Dipolar-coupling-mediated TOtal Correlation SpectroscopY (DTOCSY).

7.2. Materials and Methods

Samples of ^{13}C-labeled Gly-[U-^{13}C]Ala-[U-^{13}C]Leu (GAL), [U-^{13}C]-Tyrosine, and [U-^{13}C]-Glutamine were used for testing the feasibility of solid-state ^{13}C DTOCSY spectroscopy. Amino acids, [U-^{13}C]-Tyrosine and [U-^{13}C]-Glutamine, were purchased from the Cambridge

Isotope Laboratory (Andover, MA). The [U-^{13}C]-Tyrosine sample was dissolved in 1 M HCl solution and recrystallized by slow evaporation and the [U-^{13}C]-Glutamine sample was used without further treatment. ^{13}C-labeled GAL, was synthesized by Fmoc-based solid-state peptide synthesis at AnaSpec Inc. (San Jose, CA). The synthesized peptide was purified and identified by reverse-phase liquid chromatography and ion-spray ionization mass analyzer, respectively. Subsequently, the peptide was recrystallized by slow evaporation from an aqueous solution. About 20–40 mg of each sample was center-packed into a 4 mm MAS rotor with bottom and top spacers. The sample temperature was kept constant at 22 °C by using a Bruker BCU-X temperature control unit.

^{13}C DTOCSY NMR spectra were recorded on a Bruker Avance II 300 MHz spectrometer with ^{1}H and ^{13}C Larmor frequencies ($\omega_0/2\pi$) of 300.12 MHz and 75.48 MHz, respectively, using the pulse sequence depicted in Figure 7.1A. The 2D experiment begins with ^{1}H magnetization, generated by a $\pi/2$ excitation pulse, being transferred to ^{13}C magnetizations by ramped cross-polarization (CP) for 1 ms. ^{13}C magnetizations then evolve under the chemical shifts of ^{13}C's during the indirect time (t_1), after which they are converted into the longitudinal mode by a $\pi/2$ pulse for DTOCSY mixing for τ_m . Following a $\pi/2$ read pulse after DTOCSY mixing, ^{13}C signals are acquired for the direct acquisition time (t_2). Figure 7.1B illustrates the construction of the DTOCSY mixing sequence.[30] The basic superblock, spanning $12\tau_r$ in length, where τ_r is the rotor period, consists of four $C3_3^1$ units in combination with composite π-pulses, $(\pi/2_x - \pi_y - \pi/2_x)$ positioned at the $3\tau_r$ and $9\tau_r$ time points. The DTOCSY mixing time can be incremented by increasing m (m = 1, 2, …) for observing longer range ^{13}C–^{13}C correlations. The experiment employed a MAS spinning speed, $\omega_r/2\pi$ = 6 kHz, and 48 kHz (8 times the spinning speed) of DTOCSY mixing power to satisfy the condition for $C3_3^1$. $C3_3^1$ consists of three phase-shifted $\tau_r/4 - (90°\overline{360°}270°)_2 - \tau_r/4$ units for $3\tau_r$ (Figure 7.1B), and so a 360° pulse in this pulse block therefore has a length of $\tau_r/8$.[30] Figure 7.1C displays modified DTOCSY sequences for selective spin inversions formulated by inserting a Gaussian, a Gaussian plus a non-selective π, or cosine-modulated Gaussian pulse between two identical DTOCSY blocks. The Gaussian and cosine-modulated Gaussian pulses were generated by Bruker Topspin software with widths of $2–6\tau_r$. The offset frequency during the application of the selective pulse can be optimized for selective inversions. The ^{13}C and ^{1}H 90° pulse times were 5 μs and 3.5 μs, respectively, and spectra were

acquired with 32 scans and a recycle delay of 3.5 s. The pulse power of composite ^{13}C π-pulses was 75 kHz. 2D ^{13}C–^{13}C correlation spectra were obtained with 1024 points in t_2 and 128 points in t_1, with 128 kHz of continuous wave (CW) decoupling during DTOCSY mixing block and 63 kHz of SPINAL-64[42] decoupling during t_2.

7.3. Theoretical

7.3.1. Background

As explained in the previous section, a symmetry-based dipolar recoupling method utilizing the $C3_3^1$ sequence, originally developed as the TDR technique for obtaining ^{13}C–^{13}C dipolar distances with a minimal dipolar truncation effect,[30] can also be used in the standard 2D correlation spectroscopy as an efficient mixing block applied upon longitudinal magnetizations (Figure 7.1). The $C3_3^1$ sequence gives the recoupling terms with space-spin quantum numbers of (l, m, λ, μ) = (2, ±2, 2, 0) and (2, ±1, 2, 0) in dipolar interactions, (l, m, λ, μ) = (2, ±2, 1, 0) and (2, ±1, 1, 0) of CSA, and (l, m, λ, μ) = (0, 0, 1, 0) of both J-coupling and isotropic chemical shift interactions.[15,16,30,34] Here, the rotational properties of the space and spin part of tensors in NMR interaction Hamiltonians are characterized by the rank l and components m ($m = -l, -l + 1, .., l - 1, l$), and the rank λ and components μ ($\mu = -\lambda, -\lambda + 1, \ldots, \lambda - 1, \lambda$), respectively. A windowed double-post pulse element, $90°\overline{360°}270°\overline{90°}360°\overline{270°}$, for $\tau_r/4$–$3\tau_r/4$, combined with free evolution periods for 0–$\tau_r/4$ and $3\tau_r/4$–τ_r of each rotor period in a $C3_3^1$ unit, provides scaling factors of 0.138 and 0 for (2, ±1, 2, 0) and (2, ±2, 2, 0), respectively, of dipolar interaction; of 0.193 and 0 for (2, ±1, 1, 0) and (2, ±2, 1, 0), respectively, of CSA; and of 0.5 for (0, 0, 1, 0) of both isotropic chemical shift and J-coupling interactions.[30] The composite π-pulses placed after the first and third $C3_3^1$ blocks in the basic DTOCSY superblock refocuses both isotropic and anisotropic chemical shift interactions as well as the heteronuclear dipolar interaction terms at the end of basic $C3_3^1$ unit. Therefore, the remaining (2, ±1, 2, 0) term, the zero-order dipolar interaction, and (0, 0, 1, 0) term, the isotropic J-coupling interaction, will be effective at the end of the basic $C3_3^1$ sequence for in-phase signal transfers among magnetizations over the mixing periods.

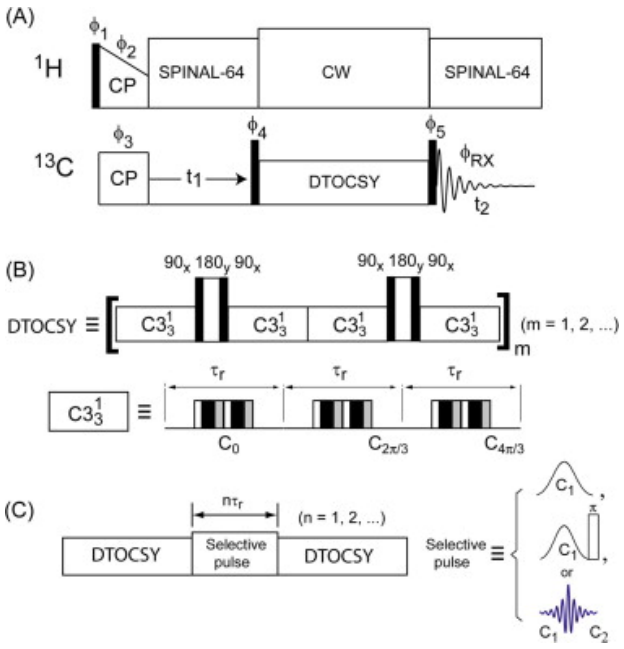

Figure 7.1. Pulse sequence background. (A) A standard 2D exchange spectroscopic pulse sequence used in this experiment incorporating the DTOCSY mixing block. ^{13}C magnetization, created by CP from ^{1}Hs, undergoes chemical shift evolution for t_1 before being converted into the longitudinal mode for DTOCSY mixing. A 90° read pulse converts signals into transverse mode for detection during t_2. Closed rectangles represent π/2 pulses. Proton decoupling was achieved using 63 kHz of SPINAL-64[42] during t_1 and t_2, and 128 kHz of CW during DTOCSY mixing. The detailed phase cycling is published.[43] (B) Schematic of the DTCOSY mixing sequence, which is identical to the TDR sequence except for the composite π-pulses in the mixing block. Each DTOCSY block consists of a total of 4-$C3_3^1$ blocks, with composite π-pulses at the τ_m /4 and 3 τ_m /4 positions of the DTOCSY sequence: the τ_m of a single DTOCSY mixing unit spans 12 rotor periods (12τ_r). The τ_m increases by increasing the index m (m = 1, 2, …). (C) A Gaussian, Gaussian plus a non-selective π, or cosine-modulated Gaussian pulse placed in between DTOCSY mixing periods, spanning ideally an integer number of rotor periods, were employed to selectively irradiate certain spins in the ^{13}C spin network, leading to spectral simplification. This composite pulse block takes 24τ_r as a basic mixing time.

The flip-flop terms of the remaining ZQ dipolar Hamiltonian thus produce correlations between ^{13}C nuclei, mimicking the J-modulated TOCSY spectroscopy developed in solution state NMR.

The negligible influence of the isotropic *J*-coupling term in the DTOCSY mixing will be proven numerically in the next section.

7.3.2. In-Phase DTOCSY Signal Transfer

An isolated homonuclear dipolar coupled spin pair, *I*–*S* (*I* = *S* = ½), is considered for understanding the basic characteristics of in-phase signal transfer of DTOCSY mixing. The average Hamiltonian, the (2, ±1, 2, 0) term of the zero-order dipolar interaction and the (0, 0, 1, 0) term of the isotropic *J*-coupling interaction, operative during the DTOCSY mixing is:[30]

$$\overline{\omega}_0 2I_z S_z + \overline{\omega}_{\pm}(I_x S_x + I_y S_y) \tag{7.1}$$

with $\overline{\omega}_0 = 2\pi(\nu_d + J/2)$ and $\overline{\omega}_{\pm} = 2\pi\nu_m = 2\pi(J - \nu_d)$, where ν_d and J are the strength of dipolar coupling and *J*-coupling interaction, respectively. Longitudinal magnetizations, $(I_z + S_z)$, under the influence of the average Hamiltonain during the DTOCSY mixing period are influenced only by the second term, $2\pi\nu_m(I_xS_x+I_yS_y)$, and propagate according to:

$$\begin{aligned} I_z &\xrightarrow{2\pi\nu_m(I_xS_x+I_yS_y)\tau_m} I_z\cos^2(\pi\nu_m\tau_m) + S_z\sin^2(\pi\nu_m\tau_m) \\ &+ (I_xS_y - I_yS_x)\sin(2\pi\nu_m\tau_m) \end{aligned} \tag{7.2}$$

and

$$\begin{aligned} S_z &\xrightarrow{2\pi\nu_m(I_xS_x+I_yS_y)\tau_m} I_z\sin^2(\pi\nu_m\tau_m) + S_z\cos^2(\pi\nu_m\tau_m) \\ &- (I_xS_y - I_yS_x)\sin(2\pi\nu_m\tau_m) \end{aligned} \tag{7.3}$$

Eqs. 7.2 and 7.3 dictate that the sum, $I_z + S_z$, is constant and the difference, $I_z - S_z$, is given by:

$$(I_z - S_z) \xrightarrow{2\pi\nu_m(I_xS_x+I_yS_y)\tau_m} (I_z - S_z)\cos(2\pi\nu_m\tau_m) + -(2I_xS_y - I_yS_x)\sin(2\pi\nu_m\tau_m) \tag{7.4}$$

When $\tau_m = n/2\nu_m$ (n = 1, 3, 5, …), I_z magnetization is completely transferred to S_z and vise versa.

In crystalline powdered sample, the magnitude of ν_d is however orientationally dependent and therefore the signal transfer efficiency will show orientation dependency.

To test the efficiency of the in-phase signal transfer of our approach, brute force calculations were carried out using a home-built program written under Matlab programming environment on a dipolar coupled system taken from C′, C^{α}, and C^{β} carbons existing in an amino acid, explicitly considering all the relevant CSA, *J*, and dipolar interactions for DTOCSY mixing. Chemical shift, dipolar coupling, and *J*-coupling parameters considered in the simulations are summarized in Table 7.1. The dipolar coupling between C′ and C^{β} is purposely not included in this simulation in order to clearly investigate the efficiency of the relayed signal transfer via $C' \rightarrow C^{\alpha} \rightarrow C^{\beta}$. The initial magnetization was given only to C′, and the signal transfer to C^{α} and C^{β} was monitored by increasing τ_m. Figure 7.2A and B shows thus obtained magnetization transfers, $C' \rightarrow C^{\alpha}$ and $C' \rightarrow C^{\alpha} \rightarrow C^{\beta}$, without (Figure 7.2A) and with (Figure 7.2B) considering *J*-coupling interactions between C′–C^{α} and C^{α}–C^{β} pairs. Both signal transfers occurred efficiently within the first point (<4 ms) and maintain efficiency within 20–30% for the $C' \rightarrow C^{\alpha}$ transfer and 10–12% for the $C' \rightarrow C^{\alpha} \rightarrow C^{\beta}$ transfer throughout the τ_ms considered. As can be seen from Figure 7.2, it is clear that *J*-coupling interactions don't significantly influence the DTOCSY signal transfers. The relayed fashion of signal transfer, $I_z \rightarrow S_z \rightarrow K_z$, would provide total correlation patterns among ^{13}C nuclei in the dipolar coupled network. This property together with the dipolar truncation effect would complicate quantitative peak interpretations. As will be explained in the next section, however, isolation of individual ^{13}C–^{13}C dipolar interactions in 2D DTOCSY spectra can be achieved in some favorable cases by incorporating selective inversion of magnetizations utilizing a soft pulse, such as a Gaussian or cosine-modulated Gaussian pulse.

Table 7.1 Chemical Shift Parameters Incorporated for Simulations in Figure 7.2

	δ_{iso} (ppm)	δ_{CSA} (ppm)	η	ν_d (C'-C^{α})	ν_d (C'-C^{β})
C'	120	81	0.91	2.18 kHz	2.22 kHz
C^{α}	0	35	0.35	J (C'- C^{α})	J (C^{α} -C^{β})
C^{β}	-15	30	0.3	55 Hz	35 Hz

Chemical shift tensor parameters are defined as δCSA = $\delta zz - \delta$iso and $\eta = (\delta xx - \delta yy)/\delta$CSA, where $|\delta zz - \delta$iso$|$ $|\delta xx - \delta$iso$|$ $|\delta yy - \delta$iso$|$ and δiso = $(\delta xx + \delta yy + \delta zz)/3$.

Similar to the *J*-coupling mediated proton TOCSY spectroscopy developed in solution state NMR,[41] the offset difference, the relative peak separation between the coupled nuclei, generally has a significant influence on the efficiency of the DTOCSY mixing.

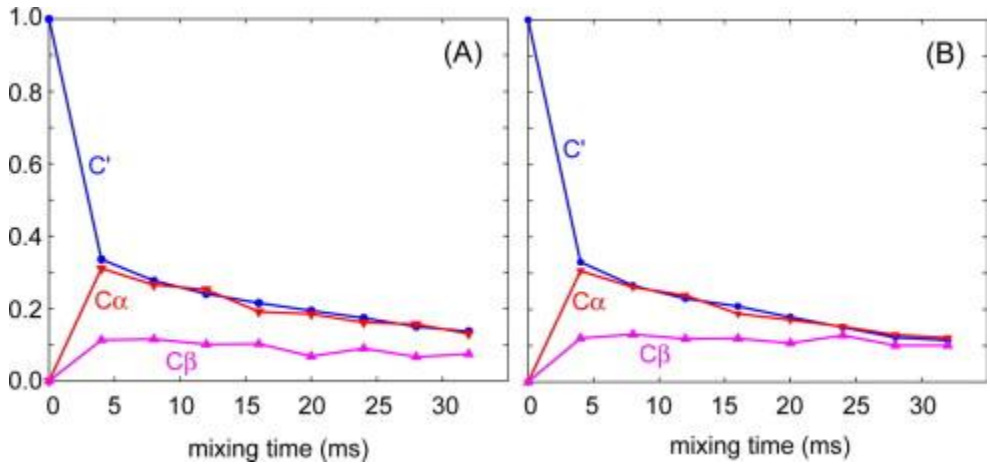

Figure 7.2. DTOCSY simulations on a three-spin system, C′–C^{α}–C^{β}, in the standard geometry of an amino acid. Simulations demonstrate the efficiencies of C′ → C^{α} and C′ → C^{α} → C^{β} signal transfers via dipolar couplings. The *J*-coupling influence is negligible as the simulation data without (A) and with (B) the *J*-coupling influences do not show any significant differences. Dipolar coupling strengths are calculated based on the known C′–C^{α} (2.18 kHz) and C^{α}–C^{β} (2.22 kHz) distances, but the C′–C^{β} coupling was omitted in the simulation to calculate the relayed signal transfer, C′ → C^{α} → C^{β} explicitly. Isotropic and anisotropic chemical shifts of typical C′, C^{α}, and C^{β} carbons as well as the *J*-coupling parameters of C′–C^{α} (55 Hz) and C^{α}–C^{β} (35 Hz) bonds were considered, while taking the isotropic chemical shift position of C^{α} as the on-resonance point. Initially, only the longitudinal magnetization of C′ was assigned before applying DTOCSY mixing. Directly bonded C′–C^{α} transfer reaches the maximum efficiency at the first point of the mixing time and maintains 20–30% of efficiency throughout the mixing time, while gradually decreasing its efficiency as the mixing time increases. The relayed signal transfer also reached its maximum efficiency at the first point and maintains about 10% relative efficiency throughout the mixing time.

However, as can be seen in Figure 7.2 and the following experimental spectra (Figure 7.7-7.9),

the offset tolerance of the DTOCSY signal transfer was evidenced in the usual chemical shift ranges of C′ ,C^{α}, and C^{β} at $\omega_r/2\pi$ of 6–8 kHz. The signal transfer between C′ and C^{α} was very efficient (20–30%) although the isotropic chemical shift difference between C′ and C^{α} (120 ppm) and the magnitude of CSA of C′ (δ_{CSA} = 81 ppm, η = 0.91) were very large.

Optimal in-phase ^{13}C–^{13}C correlations, observed by utilizing the flip-flop terms of the ZQ dipolar Hamiltonian that are reintroduced by the $C3_3^1$ sequence, have demonstrated offset-dependent dipolar recoupling conditions that reminisce the rotational resonance condition. The offset dependence on the $I_z \rightarrow S_z$ transfer efficiency was investigated by varying the offset frequencies, δ, of both nuclei, I_z and S_z, from −150 ppm to 150 ppm in the simulations as shown in Figure 7.3. The $I_z \rightarrow S_z$ signal transfer is efficient at spots on the 2D map satisfying $|\delta_1-\delta_2|=n\nu_r$ (n = 0, 1, and 2), where $\nu_r = \omega_r/2\pi$, with about 40–50 ppm widths per spot along both offset dimensions. The origin of this phenomenon is not clear, but the isotropic chemical shift difference between dipolar coupled spins obviously takes a role in that when it matches ν_r, the dipolar coupling strength between these spins is reintroduced more effectively, as in the case of the rotational resonance mechanism.[11] For instance, two adjacent favorable regions along each offset dimension are separated from each other by $\omega_r/2\pi$ as can be identified in Figure 7.3B, which is about 80 ppm ($\omega_r/2\pi$ = 6 kHz; $\omega_0/2\pi$ = 75 MHz). Regions having efficient $I_z \rightarrow S_z$ signal transfer in Figure 7.3B correspond to the regions of low I_z signal in Figure 7.3A in most cases. However, some regions with low I_z signal intensity do not possess efficient $I_z \rightarrow S_z$ transfer; these regions would produce efficient $I_z \rightarrow 2(I_xS_y-I_yS_x)$ transfers, where the $2(I_xS_y-I_yS_x)$ term corresponds to the zero-quantum coherence.

7.3.3. Simplification of Correlations and Selection of Individual Dipolar Interactions

For simplifying a 2D ^{13}C–^{13}C DTOCSY spectrum and/or isolating individual dipolar interactions, we incorporated a Gaussian, a Gaussian with a non-selective 180° pulse, or a cosine-modulated Gaussian pulse in the DTOCSY sequence (Figure 7.1C). A selective inversion pulse block is concatenating two identical ZQ-recoupling pulse blocks of the same τ_m along both sides, so that the action of the first ZQ-recoupling sequence is refocused by the second sequence when the selective inversion pulse inverts a spin in a dipolar coupled pair. Thus, any ^{13}C–^{13}C dipolar couplings that involve only a single inverted spin will be removed from the 2D

correlations in the spectra at the end of the composite DTOCSY block. When a spin is irradiated using a selective inversion pulse, the selected spin possesses a negative diagonal-peak and takes suppressed cross-peaks with any non-selected spins in the network. If both spins of a dipolar pair are inverted, then the dipolar interaction is retained after the overall mixing block.

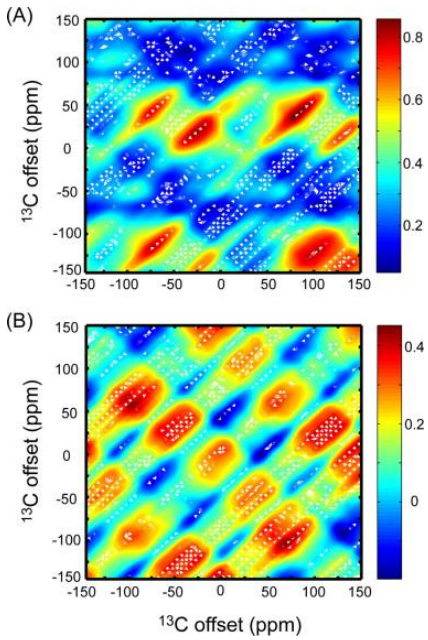

Figure 7.3. Simulations showing the offset dependencies of the $I_z \rightarrow S_z$ DTOCSY signal transfer. The signal transfer was calculated by changing the offset frequencies of *I* and *S* spins from −150 ppm to 150 ppm ($\omega_0/2\pi$ = 75 MHz), considering an arbitrary dipolar coupling strength of 1.2 kHz, and defining the CSA of *I* and *S* nuclei as 81 ppm (η = 0.91) and 30 ppm (η = 0.30), respectively. We provided only the I_z magnetization initially and monitored the $I_z \rightarrow S_z$ transfer (B) as well as the remaining I_z magnetization (A) by changing the offsets of both nuclei. Contour levels indicate relative signal intensities of the remaining I_z (A) and the transferred S_z magnetizations (B) that are normalized by the initial input intensity of the I_z magnetization. In (B), many favorable $I_z \rightarrow S_z$ transfer conditions that are formed roughly at the frequencies satisfying $|\underline{\delta_1}\text{-}\underline{\delta_2}| = n\nu_r$ (n = 0, 1, and 2), are evidenced on the two-dimensional map, with a width of ~50 ppm along both offset domains per each favorable spot.

The cross-peaks between two selected spins are retained with negative intensities. A dipolar coupling interaction between two non-selected spins, since untouched, provides both positive

diagonal- and cross-peak intensities in a 2D spectrum.

These predictions can easily be verified by considering the evolution of magnetizations under the influence of the composite DTOCSY mixing block, incorporating a selective pulse. For an *I*–*S* spin pair, when a Gaussian pulse that is placed in the middle of the two identical ZQ-recoupling mixing periods inverts only the *I*-spin, the signal produced by the whole DTOCSY mixing block will be:

$$I_z \xrightarrow{2\pi\nu_m\tau_m(I_xS_x+I_yS_y)} \xrightarrow{180°_x(I)} \xrightarrow{2\pi\nu_m\tau_m(I_xS_x+I_yS_y)} -I_z\cos(2\pi\nu_m\tau_m)+2I_yS_x\sin(2\pi\nu_m\tau_m) \qquad (7.5)$$

Therefore, the action of the pulse block results in an inverted I_z spin and $2I_yS_x$ term, half the original ZQ-coherence terms produced without the selective π-pulse (Eqs. 7.2 and 7.3), while producing no in-phase signal transfer to the *S* spin. Likewise, the non-irradiated *S* spin evolves under the *I*-spin irradiation according to:

$$S_z \xrightarrow{2\pi\nu_m\tau_m(I_xS_x+I_yS_y)} \xrightarrow{180°_x(I)} \xrightarrow{2\pi\nu_m\tau_m(I_xS_x+I_yS_y)} S_z\cos(2\pi\nu_m\tau_m)-2I_xS_y\sin(2\pi\nu_m\tau_m) \qquad (7.6)$$

The pulse block still does not produce the in-phase $S_z \rightarrow I_z$ signal transfer, and keeps the original sign of S_z as expected because it was not irradiated by the inversion pulse. Furthermore, combining Eqs. 7.5 and 7.6, the DTOCY pulse block with *I*-spin irradiation results in the zero-quantum coherence term, $2(I_yS_x - I_xS_y)$, which is still half of the ZQ-coherence terms obtained without selective π-pulse, that can be removed at the time points satisfying $\tau_m = n/2\nu_m$ (n = 1, 2, …), where $\nu_m = J - \nu_d$, and J and ν_d are ^{13}C–^{13}C *J*-coupling and dipolar coupling constants, respectively. At these time points of the mixing period, the *I*–*S* homonuclear dipolar coupling is null. Thus, an *I*–*S* dipolar coupling can be removed completely from the spin network at these time points in the mixing time when either *I*- or *S*-spin is inverted.

If both *I* and *S* spins are inverted simultaneously by, for instance, a cosine-modulated Gaussian pulse, the $I_z \rightarrow S_z$ signal transfer is retained with both spins inverted:

$$I_z \xrightarrow{2\pi\nu_m\tau_m(I_xS_x+I_yS_y)} \xrightarrow{180°_x(I,S)} \xrightarrow{2\pi\nu_m\tau_m(I_xS_x+I_yS_y)} -I_z\cos^2(2\pi\nu_m\tau_m)-S_z \times\sin^2(2\pi\nu_m\tau_m)+(I_yS_x-I_xS_y)\sin(4\pi\nu_m\tau_m) \qquad (7.7)$$

Similarly, the $S_z \rightarrow I_z$ transfer is provided as:

$$S_z \xrightarrow{2\pi\nu_m\tau_m(I_xS_x+I_yS_y)} \xrightarrow{180^\circ_x(I,S)} \xrightarrow{2\pi\nu_m\tau_m(I_xS_x+I_yS_y)} -S_z\cos^2(2\pi\nu_m\tau_m) - I_z \times\sin^2(2\pi\nu_m\tau_m) + (I_xS_y - I_yS_x)\sin(4\pi\nu_m\tau_m) \quad (7.8)$$

The sum of Eqs. 7.7and 7.8 is : $-(I_z + S_z)$. Therefore, when both *I* and *S* spins are irradiated, the spectral correlation between *I* and *S* can be isolated from the dipolar correlations involving other spins in a 2D spectrum. Potential relayed signal transfers from a non-irradiated spin, K, to *I* or *S* can be effectively blocked in this mode. However, the removal of dipolar interactions with non-irradiated spins is marginal due to the presence of ZQ-coherence terms formed with non-irradiated spins [i.e. $2(I_yK_x - I_xK_y)$ or $2(S_yK_x - S_xK_y)$] except at time points specified by $\tau_m(IK) = n/2\nu_m(IK)$ and $\tau_m(SK) = n/2\nu_m(SK)$, ($n$ = 1, 2, …). A complete isolation of an *I*–*S* spin pair from the *I*–*S*–*K* system would be feasible at certain time points. However, when multiple spin pairs are involved, it would be impractical to remove the many ZQ-coherence terms formed between non-irradiated spins and *I* or *S* simultaneously. Thus, a simultaneous irradiation of *I* and *S* provides a way to partially remove signal transfers via relayed fashions as well as dipolar truncation effects. Therefore, this irradiation mode would be useful for isolating a specific ^{13}C–^{13}C interaction more precisely from the crowded interactions in the spin network originating from an extensively/uniformly labeled protein/peptide sample. Practically, effective irradiation on both *I* and *S* would depend on the frequency selection efficiency of selective inversion pulses, the inversion profiles of selected frequency ranges, and the length of the DTOCSY mixing sequence. A selective soft pulse or a magnitude-modulated selective soft pulse scheme that provides narrow, uniform inversion profiles in the chosen spectral windows is necessary for effectively selecting a particular dipolar interaction for distance measurement.

Figure 7.4 shows numerically simulated signal transfers among nuclear spins in a model 3-^{13}C-spin system under the DTOCSY mixing, incorporating a selective inversion pulse with corresponding spin network diagrams drawn. The Larmor frequency and the MAS spinning speed used are 75 MHz and 8 kHz, respectively, the magnitudes of isotropic and anisotropic chemical shift parameters are shown in the inset table of the figure, and the strength of dipolar couplings involved are designated in the spin network diagram in the figure. Unless specified explicitly, our simulations assumed 100 kHz of the pulse power for the $90_x180_y90_x$

composite pulses and coincident dipolar/dipolar and dipolar/CSA tensor orientations.

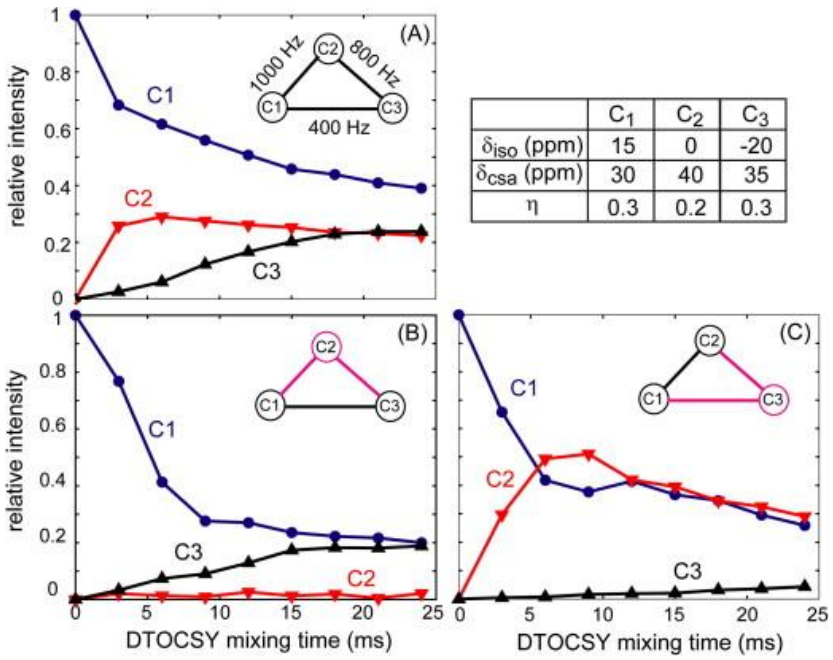

	C_1	C_2	C_3
δ_{iso} (ppm)	15	0	-20
δ_{csa} (ppm)	30	40	35
η	0.3	0.2	0.3

Figure 7.4. Simulations showing the selective signal transfers incorporating a Gaussian pulse in the DTOCSY block. A model 3-^{13}C-spin system (C_1 (blue circles/solid line), C_2 (red triangles/solid line), and C_3 (black triangles/solid line)) is considered. Isotropic and anisotropic chemical shift tensors are shown in the table. The C_1–C_2, C_1–C_3, and C_2–C_3 homonuclear dipolar coupling strengths are 1 kHz, 0.2 kHz, and 0.8 kHz, respectively (A). Simulations demonstrate the effect of the absence (A) or presence of a single Gaussian pulse irradiated at C_2 (B) and C_3 (C). In all cases longitudinal magnetization of C_1 is the initial source of magnetization for the system. The intensities of the magnetization for the spins over time is relative to the original C_1 magnetization. Selectively irradiated spins are designated as pink circles, with the bonds from those spins also in pink to indicate spin pairs with suppressed homonuclear dipolar coupling interactions. A dipolar interaction which involves a single inverted spin is suppressed as can be identified in the simulations.

In Figure 7.4A is shown a simulation in which the homonuclear dipolar coupling between all three ^{13}C spin pairs in the network are considered without a selective inversion pulse. Beginning with longitudinal magnetization of C_1 being fed into the mixing block, the C_1 magnetization can

then be transferred to C_2 and C_3 through homonuclear dipolar couplings, reducing the relative intensity of C_1 and increasing the relative intensity of C_2 and C_3, as expected. Initially there is a much faster buildup of for C_2 than for C_3 due to the stronger C_1–C_2 homonuclear dipolar coupling interaction. After reaching a maximum value, there is a constant intensity region or even a small decrease in relative C_2 intensity at a long mixing time. Figure 7.4B and C demonstrate the effect of a selective soft pulse applied on C_2 and C_3, respectively, in the 3-^{13}C-spin system, with the corresponding spin network diagrams shown adjacent to the relative intensity plots. Figure 7.4B shows the effect of the selective irradiation on C_2. It can be seen that the $C_1 \rightarrow C_2$ transfer is virtually zero, and there is only significant magnetization transfer for $C_1 \rightarrow C_3$. Due to the weak C_1–C_3 homonuclear dipolar coupling, and absence of $C_1 \rightarrow C_2 \rightarrow C_3$ transfer, magnetization buildup for C_3 takes slightly longer as compared to Figure 7.4A. When the selective inversion pulse inverts C_3 (Figure 7.4C), there is almost no noticeable magnetization buildup for C_3, but a quick relative intensity buildup for C_2. The C_2 signal experiences a quicker buildup since it is not losing its magnetization to C_3.

To examine the efficiency of selecting a spin pair using a DTOCSY sequence combined with an amplitude-modulated Gaussian pulse, a model 4-^{13}C-spin system was used (Figure 7.5); the theoretical relative intensity plots for different cases are shown with their corresponding spin network diagrams adjacent. The magnitudes of isotropic and anisotropic chemical shift parameters considered in the simulations are summarized in the inset table of Figure 7.5. $\omega_0/2\pi$ and $\omega_r/2\pi$ are 75 MHz and 6 kHz, respectively, and the strength of dipolar couplings are designated in the spin network diagram. In Figure 7.5A is shown the case where all homonuclear dipolar coupling interactions between the spins in the network are considered. The relative intensity of C_2 and C_3, which have1 kHz of dipolar coupling with C_1, has faster buildup than C_4, which only has 700 Hz of dipolar coupling with C_1. Though C_2 and C_3 possess identical dipolar coupling strengths with C_1, C_3 has a slower build-up curve because the relative offset of C_3 from C_1 is −35 ppm, whereas the offset of C_2 from C_1 is 15 ppm. Figure 7.5B exhibits the case where a cosine-modulated Gaussian pulse simultaneously irradiates both C_1 and C_2. As predicted by Eq. 7.7, Figure 7.5B demonstrates the retention of $C_1 \rightarrow C_2$ magnetization transfer and suppression of transfers to C_3 and C_4, as shown by the overall low intensities of C_3 and C_4. Low intensities are expected since inverting the magnetizations of both C_1 and C_2 retains their homonuclear dipolar coupling, but suppresses the dipolar coupling interactions with C_3 and C_4.

Simulations in Figure 7.6 examine the finite pulse effect of the composite π-pulse in the sequence (Figure 7.1), and the non-coincident dipolar/dipolar and dipolar/CSA tensor orientations.

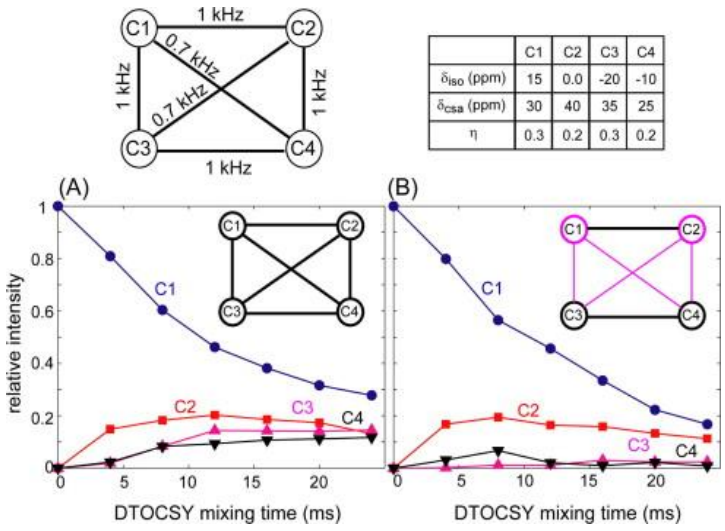

	C1	C2	C3	C4
δ_{iso} (ppm)	15	0.0	-20	-10
δ_{csa} (ppm)	30	40	35	25
η	0.3	0.2	0.3	0.2

Figure 7.5. Simulations demonstrating a retention of dipolar couplings when two spins are irradiated. A model 4-^{13}C-spin system (C_1 (blue circles/solid line), C_2 (red squares/solid line), C_3 (pink triangles/solid line), and C_4 (black triangles/solid line)) was considered under DTOCSY mixing over time in the absence (A) or presence (B) of a selective, cosine-modulated Gaussian pulse placed in between mixing blocks. As in Figure 7.4, longitudinal magnetization of C_1 is the initial source of magnetization. Dipolar coupling strengths are shown above (A): C_1–C_2 = C_1–C_3 = C_2–C_4 = C_3–C_4 (1 kHz) and C_1–C_4 = C_2–C_3 (0.7 kHz). The magnitudes of isotropic and anisotropic chemical shift interactions are specified in the inset table. Relative orientations between the dipolar and CSA tensors are ignored for simplicity. As predicted by Eq.7.6, selectively irradiated spins in a dipolar pair, indicated as in Figure 7.4, provide the retention of the signal transfer, with inverted intensities (B).

The finite pulse effect is the interference of recoupling under MAS due to the pulse length being a significant portion of $1\tau_r$, providing a window for spins to evolve during the pulse. This effect contrasts with the normal assumption of the pulses being delta pulses, meaning that they are infinitely narrow, and no spin evolution occurring during the pulse. Here, a three-spin

system (ref. Figure 7.4) was incorporated again with non-coincident dipolar/CSA (Figure 7.6A) and dipolar/dipolar (Figure 7.6B) tensor orientations.

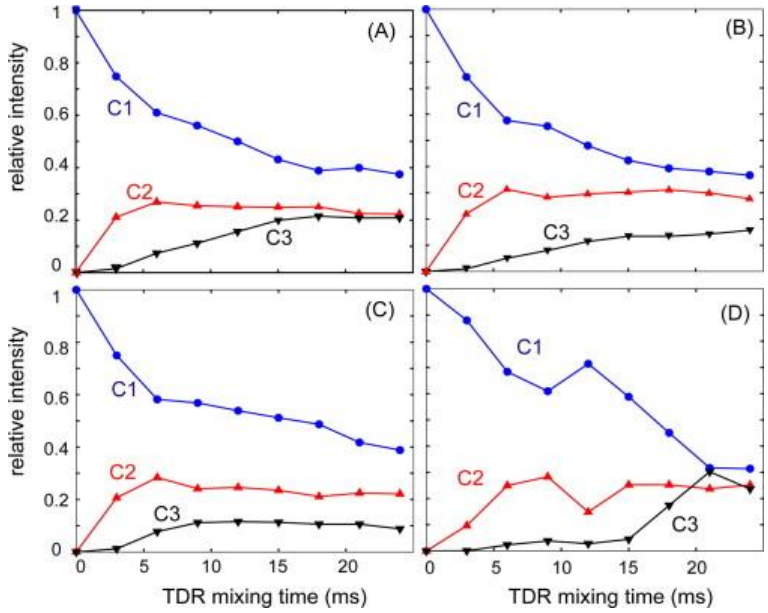

Figure 7.6. Simulations showing the finite pulse effect and the effect of non-coincident relative tensor orientations (dipolar/CSA, or dipolar/dipolar vectors) demonstrated on the three ^{13}C sites considered in Figure 7.4. The intensities of magnetization for the spins over time is relative to the original C_1 magnetization. (A) A case with non-coincident dipolar and CSA tensors, while maintaining the orientations of three dipolar vectors in parallel: $CSA(C_1) \xrightarrow{(30°,20°,0°)} D(C_1\text{-}C_2)$; $CSA(C_2) \xrightarrow{(20°,20°,0°)} D(C_1\text{-}C_2)$; $CSA(C_3) \xrightarrow{(10°,30°,0°)} D(C_1\text{-}C_2)$. (B) A case with non-parallel dipolar vectors, while maintaining coincident dipolar and CSA tensors: $D(C_1\text{-}C_3) \xrightarrow{(0°,30°,0°)} D(C_1\text{-}C_2)$; $D(C_2\text{-}C_3) \xrightarrow{(0°,40°,0°)} D(C_1\text{-}C_2)$. (C) A finite pulse effect with 50 kHz pulse power for the $90_x180_y90_x$ composite π-pulses in the sequence. (D) Case for an ill efficiency of signal transfers among spin sites when a single π-pulse version is incorporated in the sequence instead of the original composite pulse version, even with 100 kHz rf pulse power. All coincident dipolar and CSA tensor orientations are considered in (C) and (D).

Based on our numerical simulations, both non-coincident dipolar/CSA (Figure 7.6A) and dipolar/dipolar (Figure 7.6B) interactions decrease the efficiencies of internuclear signal transfers, as can be identified by comparing both Figure 7.6A and B to Figure 7.4A, which

considers coincident dipolar/dipolar and dipolar/CSA tensor orientations. This may imply that if a ZQ-dipolar recoupling technique that can suppress chemical shift interactions, i.e. RFDR or $R6_6^2$,[33] is used in the mixing scheme, interference between dipolar and CSA tensors can be eliminated. Demonstrated in Figure 7.6C is a finite rf pulse effect that results in less efficient magnetization transfers when an insufficient pulse power (50 kHz) is used for the composite π-pulses in the sequence. However, as demonstrated in Figure 7.6D, with a single π-pulse version, again the overall magnetization transfer is much less efficient than when a composite π-pulse is used, even with 100 kHz of rf pulse power. Thus, composite π-pulses are needed in the sequence of $C3_3^1$ to better refocus chemical shifts, particularly when significant offset differences or rf pulse inhomogeneities are factors. In Figure 7.6C and D, we assumed coincident dipolar/dipolar and dipolar/CSA orientations for simplicity.

7.4. Experimental Results

An objective in developing the DTOCSY sequence is to address the proton decoupling problem of the original TDR approach by applying the sequence along the longitudinal mode of magnetizations as a mixing block of a standard 2D homonuclear correlation scheme. We have tested continuous wave (CW), TPPM,[44] SPINAL-64,[42] and COMARO-2,[45] at various ^{1}H decoupling strengths during DTOCSY mixing period for performing ^{13}C–^{1}H heteronuclear dipolar decoupling; $\omega_r/2\pi$ and thus the power of ^{13}C channel during DTOCSY block were 6 kHz and 48 kHz, respectively. Figure 7.7 shows the variation in signal intensities of various ^{13}C sites in [U-^{13}C, ^{15}N]-Tyrosine·HCl as a function of DTOCSY mixing time under decoupling strengths of 128 kHz (red) and 105 kHz (black). To examine the efficiency for each decoupling technique, the intensity ratio of two experiments was calculated: (1) an experiment in which DTOCSY mixing is applied and (2) one where DTOCSY mixing is absent, while keeping the same delay time used for the DTOCSY sequence. In this approach, the proton decoupling problem is bypassed as can be seen in Figure 7.7. The application of a proton decoupling strength, $\nu_1(^1\text{H}) \geq 2\text{–}2.3\nu_1$ (^{13}C), a typical d power requirement for obtaining dipolar or CSA recoupling along the ^{13}C channel ,[46,47] was sufficient. As expected, by looking at Figure 7.7A-C, it can be noted that C′ with no attached protons is least sensitive to the heteronuclear decoupling techniques, followed by C^{α} with one attached proton, and CH_2 with two attached

protons is most sensitive. For the most part, taking into account the plots for all three sites, there is a consistent trend among the peak intensity curves that there is greater efficiency at 128 kHz decoupling, and in terms of the different methods, CW was the most efficient, follow by TPPM, COMARO-2, and SPINAL-64.

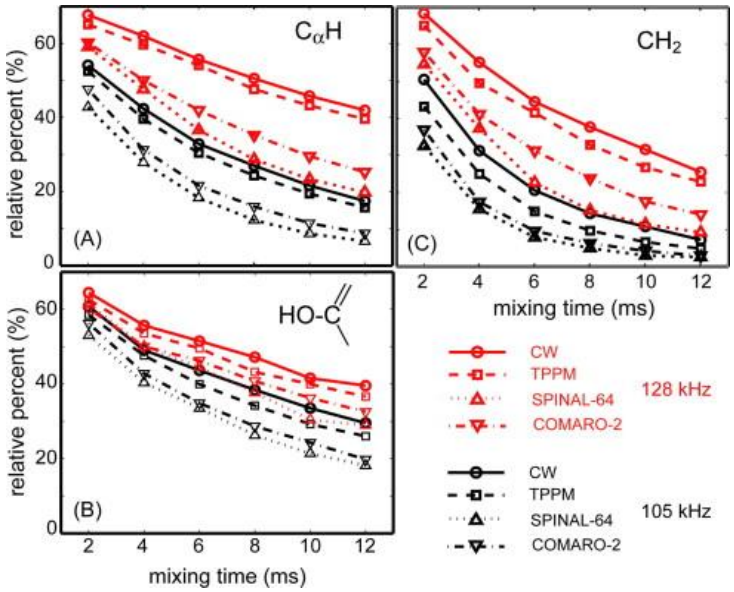

Figure 7.7. Experimental ^{13}C signal intensity curves demonstrating the efficiency of different proton decoupling schemes applied during DTOCSY mixing. Schemes are: CW (circles with a solid line), TPPM (squares with a dashed line),[44] SPINAL-64 (triangles with a dotted line),[42] and COMARO-2 (inverted triangles with a dashed-dotted line).[45] Decoupling efficiencies were compared by inspecting experimental data obtained on the C^{α} (A), C′ (B), and C^{β} (C) of the [U-^{13}C, ^{15}N]-Tyrosine·HCl, at decoupling rf field strengths of 105 kHz (black) and 128 kHz (red). The relative intensities displayed were found by comparing experiments in which DTOCSY mixing was performed to experiments where mixing was excluded. In both cases, the CW mode was the best among the specified methods when combined with DTOCSY sequence. The decoupling efficiency with a CW mode at 128 kHz ($\nu_1(^{13}C)$ = 48 kHz) was acceptable for all three types of carbons throughout the mixing time up to 12 ms.

Figure 7.8 shows experimental ^{13}C–^{13}C homonuclear correlation spectra of 20% Gly-[U-^{13}C, ^{15}N]Ala-[U-^{13}C, ^{15}N]Leu (GAL) in natural abundance GAL, measured at ν_r = 6 kHz and ν_1

($C3_3^1$) = 48 kHz, with 128 kHz of proton decoupling power and τ_m = 2–20 ms (l_2 = 1, 2, … , 10).

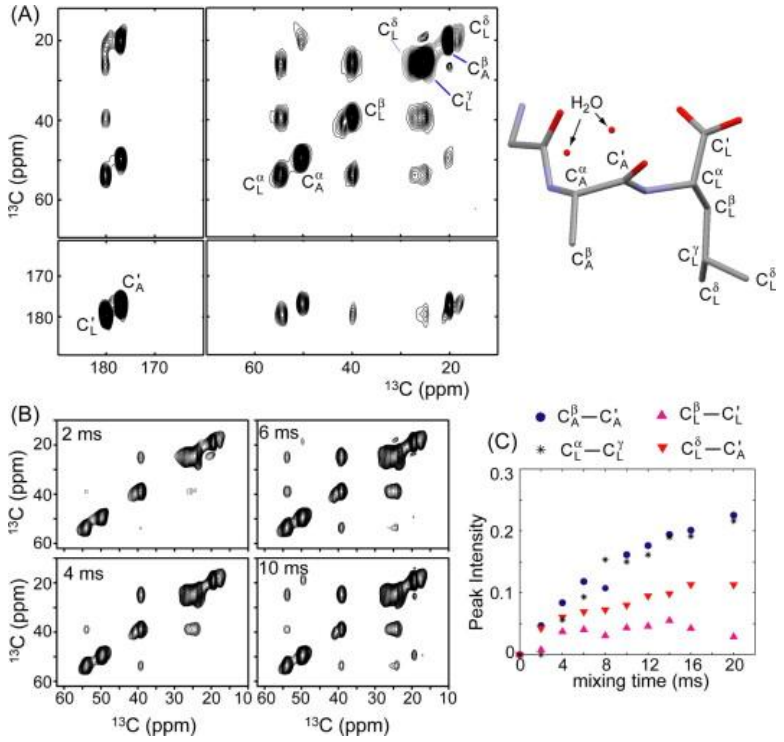

Figure 7.8. 2D ^{13}C DTOCSY spectra of the GAL sample. (A) A view of the 2D ^{13}C–^{13}C correlation spectrum, emphasizing only the frequency regions containing peaks. The pulse sequence in Figure 7.1A was used without a selective pulse. The labeled ^{13}C sites in the sample are designated along the diagonal peaks. (B) Changes in the cross-peak intensities in the 2D map, emphasizing the 0–60 ppm aliphatic region in both dimensions, as τ_{mix} increases from 2 ms to 10 ms. Cross peak correlations include: short-range interactions ($C_A^\alpha - C_A^{'}$, $C_L^\alpha - C_L^{'}$, $C_A^\alpha - C_A^\beta$, $C_L^\alpha - C_L^\beta$, and $C_L^\beta - C_L^\gamma$) and long-range interactions ($C_A^B - C_A^\gamma$, $C_L^\beta - C_L^{'}$, $C_L^\gamma - C_L^{'}$, $C_L^\alpha - C_L^\gamma$, and $C_L^\delta - C_L^{'}$). (C) Dipolar build-up curves for various ^{13}C–^{13}C correlations, showing how the relative intensity varies as a function of τ_{mix}: $C_A^\beta - C_A^\alpha$ (blue circles), $C_L^\alpha - C_L^\gamma$ (black asterisk), $C_L^\beta - C_L^{'}$ (pink triangles), and $C_L^\delta - C_A^{'}$ (red triangles). Relative intensity was found by taking the ratio of the total cross-peak intensity to the total diagonal peak intensity for each spin pair. The X-ray determined structure of GAL is shown with the designation of carbon sites.

For instance, Figure 7.8A demonstrates spectral correlations measured at $l_2 = 5$ (τ_{mix} = 10 ms) for the appropriate regions that show diagonal and cross-peaks. Diagonal peaks are visible for the different ^{13}C sites in GAL, along with many cross-peaks for different ^{13}C–^{13}C correlations. An important feature to discern from the 2D spectrum is that long-range homonuclear ^{13}C–^{13}C dipolar coupling interactions such as $C_L^{\delta} - C_L^{'}$ (4-bond distance) are observable in the presence of short-range (i.e. 1-bond distance) interactions such as $C_L^{\alpha} - C_L^{'}$ even without applying a selective pulse at, for instance, C_L^{α}. Other clearly distinguishable long-range ^{13}C–^{13}C dipolar cross-peaks include $C_A^{\beta} - C_A^{'}$, $C_L^{\beta} - C_L^{'}$, $C_L^{\gamma} - C_L^{\alpha}$, $C_L^{\alpha} - C_L^{\delta}$, $C_L^{\gamma} - C_L^{'}$, and even $C_L^{\delta} - C_A^{'}$. Some other notable features are a broad diagonal peak attributed to a combination of the resonances of one of the side chain methyl groups, C_L^{δ}, and the side chain methine group, C_L^{γ}, of leucine, and a doublet-like feature assigned to the sidechain resonances of the C_A^{β} of alanine and the other sidechain terminal C_L^{γ} of leucine. Figure 7.8B emphasizes the spectral region of 10–60 ppm for both direct and indirect spectral domains with τ_m = 2 (l_2 = 1), 6 (l_2 = 3), 10 (l_2 = 5), and 14 ms (l_2 = 7). Cross-peak intensities, particularly for the longer range ^{13}C–^{13}C coupling pairs, clearly increase as the mixing time increases. Figure 7.8C illustrates the dipolar ^{13}C–^{13}C build-up curves of $C_A^{\beta} - C_A^{'}$ (blue circle), $C_L^{\gamma} - C_L^{\alpha}$ (star), $C_L^{\beta} - C_L^{'}$ (inverted red triangle), and $C_A^{'} - C_L^{\delta}$ (purple triangle) obtained by increasing the DTOCSY mixing time. Cross-peak intensities are divided by diagonal peak intensities for signal normalization. Among these build-up curves, the relative intensity buildup was highest for $C_A^{\beta} - C_A^{'}$ and $C_L^{\alpha} - C_L^{\gamma}$, followed by $C_L^{\delta} - C_A^{'}$, and lowest for $C_L^{\beta} - C_L^{'}$. Magnetization transfers are influenced by the magnitude of dipolar interactions, the presence of intervening dipolar interactions, the spinning frequency, isotropic offsets, and anisotropic chemical shifts, including the relative tensor orientations between dipolar and chemical shift tensors. Figure 7.9 and Figure 7.10 show the results of experiments involving selective inversion pulses for simplifying correlation patterns or selecting individual couplings. Figure 7.9 shows the resulting 2D ^{13}C–^{13}C correlation spectrum from an experiment with a selective Gaussian inversion pulse irradiated at the C$^{\alpha}$s in GAL. As compared to Figure 7.8A, any dipolar pairs involving C$^{\alpha}$ carbons are not appreciable in Figure 7.9, while retaining correlations between spin pairs not involving C$^{\alpha}$. Noticeable spectral features are the negative diagonal-peak intensities of the inverted C$^{\alpha}$ sites (colored in red) and the suppressed cross-peak

intensities of any correlations involving C^{α}s. It may facilitate to measure the weaker dipolar interaction more accurately by removing the stronger one if both couplings share a spin. By inserting a selective Gaussian or cosine-modulated Gaussian in the middle of the DTOCSY mixing block, it was possible to selectively attenuate or maintain specific dipolar coupling interactions, as predicted by Eqs. 7.5-7.8 and demonstrated in Figure 7.4 and Figure 7.5.

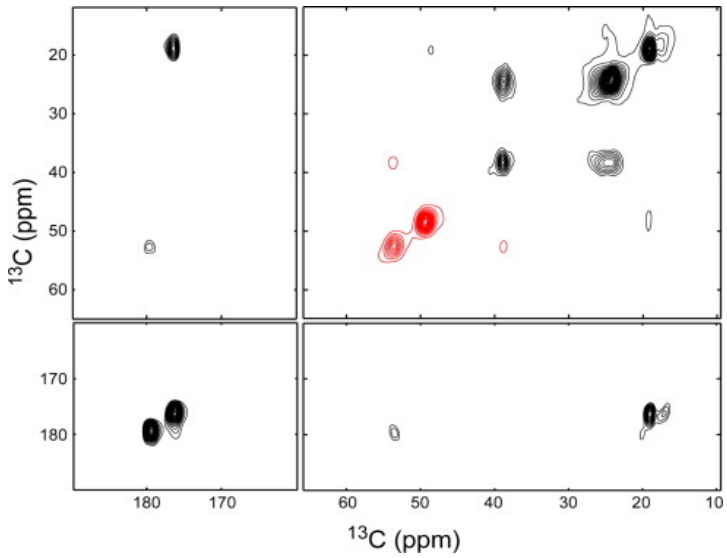

Figure 7.9. 2D ^{13}C–^{13}C correlation spectrum obtained from a DTOCSY experiment incorporating a selective Gaussian pulse set to irradiate C^{α} sites. Red contour lines are used to indicate the inverted C^{α}_{L} and C^{α}_{A} diagonal peaks. By comparing this spectrum with Figure 8A, the spectral simplification resulting from using a selective Gaussian pulse can be noticed; any correlations involving the $C^{\alpha}_{L}$and C^{α}_{A} spins are suppressed.

For instance, a selective inversion of a C^{α} carbon will improve the accuracy of measurements of the $\underline{C'–C^{\beta}}$ interaction and other long-range intra-residue ^{13}C–^{13}C interactions involving the C′ carbon. Figure 7.10 shows the 2D ^{13}C–^{13}C correlation spectrum of a model compound, U-^{13}C Glutamine, obtained from an experiment with simultaneous selective irradiations at two frequency regions (Figure 7.10C), along with reference spectra obtained without a selective pulse (Figure 7.10A) and from an experiment with a selective Gaussian pulse (Figure 7.10B). A cosine-modulated Gaussian pulse was used to simultaneously irradiate both 160–180 ppm and 20–35 ppm regions to invert carbonyl carbons and all the aliphatic carbons except the C^{α}. To

achieve a single site inversion we used a Gaussian pulse at the C^{α} carbon as before (Figure 7.9). As explained in the theoretical section, simultaneous inversions at two frequency regions provide a way to better isolate a $^{13}C–^{13}C$ dipolar coupling from a spin network because it retains a dipolar interaction if both nuclei in the pair are inverted simultaneously, while removing any homonuclear correlations in a 2D spectrum if only one spin in a pair is inverted.

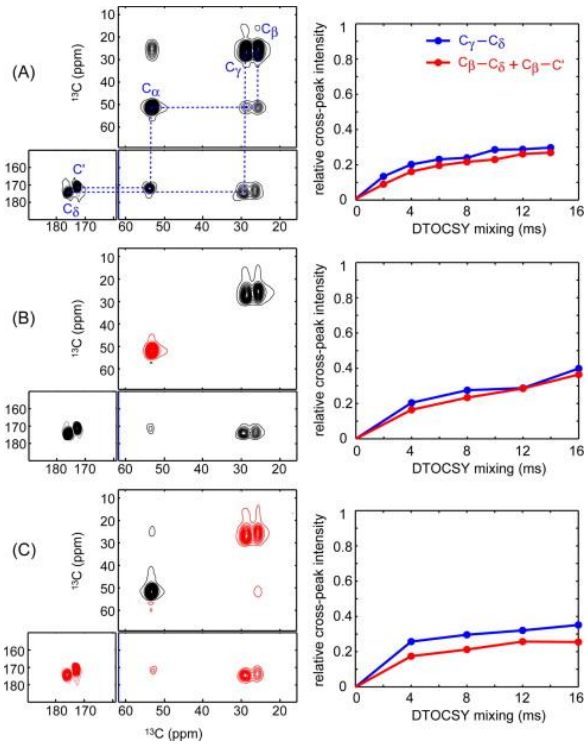

Figure 7.10. 2D $^{13}C–^{13}C$ correlation spectra of U-^{13}C Glutamine obtained from a DTOCSY experiment employing a selective cosine-modulated Gaussian pulse. Two frequency regions were simultaneously irradiated (C′, C^{β}, C^{γ}, and Cδ) (C). The 2D $^{13}C–^{13}C$ correlation spectra from experiments without any selective pulse (A) and with a single Gaussian pulse irradiated at C^{α} (B) are shown as references. By comparing Figure 7.9C with (A) and (B), an individualization of dipolar pairs involving carbon sites that are simultaneously irradiated by a cosine-modulated Gaussian pulse can be noticed. Red contour lines indicate inverted diagonal and cross-peaks. Dipolar build-up curves for the cross-peaks, $C^{\gamma}–C\delta$ and $C^{\beta}–C\delta + C^{\beta}–C'$ (C), are shown for each at the three scenarios. Notice that a selective pulse is sandwiched by two DTOCSY mixing blocks with an identical mixing time in the selective mixing scheme. In this particular case, (B) and (C) are identical in nature and, the build-up curves from both modes are very similar.

However, the removal of dipolar interactions with non-irradiated spins is marginal because only the half of the ZQ-coherence terms with non-irradiated spins is removed by simultaneous *I* and *S* spin irradiations. Upon comparing Figure 7.10A and B, negative, but clear cross-peak intensity for C^{γ}–C^{δ} and (C^{β}–C^{δ})+(C^{β}–C') are evidenced in Figure 7.10C, but cross-peaks involving the C^{α} carbon are suppressed. Also shown in Figure 7.10 are dipolar build-up curves for the cross-peak intensities for the C^{γ}–C^{δ} and the unresolved (C^{β}–C^{δ})+(C^{β}–C') correlations measured without selective pulse (Figure 7.10A), and with a selective Gaussian pulse (Figure 7.10B) or cosine-modulated Gaussian pulse (Figure 7.10C) over the mixing times of 0–26 ms. Interestingly, two different cases with selective inversions (Figure 7.10B and C) show dipolar build-up curves with higher efficiencies, demonstrating that these selective dipolar recoupling methods, particularly the scheme with a cosine-modulated Gaussian pulse, can minimize dipolar truncation effects and signal loss due to the relayed signal transfers. Hence, the DTOCSY method would be an advanced tool for measuring specific spin pairs more accurately in a complicated dipolar network in homonuclear 2D correlation spectroscopy.

7.5. Discussion

Herein we have demonstrated a new approach in 2D ssNMR to correlate ^{13}C–^{13}C dipolar couplings in the longitudinal mode, combining a symmetry-based technique introduced by Levitt and coworkers with a selective irradiation scheme, that is useful for selecting/simplifying ^{13}C–^{13}C homonuclear dipolar coupling interactions from complicated dipolar networks. This method would enable simplifications of 2D correlation patterns and extraction of certain structurally important ^{13}C–^{13}C interactions more clearly by eliminating the appearance of other ^{13}C–^{13}C homonuclear dipolar couplings in a 2D correlation spectrum. It also improves the accuracy of distance measurements of weak dipolar coupling interactions by partially eliminating terms that are responsible to the relayed signal transfers and dipolar truncation effects through the use of selective irradiation schemes. According to our numerical simulations, efficient DTOCSY signal transfers occur when the offset difference of two nuclei involved in a dipolar pair corresponds to zero, one, and two times the MAS spinning frequency used, reminiscing a rotational resonance condition. The width of each frequency window that shows a favorable signal transfer is about 3–4 kHz (40–50 ppm). The exact mechanism of the occurrence of this rotational resonance type

effect is not clear, but we hypothesize that the chemical shift interactions reintroduced by the $C3_3^1$ sequence interfere with the spinning frequency. This hypothesis can be justified by the fact that a similar effect was not visible in our simulations when a pure ZQ-recoupling technique, such as RFDR, is used in the mixing block. As we have tested various heteronuclear dipolar decoupling schemes at different rf strengths, it was found that if the proton decoupling power is at least 2.3 times the ^{13}C channel pulse power, which is in turn 8 times the MAS spinning speed, the CW decoupling mode provided acceptable decoupling efficiency for DTOCSY mixing applied along longitudinal magnetizations. For instance, we have used 128 kHz of CW proton decoupling power, 48 kHz of DTOCSY mixing power, and 6 kHz of MAS speed in our experiments (Figure 7.7-7.10). Using a ^{13}C, ^{15}N-labeled GAL sample in an experiment with non-selective recoupling of ^{13}C–^{13}C homonuclear dipolar coupling interactions, it was possible to simultaneously observe multiple long-range ^{13}C–^{13}C correlations (i.e. $C'_A - C^{\delta}_L$) in the presence of short-range interactions (i.e. $C^{\alpha}_L - C'_L$) (Figure 7.8).The adverse effect of insufficient ^{13}C–^{1}H heteronuclear dipolar decoupling during $C3_3^1$ mixing, originally reported with the introduction of TDR, was removed by switching the mixing scheme from the transverse mode of magnetization to the longitudinal mode. Contrary to the methods that produce secularized ZQ-homonuclear dipolar terms, such as TDR and ZQ-SEASHORE, the DTOCSY method utilizes the flip-flop terms of ZQ-homonuclear dipolar terms, which makes two dipolar coupling interactions that share a common spin not commute with each other. However, when a selective irradiation pulse is incorporated in the mixing scheme, it provides an alternative route of selecting individual ^{13}C–^{13}C dipolar interactions. Particularly, as shown in Figure 7.10C, it provides a potential route for extracting a single ^{13}C–^{13}C dipolar interaction with improved accuracy from a network of multiple ^{13}C–^{13}C dipolar interactions by simultaneously irradiating both spins involved in a coupling. This ability might provide much control in studying homonuclear dipolar coupling interactions to obtain more accurate distance measurements from a complicated dipolar network. The longitudinal mixing mode also provides an advantage over the transverse mixing mode in that it can incorporate a longer mixing time even when NMR signals possess short T_2-relaxation times. For reference, the $C3_3^1$-based DTOCSY scheme can be compared to one incorporating a conventional ZQ-dipolar recoupling method. For instance, the RFDR technique under a slow-to-moderate spinning condition[35] possesses a compatibility with a selective irradiation scheme, and

thus can be used as a recoupling block in DTOCSY mixing scheme. This simpler approach would possess an advantage over the $C3_3^1$ sequence in that it reintroduces only ZQ-dipolar interactions with a shorter time in the basic mixing unit. Based on our numerical simulations (data not shown), the RFDR-based mixing scheme, for instance, has demonstrated an additional advantage over the $C3_3^1$-based scheme in that it is capable of isolating a very weak ^{13}C–^{13}C interaction (ca. 300 Hz) from a stronger one (ca. 2.2 kHz) when these two couplings share a common spin in a dipolar coupled network. However, the RFDR-based scheme possesses a limited capability over the $C3_3^1$-based method when coupled spin sites are separated by small chemical shift differences. In general, the optimal recoupling regions and the range of dipolar coupling strengths that can be isolated are strongly dependent on the type of recoupling method incorporated in the DTOCSY mixing scheme. A popular ssNMR technique, proton-driven spin diffusion (PDSD),[48] which provides correlations of long-range ^{13}C–^{13}C couplings even when the chemical shift differences between the coupled spins are significant, is not compatible with a selective irradiation pulse in the DTOCSY scheme as introduced herein, and therefore, cannot be used for simplifying or isolating a specific
interaction from 2D correlations.

The ZQ-SEASHORE method that individualizes homonuclear dipolar couplings based on the secularization of the ZQ dipolar Hamiltonian is not feasible as a mixing scheme for longitudinal magnetizations because the secularized, effective dipolar Hamiltonian produced through this technique commutes with longitudinal magnetizations. Moreover, the ZQ-SEASHORE method is applicable only at high spinning speed (>30 kHz), while the DTOCSY method is advantageous if a slow-to-moderate spinning speed is inevitable in an experiment. Based on the results of this study, it is expected that the DTOCSY scheme, with appropriate ZQ-recoupling method and selective irradiation scheme, may provide an advantageous route with improved sensitivity and accuracy in studying selective spin pairs from uniformly labeled samples for elucidating structures of biological molecules.

The shape and efficiency of the selective pulse decides the selectivity in the frequencies as well as the inversion profile of the selected frequency ranges. A Gaussian or a cosine-modulated Gaussian pulse provides a relatively limited region of uniform inversion over the specified frequency ranges, particularly when the inversion window is small. Future efforts with

the DTOCSY technique should focus on developing a selective pulse scheme that provides a narrow, uniform inversion profile over the specified spectral window, as this should improve the effectiveness of DTOCSY for individualizing spin pair interactions from complicated dipolar networks. Currently, we are exploring the feasibility of various types of symmetry-based ZQ homonuclear recoupling methods Levitt and coworkers developed, such as $SR4_4^1$ and $SR6_6^2$,[33] as a basic DTOCSY mixing block to improve the efficiency at isolating weak ^{13}C–^{13}C dipolar interactions in the presence of strong one-bond ^{13}C–^{13}C dipolar interactions.

References

(1) Opella, S. J. *J. Nat. Struct. Biol* **1997**, *4*, 845.

(2) Griffin, R. *Nat. Struct. Mol. Biol.* **1998**, *5*, 508.

(3) de Groot, H. J. M. *Curr. Opin. Struct. Biol.* **2000**, *10*, 593.

(4) Tycko, R. *Annu. Rev. Phys. Chem.* **2001**, *52*, 575.

(5) Castellani, F.; van Rossum, B.; Diehl, A.; Schubert, M.; Rehbein, K.; Oschkinat, H. *Nature* **2002**, *420*, 98.

(6) Tycko, R. *Curr. Opin. Struct. Biol.* **2004**, *14*, 96.

(7) McDermott, A. E. *Curr. Opin. Struct. Biol.* **2004**, *14*, 554.

(8) Baldus, M. *Curr. Opin. Struct. Biol.* **2006**, *16*, 618.

(9) Lange, A.; Giller, K.; Hornig, S.; Martin-Eauclaire, M. F.; Pongs, O.; Becker, S.; Baldus, M. *Nature* **2006**, *440*, 959.

(10) Gullion, T.; Schaefer, J. *J. Magn. Reson.* **1989**, *81*, 196.

(11) Raleigh, D. P.; Levitt, M. H.; Griffin, R. G. *Chem. Phys. Lett.* **1988**, *146*, 71.

(12) Lee, Y. K.; Kurur, N. D.; Helmle, M.; Johannessen, O. G.; Nielsen, N. C.; Levitt, M. H. *Chem. Phys. Lett.* **1995**, *242*, 304.

(13) Dusold, S.; Sebald, A. *Annu. Rep. NMR. Spectrosc.* **2000**, *41*, 185.

(14) Tycko, R.; Dabbagh, G. *Chem. Phys. Lett.* **1990**, *173*, 461.

(15) Carravetta, M.; Eden, M.; Zhao, X.; Brinkmann, A.; Levitt, M. H. *Chem. Phys. Lett.* **2000**, *321*, 205.

(16) Brinkmann, A.; Levitt, M. H. *J. Chem. Phys.* **2001**, *115*, 357.

(17) Hohwy, M.; Rienstra, C. M.; Jaroniec, C. P.; Griffin, R. G. *J. Chem. Phys.* **1999**, *110*, 7983.

(18) Kiihne, S.; Mehta, M. A.; Stringer, J. A.; Gregory, D. M.; Shiels, J. C.; Drobny, G. P. *J. Phys. Chem. A* **1998**, *102*, 2274.

(19) Hodgkinson, P.; Emsley, L. *J. Magn. Reson.* **1999**, *139*, 46.

(20) Schmedt auf der Günne, G. J. *J. Magn. Reson.* **2006**, *180*, 186.

(21) Jaroniec, C. P.; Tounge, B. A.; Herzfeld, J.; Griffin, R. G. *J. Am. Chem. Soc.* **2001**, *123*, 3507.

(22) Jaroniec, C. P.; Filip, C.; Griffin, R. G. *J. Am. Chem. Soc.* **2002**, *124*, 10728.

(23) Petkova, A. T.; Tycko, R. *J. Magn. Reson.* **2004**, *168*, 137.

(24) Takegoshi, K.; Nomura, K.; Terao, T. *Chem. Phys. Lett.* **1995**, *232*, 424.

(25) Nomura, K.; Takegoshi, K.; Terao, T.; Uchida, K.; Kainosho, M. *J. Am. Chem. Soc.* **1999**, *121*, 4064.

(26) Costa, P. R.; Sun, B.; Griffin, R. G. *J. Magn. Reson.* **2003**, *164*, 92.

(27) Ramachandran, R.; Ladizhansky, V.; Bajaj, V. S.; Griffin, R. G. *J. Am. Chem. Soc.* **2003**, *125*, 15623.

(28) van der Wel, P. C. A.; Eddy, M. T.; Ramachandran, R.; Griffin, R. G. *ChemPhysChem* **2009**, *10*, 1656.

(29) Peng, X.; Libich, D.; Janik, R.; Harauz, G.; Ladizhansky, V. *J. Am. Chem. Soc.* **2008**, *130*, 359.

(30) Marin-Montesinos, I.; Mollica, G.; Carravetta, M.; Gansmuller, A.; Pileio, G.; Bechmann, M.; Sebald, A.; Levitt, M. H. *Chem. Phys. Lett.* **2006**, *432*, 572.

(31) Khaneja, N.; Nielsen, N. C. *J. Chem. Phys.* **2008**, *128*, 015103.

(32) Hu, K. N.; Tycko, R. *J. Chem. Phys.* **2009**, *131*, 045101.

(33) Brinkmann, A.; Schmedt Auf der G?ne, J.; Levitt, M. H. *J. Magn. Reson.* **2002**, *156*, 79.

(34) Brinkmann, A.; Ed, M. *J. Chem. Phys.* **2004**, *120*, 11726.

(35) Bennett, A. E.; Rienstra, C. M.; Griffiths, J. M.; Zhen, W.; Lansbury Jr, P. T.; Griffin, R. G. *J. Chem. Phys.* **1998**, *108*, 9463.

(36) Ishii, Y. *J. Chem. Phys.* **2001**, *114*, 8473.

(37) Paravastu, A. K.; Tycko, R. *J. Chem. Phys.* **2006**, *124*, 194303.

(38) Cadars, S.; Lesage, A.; Hedin, N.; Chmelka, B. F.; Emsley, L. *J. Phys. Chem. B* **2006**, *110*, 16982.

(39) Mou, Y.; Chan, J. C. C. *Chemical physics letters* **2006**, *419*, 144.

(40) Pileio, G.; Mamone, S.; Mollica, G.; Montesinos, I. M.; Gansm?ler, A.; Carravetta, M.; Brown, S. P.; Levitt, M. H. *Chem. Phys. Lett.* **2008**, *456*, 116.

(41) Braunschweiler, L.; Ernst, R. R. *J. Magn. Reson.* **1983**, *53*, 521.

(42) Fung, B. M.; Khitrin, A. K.; Ermolaev, K. *J. Magn. Reson.* **2000**, *142*, 97.

(43) Spano, J.; Wi, S. *J. Magn. Reson.* **2010**, *204*, 314.

(44) Bennett, A. E.; Rienstra, C. M.; Auger, M.; Lakshmi, K. V.; Griffin, R. G. *The Journal of chemical physics* **1995**, *103*, 6951.

(45) Schenker, K. V.; Suter, D.; Pines, A. *J. Magn. Reson.* **1987**, *73*, 99.

(46) Ishii, Y.; Ashida, J.; Terao, T. *Chem. Phys. Lett.* **1995**, *246*, 439.

(47) Liu, S. F.; Mao, J. D.; Schmidt-Rohr, K. *J. Magn. Reson.* **2002**, *155*, 15.

(48) Szeverenyi, N. M.; Sullivan, M. J.; Maciel, G. E. *J. Magn. Reson.* **1982**, *47*, 462.

Chapter 8

Hindered Rotation of Water near C_{60}

Reproduced in part with permission from Wi, S.; Spano, J.; Ducker, W.A. *J. Phys. Chem. C*, **2010**, 114, 14986. Copyright 2010 American Chemical Society. Samples were prepared by the Ducker Group, and solid-state NMR experiments were performed by the Wi Group, at Virginia Tech.

8.1. Introduction

Knowledge of the structure and dynamics of interfacial water can be applied to a range of applications, including the stabilization of nanoparticles, the development of filtration membranes, the folding of proteins, and ion conduction through membranes. In particular, it is important to understand the behavior of water adjacent to hydrophobic materials because hydrophobicity drives much of the organization in biological systems. Water molecules associate with each other by electrostatic interactions occurring between the hydrogen of one water molecule and the oxygen of a neighbor (hydrogen bonding). Hydrogen bonds break and form on the timescale of picoseconds, but the sum of the hydrogen bond strengths allows great cohesion that provides interesting properties to water, such as a high boiling point.[1] In liquid water molecules are disorganized, but in ice they form a regular arrangement, which makes ice less dense than the liquid state.

If a hydrophobic molecule is introduced into water, it disrupts the hydrogen bonding network of the water molecules around it, which causes an unfavorable entropy decrease. In response, water molecules will then rearrange around the hydrophobic molecule in order to minimize the number of ordered water molecules at the interface.

Consequently, the interface between water and hydrophobic solids has been the subject of intense theoretical interest.[2-5] The experimental difficulty in studying interfacial water is that it usually coexists with a vast excess of bulk water, and therefore, it is usually necessary to employ a surface-selective probe of water so that the signal from interfacial water is not totally obscured by the bulk signal.

There are a few existing techniques for studying interfacial water, including nonlinear

spectroscopy (e.g., sum frequency spectroscopy, SFS), which is selective for broken inversion symmetry. Symmetry is broken at water interfaces; therefore, SFS is selective for one or a few layers of interfacial water and has been used to identify the coordination, bonding, and orientation of interfacial water.[6,7] Vibrational SFS of the (hydrophobic) octadecyltrichlorosilane (OTS)−water interface reveals interfacial water oriented with one H bond toward the alkane and one toward bulk water.[6,8] There is also a strong dependence of the spectrum on pH, which has been assigned to interaction of the water with the dissociable charge on the silica support.[8] Recent experiments using phase-sensitive sum frequency spectroscopy has demonstrated preferential adsorption of OH^- to OTS films and that the OTS−water interface is negatively charged at neutral pH.[9] Techniques for studying interfacial water include surface-enhanced infrared and Raman spectroscopies and X-ray[10,11] and neutron reflectivity.[12] Ab initio and molecular dynamics simulations have also been applied to interfacial water, suggesting, for example, that there is a surface excess of protons at the air−water interface.[13]

Femtosecond nonlinear infrared spectroscopy has also been used to determine the dynamics of water molecules adjacent to ions.[14] The dynamics of water adjacent to anions was found to be slower than in bulk or near cations, and was attributed to the idea that it is easier for bulk water to simultaneously break and form a hydrogen bond than for the structured water around an ion.[14]

This chapter describes a novel application of nuclear magnetic resonance (NMR) spectroscopy to show that the motion of water adjacent to the C_{60} fullerene is hindered relative to bulk water. NMR can be used to study buried water interfaces because an external magnetic field polarizes nuclear spins in the entire sample. Because the absorption frequencies in an NMR experiment are element-dependent, NMR has been used extensively to study interfaces under circumstances where a particular element is confined to an interface.[15] Such an approach does not normally apply to the study of interfacial water where bulk water also exists in the same sample; the NMR signal is proportional to the concentration of a species, so the bulk water signal would dominate the spectrum due to it being in much higher amount. Here, we generate surface selectivity by performing a cross-polarization (CP) transfer between the protons of interfacial water and carbon that is confined to an interface. The range of CP depends on the element and the CP mixing time. In our experiments, the mixing time is 5 ms, and the maximum distance for CP between a proton and carbon is about 1 nm.[16,17] Thus, CP is selective for only the water

molecules that are within about 1 nm of the carbon. We have chosen C_{60} as our model hydrophobic material because C_{60} (a) is simple and small, (b) contains a spin $^1/_2$ nucleus (^{13}C in ~ 1% abundance), and (c) has no hydrogen. That is, all the hydrogen in our experimental system is part of water or its dissociation products. Thus, the CP experiments between a ^{13}C and ^1H on the C_{60}−water system is selective for only the thin layer of water molecules adjacent to the C_{60} surface. Therefore, we are able to utilize the attractive properties of NMR spectroscopy (e.g., determination of structure, chemical reaction, and dynamics) but with surface selectivity.

C_{60} has been the subject of much recent study, including work on its hydration. Molecular dynamics (MD) simulations conclude that C_{60} monomers do not induce drying of the surface and there is an increase in hydrogen bonding of the water adjacent to C_{60};[18] other work concludes that there is a greater density of water near the fullerene.[19] The solubility of C_{60} in water is extremely low (estimated at 10^{-11} M),[20] but C_{60} can be dispersed in water by stirring in water in the dark for 2 weeks[21-23] (i.e., there is no solvent other than water). In our experiments, we produced dispersions of C_{60} aggregates in this way, then allowed the dispersion to settle for several days, after which NMR experiments were conducted on the decanted supernatant. This preparation procedure produces a dispersion of aggregates with sizes ranging from tens to hundreds of nanometers and polydispersivity values ranging from .139 to .201; a low concentration of monomers are also present.[22] Though we did not explicitly explore the size of the aggregates in our sample, this could be done using dynamic light scattering or microscopy techniques. Aggregates, which form by the weathering of large particles into smaller ones and the clustering of C_{60}, are irregularly shaped and have a face-centered-cubic crystal structure.[22] Additionally, aggregates are negatively charged, with contributions occurring from electron transfer and surface hydrolysis.[24-26] However, an important thing to keep in mind when considering aqueous C_{60} studies is that the sample properties show sensitivity to the preparation conditions, and the variability can obscure clear comparisons between different studies.[22]

8.2. Experimental Methods

8.2.1. Materials

The CP measurements sampled 99.9% sublimed C_{60} (Sigma Aldrich, St. Louis, MO) that

contained the natural abundance of ^{13}C, and the T_1 measurements sampled 99+% C_{60} (MER Corporation, Tucson, AZ) that was enriched to 25−30% ^{13}C (catalog no. MR613). Solutions were prepared by adding 2 mg of C_{60} to about 5 mL of Millipore water, then stirring in the dark for 2 weeks. After two weeks, most of the C_{60} remained unsuspended, but the suspension had a silvery color, which is characteristic of C_{60} that has been solubilized through this preparation procedure.[21-23]

8.2.2. Cross-Polarization

The NMR spectra were recorded on a Bruker ^1H 600 MHz narrow-bore spectrometer equipped with a ^1H-X E-free static probe. In the experiment, spin-lock RF pulses (50 kHz) were sent simultaneously to the ^{13}C and ^1H channels for ^1H–^{13}C CP after generating transverse ^1H magnetizations by a 90° pulse (50 kHz), and then the resultant ^{13}C signal was monitored under SPINAL-64 proton decoupling (50 kHz).[27] The Hartmann−Hahn matching condition was adjusted using a crystalline powdered sample of 1−^{13}C glycine, and the same sample was used to calibrate the parts per million scale of cross-polarized ^{13}C NMR spectra (C′ = 176.4 ppm). The CP contact time was 5 ms. Each spectrum was the average of 26 000 scans with a 2.5 s acquisition delay, taking a total time of about 18 h. We confirmed that the results were independent of the offset frequency of the spectrometer. The temperature in the NMR tube was controlled by a Bruker BCU-X controller and was calibrated in a separate experiment by measuring the temperature-sensitive relative shift between the OH and CH_3 peaks in methanol.[28] The rate of change of temperature in an NMR tube filled with methanol was measured by the same method. Heating occurred at about 1 °C/min at 15 °C and at 0.5 °C/min at 5 °C; cooling was about 40% slower than heating. The heat capacity of water is greater than that for methanol, so we would expect slightly lower rates of temperature change for the C_{60} suspensions in water. To ensure temperature equilibration, the samples were left for about 60 min at each new temperature before measurements were commenced.

8.2.3. T_1 Measurement

The ^1H T_1 relaxation experiments based on a ^1H–^{13}C CP scheme were performed on a

Bruker Avance II-300 wide-bore NMR spectrometer (7.05 T) operating at Larmor frequencies of 75.47 MHz for ^{13}C and 300.13 MHz for ^{1}H nuclei. Static ^{13}C NMR spectra of ^{13}C-labeled C_{60} (25%) were acquired by measuring the ^{13}C magnetization of C_{60} created by CP from the ^{1}H magnetization of liquid water, according to the sequence shown in Figure 8.1A.

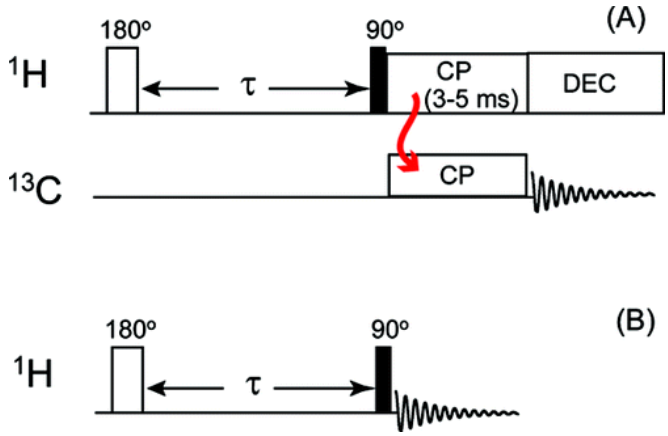

Figure 8.1. Pulse sequences used in our experiments for measuring the ^{1}H T_1 of surface water (A) and bulk water (B). A variable delay time τ following the initial 180° pulse along the ^{1}H channel was allowed for measuring the T_1 of water ^{1}Hs, which are monitored directly along the^{1}H channel by a 90° read pulse for detecting bulk water (B) or indirectly via the ^{13}C signal of C_{60} via a CP scheme for selective detection of surface water (A). A CP mixing time of 3−5 ms was applied for obtaining the ^{1}H–^{13}C polarization transfer with a 4 s acquisition delay (A).

An inversion recovery method,[29] implemented on a static CP-based ^{13}C-detection scheme, has been incorporated to measure the T_1 relaxation time of ^{1}Hs of water molecules that maintain direct contact with C_{60} molecules. These ^{1}H T_1s were detected indirectly along the ^{13}C signals via CP (3−5 ms) transfer as shown in Figure 8.1A. The T_1 relaxation time of bulk water was directly observed along the ^{1}H channel (Figure 8.1B). Resulting data also includes the contribution of surface water, but its influence on T_1 is negligible since it is such a small amount of the total water composition. An inverted population of equilibrium proton magnetizations created by a 180° pulse is followed by a variable delay time τ and, consecutively, by either a 90° read pulse for bulk water (Figure 8.1B) or a 90° pulse that is combined with a ^{1}H–^{13}C CP scheme (Figure 8.1A) for signal encoding of surface water. The NMR signal averaging was achieved by

coadding 4 transients with a 20 s acquisition delay time for bulk water and 4096 transients with a 4 s acquisition delay time for surface water. The sample temperature in the NMR probe was regulated by a nitrogen flow, which was under the control of a BVT-3000 digital temperature control unit and a BCU-X precooling and stabilization accessory. The sample temperatures incorporated in our NMR T_1 experiments were 22, 8, 3, and −15 °C for both bulk and surface water. ^{1}H $\pi/2$ and π pulse lengths were 4.5 and 9 μs, respectively. The SPINAL-64 decoupling sequence[27] at 50 kHz power was used for proton decoupling during ^{13}C signal detection. Samples for T_1 measurement were degassed by repeating four cycles of a freeze (under nitrogen purge)−pump (vacuum)−thaw procedure to remove oxygen molecules, which act as paramagnetic relaxation agents. Degassing is important because we are interested in how the water ^{1}H T_1 changes depending on whether bulk or surface water is probed; dissolved oxygen would corrupt the data by providing an additional factor to shorten T_1

8.3. Results and Discussion

A sample of C_{60} that had been in water for about 1 month was separated into its supernatant and precipitate portions. The precipitate was freeze-dried at −45 °C and 0.3 mbar for 10 h and served as our no-water control, and the supernatant was used without further treatment over a period of about 2 months. A ^{13}C DP experiment of the dried sample at 22 °C showed a motionally averaged sharp peak for the fullerene at 143 ppm (Figure 8.2), as described previously.[30] Further evidence for a lack of contamination, though the signal-to-noise for the peak is ~4:1 due to the ~1.1% natural abundance of ^{13}C, is that the purity of the commercially obtained sample was 99.9%, and no other significant peaks were observed above the noise level. Also, generally in NMR if the amount of sample is at least a few parts per million, a signal can be observed with a few hundred scans, but no additional signals were observed here with 1024 scans. A ^{1}H−^{13}C CP experiment on the dried sample produced no signal. If the C_{60} had reacted with water to incorporate hydrogen (e.g., formed −COH groups), then we would expect to detect that hydrogen via CP in this experiment. The absence of CP signal in our dry experiment supports the signals in our wet experiments arising from water, rather than from hydrogen that is covalently bound to the fullerene. The theoretical sensitivity gain in ^{13}C spectra obtained with ^{1}H-^{13}C CP is ~4, so if a significant proton concentration (i.e. a few ppm) was present a higher

signal should be seen in Figure 8.2B, especially considering that Figure 8.2A and B both had the same number of scans.

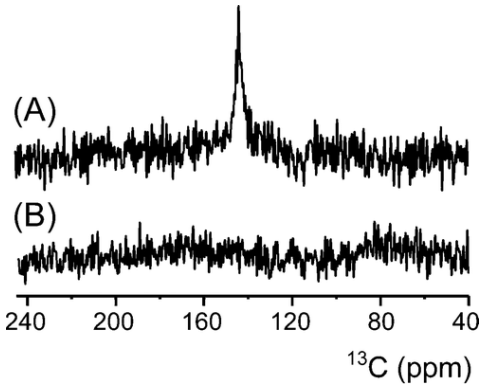

Figure 8.2. ^{13}C NMR spectra of 2 mg of dried C_{60} at 22 °C. (A) Direct polarization (DP). (B) ^{1}H–^{13}C CP under static conditions. The DP spectrum of C_{60} clearly demonstrates a motionally averaged sharp peak at 143 ppm due to the rapid rotational tumbling motions of C_{60} whose CSA tensor elements are σ_{11} = 220 ppm, σ_{22} = 186 ppm, and σ_{33} = 40 ppm.[31,32] As expected, the dried C_{60} does not produce ^{1}H–^{13}C CP because C_{60} does not contain any protons. Each spectrum consisted of 1024 coadded scans with a 20 s acquisition delay time for measuring the DP spectrum and 2.5 s for the CP spectrum.

Hydrocarbon contamination from water would also affect our results. Thus, we performed ^{1}H–^{13}C CP measurements on the water, but we observed no signal, which would at least indicate that if there is a hydrocarbon contaminant, the ^{1}H-^{13}C dipolar coupling is averaged away, and so it would not contribute to a ^{13}C CP spectrum. These results show that ^{1}H–^{13}C CP arising from the suspension of C_{60} in water (a) does not arise from contaminants in C_{60} and (b) does not arise from contaminants in the water and, therefore, arises from an interaction between C_{60} and water. All other experiments utilized the transparent, supernatant portion of the C_{60} suspension in water.

^{1}H–^{13}C CP spectra of the supernatant as a function of temperature are shown in Figure 8.3. At −5 °C, where bulk water is frozen, there is a finite signal since here the proton positions are fixed relative to the C_{60}, and so the ^{1}H-^{13}C dipolar interactions are not averaged to zero. The structure and dynamics of the water immediately adjacent to the C_{60} may be modified by the C_{60}, but the CP spectrum clearly shows that the water is at least partially immobilized at −5 °C.

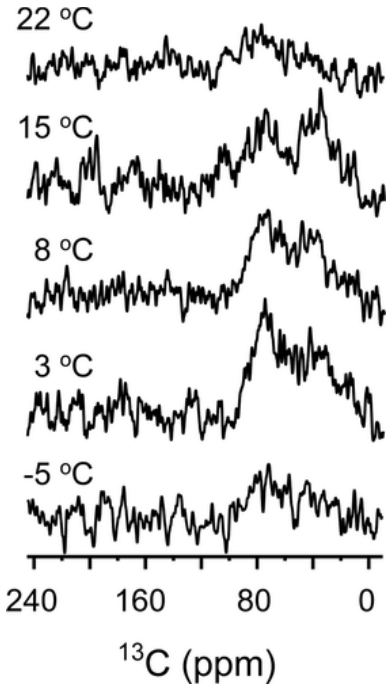

Figure 8.3. $^{1}H-^{13}C$ CP spectra of C_{60} dispersed in water as a function of temperature. Spectra were obtained by a simultaneous 50 kHz CP mixing time applied along both ^{1}H and ^{13}C channels for 5 ms after polarizing the water ^{1}H signals by a 5 μs 90° pulse. 50 kHz of SPINAL-64 proton decoupling was applied for the signal acquisition of the ^{13}C spectrum of C_{60}. Note that the greatest signal intensity was obtained at a temperature above the freezing point of bulk water (3 °C). All ^{13}C spectra were acquired by an off-resonance condition (55 ppm). Transient signals from 26000 scans were coadded with a 2.5 s acquisition delay. Experiments were done in order of increasing temperature with 1 h of equilibration between each temperature and 18 h at each temperature.

The central observation of this paper is that the $^{1}H-^{13}C$ CP signal also occurs when bulk water is in the liquid phase (>0 °C). The $^{1}H-^{13}C$ CP signal is strongest at 3°C and diminishes with increasing temperature (Figure 8.3). The greater density of water at ~4°C could be one explanation to the high signal intensity at 3°C. However, future work using theoretical calculations could be used to provide a better understanding of the water environment around C_{60} that may provide additional insight on this phenomena. Even though overall the signal-to-noise ratio (SNR) is poor, the SNR of the 3°C spectrum is ~3 times better than that of the -5°C spectrum, so the differences noticed should be significant. An interesting feature is that

structured water, which is evidenced by the signals at the low temperatures, is stable for an extended time (i.e. 10's of hours). Though it would appear that two peaks are actually present, especially at 15 and 8°C, we tentatively attribute this to noise spikes; future experiments with ^{13}C labeled C_{60} could be used to test this conclusion further. Similar results were obtained on a ^{1}H-300 MHz NMR with a larger sample volume (spectra not shown). The presence of the ^{1}H–^{13}C CP signal demonstrates that residual dipolar interactions are present (i.e., the dipolar interactions do not average to zero), so the water adjacent to the C_{60} is not isotropic. Additionally, for there to be dipolar coupling, the tumbling motion of the water must occur on a time scale that is similar to, or longer than, the time scale of the NMR measurement, which is the inverse of the Larmor frequency (1.7 ns for the 600 MHz experiment and 3 ns for the 300 MHz experiment). However, for the CP measurement to produce a signal, the interaction between the ^{1}H and ^{13}C must not average to zero during the CP mixing time, which is 3−5 ms for the experiments described here. Additionally, the CP mixing time must be greater than the inverse of the apparent dipolar coupling frequency. The exact relationship between the apparent dipolar coupling frequency and the rotational (tumbling) frequency is not known, but the experiment suggests that the rotational correlation time is greater than the microsecond range. Most of the C_{60} in our sample is associated into aggregates of many C_{60} molecules, so some of the sampled water will be in regions where it is near more than one C_{60} molecule, meaning that water would be taking part in more intermolecular associations. The slowing of water rotation may be related to this proximity to several C_{60} molecules in an aggregate.

These spectra additionally support the conclusion from Figure 8.2B that no significant proton concentration is present in the dry C_{60} samples. The CP spectra in Figure 8.3 have a poor signal-to-noise ratio, even with 26 times the number of scans in Figure 8.2B. The case in Figure 8.3 is also one where the ^{1}H-^{13}C internuclear distance would be farther than if a –COH group had formed, so the CP transfer would be less efficient. If –COH groups had formed, and there was signal observable for a solution case, there should have been signal observable in the solid case.

The measured rotational time scales for pure liquid water depend somewhat on the measurement technique, but the generally accepted rotational time is about 10^{-12}–10^{-11} s.[4,33,34] Thus, our results show that the tumbling (rotational) motion for water in the 1 nm film adjacent to the C_{60} is slowed by more than a factor of about 10^{5} compared with pure bulk water. The fact that the magnitude of the CP signal diminishes with increasing temperature, and is barely

detected at 22 °C, shows us that the ordering of the water adjacent to the C_{60} diminishes with temperature.

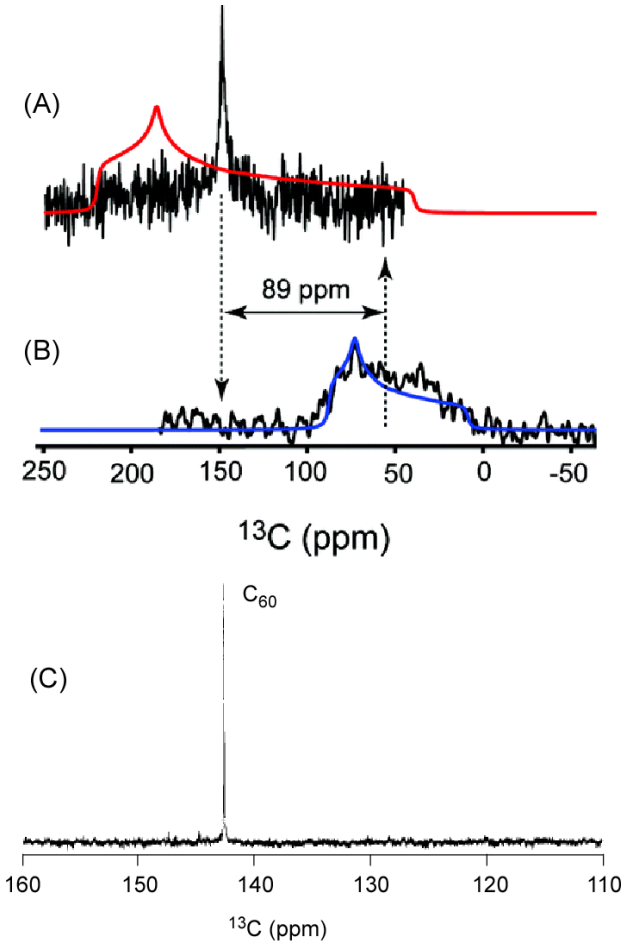

Figure 8.4. ^{13}C NMR spectra of C_{60} in different environments. (A) ^{13}C DP spectrum of the dried C_{60} sample measured at 22°C. The red line represents a simulated spectrum of dried C_{60} without considering rapid, reorientational tumbling motions of molecules (σ_{11} = 220 ppm, σ_{22} = 186 ppm, and σ_{33} = 40 ppm).[31,32] (B) $^{1}H–^{13}C$ CP spectrum of C_{60} dispersed in water measured at 3°C. The blue line is our best-fit simulation of C_{60} in 3°C water, with apparent CSA tensor elements of σ_{11} = 83 ppm, σ_{22} = 70 ppm, and σ_{33} = 10 ppm. Note the shift of the isotropic chemical shift position from 143 to 54 ppm. (C) ^{13}C NMR spectrum of C_{60}/C_{70} in CCl_4. The prominent sharp peak can be attributed to C_{60}, and the minor peaks downfield were attributed to C_{70}. Reproduced with permission from Johnson, R.D.; Meijer, G.; Bethune, D.S. *J. Am. Chem. Soc.* **1990**, 112, 8983. Copyright 1990 American Chemical Society.

Earlier work shows a freezing point depression near lipid layers[35] and that water can be immobilized near hydrophilic particles, such as micelles and proteins,[33,36] but, here, we demonstrate that immobilization can occur near a hydrophobic surface. Molecular dynamics simulations also show a slowing of water hydrogen-bonding kinetics neighboring hydrophobic peptides, but the predicted hydrogen bond relaxation time increases by a factor of only 2.[37]

The line shape of the CP spectra also allows us to extract the effective chemical shift anisotropy (CSA) tensors. Figure 8.4B shows a spectrum measured with an on-resonance condition but possesses an identical pattern to that shown in Figure 8.3. The agreement means that the $^{1}H–^{13}C$ CP spectrum we obtained is offset independent, and thus, is not a spurious signal. The apparent CSA tensor elements are σ_{11} = 83 ppm, σ_{22} = 70 ppm, and σ_{33} = 10 ppm. It should be noted that the best fit simulation considers the powder pattern width, and the match of the σ_{22} element of the simulation and the sharp feature of the experimental powder pattern is coincidence. The broad powder pattern lineshape indicates an overlap of NMR signals that are simultaneously occurring. We take this to represent that on the NMR timescale C_{60} aggregates tumbles slow enough in water that different orientations are simultaneously present, causing peak overlap due to the chemical shift's orientation dependence. Additionally, there could be contributions from magnetically inequivalent positions occurring in aggregates. Interestingly, the isotropic chemical shift position changes from 143 ppm in the dry sample (in agreement with refs 28 and 30) to 54 ppm in the wet sample. The chemical shift of the ^{13}C resonance is a function of the chemical environment of the fullerene, so it reflects the structure of the surrounding water. The observed upfield shift relative to CCl_4 or solid samples suggests a more electron-rich environment. While we do not clearly understand this, it could mean that a predominance of hydrogen, rather than oxygen of water, is pointing toward the C_{60}. Future work using theoretical calculations, which could provide a view of the water environment around C_{60}, would help elucidate the validity of this idea. Another explanation could be that it indicates an impurity. Though our earlier results shown indicate otherwise, upfield shifts would be consistent with some fullerene derivatives.[38] This possibility was not explicitly explored, but the presence of $C_{60}O$ could be revealed using chromatography or mass spectrometry.

One possible interpretation of our measurements is that the temperatures are incorrect; some water that was once frozen remains frozen, even at 15°C. We have excluded this possibility as follows: (a) One hour was allowed at each temperature before measurement, which

is much longer than the time required to reach the stated temperature inside the NMR tube. (b) The experiments were done in two different ways, once with increasing temperature and once with decreasing temperature, and no significant difference was observed. It is also important to note that each measurement was for a period of about 18 h, so in the increasing temperature run, the 15 °C measurement was commenced about 40 h after the sample was brought above 0 °C. For the decreasing temperature run, the sample had never been frozen.

In addition to water, NMR spectra also probes the motion of the fullerene. The peak width in the ^{13}C spectrum of the dried solid sample at 22 °C (Figure 8.2) is much narrower than that for the wet sample (Figure 8.3), which shows that the rotational motion of the C_{60} is slowed in water. This peak broadening is consistent with the presence of a structured pocket in the solvent providing a structured force field around the C_{60}, and thus an activation energy to tumbling. This hindered motion is additional evidence for structuring of the water. Previous work has shown that the motion of C_{60} is also hindered in tetrachlorethane relative to the solid.[30] In contrast, the NMR spectrum of C_{60} in (apolar) CCl_4[39] shows a sharp solution peak with the same chemical shift as in solid C_{60}. The spectrum of C_{60} in water is very broad and is shifted upfield by 89 ppm (from 143 to 54 ppm). The breadth of the peak shows a much more structured environment for C_{60} in water than in CCl4.

The existence of the CP signal shows that the rotational tumbling motion of water adjacent to C_{60} is greatly slowed compared with the motion in bulk. It is reasonable that a large hydrophobic molecule, with its inability to hydrogen bond to water, should alter the structure of water nearby, but the observed extent of slowdown in rotational motion is rather large. To further examine the water dynamics, we have performed T_1 measurements on the interfacial water. T_1 is the rate of decay of the perturbed, longitudinal magnetization to the equilibrium state in the direction parallel to the external (B_0) field in an NMR experiment. This decay occurs via interactions between the nucleus under investigation (^1H here) and the surrounding material (lattice), which is usually referred to as spin−lattice relaxation. The H T_1 of interfacial water would be governed by the motional correlation times of the interfacial water molecules themselves and neighboring molecules or molecular segments that are communicating with the interfacial water molecules via ^1H (interfacial)−^1H (interfacial), ^1H (interfacial)−^1H (bulk), and ^1H (interfacial)−^{13}C (C_{60}) dipolar interactions.

T_1 measurements were performed on the water immediately adjacent to the C_{60} by

performing a $^{1}H–^{13}C$ CP experiment after a variable delay (Figure 8.1A). T_1 is obtained from the intensity of magnetization M(τ) measured after delay τ via[40]

$$\ln(1 - M_z(\tau)) = \ln 2 - \frac{\tau}{T_1} \tag{8.1}$$

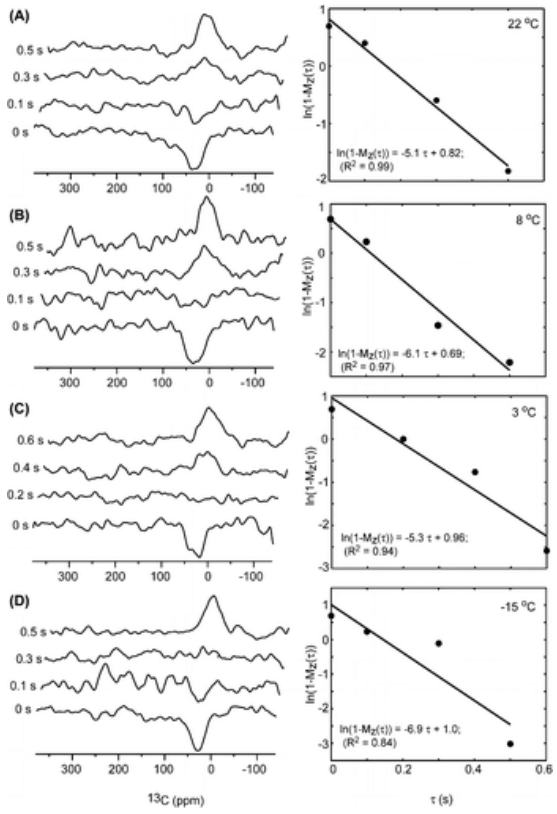

Figure 8.5. Results from variable temperature ^{1}H T_1 measurements of surface water. Shown are inversion recovery profiles of $^{1}H–^{13}C$ CP spectra and the graph of resultant T_1 fitting data for measurements at 22, 8, 3, and −15 °C. The variable delay time, τ, is designated on the left of each $^{1}H–^{13}C$ CP spectrum. The signal intensity measured at τ = 0 s is normalized to −1. The linear regression equation obtained for each temperature set is included in each graph. The regression coefficients for the least-squares data fittings were 0.99 (A), 0.97 (B), 0.94 (C), and 0.84 (D). T_1 relaxation times are summarized in Table 8.1.

The values of T_1 at various temperatures are shown in Table 8.1. For comparison, we have also measured T_1 of the same sample via DP (Figure 8.1B). Whereas the CP T_1 measurement is

selective for water molecules adjacent to the C_{60}, the DP measured T_1 of protons in the entire sample and is dominated by the bulk signal. Results are shown in Figure 8.6, and the T_1 values are also in Table 8.1.

Table 8.1. T_1 Values of Bulk Water and Surface Water as a Function of Temperature

Temperature (°C)	Bulk Water T_1 (s)	Surface Water T_1 (s)
22	3.48 ± .01	0.20 ± .01
8	2.92 ± .01	0.20 ± .02
3	2.48 ± .02	0.20 ± .03
-15	1.51 ± .03	0.2 ± . 1

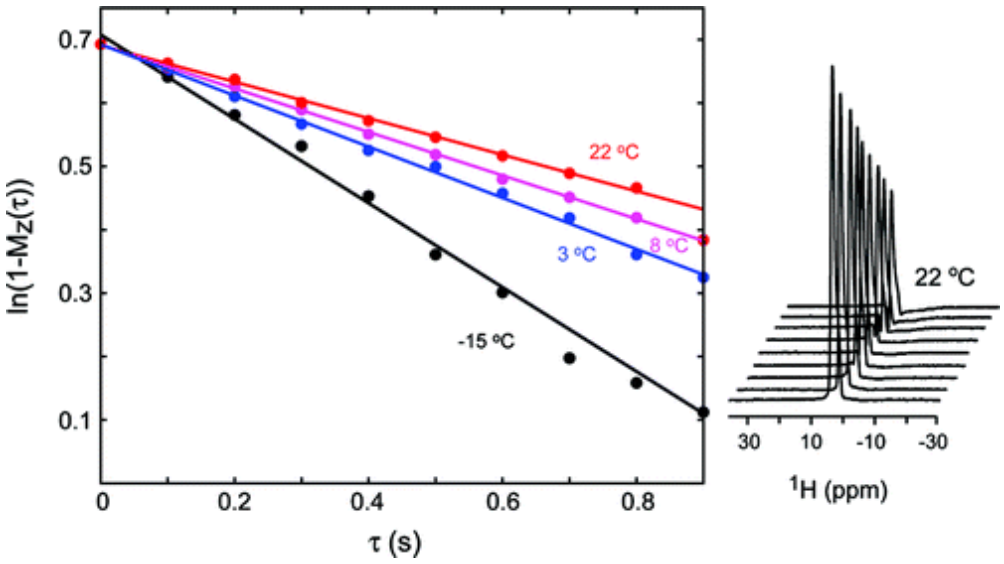

Figure 8.6. Inversion recovery T_1 data for the protons in bulk water measured at 22, 8, 3, and −15 °C. An example of inversion recovery spectra of ^{1}H measured at 22 °C by varying the delay time τ is shown on the right of the graph. The signal intensity measured at τ = 0 s at each temperature set is normalized to −1. The regression coefficients for the least-squares data fittings were 0.998 (22 °C), 0.999 (8 °C), 0.997 (3 °C), and 0.993 (−15 °C).

The first point to note from Table 8.1 is that, for bulk water, both the magnitude of T_1 and the decrease in T_1 with temperature are normal for spin systems in extreme narrowing regimes with short correlation times,[40] that is, for a small molecule in a low viscosity medium, and are

reasonable for water in bulk water. In this regime, as correlation time increases T_1s decreases; correlation time would get longer as the water molecules go from liquid to ice state. The T_1s for the surface water are much smaller than those for bulk water and smaller even than those for ice. Furthermore, T_1 for the surface water is almost independent of the temperature. The smaller values of T_1 and the independence or increase in T_1 with lower temperature is more typical of a solid with a long correlation time between the motion of adjacent spins.[40] The independence would indicate that the structured water around C_{60} is a strongly associated network and the constituent water molecules have a high energy barrier to rotation. Thus, the surface water is acting like a molecule in solid with restricted motion, a result that is consistent with the observation of the CP signal. Unfortunately, we are not able to offer a quantitative description of the correlation times.

Finally, we note that we have used two different samples of C_{60} from two different manufacturers, both with purities $\geq$ 99 %. Both the natural abundance and the ^{13}C-enriched samples gave a CP signal, and both of the signals showed a chemical shift around 50 ppm, validating this as the correct frequency position. Furthermore, the enriched sample gave a CP signal that was roughly enhanced in proportion to the enrichment. This is strong evidence that the measured CP signal arises from C_{60} and not from contamination, since the C_{60} is what was labeled, and there would be no means for a contamination ^{13}C peak to increase upon labeling.

8.4. CONCLUSION

In summary, we show that water near C_{60} molecules in clusters is anisotropic, and its motion is hindered relative to bulk water in the temperature range of 3−22 °C, when bulk water is liquid; the situation is depicted in Figure 8.7. Thus, this study provides one example of water being immobilized by a hydrophobic substance. The surface-selective examination of water adjacent to a hydrophobic material is made possible through a novel application of cross-polarization NMR experiments in the liquid state. The CP experiment is surface-selective because dipolar coupling decays on a molecular length scale. Future work involving theoretical calculations may help to elucidate the currently unknown rotational correlation time of C_{60} aggregates, as well as the structure of the water around the aggregates, which would provide valuable insight for better interpreting our NMR data.

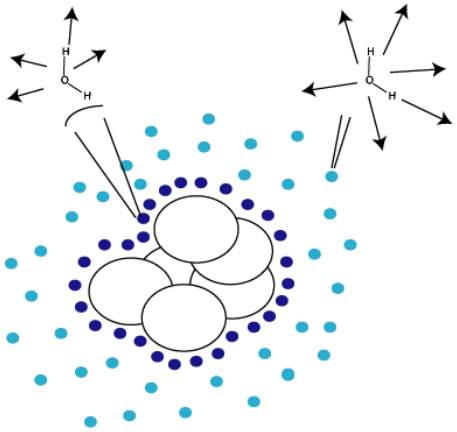

Figure 8.7. Schematic of the envisioned aqueous C_{60} sample. The ordered surface water phase (dark blue circles), disordered bulk water phase (light blue circles), and C_{60} aggregate (cluster of white circles) are shown, along with blown-up views of a surface and bulk water molecule. It is imagined that the surface water would have freedom to tumble and move laterally in all directions, with a short correlation time (long arrows), while the surface water would be much more restricted in its lateral and tumbling motions (short arrows) due to strong associations with other surface water molecules and proximity to C_{60} (curved surface in blown-up view).

The technique that we describe, in common with other NMR techniques, is limited to atoms with quantized nuclear spin states and is easier to interpret for atoms with a spin-quantum number of $I = {}^1/_2$, for example, ^{1}H, ^{13}C, ^{19}F, and ^{31}P. The use of CP requires a pair of different nuclei. In surface selective studies, each of the pair must be in only one of the phases. For example, the interface between a fluorocarbon solid or liquid and water could also be studied, but for hydrocarbon−water studies, a deuterated hydrocarbon would be required.

References

(1) Nelson, D. L.; Cox, M. M. *Lehninger Principles of Biochemistry*; 4 ed.; W.H. Freeman and Company: New York, 2005.

(2) Pratt, L. R.; Pohorille, A. *Chem. Rev.* **2002**, *102*, 2671.

(3) Lum, K.; Chandler, D.; Weeks, J. D. *J. Phys. Chem. B* **1999**, *103*, 4570.

(4) Luzar, A. *Faraday Discuss.* **1996**, *103*, 29.

(5) Benjamin, I. *Chem. Rev.* **1996**, *96*, 1449.

(6) Hopkins, A. J.; McFearin, C. L.; Richmond, G. L. *Curr. Opin. Solid State Mater. Sci.* **2005**, *9*, 19.

(7) Tarbuck, T. L.; Ota, S. T.; Richmond, G. L. *J. Am. Chem. Soc.* **2006**, *128*, 14519.

(8) Ye, S.; Nihonyanagi, S.; Uosaki, K. *Phys. Chem. Chem. Phys.* **2001**, *3*, 3463.

(9) Tian, C. S.; Shen, Y. R. *Proc. Natl. Acad. Sci. U.S.A.* **2009**, *106*, 15148.

(10) Poynor, A.; Hong, L.; Robinson, I. K.; Granick, S.; Zhang, Z.; Fenter, P. A. *Phys. Rev. Lett.* **2006**, *97*, 266101.

(11) Mezger, M.; Reichert, H.; Scho?der, S.; Okasinski, J.; Schro?der, H.; Dosch, H.; Palms, D.; Ralston, J.; Honkimaki, V. *Proc. Natl. Acad. Sci. U.S.A.* **2006**, *103*, 18401.

(12) Steitz, R.; Gutberlet, T.; Hauss, T.; Klosgen, B.; Krastev, R.; Schemmel, S.; Simonsen,
A. C.; Findenegg, G. H. *Langmuir* **2003**, *19*, 2409.

(13) Buch, V.; Milet, A.; Vacha, R.; Jungwirth, P.; Devlin, J. P. *Proc. Natl. Acad. Sci. U.S.A.* **2007**, *104*, 7342.

(14) Kropman, M. F.; Bakker, H. J. *Science* **2001**, *291*, 2118

(15) Haw, J. F.; Nicholas, J. B.; Xu, T.; Beck, L. W.; Ferguson, D. B. *Acc. Chem. Res.* **1996**, *29*, 259.

(16) Parmer, J. F.; Dickinson, L. C.; Chien, J. C. W.; Porter, R. S. *Macromolecules* **1987**, *20*, 2308.

(17) Gobbi, G. C.; Silvestri, R.; Russell, T. P.; Lyerla, J. R.; Fleming, W. W.; Nishi, T. *J. Polym. Sci., Part C: Polym. Lett.* **1987**, *25*, 61.

(18) Weaver, D. R.; Raschke, T. M.; Levitt, M. *J. Phys. Chem. B* **2008**, *112*, 2981.

(19) Li, L. W.; Bedrov, D.; Smith, G. D. *J. Chem. Phys.* **2005**, *123*, 204504.

(20) Jafvert, C. T.; Kulkarni, P. P. *Environ. Sci. Technol.* **2008**, *42*, 5945.

(21) Avdeev, M. V.; Khokhryakov, A. A.; Tropin, T. V.; Andrievsky, G. V.; Klochkov, V. K.; Derevyanchenko, L. I.; Rosta, L.; Garamus, V. M.; Priezzhev, V. B.; Korobov, M. V.; Aksenov, V. L. *Langmuir* **2004**, *20*, 4363.

(22) Duncan, L. K.; Jinschek, J. R.; Vikesland, P. J. *Environ. Sci. Technol.* **2008**, *42*, 173.

(23) Chang, X. J.; Vikesland, P. J. *Environ. Pollut.* **2009**, *157*, 1072.

(24) Lecoanet, H.; Hotze, M.; Wiesner, M. *Environ. Sci. Technol.* **2005**, *39*, 6343.

(25) Chaplin, M.; Blitz, J. P.; Gunko, V. M. In *Proceedings of the NATO Advanced Research Workshop on Surface Chemistry in Biomedical and Environmental Science* Kiev, Ukraine, 2005, p 1.

(26) Andrievsky, G. V.; Klochkov, V. K.; Bordyuh, A. B.; Dovbeshko, G. I. *Chem. Phys. Lett.* **2002**, *364*, 8.

(27) Fung, B. M.; Khitrin, A. K.; Ermolaev, K. *J. Magn. Reson.* **2000**, *142*, 97.

(28) Raiford, D. S.; Fisk, C. L.; Becker, E. D. *Anal. Chem.* **1979**, *51*, 2050.

(29) Harris, R. K. *Nuclear Magnetic Resonance Spectroscopy*; Pitman: London, 1983.

(30) Johnson, R. D.; Yannoni, C. S.; Dorn, H. C.; Salem, J. R.; Bethune, D. S. *Science* **1992**, *255*, 1235.

(31) Tycko, R.; Haddon, R. C.; Dabbagh, G.; Glarum, S. H.; Douglass, D. C.; Mujsce, A. M. *J. Phys. Chem.* **1991**, *95*, 518.

(32) Yannoni, C. S.; Johnson, R. D.; Meijer, G.; Bethune, D. S.; Salem, J. R. *J. Phys. Chem.* **1991**, *95*, 9.

(33) Bagchi, B. *Chem. Rev* **2005**, *105*, 3197.

(34) Coridan, R. H.; Schmidt, N. W.; Lai, G. H.; Godawat, R.; Krisch, M.; Garde, S.; Abbamonte, P.; Wong, G. C. L. *Phys. Rev. Lett.* **2009**, *103*, 237402.

(35) Lee, D. K.; Kwon, B. S.; Ramamoorthy, A. *Langmuir* **2008**, *24*, 13598.

(36) Balasubramanian, S.; Pal, S.; Bagchi, B. *Phys. Rev. Lett.* **2002**, *89*, 115505.

(37) Xu, H. F.; Berne, B. J. *J. Phys. Chem. B* **2001**, *105*, 11929.

(38) Fileti, E. E.; Rivelino, R. *Phys. Rev. Lett.* **2009**, *467*, 339.

(39) Johnson, R. D.; Meijer, G.; Bethune, D. S. *J. Am. Chem. Soc.* **1990**, *112*, 8983.

(40) Levitt, M. *Spin Dynamics: Basics of Nuclear Magnetic Resonance*, 2001.

Chapter 9
Conclusions

9.1. General Statement

Due to the ability of ssNMR to probe samples in their practical forms (i.e. the polymer membranes discussed herein), determine molecular motion and geometry over timescales ranging from nanoseconds to seconds, understand a molecule's conformation/spatial arrangement by using the orientation dependence of spin interactions, and its non-destructive measurement nature, it is an ideal technique to solve a great number of scientific problems today. Hence, there is a drive in the field of NMR science to find new applications, and the goal of the work in this dissertation was to demonstrate some of ssNMR's strengths and application areas by way of demonstrating its value for understanding different systems, particularly polymers and biomembranes. Additional topics which were not explicitly related to membranes was the study of the interface between water and hydrophobic molecules, and distance measurement using homonuclear dipolar coupling.

9.2. Polymer Dynamics[1-3]

This dissertation highlighted work on two polymer systems. First was discussed the investigation of the water permeation and dynamics-transport correlations of the K^+ salt form disulfonated poly(arylene ether sulfone) (PAES) random copolymer (BPS-20) blended with poly(ethylene glycol) (PEG) oligomers (BPS20_PEG). BPS-20 is being developed as an alternative reverse osmosis (RO) membrane to the state-of-the art-material, aromatic polyamide (PA), because it is stable to chlorine degradation. Cross-polarization magic-angle-spinning ssNMR spectra of BPS-20 and PA under different chlorine exposure conditions demonstrated their respective tolerances by changes in aromatic ^{13}C signals for PA, reflecting the replacement of aromatic protons by chlorine, that did not occur in BPS-20. PEG acts as a plasticizer, and was blended with BPS-20 to improve its unacceptably low water permeation. The PEG oxyethylene units undergo ion-dipole interactions with up to 7 K^+ ions, which causes pseudoimmobilization of the BPS-20 chains and promotes strong interactions between PEG and BPS-20. The

plasticization effect and the presence of ion-dipole interactions were evidenced by shorter ^{1}H spin-lattice relaxation times (T_1) and rotating-frame spin-lattice relaxation times ($T_{1\rho}$) of BPS-20 aromatic methine ^{1}Hs and PEG oxyethylene ^{1}Hs, respectively. Shorter T_1 and $T_{1\rho}$ indicates that motions with rates of MHz and kHz, respectively, both increase with PEG addition. The blending resulted in the formation of nanophase separated hydrophobic and hydrophilic domains connected hydrophilic channels, features that are favorable for increases in free volume, water uptake, and water permeation. After exploring blends with different PEG sizes (M_n = 0.6, 1, or 2 kDa), at 5 or 10 weight percent (relative to BPS-20), it was found that the blend with 0.6 kDa at 10 weight percent had the best water permeability. Atomic force microscopy showed that the lower M_n PEG blends had well dispersed domains, while the 2 kDa PEG lead to tortuous channels that were detrimental for water permeation. Results from these measurements could be correlated to the ssNMR results, where the samples with the best water permeability had the shortest T_1 and $T_{1\rho}$ times. Furthermore, using variable temperature ^{1}H T_1 measurements, a thermal annealing effect in BPS-20 was evidenced. Overall, by comparisons with measurements employing additional analytical methods, it was possible to develop *ad hoc* empirical correlations between the molecular-level attributes, obtainable by ssNMR, and macroscopic properties.

The second polymer system mentioned was PAES polymers modified by the addition of 1,4-cyclohexylene ring segmented blocks for the development of PAES with better temperature and solvent stability. Four analogues, incorporating segments consisting of purely aromatic, aromatic and aliphatic, or purely aliphatic rings, were explored using ssNMR experiments on the aromatic ^{1}H and ^{13}C sites of the PAES phenylene rings. Segments that had more conformational freedom produced shorter ^{1}H T_1 and longer ^{1}H $T_{1\rho}$ times. It was observed that the trend in T_1 followed that of polydispersity, which shows that blends with a greater portion of long chains have longer correlation times for MHz scale vibrational motions. Results of the centerband-only detection of exchange (CODEX) experiment, analyzed assuming an isotropic rotational diffusion model with a log-Gaussian distribution of correlation times, showed that correlation times for polymer chain rotations became longer and more dispersed as the conformation flexibility of the segment improved. The long correlation times from CODEX for the bulkier segments, along with their corresponding longer $T_{1\rho}$ values, could be due to restrictions on motion considering

their size, and the possibility of multiple motional modes existing. Finally, two-dimensional wideline separation spectroscopy (WISE) evidenced changes in the ^{1}H-^{1}H homonuclear dipolar coupling network resulting from the addition of different segmented blocks.

9.3. Peptide-Induced Membrane Perturbations[4]

An interesting class of membrane acting peptides, antimicrobial peptides (AMPs), hold much promise as disease therapies because they are potential treatments themselves, and a better understanding of their modes of action could fuel the synthesis of novel drugs. To exploit their therapeutic potential though, it is necessary to gain a molecular-level understanding of peptide-lipid supramolecular assemblies resulting from AMP-membrane interactions. To this effect, lipid molecules in oriented phospholipid bilayers prepared between coverglass plates, exposed to AMPs magainin-2 and aurein-3.3, were monitored using static ^{31}P and ^{2}H ssNMR. ^{31}P and ^{2}H ssNMR allows selective measurement of hydrophilic phosphate headgroups and hydrophobic acyl chains, respectively. Selective measurement can be very informative because the phosphate heads make up outer boundaries of the bilayer , and the acyl chains the interior, so this methodology allows one to follow interactions occurring in different parts of the membrane. Experiments on bilayers of different lipid compositions employed peptide:lipid (P:L) molar ratios of 1:80, 1:50, and 1:20. Resulting experimental anistropic lineshapes were able to be simulated using a published analysis procedure[4] that assumes toroidal pore or thinned membrane lipid (dimple) geometries with various lipid lateral diffusion coefficients (here, $\leq 10^{-11}$ cm^2/s for toroidal pores, and $10^{-7} - 10^{-8}$ cm^2/s for thinned membrane dimples). A torodial pore could be visualized as the inside of a donut, and the d/b ratio, which describes the shape, can be used to visualize how curved the pore walls are; a higher d/b represents greater curvature. In each case, greater perturbations in the lipid bilayer were observed through ^{2}H spectra, evidencing more significant interactions between the AMP and lipid acyl chains. Decreasing anisotropic frequency spans in ^{31}P and ^{2}H spectra were attributed to thinned membrane regions existing in the bilayer along with toroidal pores.

Three oriented lipid bilayer compositions were explored. For pure POPC-d_{31} oriented bilayers, which could mimic the zwitterionic environment of eukaryotic cell membranes, both peptides induced toroidal pores with decreasing d/b ratios as concentration increased, with

aurein-3.3 producing the lower ratios. A lipid composition of POPC-d_{31}/POPG (3:1 molar ratio) was used to create anionic lipid membranes that would mimic the environment of prokaryotic cells. Compared to the pure POPC-d_{31} case, the only difference with magainin-2 was greater narrowing of the frequency span of ^{2}H spectra, which would indicate membrane thinning with a fast lipid lateral diffusion rate; for aurein-3.3 though, d/b significantly increased. Finally, the impact of cholesterol was explored by incorporation in POPC-d_{31} oriented bilayers (1:1 molar ratio). Cholesterol is a key component of eukaryotic cell membranes that restricts the mobility of neighboring lipids, and its presence in the experimental setup would be important for gaining more of a real-world perspective on peptide-lipid interactions in humans. Oriented bilayers containing magainin-2 provided lineshapes that matched to toroidal pores with d/b less than that observed in the pure POPC-d_{31} case, and for aurein-3.3 d/b was larger except for the P:L = 1:20 condition. All ^{2}H spectra exhibited higher ^{2}H quadrupole coupling (QC) parameters, but not ^{31}P CSA values, compared to the pure POPC-d_{31}/peptide system. Higher QC or CSA values correspond to more restricted motion, so this result indicates that cholesterol affects the mobility of the lipid chains, but has a negligible effect on the motion of the headgroups.

9.4. Selection of Individual ^{13}C-^{13}C Dipolar Interactions[5]

Exploitation of dipolar coupling interactions between spin pairs, which depend on r^{-3} (r = internuclear distance), is a cornerstone method in NMR for structure determination. Within ^{13}C NMR, the maximum information content would come from a molecule that is uniformly/ extensively ^{13}C-labeled, but this brings the difficulty that the informative, long-range interactions are obscured by those of short-range pairs (dipolar truncation). A novel two-dimensional (2D) ^{13}C- ^{13}C dipolar recoupling technique utilizing longitudinal mode $C3_3^1$ mixing,[6-8] DTOCSY, that allows the observation of long-range interactions in the presence of short-range couplings, and the selection of specific ^{13}C-^{13}C pairs using frequency selective pulses, was introduced. DTOCSY holds advantages over the TDR method[9] on which it is based, including that it is suitable for protonated solids because it longitudinal mixing mode allows for lower power ^{1}H-^{13}C decoupling. After trying various heteronuclear decoupling schemes with different powers, 128 kHz of continuous wave (CW) decoupling proved optimal. DTOCSY was demonstrated on uniformly ^{13}C-labled Glutamine and selectively ^{13}C-labeled Glycine-Alanine-Leucine (GAL).

With recoupling of all dipolar pairs in GAL, it was even possible to observe coupling between C′ (Alanine) and C^{δ} (Leucine), a 6-bond separation, in the presence of directly bonded C^{α}-C′ (Leucine) coupling. By using Gaussian or cosine-modulated Gaussian pulses, it is even easier to observe correlations between long-range pairs because this step maintains the coupling between the two irradiated nuclei, but removes their coupling with other non-selected spins within the system.

9.5. Evidencing Hydrophobic Hydration by ssNMR[10]

Interactions involving water at the interface of hydrophobic molecules is of great interest in science, but the system is difficult to study because the selection of interfacial water is hindered by it being in the presence of the much more abundant bulk water. We demonstrated by static ^{1}H-^{13}C CP ssNMR the ability to detect a hydration shell around a model hydrophobic molecule, C_{60}. The experiment took advantage of the short distance range ($\leq$ 1 nm) accessible by CP, and the fact that interfacial water, due to ordered structuring around C_{60}, would be slow enough for ^{1}H-^{13}C heteronuclear coupling to be maintained. Though rotational correlation time was not directly measured, the maintenance of dipolar coupling would suggest that the rotational correlation time of interfacial water is orders of magnitude slower than the bulk. Variable temperature CP experiments on an aqueous C_{60} solution provided ^{13}C signals at temperatures above the freezing point of water, with the greatest signal intensity at 3°C, evidencing an ordered water structure around C_{60} that became thermally disrupted at higher temperatures. Variable temperature ^{1}H T_1 experiments showed that bulk water T_1s were longer than those of surface water, demonstrating a shorter rotational correlation time for bulk water. Furthermore, while bulk water T_1s decreased with temperature, those for surface water stayed fairly constant.

References

(1) Spano, J.; Zhang, B.; Chen, Y.; Turner, R.; Wi, S. *J. Polym. Sci. B: Polym. Phys.* **submitted.**

(2) Lee, C. H.; VanHouten, D.; Lane, O.; McGrath, J. E.; Hou, J.; Madsen, L. A.; Spano, J.; Wi, S.; Cook, J.; Xie, W.; Oh, H. J.; Geise, G. M.; Freeman, B. D. *Chem. Mater.* **2011**, *23*, 1039.

(3) Lee, C. H.; Spano, J.; McGrath, J. E.; Cook, J.; Freeman, B. D.; Wi, S. *J. Phys. Chem. B* **accepted for publication.**

(4) Kim, C.; Spano, J.; Park, E.-K.; Wi, S. *Biochim. Biophys. Acta Biomembr.* **2009**, *1788*, 1482.

(5) Spano, J.; Wi, S. *J. Magn. Reson.* **2010**, *204*, 314.

(6) Carravetta, M.; Eden, M.; Zhao, X.; Brinkmann, A.; Levitt, M. H. *Chem. Phys. Lett.* **2000**, *321*, 205.

(7) Eden, M.; Levitt, M. H. *J. Chem. Phys* **1999**, *111*, 1511-1519.

(8) Brinkmann, A.; Levitt, M. H. *J. Chem. Phys.* **2001**, *115*, 357-384.

(9) Marin-Montesinos, I.; Mollica, G.; Carravetta, M.; Gansmuller, A.; Pileio, G.; Bechmann, M.; Sebald, A.; Levitt, M. H. *Chem. Phys. Lett.* **2006**, *432*, 572.

(10) Wi, S.; Spano, J.; Ducker, W. A. *J. Phys. Chem. C* **2010**, *114*, 14986-14991.